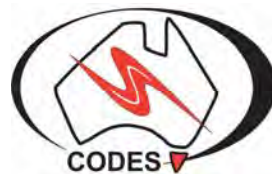


# **Petrophysical Characterization of Comminution Behavior**

**Adel Vatandoost**

MSc. Geophysics, University of Tehran, 2002  
BSc. Mining Engineering, University of Tehran, 1999

Submitted in fulfilment of the requirements for the degree of  
Doctor of Philosophy (Geometallurgy)



ARC Centre of Excellence in Ore Deposits  
University of Tasmania  
December 2010



## Statement of Originality \_\_\_\_\_

This thesis contains no material that has been accepted for a degree or diploma by the University of Tasmania or any other institution, except by way of background information which is duly acknowledged in the thesis, and to the best of the candidate's knowledge and belief, contains no material previously published or written by another person, except where due acknowledgement is made in the text of the thesis.

Adel Vatandoost

Date:

## Authority of Access \_\_\_\_\_

This thesis is confidential to the sponsors of the AMIRA P843 project and shall not be made available for loan, or copying in accordance with the *Copyright Act 1968*, until 1<sup>st</sup> January 2011.

Adel Vatandoost

Date:



## Statement of Co-authorship \_\_\_\_\_

This research was conducted as a component of the major AMIRA P843 project on Geometallurgical Mapping and Mine Modeling. The author contributed to this research program as part of a large team of researchers but had primary responsibility for the conduct of the petrophysical research program within P843.

Several conference papers have been published by the candidate and his supervisors in the course of this research. Chapter 3 has been partly published as a scientific manuscript in co-authorship with supervisors Dr. Peter Fullagar and Dr. Michael Roach. Some sections of Chapters 2 and 6 have also been published in co-authorship with Dr. Peter Fullagar. Chapter 5 has been partly published in co-authorship with Dr. Peter Fullagar, Prof. Steve Walters and Dr. Toni Kojovic.

Dr. Peter Fullagar has developed the linear programming algorithm as used and clearly referenced in Chapter 7. The candidate had the main responsibility for data collection, analysis, interpretation, modeling, documentation and presentation. Comminution data were provided by Dr. Simon Michaux and Dr. Toni Kojovic. The supervisors contributed to data analysis and interpretation of result. A series of programs developed by Dr. Peter Fullagar was used during data processing.

The candidate planned the thesis outline and was responsible for writing the full thesis. Dr. Peter Fullagar, Dr. Michael Roach and Prof. Steve Walters provided editorial assistance on all chapters.



# Abstract

---

Comminution or feed size reduction is typically the first stage of ore processing at mines. Comminution tests are commonly conducted to assess the processing behavior of ore and to aid in process design and equipment selection. Testing for Bond mill work index (BMWi), a measure of the ore grindability, and  $A^*b$ , a measure of the ore crushability, is common in this regard. These destructive tests are expensive and time consuming and, hence, are conducted on a limited number of large volume samples which in most cases are not representative of the entire orebody. Therefore alternative means are desirable for efficiently characterizing comminution behavior.

Petrophysical properties have the potential for effective characterization of ore comminution behavior for a truly representative suite of samples. Petrophysical measurements are quick, non-destructive, and relatively cheap. Petrophysical data can be recorded either downhole or on core. If calibrated against measures of ore crushability and grindability, petrophysically-based models could provide virtually continuous downhole prediction of comminution attributes in intervals of drill holes where these parameters are not available. This thesis presents a new approach for characterization of ore comminution behavior based on petrophysical measurements.

As an alternative to downhole geophysical logging, a Geotek multi-sensor core logger (MSCL) was evaluated. Density, P-wave velocity, P-wave amplitude and magnetic susceptibility, as well as core imagery, were measured on drill cores from two Australian copper-gold deposits, namely Cadia-East, NSW, and Ernest Henry, QLD. The Geotek system had never previously been used at metalliferous mines. It provides data with acceptable accuracy if carefully and systematically calibrated but the data quality is adversely affected by the small size and condition of the core. The accuracy achieved in production logging was approximately  $\pm 1.35\%$  for density,  $\pm 6.5\%$  for P-wave velocity, and  $\pm 1\%$  for magnetic susceptibility.

The relationships between petrophysical properties and comminution attributes ( $A^*b$  and BMWi) was directly investigated, since small-scale comminution tests had been performed on selected 2m intervals of the same drill core. At Cadia East, the ore is hard in terms of both crushing and grinding. At Ernest Henry the ore is more variable but generally softer.

In most cases the relationship between petrophysical properties and comminution parameters is dependent on ore type. Hence class-based approaches for comminution modeling were devised and implemented. Crushability ( $A^*b$ ) can be related to petrophysical properties more reliably than grindability (BMW<sub>i</sub>). This is consistent with the fact that petrophysical properties and crushability are measured on whole rock while BMW<sub>i</sub> is measured on crushed composite samples. Prediction of high BMW<sub>i</sub> materials (>10 kWh/t) proved difficult, perhaps because particles are more competent at crushed size.

An important outcome is that magnetic susceptibility is a good indicator of  $A^*b$  at both sites and can be used to define different comminution domains. At Ernest Henry, as susceptibility increases  $A^*b$  increases (samples are easier to crush) because magnetite acts as crack initiator. At Cadia East, ore becomes harder to crush as susceptibility increases; the association of feldspar with magnetite was most probably the reason for the low values of  $A^*b$  in this case.

At Ernest Henry, models were developed for prediction of  $A^*b$  and BMW<sub>i</sub> values in depth intervals where petrophysical measurements are available but comminution test data are not. Four petrophysical classes were defined based on P-wave velocity, P-wave amplitude, density and susceptibility using cluster analysis. Regression models were developed for  $A^*b$  and BMW<sub>i</sub> using petrophysical properties for each class. The overall root mean square (RMS) error of prediction for BMW<sub>i</sub> and  $A^*b$  are 1.39 kWh/t and 27.3 respectively.

Comminution modeling at Cadia East was difficult due to the limited variability of comminution parameters. Four classes were defined based on variability of  $A^*b$  and BMW<sub>i</sub> around their respective mean values.  $A^*b$  and BMW<sub>i</sub> were then linked to petrophysical properties and assays using a neural network approach. The performance of neural networks for prediction of comminution classes was tested by successively treating each hole as an independent hole. The prediction accuracy ranged from 51% to 77%.

A novel approach for prediction of petrophysical properties and comminution attributes from core images was also investigated at Ernest Henry. Estimates of mineral abundance from classified core images were first adjusted to achieve compatibility with assay data. Bulk density was then predicted from mineral volumes and densities with a relative error of prediction of 3.5%. Regression coefficients for  $A^*b$  and BMW<sub>i</sub> were estimated for each mineral phase via least squares optimization. This method provides a means for

prediction of  $A^*b$  and  $BMWi$  in depth intervals where classified imagery is available but comminution test data are not. The RMS errors of prediction for  $A^*b$  and  $BMWi$  are 33.3 and 1.68 kWh/t respectively.

The two case studies from different geological environments show that petrophysical data can provide useful information for characterization of comminution behavior and hence prediction of mill throughput. Petrophysics-based comminution models have limitations but they are adequate for use during process planning. The accuracy of such models can be improved by reducing uncertainties in petrophysical and comminution measurements, refining data classification techniques, by increasing the number of petrophysical properties recorded, and by incorporating other data including assays in the analysis.



# Acknowledgments

---

First and foremost, I would like to thank my wife, Maryam, for all her support, patience, love and encouragements.

I would like to extend my sincere thanks to my supervisors, Dr. Michael Roach, Dr. Peter Fullagar and Prof. Steve Walters. I am grateful to Michael for his help, support and for his numerous useful comments and suggestions on this thesis. I am indebted to Peter for his help, guidance and great ideas during the course of this research, and for his invaluable comments on all chapters of this thesis. I sincerely wish to thank Steve for the generous financial support of my research and for his critical comments to improve this thesis.

This research was part of a major collaborative geometallurgical project being undertaken at CODES (University of Tasmania), JKMRC and BRC (The University of Queensland) and CSIRO (Division of Exploration and Mining). I would like to acknowledge financial support from CODES and industry sponsors of the AMIRA International P843 GEM<sup>III</sup> Project—Anglo Gold Ashanti, Anglo Platinum, Barrick, BHP Billiton, Codelco, Datamine, Golder Associates, GEOTEK, ioGlobal, Metso Minerals, Newcrest, Newmont, Oz Minerals, Peñoles, Rio Tinto, Teck Cominco, Vale, Vale Inco and Xstrata Copper.

I would like to thank GEM<sup>III</sup> project team members for their collaborations throughout the project. I have benefited from the technical discussions that I had with many people at the project. In particular I am grateful to Dr. Toni Kojovic and Dr. Ron Berry for their help and technical advice on various occasions. I would like to thank Xstrata Copper and Newcrest site personnel for their onsite help and support. Many thanks to Dr. Pedro Carrasco and Marcella Oyarzun for giving me the opportunity to visit Andina mine, Chile. Thank you to Dr. Dariush Nadri for his help in organizing my visit to Curtin University and his assistance in velocity measurements of the rock samples. I am also grateful for the help and administrative assistance provided by many people at CODES including: Peter Cornish, Keith Dobson, June Pongratz, Simon Stevens, Karen Mollross, Helen Scott, and Alexander Cuision.



# CONTENTS

<b>CHAPTER 1 : Introduction</b>	<b>1</b>
1.1. Background and motivation	1
1.2. Research aims and objectives	4
1.3. Methodology	5
1.4. Previous petrophysical work in mining	5
1.5. Research Innovation	7
1.6. Outline of the Thesis	8
<b>CHAPTER 2: Relating Petrophysical Properties to Comminution Parameters</b>	<b>11</b>
2.1. Introduction	11
2.2. Comminution Parameters	12
2.2.1. Bond Mill Work Index (BMWI)	13
2.2.2. JKMRC Rotary Breakage Test (JKRBT)	14
2.3. Destructive Rock Strength Parameters	16
2.3.1. Uniaxial Compressive Strength (UCS)	17
2.3.2. Point Load Index (PLI)	18
2.3.3. Young's Modulus (E)	18
2.4. Non-Destructive Rock Strength Parameters	19
2.4.1. P-Wave Velocity ( $V_p$ )	20
2.4.2. Density ( $\rho$ )	24
2.4.3. P-wave Modulus (M)	25
2.4.4. Acoustic Impedance (Z)	27
2.4.5. Magnetic Susceptibility (k)	27
2.4.6. Electrical Conductivity	28
2.5. Relationship Between Rock Strength and Comminution	29
2.5.1. Rock Strength and Crushability	30
2.5.2. Rock Strength and Grindability	32
2.6. Concluding Remarks	34
<b>CHAPTER 3: Automated Multi-Sensor Core Logger</b>	<b>37</b>
3.1. Introduction	37
3.2. Geotek System	39
3.3. Geotek Sensors	39
3.3.1. Digital Imaging System	40
3.3.2. Core Thickness Sensor	42
3.3.3. Ambient Temperature	43
3.3.4. Gamma Ray Attenuation Density	43
3.3.4.1. Basic principle of measurement	44
3.3.4.2. Gamma Density Precision	44
3.3.4.3. Gamma Density Calibration	46
3.3.4.4. Gamma Density versus Temperature	49
3.3.4.5. Gamma Density Accuracy	50

3.3.5.	Acoustic Velocity	51
3.3.5.1.	Sonic System Delay Time	54
3.3.5.2.	Accuracy of Sonic Velocity	54
3.3.5.3.	Sonic Full Waveform	56
3.3.5.4.	P-wave Amplitude	56
3.3.5.5.	Redesign of the Acoustic Velocity System	56
3.3.6.	Non Contact Resistivity (NCR)	58
3.3.7.	Loop Conductivity Meter	59
3.3.7.1.	Loop Conductivity Meter Calibration	60
3.3.8.	Magnetic Susceptibility	61
3.3.8.1.	Sample Volume Effect	63
3.3.8.2.	Loop Size Correction	63
3.3.8.3.	Susceptibility Volume Correction	65
3.3.8.4.	Temperature Effect	66
3.3.8.5.	Comparison of Measurements	67
3.4.	Core Logging	68
3.4.1.	Core Preparation	68
3.4.2.	Data Acquisition and Processing	69
3.4.3.	Repeatability and Reproducibility	70
3.4.4.	Sampling Intervals	72
3.4.5.	Geotek Core Logging Throughput	74
3.5.	Concluding Remarks	75
<b>CHAPTER 4 : Geometallurgical Modeling Methodology</b>		<b>77</b>
4.1.	Introduction	77
4.2.	Classification Schemes	79
4.2.1.	Geological Classes (GC)	80
4.2.2.	Petrophysical Classes (PC)	81
4.2.3.	Comminution Classes (CC)	82
4.2.4.	Comminution and Petrophysical Classes (CPC)	83
4.3.	Classification Methods	83
4.3.1.	Geological Classification	83
4.3.2.	Cluster Analysis	84
4.3.3.	Relative Average Approach	85
4.4.	Modeling and Prediction	85
4.4.1.	Regression	85
4.4.2.	Minimum Distance Algorithm	88
4.4.3.	Neural Networks	89
4.5.	Geometallurgical Modeling Applications	92
4.5.1.	Process Planning	93
4.5.2.	Process Optimization	94
4.6.	Concluding Remarks	94
<b>CHAPTER 5: Characterization of Comminution Behavior at Ernest Henry Iron-Oxide Cu-Au Mine</b>		<b>97</b>
5.1.	Introduction	97
5.2.	Geology of Ernest Henry Mine	99
5.3.	Data Collection Summary	100

5.4.	Petrophysical Data Processing	101
5.5.	Quality of Petrophysical Data	102
5.6.	Petrophysical Data Interpretation	105
5.6.1.	Petrophysical Data from Borehole EH635	107
5.6.2.	Petrophysical Data from Borehole EH633	109
5.6.3.	Petrophysical Data from Borehole EH574	111
5.6.4.	Petrophysical Data from Borehole EH556	113
5.6.5.	Petrophysical Data from Borehole EH446	115
5.6.6.	Petrophysical Data from Borehole EH432	117
5.7.	Petrophysical Signature of Ernest Henry	119
5.8.	Comminution Modelling	124
5.8.1.	Comminution Modelling : GC Approach	127
5.8.2.	Comminution Modelling : PC Approach	129
5.8.3.	Comminution Modelling : CC Approach	136
5.8.4.	Comminution Modelling : CPC Approach	140
5.9.	Mill Throughput Modelling	142
5.10.	Concluding Remarks	147
<b>CHAPTER 6 : Characterization of Comminution Behavior at Cadia East Au-Cu Porphyry Deposit</b>		<b>151</b>
6.1.	Introduction	151
6.2.	Geology of Cadia East Deposit	153
6.3.	Data Collection Summary	155
6.4.	Quality of Petrophysical Data	157
6.5.	Petrophysical Data Processing	158
6.6.	Petrophysical Data Interpretation	159
6.6.1.	Petrophysical Data from Borehole CE082	160
6.6.2.	Petrophysical Data from Borehole CE098	163
6.6.3.	Petrophysical Data from Borehole CE109	165
6.6.4.	Petrophysical Data from Borehole CE110	167
6.6.5.	Petrophysical Data from Borehole CE143	170
6.7.	Petrophysical Signatures of Cadia East	172
6.8.	Comminution Modeling	174
6.8.1.	Comminution Modeling: GC Approach	182
6.8.2.	Comminution Modeling : PC Approach	184
6.8.3.	Comminution Modeling : CC Approach	185
6.8.4.	Comminution Modeling : CPC Approach	193
6.9.	Mill Throughput prediction	193
6.10.	Concluding Remarks	196
<b>CHAPTER 7: Prediction of Petrophysical Properties from Core Imagery</b>		<b>199</b>
7.1.	Introduction	199
7.2.	Core Image Processing	202
7.3.	Bound Models	203

7.4.	Intrinsic Properties of Minerals	204
7.5.	Prediction of Petrophysical Properties	207
7.5.1.	Prediction of Density from Visual Mineral Grade Estimates	207
7.5.2.	Assay-based Volume Correction of Mineral Phases	209
7.5.3.	Prediction of Density from Core Imagery and Assays	212
7.5.4.	Prediction of Magnetic Susceptibility	214
7.5.5.	Prediction of P-wave Velocity	215
7.6.	Relating Mineral Grades to Comminution Attributes	219
7.7.	Concluding Remarks	222
<b>CHAPTER 8 : Conclusions</b>		<b>225</b>
8.1.	Summary of Main Results	225
8.2.	Relationship Between Petrophysics and Comminution	227
8.3.	GEOTEK Multi-Sensor Core Logger (MSCL) System	228
8.4.	Geometallurgical Modeling : Universal Approach	230
8.5.	Geometallurgical Modeling : Class-based Approach	231
8.5.1.	Ernest Henry Comminution Modeling	231
8.5.2.	Cadia East Comminution Modeling	232
8.6.	Image Based Prediction of Comminution Behavior	233
8.7.	Concluding Remarks	234
<b>Bibliography</b>		<b>237</b>

# LIST OF SYMBOLS/ABBREVIATIONS\_\_\_\_\_

## Symbol/Abbreviation

A*b	A and b are ore specific parameters determined from laboratory testing and their product is related to ore crushing behavior
AMIRA	Australian Mineral Industry Research Association
ANN	Artificial Neural Network
ASTM	American Society for Testing and Materials
BMWi	Bond Ball Mill Work index - a measure of ore grindability
CC	Comminution Classes - an approach for geometallurgical modeling
CMTE	The Cooperative Research Centre for Mining Technology and Equipment
Comminution	First stage in ore processing that involves crushing and grinding of ore materials
CPC	Comminution and Petrophysical Classes - an approach for geometallurgical modeling
Cyclone	A device used in ore grinding circuit for classification of materials at a certain size
DWT	Drop Weight Test – the conventional laboratory method for determination of A*b
E	Young's modulus (GPa) - a measure of a material's elasticity
F <sub>80</sub>	Size at which 80% of the feed passes (µm)
GC	Geological Classes - an approach for geometallurgical modeling
GeM <sup>III</sup>	Geometallurgical Mapping and Mine Modeling Project
GPa	Giga Pascals
HQ	Conventional name for drill core with a diameter of ~60mm
IOCG	Iron Oxide Copper Gold - a type of ore deposit

ISRM	International Society of Rock Mechanics
JKCi	JKMRC Crushing index test - a comparative small scale rock crushing test
JKMRC	Julius Kruttschnitt Mineral Research Centre
JKRBT	JKMRC Rotary Breakage Test - a method for determination of A*b
kHz	Kilo Hertz
$K_r$	Reuss estimate for bulk modulus of elasticity
$K_v$	Voigt estimate for bulk modulus of elasticity
kWh/t	Kilo Watt Hour per ton
M	P-wave modulus of elasticity defined as $\rho V_p^2$
MPa	Mega Pascals
MSCL	Multi-Sensor Core Logger
Mt	Million ton
Mtpa	Million ton per annum
MW	Mega Watt - unit of power
NQ	Conventional name for drill core with a diameter of ~44mm
$P_{80}$	Size at which 80% of the product passess ( $\mu\text{m}$ )
PC	Petrophysical Classes - an approach for geometallurgical modeling
PLI	Point Load Index - a destructive test for determination of material strength
PQ	Conventional name for drill core with a diameter of ~85mm
Pundit	Portable Ultrasonic Non-destructive Digital Indicating Tester - an instrument for measuring the velocity of propagation of ultrasonic mechanical waves.
$R^2$	Regression Coefficient of Determination

REP	Relative Error of Prediction
RMS Error	Root Mean Square Error - a statistical measure for goodness of fit
RMWi	Rod Mill Work index - a test for determination of ore grindability
SAG	Semi-Autogeneous Mill - a type of mill used at grinding circuit
SMC	SAG Mill Comminution Test - a test for rock breakage characterization
$t_{10}$	Breakage index or percent passing 1/10 <sup>th</sup> of the initial particle size
TPH	Ton Per Hour - unit of mill throughput
UCS	Uni-axial Compressive Strength- a destructive test for determination of material strength
$V_i$	Volume fraction of the $i^{\text{th}}$ component
$V_p$	Compressional Wave Velocity (m/s)
$V_s$	Shear Wave Velocity (m/s)
W	Required energy for ore breakage in Kilo Watt Hour per Ton (kWh/t)
Wi	Work index in kWh/t determined during Ball or Rod mill testing- it is indicative of resistance of a material to grinding
WI-5	Batch Ball Mill Operating Work index - a small scale comparative grinding test to rank the grinding behavior of materials
Z	P-wave acoustic impedance
$\rho$	density (g/cc)
$\sigma$	Poisson Ratio



## LIST OF FIGURES

---

Figure 2.1. Schematic of the JKMRC Rotary Breakage Testing device (Kojovic, 2008a). .....	15
Figure 2.2. The relationship between fines produced and specific breakage energy for a single particle size , hard ore, (Kojovic et al, 2008).....	16
Figure 2.3. Unconfined compressive strength for a variety of rock types after Lama and Vutukuri (1978). Each box presents $\pm 25\%$ of the data about the median value (vertical line).....	17
Figure 2.4. Uniaxial compressive strength versus sonic transit time, for sandstones and siltstones of the German Creek Formation, Bowen Basin, Queensland (McNally, 1990) .....	22
Figure 2.5. The relationship between P-wave velocity and Point load index. The red line is the best regression fit to the data. Data compiled from literature (Kahraman and Alber, 2006; Hecht et al., 2005; Karakus and Tutmez, 2006; Kilic and Teymen, 2008). .....	23
Figure 2.6. The relationship between P-wave velocity and Bond work index for sedimentary and volcanic rocks. The relationship established after extracting data from dataset of Deniz and Ozdag (2003). .....	24
Figure 2.7. Relationship between compressive strength and density (Raghu and Ghose, 2006). .....	25
Figure 2.8. Scatter plot of specific gravity and Bond work index for seventeen different ore types. Data compiled by Gupta and Yan (2006). .....	25
Figure 2.9. Degree of liberation versus particle size for three types of ore texture: banded (a), rod (b), and spherical (c) texture models (after Ferrara et al 1989). St is the size of inclusion in the rock model as defined by Ferrara et al (1989).....	29
Figure 2.10. Relationship between $A^*b$ and PLI for Mine to Mill project (MTM) dataset with the P843 Ernest Henry EH512 (EHM) sample results shown in pink (Kojovic, 2008b). The black line is the best fitted regression line (Power).....	30
Figure 2.11. Relationship between $A^*b$ and PLI for P843 project dataset. There is no correlation between PLI and $A^*b$ at Cadia East and Boddington sites but a moderate correlation in the other two sites is evident.....	31
Figure 2.12. Correlation between $A^*b$ and Young's modulus for six ore types at Cerro Colorado copper mine, Chile. Data compiled from Scott et al (1998).....	31
Figure 2.13. Correlation between Bond Work Index and tensile strength (left) and correlation between Bond Work Index and UCS (right). Closed squares are data compiled from Briggs (1991) and open squares are data compiled from Yan (1993) as quoted in Gupta and Yan (2006). Note that the two graphs refer to the same rock samples.....	32
Figure 2.14. Cross plot of UCS and Bond ball mill work index for a data set from 11 different mine (after Doll et al, 2003). .....	33
FIGURE 2.15. THE RELATIONSHIP BETWEEN DYNAMIC BULK MODULUS AND BOND WORK INDEX FOR SEDIMENTARY AND VOLCANIC ROCKS. DATA EXTRACTED FROM DATASET OF DENIZ AND OZDAG (2003).....	33

Figure 3.1. Schematic diagram of a Geotek Multi-sensor core logger.....39

Figure 3.2. Geotek MSCL camera system for capturing half core imagery.....41

Figure 3.3. Geotek RGB raw image and classified image (Berry, 2008a).....41

Figure 3.4. Comparison of core thickness measurement with Geotek thickness sensor and a digital hand held calliper.....43

Figure 3.5. Schematic diagram of gamma density operating system. ....43

Figure 3.6. Gamma density histogram for a 5mm diameter collimated beam, illustrating the improvement in precision afforded by longer integration times.....45

Figure 3.7. Gamma density precision versus integration time for a 5mm diameter collimated beam. An 8 second integration time provides the best compromise between data precision and system productivity. ....45

Figure 3.8. An aluminium cylinder used for gamma density calibration .....46

Figure 3.9. Gamma density calibration regression line for a cylindrical aluminium calibrator, relating count rate to aluminium bulk density.....47

Figure 3.10. An aluminium cylinder machined into steps for gamma density calibration of half cores .....48

Figure 3.11. Variation of gamma count differences for each calibrator thickness. Note that at small thicknesses (close to the size of most archival half cores) the variation is larger.....48

Figure 3.12. Gamma density calibration regression line for two aluminium calibrators ..49

Figure 3.13. Gamma-density temperature sensitivity curve for 60 second integrations through 50mm of aluminum (a) and gamma density variation with temperature for a 50mm diameter aluminium calibration piece (b). Variation is attributed to temperature sensitivity of the gamma ray detector system.....50

Figure 3.14. Comparison of average gamma density measured by the Geotek MSCL versus water immersion density. Gamma densities are calibrated with the cylindrical calibration (Figure 3.8) piece (a) and the half core calibration (Figure 3.10) piece (b). ....51

Figure 3.15. Schematic diagram of P-wave velocity transducers in half core mode of acquisition.....52

Figure 3.16. Schematic diagram of horizontally opposed P-wave velocity transducers in whole core mode of acquisition.....52

Figure 3.17. P-wave signal recorded on a half NQ size core sample. (a) without acoustic gel between the core and core boat. Signal amplitude is significantly attenuated. (b) with acoustic gel between core and core boat. Note the significant improvement in amplitude when compared to (a) and also the subtle differences in the waveform. 53

Figure 3.18. Comparison of average Geotek P-velocity versus average Pundit P-velocity for a series of half cores (a) and for a series of whole cores (b). Note that the vertical mode of measurement was conducted by Geotek MSCL.....55

Figure 3.19. Geotek P-velocity transducers in vertical mode for both half and whole core acquisition.....57

Figure 3.20. Non-contact resistivity response schematic. (a) for a thick zone of homogenous conductive material. (b) for a heterogeneous zone of conductive material.....58

Figure 3.21. Loop Conductivity meter incorporated into the Geotek logger.....	60
Figure 3.22. Conductivity of a core sample recorded using a 63.5mm diameter loop with different frequencies. Note that the vertical bar indicates the calculated standard deviation.....	60
Figure 3.23. Conductivity of aluminium calibrator versus its thickness for 125kHz frequency and 63.5mm loop sensor (a). The vertical bars on data indicate the standard deviation for each thickness. Conductivity versus temperature for a sample fixed in place (b). .....	61
Figure 3.24. The relationship between apparent susceptibility and ratio of loop sensor diameter to sample diameter. ....	62
Figure 3.25. Correlation between apparent magnetic susceptibility as measured using 60mm and 72 mm (a) 60mm and 150mm (b) 70mm and 150mm (c) loop sensors. A 15 point moving average has been applied to the 60mm (b) and 70mm (c) loop data to account for the difference in spatial resolution of the two sensor.....	64
Figure 3.26. Magnetic susceptibility of whole core versus magnetic susceptibility of half cores derived from it. ....	65
Figure 3.27. Schematic section through (half) core.....	66
Figure 3.28. Magnetic susceptibility versus temperature recording for a sample with high susceptibility fixed placed within a loop sensor for about 24hours. The recording has not affected by temperature variations but sensor subject to random fluctuations. ....	67
Figure 3.29. Magnetic susceptibility versus temperature recording for a sample with low susceptibility placed within a loop sensor for about 24hours. There is no evidence of temperature sensitivity but random negative spikes in the data are apparent. ....	67
Figure 3.30. Comparison of Magnetic susceptibility recorded by Geotek and KT-9 Kappameter. ....	68
Figure 3.31. Geotek raw data displayed by MSCL software during core logging.....	70
Figure 3.32. Reproducibility of Geotek MSCL Gamma density .....	71
Figure 3.33. Repeatability of Geotek P-wave velocity (a) P-wave amplitude (b), gamma density (c) and magnetic susceptibility (d) on NQ half-core test pieces.....	72
Figure 3.34. Semivariogram of gamma density (a), P-Velocity (b) and magnetic susceptibility (c) for 20m of cores from Cadia East. Note that the range for density and susceptibility is about 15cm and for P-velocity is about 12cm. ....	73
Figure 3.35. Geotek logging production rate without core imagery. Note that throughput is a user defined function of sampling interval and time required to take a set of measurements.....	74
Figure 4.1. Correlation between X and Y dataset showing a nonlinear (a) and linear (b) regression fit. Note that although the correlation coefficient between the dataset (a) is higher than the dataset (b) but the accuracy of regression model for the dataset (b) is better than (a). RMS error value for dataset a and b is 24.15 and 25.11 respectively. ....	87
Figure 4.2. Scatterplot of density and gamma ray (after Emilsson, 1993) to illustrate operation of LogTrans algorithm (Fullagar et al., 1999). Coloured dots represent data from control holes. Points A, B, and C represent measurements to be interpreted. Classes are assigned to these points according to their normalised distance from the centre of each lithological “domain”.....	89

Figure 4.3. Structure of an artificial neural network showing three layers. Note that there is no connection between nodes of a given layer. .... 90

Figure 4.4. Criteria for selection of optimum network and training cycle (Basheer and Hajmeer, 2000). As the training cycles increases the prediction error reduces, however the prediction error for validation data (Testing) will start to increase after a certain training cycle known as optimum training point. This point that defines the optimum number of training cycles is regarded as the sufficient number of cycles for best performance of the network..... 92

Figure 5.1. Photographs of drill cores from Ernest Henry captured using MSCL system. Felsic Volcanic (FV2) with carbonate (Calcite) alteration from drill hole EH446 - depth 430m (a), Felsic volcanic (FV3) with potassic (Kf) alteration from drill hole EH635 depth 1019m (b), Altered mafic volcanic rock (AMV2) with potassic (kf) alteration from drill hole EH635 depth 888m (c), and felsic volcanic rock (FV2) with magnetite (mt) alteration from drill hole EH635 depth 922m (d). .... 100

Figure 5.2. Perspective view of Ernest Henry showing the pit outline, the plunging pipe-like orebody and location of the six drill holes selected for this study (Walters, 2009). .... 101

Figure 5.3. Comparison of gamma density and water immersion density measured on drill cores from five holes from Ernest Henry. The blue line represents a 1:1 line and the red line is the best regression fit. .... 104

Figure 5.4. Comparison of the Geotek P-wave velocity measurements (2m averages) on drill cores from six holes from Ernest Henry with high frequency P-wave velocity measurements on slabs derived from drill cores. The samples originating from each drill holes are in depth order. .... 105

Figure 5.5.. Strip logs of geological, geochemical, petrophysical, geotechnical and metallurgical composite for EH635..... 108

F Figure 5.6. Strip logs of geological, geochemical, petrophysical, geotechnical and metallurgical composite for EH633..... 110

Figure 5.7. Strip logs of geological, geochemical, petrophysical, geotechnical and metallurgical composite for EH574..... 112

Figure 5.8. Strip logs of geological, geochemical, petrophysical, geotechnical and metallurgical composite for EH556..... 114

Figure 5.9. Strip logs of geological, geochemical, petrophysical, geotechnical and metallurgical composite for EH446..... 116

Figure 5.10. Strip logs of geological, geochemical, petrophysical, geotechnical and metallurgical composite for EH432..... 118

Figure 5.11. Scatter plot of gamma density versus magnetic susceptibility from all the six drill holes of Ernest Henry..... 119

Figure 5.12. Histograms of (a) density, (b) P-wave velocity, (c) magnetic susceptibility (d) logarithm of magnetic susceptibility and (e) P-wave amplitude from drill holes EH633, EH635, EH574, EH432, EH556, and EH446..... 120

Figure 5.13. Medians and spreads of (a) density, (b) magnetic susceptibility (c) P-wave velocity and (d) P-wave amplitude in 2m intervals from drill holes EH633, EH635, EH574, EH432, EH556, and EH446, classified by litho-alteration classes. Pink square = median, black bar = range (16th – 84th percentile), gery histogram = number of samples for each litho-alteration class. Abbreviations as defined in Table 5.2. .... 122

Figure 5.14. Correlation of Fe with Au and Cu in all six holes of Ernest Henry.....	123
Figure 5.15. Cross plot of Fe with density and susceptibility in all six holes of Ernest Henry. Note that the relationship between Fe and density is effectively linear while the relationship between Fe and susceptibility is nonlinear.....	123
Figure 5.16. Cross plot of A*b and JKMRC estimated Bond mill work index for all comminution test samples of Ernest Henry.....	124
Figure 5.17. Cross-plots of A*b versus 2m averages of (a) density, (b) logarithm of magnetic susceptibility, (c) P-wave amplitude, and (d) P-wave velocity for all comminution test samples from all drill holes. The red line in each case is the best regression fit to the data which has been shown for comparative purposes even when correlations are very poor.....	125
Figure 5.18. Cross-plots of JKMRC estimated BMWi versus 2m averages of (a) density, (b) logarithm of magnetic susceptibility, (c) P-wave amplitude, and (d) P-wave velocity for all comminution test samples from all drill holes. The red line is the best regression fit to the data.....	126
Figure 5.19. Measured versus predicted A*b (a) and Estimated versus predicted BMWi (b) for all 142 test samples using multiple regression of four petrophysical parameters (P-velocity, P-amplitude, gamma density and magnetic susceptibility). R2 is regression correlation coefficient and REP is relative error of prediction....	127
Figure 5.20. Scatter plot of mean A*b and Bond mill work index for litho-alteration classes at Ernest Henry. The red squares and the blue bars indicate the mean and standard deviations of comminution attributes respectively. ....	128
Figure 5.21. Cross-plot in principal component space, with data points differentiated according to petrophysical cluster.....	130
Figure 5.22. A radar diagram of petrophysical parameters for four-cluster solution .....	131
Figure 5.23. Cluster proportions for litho-alteration classes.....	132
Figure 5.24. Measured versus predicted A*b (a) and Estimated versus predicted BMWi (b) in four petrophysical clusters. Predicted values are derived from petrophysical parameters. ....	133
Figure 5.25. Comminution test samples (EH556, EH574, EH635, EH633, EH432 and EH446) for each cluster projected onto principal component space, c.f. Figure 5.21. ....	134
Figure 5.26. Predicted A*b and measured A*b (a) versus depth in four clusters for test samples of EH574 using regression model presented in Figure 5.24a and predicted Bond mill work index and JKMRC estimated Bond mill work index versus depth in four clusters for test samples of EH574 using regression model presented in Figure 5.24b.....	135
Figure 5.27. Predicted A*b (a) and predicted BMWi (b) for the entire dataset (~800 2m intervals). The measured A*b and JKMRC estimated BMWi are also plotted for comparison. The samples originating from each drill hole are plotted in depth order. ....	136
Figure 5.28. Crossplot between A*b and Bond mill work index (BMWi) for all 142 comminution test samples determined by cluster analysis.....	137
Figure 5.29. Prediction of metallurgical classes in control drill hole EH633 using LogTrans. First column shows the metallurgical classes. The second column is predicted metallurgical classes based on magnetic susceptibility, P-velocity and Cu grade.....	138

Figure 5.30. Prediction of metallurgical classes in independent drill hole EH574 using LogTrans . First column shows the metallurgical classes. The second column is predicted metallurgical classes based on magnetic susceptibility, P-velocity and Cu grade. ....	139
Figure 5.31. Normalized data means for clusters, three-cluster solution. ....	141
Figure 5.32. Measured versus predicted A*b (a) and Estimated versus predicted BMWi (b) for all 142 test samples derived from a 4th order polynomial regression of Cu%. ....	142
Figure 5.33. Comparison of throughput predictions for 142 GeM 2m samples. The current mine site (EH) model is based on Cu-grade; the GeM model is based on actual A*b, estimated BMWi and gamma density. ....	143
Figure 5.34. Schematic diagram of Ernest Henry comminution circuit (Kojovic, 2008)	144
Figure 5.35. Comparison of throughput predictions for subset of GeM 2m samples. The current EH model is based on Cu-grade; the GeM model is based on actual A*b, estimated BMWi and gamma density. Only samples which conform to the typical assay range and ore hardness have been included. ....	145
Figure 5.36. Predicted mill throughput for a larger dataset. The blocks of samples originating from each drill hole are plotted in increasing depth order. ....	146
Figure 5.37. Mill throughput estimate for clusters defined using PC approach (section 5.8.2).....	147
Figure 6.1. Scatter plot of A*b versus BMWi for Cadia East and Ernest Henry data. ...	152
Figure 6.2. Images of drill cores from Cadia East captured using MSCL system. Volcaniclastic with phyllic alteration from drill hole CE082 - depth 150m (a), Volcaniclastic with propylitic alteration from drill hole CE082 at depth 195m (b), volcaniclastic with transitional sodic propylitic alteration from drill hole CE098 depth 245m (c), Monzonite porphyry with intense potassic alteration CE143 depth 1420m (d), Volcaniclastic with albite pyrite alteration from CE109 depth 338 (e) and volcaniclastic with skarn porphyry alteration from CE098 depth 368m (f).....	155
Figure 6.3. Isometric view of Cadia East showing the previously proposed open pit (blue), selected drill holes and their relationship to upper disseminated Cu zone and the lower veined Cu zone. Modified after Walters (2008). ....	156
Figure 6. 4. Strip logs of geological, geochemical, petrophysical and geotechnical composite for CE082.....	162
Figure 6. 5. Histogram of Logarithm of magnetic susceptibility for drill hole CE082 ...	163
Figure 6. 6. Strip logs of geological, geochemical, petrophysical, geotechnical and comminution composite for CE098.....	164
Figure 6.7. Histogram of Logarithm of magnetic susceptibility for drill hole CE098 ....	165
Figure 6. 8. Strip logs of geological, geochemical, petrophysical, geotechnical and comminution composite for CE0109.....	166
Figure 6. 9. Histogram of Logarithm of magnetic susceptibility for drill hole CE109 ...	167
Figure 6. 10. Strip log of geological, geochemical, petrophysical ,geotechnical and comminution composite for CE110.....	168
Figure 6. 11. Histogram of Logarithm of magnetic susceptibility for drill hole CE110.	169
Figure 6. 12. Strip log of geological, geochemical, petrophysical, geotechnical and comminution composite for CE143.....	171

- Figure 6.13. Histogram of Logarithm of magnetic susceptibility for drill hole CE143.. 172
- Figure 6. 14. Medians and spreads in average (a) P-wave velocity, (b) density and (c) magnetic susceptibility (log scale, 10<sup>-5</sup> SI) over 2m assays splits from drill holes CE082, CE098, CE109, CE110 and CE143, classified by litho-alteration type. Pink square = median, black bar = range (16th – 84th percentile), grey histogram = number of samples for each litho-alteration type..... 173
- Figure 6. 15. Cross-plot of P-wave modulus and logarithm of magnetic susceptibility, grouped according to alteration styles in all five boreholes..... 174
- Figure 6.16. Scatter plot of JKMRC estimated BMW<sub>i</sub> versus medians of (a) density, (b) logarithm of magnetic susceptibility and (c) P-wave velocity for all comminution test samples. Also scatter plot of A\*b versus medians of (d) density (e) logarithm of magnetic susceptibility and (f) P-wave velocity for all comminution test samples. The red line in each panel is a linear regression fit to data which has been shown even when correlation coefficients are poor. .... 176
- Figure 6. 17. Scatter plot of A\*b versus (a) P-wave velocity (b) P-wave modulus and (c) reciprocal of P-wave modulus for all comminution test samples. The red line is a regression fit to data..... 177
- Figure 6.18. P-velocity versus the ratio of stress to strain (i.e. Young's modulus) for different values of Poisson ratio (modified after Hatherly et al., 2003)..... 178
- Figure 6.19. Medians and spreads of P-wave velocity (a), density (b) and logarithm of magnetic susceptibility (c) over comminution intervals for each drill hole from Cadia East. Note that susceptibility measurements were not recorded on some intervals..... 180
- Figure 6.20. Comparison between measured A\*b and the A\*b values predicted using multiple regression (MR) of P-wave modulus and logarithm of magnetic susceptibility (equation 6.2) and A\*b predicted using neural network (NN). The samples originating from each drill hole are plotted in depth order. .... 181
- Figure 6.21. Scatter plot of mean A\*b and Bond mill work index for six different alteration classes at Cadia East. The blue bars indicate the standard deviation of comminution attributes. .... 183
- Figure 6.22. Scatter plot of P-wave velocity versus A\*b for phyllic cap (a) and albite-pyrite (b) alteration classes. The red line is a linear regression fit to data. The blue lines are 95% confidence intervals and the dashed lines are regression prediction limits. Outliers rejected during model development for the albite-pyrite alteration class are specifically highlighted in (b)..... 184
- Figure 6. 23. Bar chart of normalized petrophysical property means for three petrophysical clusters..... 185
- Figure 6.24. Cross-plots of A\*b versus Bond mill work index (BMW<sub>i</sub>) for all comminution samples from Cadia East (a) and a scatter plot of comminution data grouped by colors representing comminution classes (b) as defined in the text (G1 to G4). G1,G2,G3 and G4 are colored by red, green, blue and pink respectively..... 187
- Figure 6.25. Averages and standard deviation of (a) P-wave velocity, (b) density and (c) sulphur content in comminution classes in five holes of Cadia East (CE082, CE098, CE109, CE110 and CE143). Black square = Average, black bar = standard deviation, grey histogram = number of samples for each comminution class. .... 189
- Figure 6.26. Prediction of metallurgical classes in drill hole CE082 (control hole) using LogTrans. The first column shows that metallurgical classes determined for training set. The second column is the predicted metallurgical classes based on petrophysical

and assay data shown in the remaining logs. Note that P-modulus is denoted with M. LogTrans window length during fluster analysis was 0.25m. ....	190
Figure 6.27. Prediction of metallurgical classes in drill hole CE110 (control hole) using LogTrans. The first column shows that metallurgical classes determined for training set. The second column is the predicted metallurgical classes based on petrophysical and assay data shown in the remaining logs. Note that P-modulus is denoted with M. LogTrans window length during fluster analysis was 0.25m. ....	191
Figure 6. 28. Schematic diagram of Cadia Hill processing circuit (Kojovic, 2009) .....	193
Figure 6.29. Prediction of metallurgical classes in independent drill hole CE098 using LogTrans. The first column shows that metallurgical classes. The second column is predicted metallurgical classes based on petrophysical and assay data. Note that P-modulus is denoted with M and estimated mill throughput is denoted with TPH..	195
Figure 6.30. Proportions of comminution classes and predicted mill throughput.....	196
Figure 7.1. Predicted density from classified core images, based on original volume estimates, versus measured density (i.e. medians of 2m assay intervals) for samples from six Ernest Henry drill holes.....	208
Figure 7.2. Correlation between total volume fraction of magnetite based on original image classification and (a) magnetic susceptibility and (b) Fe grade at Ernest Henry. Correlation between original image-based estimate of volume fraction of chalcopyrite versus and (c) total volume fraction of magnetite and (d) Cu grade. All samples are 2m assay intervals from all six drill holes.....	209
Figure 7.3. Correlation of adjusted volume fraction of magnetite with (a) magnetic susceptibility and (b) Fe grade. Correlation of adjusted volume fraction of chalcopyrite with (c) volume fraction of magnetite and (d) Cu grade. All samples are 2m assay intervals from all six drill holes. ....	212
Figure 7.4. Predicted density from classified core imagery (after volume adjustment) versus measured density (Geotek and JKMRC) for 2m assay samples from all drill holes at Ernest Henry.....	213
Figure 7.5. Predicted maximum and minimum densities from classified core images (after adjustment of volume fraction of mineral phases) versus measured densities for 2m assay samples from all six drill holes. ....	214
Figure 7.6. Total volume fraction of magnetite determined from classified core images (after adjustment) versus medians of magnetic susceptibility for 2m assay intervals from all drill holes from Ernest Henry. The red line is the linear regression line and as evident from regression equation the slope of regression suggests a high susceptibility of ~6.5 SI for magnetite. ....	215
Figure 7.7. Predicted Reuss and Voigt P-wave velocity from classified core images (after adjustment to mineral volumes) compared with measured Geotek P-velocity for 2m assay samples from all drill holes of Ernest Henry. The samples originating from each hole are plotted in depth order. The triangles denote high frequency P-wave velocity measurements on small slabs derived from drill cores .....	216
Figure 7.8. Volume fraction of chlorite estimated from classified core images plotted according to drill hole in depth order. ....	217
Figure 7.9. Predicted Reuss and Voigt P-wave velocity from classified core images (after adjustment to mineral volumes) using derived P-velocity from Table 7.4 compared with measured Geotek P-velocity for 2m assay samples from all drill holes of Ernest Henry. The samples originating from each hole are plotted in depth order. ....	218

- Figure 7.10.  $A^*b$  predicted from core imagery for the entire Ernest Henry dataset. The measured  $A^*b$  values are plotted for comparison. The samples originating from each drill hole are plotted in depth order..... 220
- Figure 7.11.  $BMWi$  predicted from core imagery for the entire Ernest Henry dataset. The estimated  $BMWi$  is also plotted for comparison. The samples originating from each drill hole are plotted in depth order..... 221
- Figure 7.12. Predicted mill throughput. The samples originating from each drill hole are plotted in depth order. .... 221



# CHAPTER 1

---

## Introduction

### 1.1. Background and Motivation

During the last decade there has been a growing recognition of different factors (e.g. ore hardness) that have an impact on the efficiency of mineral processing operations. Ore variability is a significant factor controlling mill performance and throughput in almost every processing plant. Petrophysical measurements have the potential to characterize ore variability and its processing behavior in detail. Such measurements could enable effective metallurgical domaining of ore deposits for process planning and optimization.

Conventional metallurgical tests (e.g. Bond mill work index) are commonly conducted to characterize ore processing behavior. The ore crushing and grinding behavior as a result of such tests are considered during mill design and processing equipment selection (Napier-Munn et al., 1996). Cost, time and sampling (i.e. size and representivity) are common issues in metallurgical characterization. A large amount of material (~50 kg) is required for a single metallurgical test with the result that metallurgical tests are both expensive and time consuming. Thus these tests are usually limited in number. The samples selected from a few zones of the orebody for metallurgical tests are composited, as per industry sampling practices to represent the feed materials of a mill. However a sampling strategy such as this is not representative of a given ore-body as compositing and blending can change the actual metallurgical variability of the ore.

Geological variability has been recognized as a critical issue in cases where metallurgical test work has failed to truly characterize the processing behaviour (Bulatovic et al, 1997; McNulty, 1998; David, 2007). For this reason a strong incentive exists for efficiently characterizing metallurgical behavior for a truly representative suit of samples. “Representative” here means typical geological and metallurgical characteristics of run of mine (ROM) material.

Ore variability and its impact on downstream processing have attracted the attention of process engineers to a new field of research known as “geomallurgy”. Geomallurgy is a cross disciplinary approach to define the relationship between geology and processing characteristics of mineral deposits. In particular, a major AMIRA (Australian Mineral

Industry Research Association) Project, P843, entitled Geometallurgical Mapping and Mine Modelling (GeM<sup>III</sup>), was initiated in 2005 “to develop fundamental new approaches to the quantification and integration of geological characterization with mineral processing performance and mine optimization”. P843 is a mining industry-sponsored collaborative research project undertaken at CODES (Centre of Excellence in Ore Deposits) at the University of Tasmania, JKMRC (Julius Kruttschnitt Mineral Research Centre) and BRC (Bryan Research Centre) from the University of Queensland, and CSIRO Division of Exploration and Mining.

The GeM<sup>III</sup> project was focused primarily on development of a suite of new measurements at diamond drill core scale for geometallurgical modeling. A new approach for comminution test program, namely small scale physical testing (Walters and Kojovic, 2006) was developed within the GeM<sup>III</sup> that could be used on highly constrained and relatively smaller volumes of rock than conventional metallurgical sampling and testing.

The GeM<sup>III</sup> project was divided into six modules: Automated core logging, Mineral identification and mapping of core images, Textural classification, Small-scale physical testing, Ore-body modeling, and Education and training. Within the “Automated core logging” module, three streams of direct core-based information have been acquired: short wavelength infrared reflectance (SWIR) spectra from the HyLogger<sup>TM</sup> automated system (Huntington et al, 2006); petrophysical properties recorded using a Geotek automated multi sensor petrophysical core logger (Vatandoost et al., 2008a); and high resolution core imagery also recorded by the Geotek system for image analysis e.g. ore textural characterization. The research described in this thesis is part of “Automated core logging” module of AMIRA P843 and is devoted to characterization of comminution behavior on the basis of petrophysical properties of drill core.

Investigation of physical rock properties and their relation to processing attributes is the focus of this thesis. P-wave velocity and its amplitude, density and magnetic susceptibility are petrophysical properties that are considered in this thesis. Petrophysical properties and measures of rock strength are both affected by mineralogy, texture, porosity/permeability and degree of fracturing (Schön, 1996; Raghu and Ghose, 2006). The effect of rock strength parameters (e.g. point load index) on processing performance has been investigated by Bearman et al (1997). They have established a relationship between rock strength parameters and comminution attributes so that the required energy in crushing circuit can be estimated from rock strength data.

The basic premise of this research is that since petrophysical properties (e.g. sonic velocity) can be related to rock mass strength, they could provide a means for prediction of comminution behavior as well. In addition to P-wave velocity, density and magnetic susceptibility have the potential for characterization of ore processing behavior. A program of small-scale physical testing at JKMRRC (University of Queensland) within the P843 project provided an opportunity to conduct comminution tests on exactly the same drill core samples in which petrophysical properties were acquired. This program facilitated direct comparison of petrophysical properties with results of comminution tests.

Geological observations that are routinely recorded during exploration phase also have the potential to be used for characterization of processing performances. Such observations could be calibrated against processing indices. However little attention is paid to prediction of comminution behavior purely based on visual geological logging. There are many reasons for the limited utilization of geological observations in downstream processing. For example visual logging is highly subjective and experience-based and is not quantitative. However, by combining visual logging with measurements of conventional physical properties, such as acoustic velocity, it may be possible to predict comminution parameters reliably in different rock types. In this manner the combination of geological and geophysical logging could characterize processing performance in detail, thereby enabling metallurgists to exercise a greater degree of control in downstream processing.

Ideally geophysical wireline logging would be used to acquire petrophysical data. Downhole logging is cheap, fast, and provides a continuous record of a wide range of parameters even in zones of poor or no core recovery. Although such techniques are commonly used at coal, iron ore and uranium mines but they are rarely used at precious and base metal mines, notwithstanding the large number of possible applications (Fullagar, 2000). There are a number of reasons for this lack of uptake (Mutton, 1994). In particular, issues of borehole access can arise, related both to equipment/crew logistics and to borehole integrity.

At case study sites described in this thesis, the boreholes were not accessible and downhole logging was not possible. Moreover the GeM geometallurgical mapping and modeling approach was focused primarily on drill core information. A Geotek multi sensor core logger (MSCL) system was commissioned, modified and used for measurement of petrophysical properties and capturing core images along the sections of

drill cores. The use of MSCL system within P843 project provided an opportunity to assess suitability of such system for production petrophysical core logging.

The use of petrophysical data for predicting metallurgical performance indices is a new field which presents a number of challenges. These include accurate and precise semi-automated measurement of physical properties on drill cores, and development of methodologies for relating petrophysical data to metallurgical attributes. This thesis attempts to address these issues as presented in Chapter 3 and Chapter 4.

The anticipated benefit of detailed petrophysical measurements is that petrophysical properties will provide a more complete understanding of the physical characteristics of ore being fed to the mill in a processing circuit. Such valuable information enables metallurgists to reduce the effect of ore variability on recoveries during mine planning and process optimization.

## **1.2. Research Aims and Objectives**

The ultimate goal of this research is to develop a capability for prediction of comminution attributes based on petrophysical characterisation of drill cores. This is a new approach for characterization of ore metallurgical behavior. Petrophysical measurements are cost effective, quick and non-destructive. Such measurements provide a means to characterize physical properties of material. If petrophysical properties can be linked to processing indices then they will be valuable source of information for both mine design and ore processing operations.

The specific objectives for this research can be summarized as follows:

1. Evaluation of the Geotek automated petrophysical core logging system for routine petrophysical core logging in metalliferous mines,
2. Petrophysical characterization of drill cores from case study sites,
3. Development of geometallurgical modeling approaches to predict comminution attributes based on petrophysical properties from case study sites,
4. Prediction of petrophysical parameters from core imagery as an alternative means for obtaining petrophysical property data and also predicting comminution attributes.

This research focused on two mine sites in Australia that were investigated as part of the GeM<sup>III</sup> project, namely the Cadia East Au-Cu porphyry deposit (New South Wales) and the Ernest Henry iron oxide copper-gold (IOCG) mine (Queensland).

### **1.3. Methodology**

The MSCL system was used for measurement of petrophysical properties and for capturing core imagery of diamond drill cores. Drill cores from five boreholes from Cadia-East and from six boreholes from Ernest Henry were used in this research.

The MSCL system had never previously been used in metalliferous mines; therefore comprehensive evaluation of the MSCL system was required. This work consisted of sensor modification, evaluation and refinement of sensor calibration procedures, and precision and accuracy tests, together with documentation of suitable data acquisition procedures and processing sequences.

Once the petrophysical properties and core imagery had been recorded on drill cores, then a suite of small-scale metallurgical tests were conducted at JKMRM on a subset of samples over selected assay intervals that petrophysical properties were recorded. Methodologies for geometallurgical class definition and comminution modeling based on petrophysical properties were then devised and implemented for each case study.

An alternative approach to obtain petrophysical properties was investigated using the high resolution core images. The approach provides an additional means for estimation of comminution attributes from analysis of core imagery.

### **1.4. Previous Petrophysical Work in Mining**

Geometallurgical studies are not new and a number of papers have been published in this regard (e.g. Williams and Richardson, 2004) but to the best of the author's knowledge there has been no research published for comminution modeling based on petrophysical properties.

The objective of this section is to describe the use of petrophysical properties in the mining and petroleum industries for a variety of applications such as rock engineering, resource exploration, grade estimation and reservoir characterization, as a prelude to a

more complete discussion of the link between petrophysical properties and metallurgy in Chapter 2.

Petrophysical properties have extensive applications from early stages of exploration through to feasibility and mine design. Physical properties (e.g. density) measured from downhole logging are widely used in the petroleum industry for reservoir characterization and have been successfully used in coal and iron ore deposits for lithology identification (mineralogy, depth and thickness), hole to hole correlation, grade estimation and resource evaluation (e.g. Hearst et al, 2000; Lipton, 1997; Borsaru, 1993).

Considerable research in the coal industry has been devoted to prediction of coal quality parameters from petrophysical properties (Edwards and Banks, 1978; Borsaru et al, 1991; Campbell, 1994; Borsaru, 1993; Borsaru et al, 2000; Nichols, 2000).

Many authors have also documented that geophysical logging can also be effectively applied for characterization of metalliferous deposits as well (Nelson, 1994; Killeen et al, 1995; Killeen, 1997; Killeen et al, 1997; Morris and Walker, 1997; Mueller et al, 1997; Pflug et al, 1997; Selfe, 1997; Fullagar, 2000; Salisbury et al, 2000; Basford et al, 2001). However these studies do not attempt to use the petrophysical properties to predict metallurgical performance.

Although petrophysical contrasts between ore and host rock may not be enough for direct geophysical detection of the economic mineral phases in gold and some base metal exploration, an association may exist between ore and an associated mineral (e.g. presence of pyrrhotite as a magnetic mineral in sulfide nickel deposits) which renders the ore detectable by geophysical methods. Correlation between uranium content and gold grade in South African mines has led to prediction of gold grade using natural gamma logging (Campbell, 1994). Conductivity has also proved to be a good indicator of grade for some base metal sulphide ores, e.g. at the Enonkoski nickel deposit in Finland (Hattula and Rekola, 2000).

Grade control during mine production is of great importance. Petrophysical properties can also be applied for grade estimation (Fallon et al, 2000). Natural gamma radiation has proved effective for estimation of the mean grades of iron ore in dry blast holes and exploration boreholes traversing layered mixtures of hematite and shale (Aymler et al, 1976). At the Rosebery deposit, Tasmania, the ratio of density to natural gamma correlates well with zinc-equivalent grade (Fallon and Fullagar, 1997).

From mining and subsequent mineral processing point of view, simple discrimination between ore and waste is critical. Petrophysical contrasts can be helpful in this case. Discrimination of ore from waste between mine and mill, e.g. using contrasts in natural gamma (Bohme, 1983) or conductivity (Balint, 1975), eliminates the costs of grinding and processing waste, and reduces the volume of tailings.

There are numerous studies in petroleum (e.g. Chang et al. 2006) and coal (e.g. Hatherly et al, 2005) environments for rock mass geotechnical characterization using petrophysical properties.

Petrophysical measurement can enhance geological observations in terms of consistency by providing additional information about different rock types. The studies cited above illustrate the wide range of application of petrophysical attributes in different technical domains. These studies encourage implementation of petrophysical measurement in metalliferous mines in general. Moreover interaction of mineral processing attributes with mineral grades and the possibility of prediction of mineral grade from petrophysical properties provide encouragement for investigation of potential relationship between petrophysical properties and metallurgical attributes in particular.

### **1.5. Research Innovation**

The research presented in this thesis investigates the potential use of petrophysical properties for comparative comminution and throughput modeling. This is the first time that petrophysical properties have been used for such purposes.

A novel approach for petrophysical measurements on representative intervals of drill cores section from an orebody are considered here. The Geotek MSCL system used in this research had never been applied before in metalliferous mines. This is a novel approach for continuous semi-automated measurement of petrophysical properties and for capturing core imagery of diamond drill cores. Petrophysical characterization of drill cores can be an alternative approach to traditional visual core logging techniques that are subjective and qualitative. Vatandoost et al (2008a) have documented initial evaluation and refinement of sensor calibration procedures, and precision and accuracy tests.

Petrophysical properties used in this research are density, P-wave velocity and its amplitude and magnetic susceptibility. Density and P-wave velocity can provide an estimate of dynamic Young's modulus (Vatandoost and Fullagar, 2007). The estimated

Young's modulus has the potential for prediction of comminution behavior (Vatandoost and Fullagar, 2009).

Novel approaches for geometallurgical class definition and comminution modeling are devised and implemented in this research. The approaches are based on petrophysical properties; however they are robust enough to be applied using other available data (e.g. assays) in absence of petrophysical properties. Application of class-based geometallurgical class definition for mill throughput modeling at Ernest Henry using petrophysical properties has been documented by the author in a publication (Vatandoost et al, 2009).

Prediction of petrophysical properties from core images have been reported in petroleum industry (e.g. Oyno et al, 1998). However predicted properties are limited to porosity, resistivity and permeability. A novel approach for prediction of density from core images is illustrated in this thesis. Prediction of density from core images has never been investigated by any researcher. Moreover such approach has never been investigated before in metalliferous mines.

## **1.6. Outline of the Thesis**

The remainder of this thesis consists of seven Chapters. In Chapter 2, a review of metallurgical testing and potential application of petrophysical properties for prediction of comminution parameters will be presented. Review of the published literature provides encouragement that petrophysical properties can be related to comminution parameters.

Chapter 3 introduces the methodology for measurement of petrophysical properties on drill core sections. The Geotek multi sensor core logger (MSCL) is described in detail. The MSCL operation procedures, sensor issues (e.g. calibration), accuracy and data quality are presented in this chapter.

The strategy adopted for comminution modeling in this project is described in Chapter 4. The methodologies for geometallurgical class definition and comminution modeling, primarily based on petrophysical parameters, will be explained. A review of statistical techniques such as cluster analysis for class definition is presented. Regression analysis, a minimum distance method and an artificial neural networks approach for comminution modeling will be introduced.

In Chapter 5, petrophysical data acquisition, processing and interpretation will be presented for the first case study site, Ernest Henry mine. The correlation between petrophysical properties and corresponding small scale comminution test results was investigated using regression analysis. At Ernest Henry  $A^*b$  and  $BMWi$  vary from 36 to 267 and from 6 to 14 kWh/t respectively. This large variability in comminution behavior results in a large variability of mill throughput from 1100 t/h to 2700 t/h. Class-based comminution modeling approaches discussed in Chapter 4 yield predictive models of  $A^*b$  and  $BMWi$  via multiple regression of petrophysical properties. Petrophysical based comminution models provided a means for characterisation of mill throughput at Ernest Henry.

Chapter 6 will describe the second case study at Cadia East. This chapter will cover petrophysical data acquisition and processing from five drill holes. At Cadia East the ore is harder in terms of both crushing and grinding;  $A^*b$  and  $BMWi$  vary from 22 to 77 and from 13 to 20 kWh/t respectively. Although the comminution variability is relatively smaller than at Ernest Henry, however this range of variability results in mill throughput variability from 1460 t/h to 2070 t/h. Petrophysical characterization of comminution at Cadia East is difficult due to limited variability of comminution parameters. However, magnetic susceptibility and P-wave velocity are related to ore crushability ( $A^*b$ ).

The aim of Chapter 7 is to demonstrate an alternative approach for obtaining petrophysical properties and prediction of comminution attributes from classified core images. Core images from Ernest Henry drill holes recorded using the MSCL system. Bulk density is predicted from estimates of volume abundance and density of individual mineral phases. An algorithm was employed to adjust the volume fraction of mineral phases for consistency with assays. The approach presented in this chapter also provides an additional means for estimation of comminution attributes from core images.

Finally in Chapter 8 a synthesis and discussion of the outcomes of this research will be presented.



# CHAPTER 2

---

## Relating Petrophysical Properties to Comminution Parameters

### 2.1. Introduction

The objective of mineral processing is to extract valuable minerals from ores. Comminution is the process of size reduction to give sufficient liberation of the valuable mineral for optimal economic recovery. Size reduction steps (crushing and grinding) in any plant consume large amounts of energy (more than 50% of a plant's energy) in comparison to other stages (e.g. flotation) in the concentrator (Weiss, 1985; Wills, 1997). Therefore, design and selection of appropriate size reduction equipment is crucial. Size reduction equipment is selected mainly on the basis of comminution test results e.g.  $A^*b$  for crushing and Bond mill work index for grinding.

As discussed in Chapter 1, metallurgical tests are usually conducted off site on a very limited number of large samples, owing to the high costs and long lead times involved. Hence there is a strong incentive to find alternative means for efficiently characterizing comminution behaviour for a truly representative suite of samples. The objective of this chapter is to review published literature in order to investigate the potential link between petrophysical properties and comminution attributes.

One of the main factors that control the selection of hard-rock comminution equipments and the design of a processing circuit is the hardness (e.g. Bond mill work index) of the ore(s). Much research has been undertaken in an attempt to relate comminution behaviour to standard rock strength tests such as uniaxial compressive strength (e.g. Bearman et al, 1997). It has been demonstrated that the data required for comminution plant design can be obtained from mechanical tests on drill core samples.

Previous research in the petroleum, coal and metalliferous industries has shown that rock strength (uniaxial compressive strength) can be predicted from petrophysical properties (e.g. McNally, 1990; Chang et al., 2006; Barton, 2007). Given the relationship between rock strength parameters and comminution attributes and similarly between rock strength parameters and petrophysical properties, it is envisaged that a link between petrophysical properties and comminution attributes can also be established.

This chapter is divided into six sections. Sections two and three briefly review the comminution attributes and destructive rock strength parameters respectively. A discussion on petrophysical parameters derived from non-destructive tests and their potential as proxies for comminution attributes is presented in section four. The relationship between comminution attributes and rock strength parameters (derived from destructive tests) is presented in section five. Given the relationship between static and dynamic Young's modulus, investigation of the relationship between comminution parameters and dynamic Young's modulus is highly desirable. Dynamic measurements are non-destructive, easier and quicker than static measurements. Concluding remarks for the whole chapter are presented in section six. The review of the published literature provides encouragement that comminution attributes can be predicted from petrophysical properties.

## 2.2. Comminution Parameters

The aim of comminution or size reduction is to maximize the liberation of valuable minerals from the host rock for subsequent processing such as flotation and leaching. The two most commonly used devices for comminution are crushers and grinding mills. Design and implementation of crushing and grinding equipment at mine sites requires specific tests.

There are a wide array of commonly used comminution tests such as Bond ball mill work index (BMWi); rod mill work index (RMWi); semi-autogenous grinding (SAG); Bond Abrasion; JK Ore Abrasion; Bond crushing work index (CWi); Drop Weight test (DWT); SAG mill comminution (SMC) and  $A^*b$  (from JKMRC rotary breakage test). Details on most of these tests can be found in Napier-Munn et al. (1996).

The objective of the small-scale physical testing within the P843 project was to develop comminution tests that could be used on smaller volumes of rock than traditional sampling for large scale tests. The sample size could then match the assay interval and provides a means to conduct comminution tests on exactly the same samples in which petrophysical properties were acquired. Hence the emphasis here is on those tests that have been employed within this research i.e. BMWi for grinding and  $A^*b$  for crushing.

### 2.2.1. Bond Mill Work Index (BMWi)

The Bond equation (Bond, 1952) is almost universally used in mineral processing for design of size reduction equipment. The BMWi estimates the required energy to grind an ore sample using a specific lab-scale mill (Bond, 1960). The Bond equation is given by:

$$W = 10W_i \left( \frac{1}{\sqrt{P}} - \frac{1}{\sqrt{F}} \right) \quad (2.1)$$

where  $W$  is the required energy of breakage in kWh/t and  $W_i$  is the work index (BMWi) in kWh/t.  $P$  and  $F$  are the sizes of screens in microns through which 80% of product and feed pass respectively. Numerically  $W_i$  is the energy in kilowatt hours per tonne required to reduce the material from notional infinite feed size to 80% passing 100  $\mu\text{m}$ . In practice  $W_i$  has to be determined from plant data or by conducting laboratory grinding tests in which  $W$ ,  $P$  and  $F$  are measured.

The BMWi is a measure of ore grindability. A typical classification of BMWi for ore grinding behaviour is documented by Napier-Munn et al. (1996). Based on their classification, an ore with BMWi value of less than 9kWh/t is regarded as soft for grinding and a BMWi value of more than 14kWh/t is hard. The BMWi values between 9 and 14 kWh/t are considered as medium for grinding

Measurement of Bond ball mill work index requires a large amount of material (~30Kg) for sample preparation. This large sample mass requirement was an issue for the purpose of P843 project, especially given that only half drill cores were available at most sites. For this reason small scale physical testing (Walters and Kojovic, 2006) was developed at JKMRC to estimate Bond ball mill work index from batch grind tests and JKMRC crushing index tests (Michaux and Kojovic, 2008). The sample requirement based on small scale protocols, for estimation of BMWi is 5Kg of -3.35mm (i.e. not larger than 3.35mm) material which is equivalent to approximately 2m of half NQ drill core. These protocols within the P843 project provided an opportunity to conduct comminution tests on exactly the same drill core samples for which petrophysical properties were acquired.

Overall estimated BMWi carries uncertainty due to crushing index and batch grinding test results. The softer ores are more variable in practice, hence the uncertainty in estimated BMWi is greater ( $\pm 10\%$ ) for the softer ore samples (i.e. BMWi < 10kWh/t) and relatively smaller ( $\pm 5\%$ ) for harder ore samples, e.g. BMWi of 15 kWh/t (Kojovic, 2008a).

### 2.2.2. JKMRC Rotary Breakage Test (JKRBT)

The JKRBT provides a rapid means for characterising ore crushability and is suitable for testing drill cores in a geometallurgical context. The JKRBT device (Figure 2.2) was designed and developed at JKMRC in an attempt to overcome some of the limitations of pre-existing impact tests (e.g. drop weight test), including the precision of the energy input, the time required to run the test, and the smallest particle size that can be readily tested (Kojovic, 2008b). Comparative breakage tests using the JKRBT and the traditional JKMRC Drop Weight tester have shown that the two devices generate a nearly identical breakage–energy relationship for the same ore of the same size (Kojovic et al, 2008). A summary of the JKRBT system operation and the resulting  $A \cdot b$  measurement is given below.

The operating system consists of a vibrating feeder, a rotor-stator impacting device plus drive system, and an operation control unit (Figure 2.1). Like a conventional drop weight test, the particles need to be pre-sized into narrow fractions. Particles of the selected size are then fed into the rotor-stator impacting system. After impact breakage, the product is collected and the  $t_{10}$  values (breakage index) are determined using the same techniques used for a drop weight test. The  $t_{10}$  value is the percent of breakage product that passes 1/10 of the initial particle size. The  $t_{10}$  value is normally related to the specific breakage energy,  $E_{cs}$ , according to

$$t_{10} = A \times (1 - e^{-b \times E_{cs}}) \quad (2.2)$$

where  $A$  and  $b$  are ore specific parameters, and where  $E_{cs}$  is specified in kWh/t.

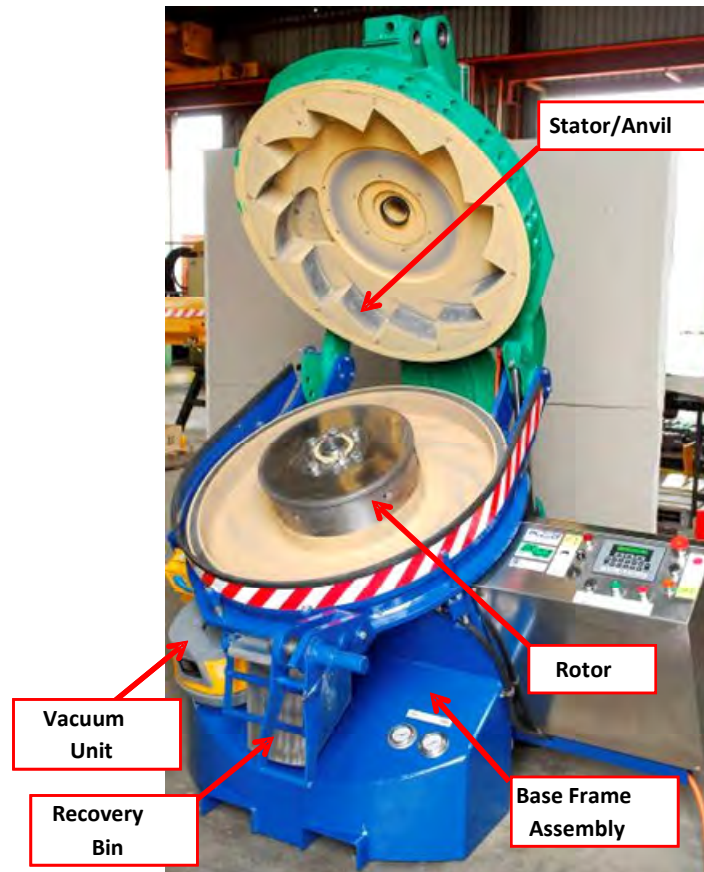


Figure 2.1. Schematic of the JKMRC Rotary Breakage Testing device (Kojovic, 2008a).

Parameter  $A$  is the maximum value of  $t_{10}$ , i.e. the highest possible level of size reduction from a single impact event. Figure 2.2 illustrates the results from a test on one size fraction,  $-16+13.2\text{mm}$  (i.e. there is no particle larger than 16mm and less than 13.2mm). The slope of this plot at the origin is defined by the product of the ore specific parameters,  $A^*b$  and is related to the rock crushing behaviour. A small value of  $A^*b$  is an indication of rocks that are hard to crush while a high  $A^*b$  indicates rocks that are easy to crush. For the tests illustrated in Figure 2.2, the initial average size of feed was 14.5mm. At the lowest energy level (0.25 kWh/t), 5.4% of the product was finer than 1.45mm. The sample broken at 2.5kWh/t yielded 43.2% of fines (smaller than 1.45mm). The  $A^*b$  value determined for such sample was 23, indicating a very high resistance to impact breakage (Kojovic et al, 2008). Thus low values of  $A^*b$  imply low crushability.

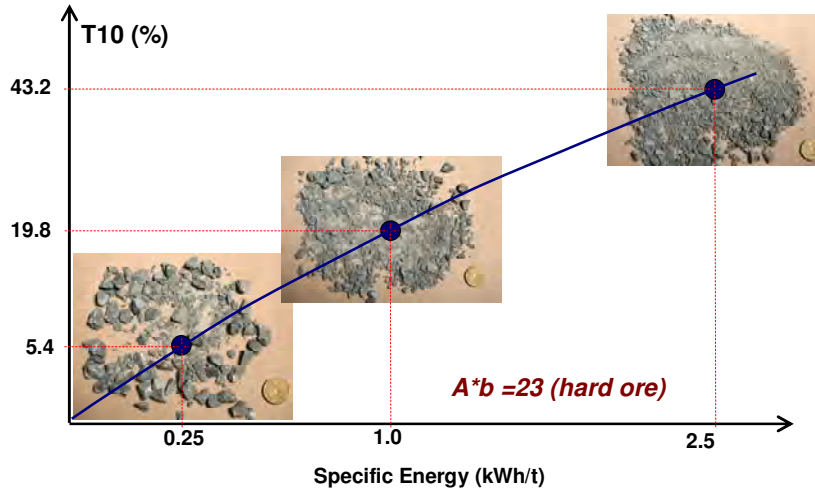


Figure 2.2. The relationship between fines produced and specific breakage energy for a single particle size , hard ore, (Kojovic et al, 2008).

Comparison of  $A^*b$  measurement between DWT and JKRBT test results for a hard-to-crush ore (e.g.  $A^*b < 30$ ) suggests an uncertainty of about 7.5% for the JKRBT results (Kojovic, 2008a). For softer ore samples (e.g.  $A^*b > 100$ ) there would be more variability, therefore the uncertainty in  $A^*b$  values would likely be even greater than 7.5%.

### 2.3. Destructive Rock Strength Parameters

Intact rock materials may exhibit a wide variety of strength properties. Rock strength is affected by the presence of discontinuities such as bedding planes, fractures or cracks and joints, often oriented in different directions (Schön, 1996).

Rock strength in the context of comminution can be defined as resistance of materials to breakage. In this case measures of rock strength are based on destructive tests such as uniaxial compressive strength and Point load index defined below. It has been a common practice in the mineral industry to relate such tests to comminution attributes (Bearman et al, 1997).

There are many mechanical tests available to measure the strength of the rock mass. In the following sub-sections common rock strength parameters such as uniaxial compressive strength (UCS), point load index (PLI), and Young’s modulus will be briefly explained. Detailed procedures of such tests are documented by International Society of Rock Mechanics (ISRM, 1985).

Another definition of rock strength is the resistance of materials against deformation, which can be measured in non-destructive tests. Thus P-wave velocity and Young's Modulus can be regarded as measures of rock strength. Due to their ease of measurements, they are normally related to measures of breaking strength (e.g. UCS). However, much less effort has been made to relate deformational (non-destructive) measurements to comminution attributes.

### 2.3.1. Uniaxial Compressive Strength (UCS)

Uniaxial compressive strength (UCS) normally referred to intact rock is a widely used rock strength parameter in geomechanical engineering. The values of this parameter can be obtained in rock mechanics laboratories on core samples. This involves an accurately trimmed, right-cylindrical rock sample, with a length:width ratio of 2.5-3.0, being compressed, parallel to its long axis, to the point of failure (Goodman, 1980). Thus the test is destructive. UCS is the failure stress, usually expressed in MPa.

Values of UCS range from in excess of 250MPa in extremely strong rocks such as fresh basalt, quartzite and granite to values of 5 to 25MPa for weak rocks such as chalk and potash (Hoek et al, 1995). Figure 2.3 shows the range of unconfined compressive strength for a variety of rock types (Lama and Vutukuri, 1978).

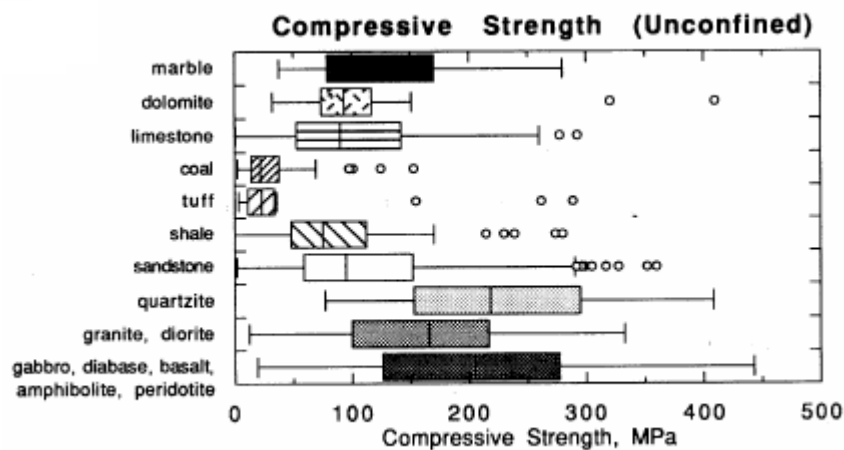


Figure 2.3. Unconfined compressive strength for a variety of rock types after Lama and Vutukuri (1978). Each box presents  $\pm 25\%$  of the data about the median value (vertical line)

### 2.3.2. Point Load Index (PLI)

The point load test has often been utilised as an indirect measure of the compressive or tensile strength of rock (D'Andrea et al, 1964; Bieniawski, 1975). The point load test is simpler and faster than UCS test. It is normally used where UCS test equipment is not available, or a large number of tests are required to cover a wide range of rock properties.

The PLI test is destructive, and involves positioning a ~50 mm length of drill core in a hydraulic press, with two hardened steel points diametrically opposed. The point load index ( $I_s$ ) is calculated from the peak pressure (P) at which the core breaks, divided by the diameter of the core (D) squared:

$$I_s = P / D^2 \quad (2.3)$$

PLI data are typically scattered, and a large number of tests (>100) may be required to get a reliable estimate of rock strength. Nevertheless, it is widely used. Although the rock fractures by induced tension, the averaged point load test results are roughly correlated to UCS data (Brady and Brown, 1985).

### 2.3.3. Young's Modulus (E)

Elastic modulus also known as Young's modulus is the parameter that relates stress to strain for elastic deformation. In most rocks, the uniaxial stress-strain curve in the elastic regime before failure is approximately linear as expressed in equation 2.4 (Jaeger and Cook, 1976).

$$\sigma = E\varepsilon \quad (2.4)$$

where  $\sigma$  is the stress,  $\varepsilon$  is the strain induced in the direction of the applied stress and E is the constant is called Young's modulus. E has the units of stress and is typically reported in GPa. A material is elastic if the above relation holds accurately.

Young's modulus describes the capacity of a rock to resist deformation, and can be considered as the "stiffness" of a rock. A rock with high Young's modulus resists deformation while a low Young's modulus rock, is more deformable.

Young's modulus or elastic modulus measurement of rocks can be carried out in two ways, static or dynamic. Static Young's modulus ( $E_s$ ) measurements can be obtained

through either uniaxial or triaxial compressive experiments on cores. Thus  $E_s$  is usually determined via destructive testing. The dynamic Young's modulus ( $E_d$ ) is a non-destructive indicator of strength, calculated from elastic wave velocities ( $V_p$  and  $V_s$ ) and density ( $\rho$ ).

In general, the dynamic Young's modulus is greater than the static Young's modulus. Studies by researchers (e.g. Howarth, 1984; McCann and Entwisle, 1992) showed that this discrepancy was greater for soft rocks (e.g. sandstone) than hard rocks (e.g. granite). The differences between the dynamic and static Young's modulus in soft rocks have been widely attributed to micro-cracks and pores in the rocks (Peng and Zhang, 2007). McCann and Entwisle (1992) showed that  $E_s$  and  $E_d$  are in close agreement for hard rocks (i.e. granite). Given the low porosity of rock samples from Cadia East and Ernest Henry, it is therefore expected that  $E_d$  measurements would be in good agreement with measurements of  $E_s$ .

As dynamic measurement of Young's modulus is easier than static measurement, therefore determination of dynamic Young's modulus for prediction of comminution behaviour is more desirable.

#### **2.4. Non-Destructive Rock Strength Parameters**

The ultimate aim of this research is to investigate the relationship between the petrophysical properties of ore to comminution attributes. It is a common practice in the oil and gas industry to develop empirical models between rock strength and geophysical well log data (Peng and Zhang, 2007). Most proposed models for determination of rock strength from geophysical data use P-wave velocity (or its reciprocal, the travel time) alone or estimates of elastic moduli such as Young's modulus.

The following subsections present the potential use of petrophysical properties (P-wave velocity, density, P-wave modulus, acoustic impedance, magnetic susceptibility and electrical resistivity) as non-destructive measures of rock strength. Given the existence of relationships between strength and comminution attributes (Section 2.5), these petrophysical measures of rock strength could serve as proxies for comminution attributes.

### 2.4.1. P-Wave Velocity ( $V_p$ )

Seismic techniques are widely used in applications such as petroleum exploration, geotechnical assessment and geomechanical engineering. One of the main advantages of seismic methods is their non-destructive nature compared with conventional mechanical tests (e.g. UCS) and the ability to apply them both in the field and in the laboratory (i.e. velocity measurements).

Sonic velocity is the principal geophysical parameter that has been utilised for rock mass characterisation, since seismic velocity and attenuation are sensitive to rock stress, strength, degree of fracturing, porosity and the nature of the material occupying the voids (Fullagar and Fallon, 1997). Sonic velocity measurements are employed in the laboratory for the determination of the dynamic elastic properties of rocks. Attempts have been made to use seismic velocity for quality assessment of grouting (Knill, 1970; Turk and Dearman, 1987), rock bolt reinforcement (Price et al, 1970), blasting efficiencies in the rock mass (Young et al, 1985) and rock mass characterization (Turk and Dearman, 1986). The prediction of rock mass deformation and stress (Onodera, 1963; Gladwin, 1982), digging resistance measurement of overburden rocks (Davies and McManus, 1990), the estimation of the extent of fracture zones developed around underground openings (Hudson et al, 1980), the determination of degree of weathering (Karpuz and Pasamehmetoglu, 1997), and fractured rock mass characterization (Boadu, 1997) are some other applications of the seismic velocity measurements.

According to elastic wave theory, the P and S wave velocities ( $V_p$ ,  $V_s$ ) are a function of a medium's elastic parameters and density (Schön, 1996)

$$V_p = \sqrt{\frac{K + \frac{4}{3}\mu}{\rho}} \quad (2.5)$$

$$V_s = \sqrt{\frac{\mu}{\rho}} \quad (2.6)$$

where  $K$  and  $\mu$  are the effective bulk and shear moduli of the medium respectively and where  $\rho$  is the density. From measurements of  $V_p$  and  $V_s$  together with density, it is therefore possible to calculate bulk and shear modulus (equation 2.5 and 2.6). The modulus calculated in this way is termed the dynamic modulus.

These formulae (i.e. equation 2.5 and 2.6) suggest that the firmer or more inflexible a material is (higher  $K$  and  $\mu$ ), the higher its velocity. They also imply an inverse relationship between density and velocity. However, empirical evidence indicates that  $V_p$  normally increases with increasing density for sedimentary rocks since elastic moduli typically increase with increasing density. Some sulphide minerals provide exceptions to this rule, e.g. galena has a high density of 7.4g/cc but a low P-wave velocity of 3750m/s.

Overall the most important effect on  $V_p$  for typical rocks is due to variation in elastic properties rather than density. This is mainly due to the wide variation in Young's modulus (40-160 GPa) between minerals that corresponds to very small variations in densities (2.4-3.2g/cc).

There are a large number of empirical models for prediction of UCS from P-wave velocity using either linear or nonlinear regression models. McCann et al (1990) suggest a relationship between UCS and P-wave velocity of general form

$$UCS = aV_p^b \quad (2.7)$$

where  $a$  and  $b$  are empirical constants.

In the Australian coal mining industry, a relationship proposed by McNally (1990) is widely used for estimation of uniaxial compressive strength

$$UCS = 1450e^{-0.038t} \quad (2.8)$$

where the transit time,  $t$ , is measured in  $\mu$ s/ft and the UCS is measured in MPa (Figure 2.4).

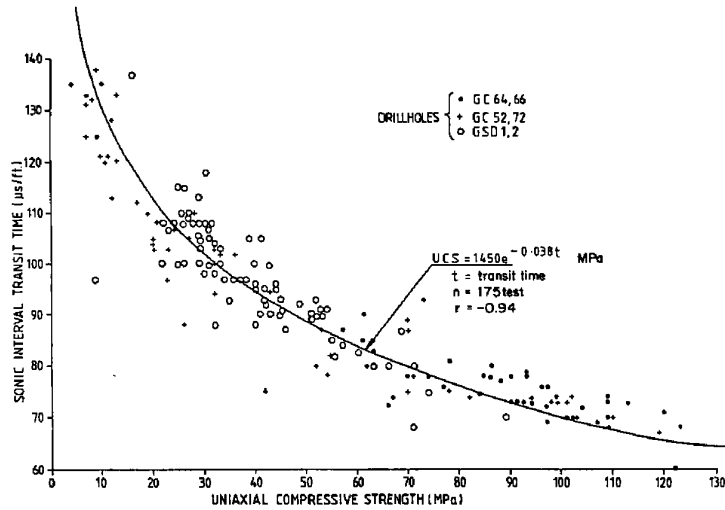


Figure 2.4. Uniaxial compressive strength versus sonic transit time, for sandstones and siltstones of the German Creek Formation, Bowen Basin, Queensland (McNally, 1990)

Within specific formations and at particular locations, different coefficients have been derived. For example, Ward (1998) suggests an alternative expression for the German Creek Mine in Central Queensland. Lawrence (1999) has also illustrated how lithological variations can affect the UCS/sonic transit time correlation.

Chang et al. (2006) have compiled models to illustrate the dependence of uniaxial compressive strength (UCS) on P-wave velocity, porosity and Young’s modulus for sedimentary rocks (i.e. sandstone, shales, limestone and dolomite). The correlation was positive between UCS and P-wave velocity and Young’s modulus, and negative between UCS and porosity.

Recently Kilic and Teymen (2008) studied the relationship between P-wave velocity and UCS for range of rock types (sedimentary, igneous and metamorphic). Although they have proposed a nonlinear model for UCS with strong correlation ( $R^2=0.94$ ), their model was based on a small number of samples (i.e. 19 samples in total). A similar study has also been conducted by Sharma and Singh (2008) but on limited number of samples.

All cited studies above indicated that P-wave velocity has a positive relationship with UCS in almost all rock types. The mathematical form of the relationship is either linear or nonlinear. Such observations could potentially suggest a relationship between P-wave velocity and comminution attributes as well.

To assess the relationship between P-wave velocity and point load index, a total of 40 point load index tests and the corresponding P-wave velocity measurements were

compiled from literature for a series of sedimentary, metamorphic and igneous rocks (Kahraman and Alber, 2006; Hecht et al., 2005; Karakus and Tutmez, 2006; Kilic and Teymen, 2008). Figure 2.5 shows a moderate positive correlation between point load index (tensile breakage strength) and P-wave velocity (deformational strength).

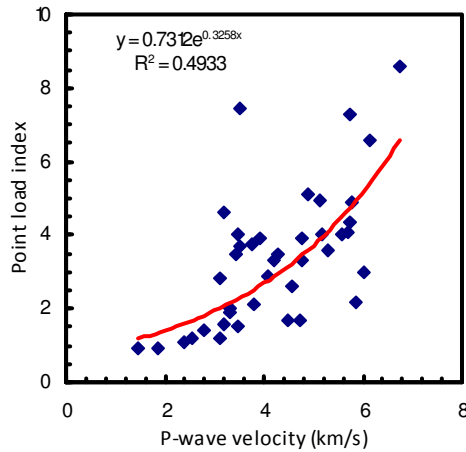


Figure 2.5. The relationship between P-wave velocity and Point load index. The red line is the best regression fit to the data. Data compiled from literature (Kahraman and Alber, 2006; Hecht et al., 2005; Karakus and Tutmez, 2006; Kilic and Teymen, 2008).

Figure 2.6 shows the relationship between compressional velocity and Bond work index based on the dataset extracted from Deniz and Ozdag (2003) for a suite of sedimentary and volcanic rocks. There is a strong correlation between P-wave velocity and Bond mill work index which shows that P-wave velocity alone can be a good parameter for prediction of Bond mill work index. Although the correlation is specific to sedimentary and volcanic rock types, such correlation encourages investigation of relationships between these attributes for other rock types.

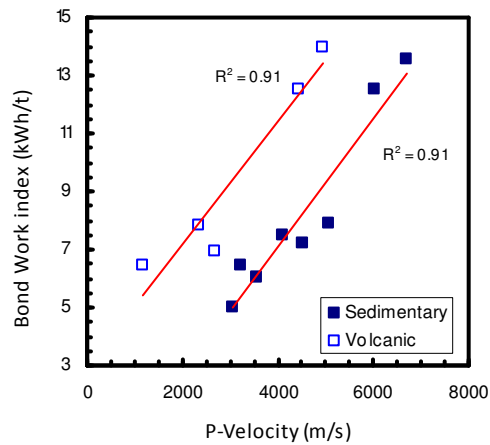


Figure 2.6. The relationship between P-wave velocity and Bond work index for sedimentary and volcanic rocks. The relationship established after extracting data from dataset of Deniz and Ozdag (2003).

#### 2.4.2. Density ( $\rho$ )

Density is fundamentally important in ore reserve estimation. Ore density also has a significant impact on power draw of auto-geneous (AG) and semi auto-geneous (SAG) mills (Napier-Munn et al, 1996). Density determination is a standard test in all geomechanical programs and has been routinely applied in industry. Density is required together with acoustic velocities in order to calculate elastic moduli (e.g. dynamic Young's modulus). The relationships between density and rock strength have been studied by many researchers (e.g. Preston, 1976). Raghu and Ghose (2006) showed that in general the denser the rock, the higher its compressive strength (Figure 2.7). However, they have not stated any information in regard to source and nature of the rock type. There is considerable scatter in the data (Figure 2.7) that precludes application of a simple universal relationship. In fact in the higher density range (i.e. above 2.5g/cc) there is no correlation with compressive strength. This can be explained by the fact that density is dependent on mineral grade, while rock strength parameters additionally depend on interaction between grains, and their stiffness (Hecht et al, 2005).

Gupta and Yan (2006) have compiled Bond mill work index and specific gravity data for a series of minerals and ore types from the literature. A scatter plot of specific gravity and Bond mill work index for a range of ore types shows a moderate negative correlation (Figure 2.8). This relationship suggest that the denser the ore the less energy is required for grinding. Thus ore density can provide useful information in regard to selection of comminution equipment. Such relationship may exist at some ore deposits (e.g. Ernest Henry).

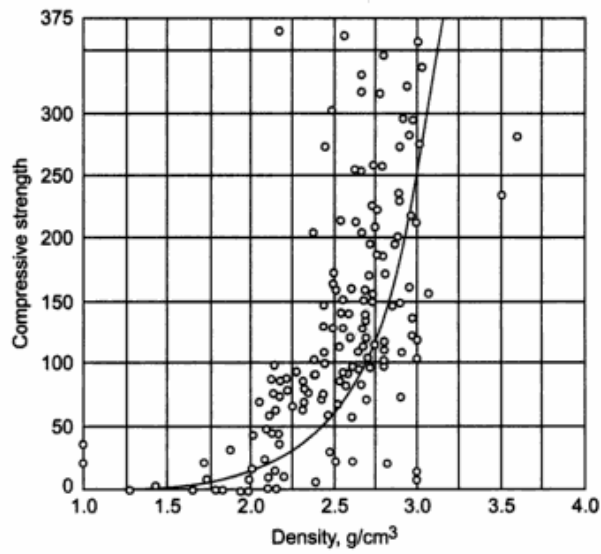


Figure 2.7. Relationship between compressive strength and density (Raghu and Ghose, 2006).

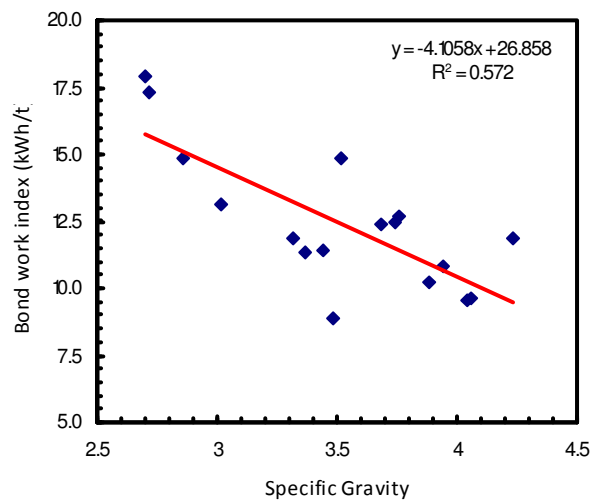


Figure 2.8. Scatter plot of specific gravity and Bond work index for seventeen different ore types. Data compiled by Gupta and Yan (2006).

### 2.4.3. P-wave Modulus (M)

The P-wave modulus,  $M$ , is calculated from compressional velocity ( $V_p$ ) and density ( $\rho$ ):

$$M = \rho V_p^2 \quad (2.9)$$

P-wave modulus is also known as stiffness modulus (Serra, 1986), plane-wave modulus (after White, 1983) and the modulus of one-sided compression (Rzhevsky and Novik, 1971).

The dynamic elastic moduli can be derived from the compressional and shear wave velocities ( $V_p$  and  $V_s$ ), and the density ( $\rho$ ).  $V_p$  and  $V_s$  can be determined from a full waveform sonic log. However, with conventional sonic tools, often only  $V_p$  is measured. Therefore there is frequently a need to predict elastic moduli from  $V_p$  and  $\rho$  alone.

Many techniques have been developed for prediction of shear wave velocity from compressional velocity in sedimentary environments, e.g. Castagna et al. (1985), Entwisle and McCann (1990), Lee (2006). However, there is little published research on prediction of shear wave velocity in hard rock environments. One approach for prediction of shear wave velocity is using Christensen's equation (Entwisle and McCann, 1990; Firth, 1999). The equation has the following form:

$$V_s = V_p \left[ 1 - 1.15 \left( \frac{1/\rho + 1/\rho^3}{e^{1/\rho}} \right) \right]^{3/2} \quad (2.10)$$

Where  $V_p$  and  $V_s$  are compressional and shear wave velocities respectively and  $\rho$  is the density.

The origin of this formula (equation 2.10) is somewhat obscure, but it is believed to be based on empirical results from sediment samples. Consequently, Christensen's equation should be applied with caution.

Vatandoost and Fullagar (2007) have shown that measured  $M$  has a strong correlation ( $R^2=0.98$ ) with measured dynamic Young's modulus for a series of minerals and rocks. Calculation of  $M$  facilitates prediction of dynamic Young's modulus when  $V_s$  is not available.

Given the relationship between Young's modulus and  $A^*b$  presented in section 2.5.1 (Figure 2.12) it is possible that  $M$  can be used as a potential parameter for prediction of  $A^*b$ . Studies by Vatandoost and Fullagar (2009) reinforce the relationship between  $M$  and  $A^*b$ . They have found a negative correlation between  $M$  and  $A^*b$  measured on drill core samples from Cadia East deposit.

#### 2.4.4. Acoustic Impedance (Z)

The P-wave acoustic impedance (Z) is defined as the product of compressional velocity and bulk density:

$$Z = \rho \cdot V_p \text{ (Kg/m}^2\text{s)} \quad (2.11)$$

The contrast in acoustic impedance governs the strength of seismic reflections at geological boundaries. Petrosyan (1994) has defined “Z” as a measure of resistance to breakage (i.e. strength) and Scott (1996) has adopted “Z” as a measure of rock blastability.

Lu (2006) showed that there is a positive correlation between acoustic impedance and Young’s modulus on a series of volcanic and sediment samples. This is not surprising given that dynamic Young’s modulus correlates with M (Vatandoost and Fullagar, 2007).

#### 2.4.5. Magnetic Susceptibility (k)

Magnetic susceptibility is a measure of the ability of a substance to become temporarily magnetized in a magnetic field. The susceptibility is a reliable indicator of the presence of ferromagnetic minerals in a rock such as magnetite and pyrrhotite.

Magnetic susceptibility is a function of not only to the volume amount of magnetic minerals (usually magnetite) but also grain size. For a given magnetite content, susceptibility decreases with decreasing grain size of magnetite (Schön, 1996).

Given the influence of rock compositional variations and grain size (i.e. a texture term) on ore breakage and recovery (Bojcevski et al, 1998; Petruk, 2000), variation in susceptibility may play an important role in ore breakage characterisation provided that magnetic mineralogy (e.g. magnetite or pyrrhotite) is present. At Ernest Henry mine, the hardness of the rock types is inversely proportional to magnetite content (Strohmayr et al., 1998). Therefore it is expected that magnetic susceptibility should correlate negatively with Bond ball mill work index (BMWi).

Numerical modelling conducted by Djorjevic (2008) on classified core images from Ernest Henry mine suggest that magnetite acts as a crack initiator; hence it makes the rocks softer in terms of crushing. He interpreted this behaviour of magnetite based on its crystal structure and contrast in elastic properties of adjacent mineral phases. Cubic minerals (e.g. magnetite, pyrite) have the best crack initiating function. Magnetite and

pyrite have higher Young's modulus than other minerals present in Ernest Henry ore. However magnetite has higher Poisson ratio (0.25) than pyrite (0.19) that makes magnetite more deformable than pyrite and hence increases its tendency to act as a crack initiator (Djorjevic, 2008).

Susceptibility measurements have been used for lithological interpretation, estimation of degree of homogeneity and alteration (Ellwood, 1980; Schonharting and Hall, 1983) and grade prediction (e.g. Wanstedt, 1993). In some cases susceptibility measurements have proven to be correlated to rock quality (i.e. degree of fractures). For example, in the Lac du Bonnet granite batholith (Manitoba, Canada) magnetic susceptibility was used to differentiate between various rock qualities (Lapointe et al, 1984). Low values of magnetic susceptibility (<0.05 SI) corresponded to altered zones with many fractures while high magnetic susceptibility (>0.1 SI) was related to unaltered and non-fractured zones. Given that first breakage of an ore happens along fractures (Petruk, 2000), the high and low susceptibilities could be regarded as a proxy to comminution properties in some cases. Similar observations apply at Cadia East (Chapter 6), where high susceptibility is regarded as indicative of materials that are hard in terms of crushing.

Thus magnetic susceptibility could either directly be related to comminution behaviour (e.g. Ernest Henry) or acts as a proxy to comminution behaviour (e.g. Cadia East).

#### **2.4.6. Electrical Conductivity**

A limited number of studies have been conducted on the relationship between electrical conductivity of rock samples and corresponding rock strength (Donaldson and Keller, 1974; Kate and Sthapak, 1995; Kahraman and Alber, 2006). These researchers have found a negative correlation between electrical conductivity and rock strength. The reason for such relationship is mainly due to sensitivity of both measures of rock strength (e.g. UCS) and electrical conductivity to porosity and micro-cracks.

Electrical conductivity is also sensitive to ore texture (Emerson and Yang, 1994). Given the sensitivity of electrical conductivity to ore texture and the impact of texture on comminution and recovery (Bojcevski et al, 1998), electrical conductivity could also be a useful proxy for ore comminution and liberation attributes.

Ferrara et al (1989) used textural models similar to those used by Yang and Emerson (1997) and showed that for a given particle size resulting from a size reduction, a

spherical model will liberate more of the mineral of interest in an ore than a rodded-texture model which in turn will liberate more than a banded texture model (Figure 2.9). Laboratory tests conducted by Bojcevski et al (1998) on George Fisher ore samples showed that ores with large proportion of banded pyrite texture are complex to process and have poor liberation.

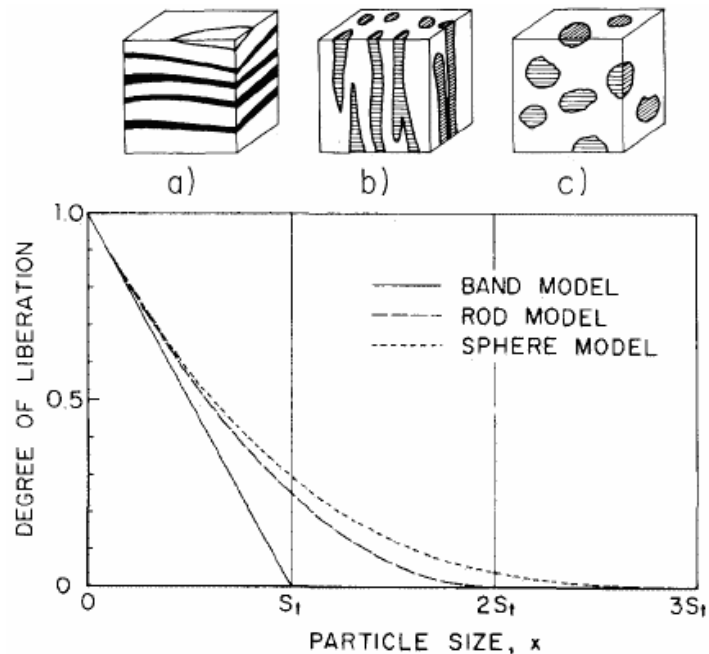


Figure 2.9. Degree of liberation versus particle size for three types of ore texture: banded (a), rod (b), and spherical (c) texture models (after Ferrara et al 1989).  $S_t$  is the size of inclusion in the rock model as defined by Ferrara et al (1989).

## 2.5. Relationship Between Rock Strength and Comminution

Both measures of rock strength and comminution involve breakage process. The breakage process during strength measurement continues till the rock sample breaks apart while comminution process continues until desired product size is achieved. Moreover the scale of samples in which rock strength parameter (e.g. UCS) are measured is relatively larger than for comminution tests. Therefore establishing a relationship between these properties is rather difficult. Nevertheless many researchers have attempted to establish a relationship between measures of strength and comminution attributes.

### 2.5.1. Rock Strength and Crushability

Everell et al. (1972) investigated the physio-mechanical properties of a series of carbonate rocks and their relationship with grinding selection function (breakage rate). The relationship defined made it possible to predict energy demands in the comminution circuits from rock strength data (i.e. UCS) determined on drill core. Bearman (1991) has also shown that a significant correlation exists between the measures of strength (i.e. Point load index) for twelve rock types used in quarrying with crusher performance.

Extensive data from the AMIRA P483 Mine-to-Mill project has shown that  $A^*b$  can be correlated quite well with the point load index (Kojovic, 2008b), as illustrated in Figure 2.10. However Kojovic (2008a) believes that at the lower range of point load index there is significant variability in terms of  $A^*b$  and therefore the PLI provides a relatively imprecise measure of comminution behaviour for soft ores (high values of  $A^*b$ ).

A large number of  $A^*b$  and point load index tests were conducted on drill cores from sponsor sites during the AMIRA P843 project. These data were compiled in order to assess the relationships between these two parameters further. As represented in Figure 2.11 the correlation between  $A^*b$  and point load index appears to be site dependent.

The point load index is a geomechanical parameter which is highly affected by the presence of fractures and weakness planes in the sample. Therefore the correlation between point load index and  $A^*b$  can be local and dependent on rock type and the fracture frequency within the rock.

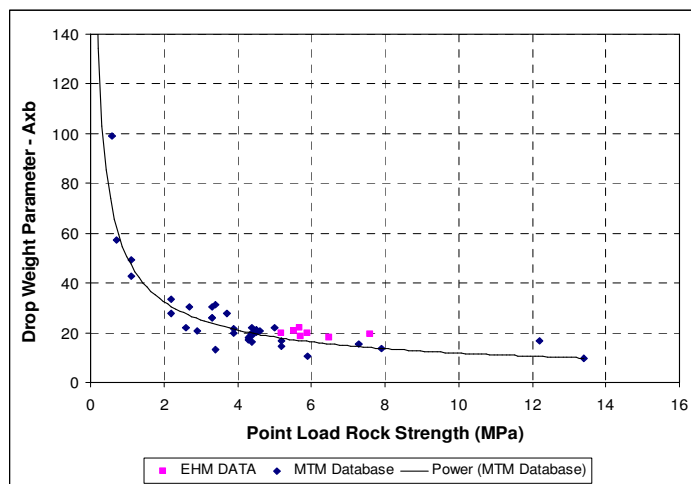


Figure 2.10. Relationship between  $A^*b$  and PLI for Mine to Mill project (MTM) dataset with the P843 Ernest Henry EH512 (EHM) sample results shown in pink (Kojovic, 2008b). The black line is the best fitted regression line (Power).

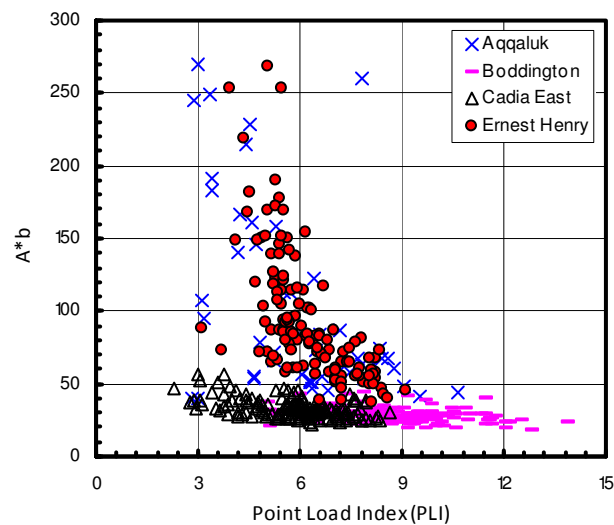


Figure 2.11. Relationship between A\*b and PLI for P843 project dataset. There is no correlation between PLI and A\*b at Cadia East and Boddington sites but a moderate correlation in the other two sites is evident.

Scott et al (1998) completed a geometallurgical study at Cerro Colorado copper porphyry mine in Chile. They conducted a series of geomechanical tests and also A\*b measurements on six different ore types in an attempt to characterize the ore breakage. However they have not studied the relationship between measured parameters (UCS, Tensile strength, Young's modulus, density, Poisson ratio and A\*b) for defined ore types. Compiling measurements of A\*b and static Young's modulus (Scott et al, 1998) for identified ore types a strong negative correlation was found (Figure 2.12). These data confirm the intuitive relationship that with an increase of Young's modulus, the value of A\*b reduces and hence the ore becomes more competent in terms of crushing.

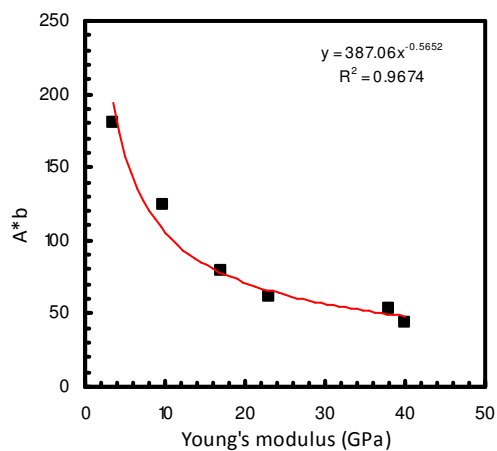


Figure 2.12. Correlation between A\*b and Young's modulus for six ore types at Cerro Colorado copper mine, Chile. Data compiled from Scott et al (1998).

Given the correlation between dynamic and static Young’s modulus, a similar correlation between  $A^*b$  and dynamic Young’s modulus is not unexpected and hence could provide a quicker and more cost effective way for estimation of comminution attributes.

**2.5.2. Rock Strength and Grindability**

Gupta and Yan (2006) studied the correlation between Bond mill work index and strength parameters. As quoted in Gupta and Yan (2006), Briggs (1991) measured the tensile strength, using the Brazilian tensile test, and the point load strength of four rock types of different grindabilities. These results were compared to the Bond Work Index of the ores as measured by the Magdalinovic (1989) method. The results in Figure 2.13 show that there is a good correlation between the Bond Work Index, the tensile strength and the uniaxial compressive strength (UCS). However studies by Doll et al (2003) suggest that there is no correlation between UCS and Bond ball mill work index (Figure 2.14). They concluded that UCS may only be related to Work Indices in rock types that have minimal fractures and where the UCS test measures the energy to break grain boundaries rather than the energy to break fractures.

Gupta and Yan (2006) stated that the poor correlation between UCS and Bond mill work index is because the grinding tests are normally carried out at relatively small particle sizes in which the planes of weakness are no longer present and the ore appears to be more competent. These studies show that measures of rock strength (e.g. UCS) are scale dependent i.e. strength is sample size related, it increases as the sample size decreases.

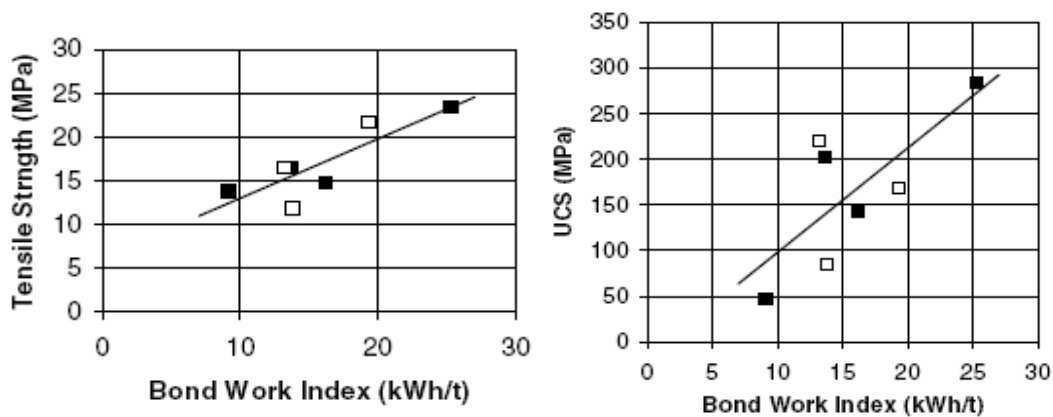


Figure 2.13. Correlation between Bond Work Index and tensile strength (left) and correlation between Bond Work Index and UCS (right). Closed squares are data compiled from Briggs (1991) and open squares are data compiled from Yan (1993) as quoted in Gupta and Yan (2006). Note that the two graphs refer to the same rock samples.

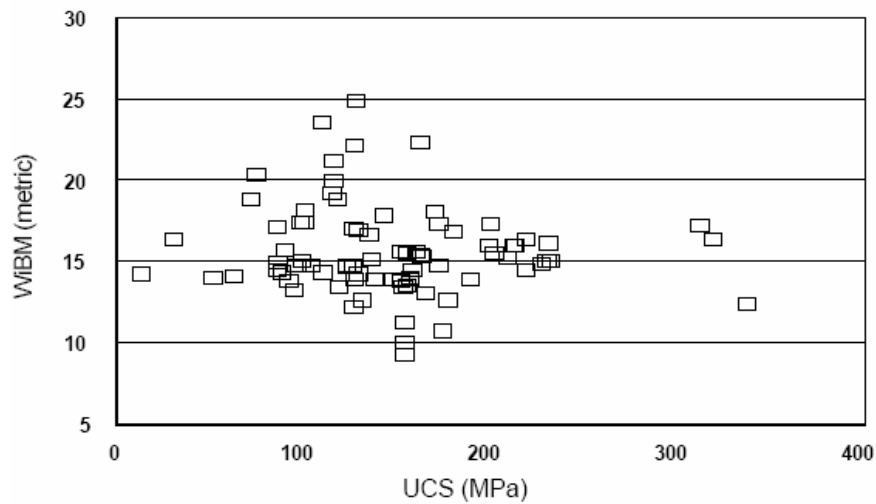


Figure 2.14. Cross plot of UCS and Bond ball mill work index for a data set from 11 different mine (after Doll et al, 2003).

Deniz and Ozdag (2003) investigated the correlation between dynamic elastic modulus and Bond work index for unmineralized rocks. They have found a good positive correlation between dynamic bulk modulus and Bond ball mill work index (Figure 2.15) but their work was limited to 13 samples (from different locations), five of which were volcanic rocks and the rest sedimentary. In their study they related dynamic elastic parameters to Bond work index. Calculation of elastic parameters was based on shear wave and compressional wave velocities and density.

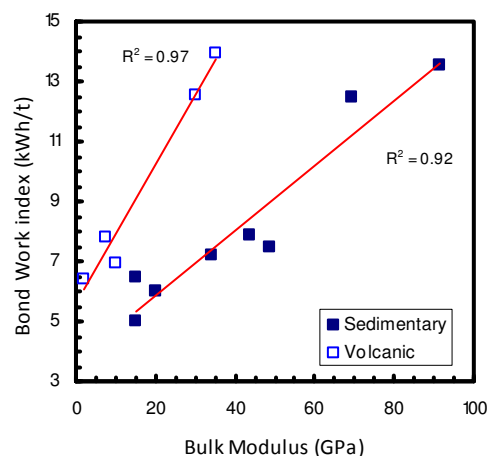


Figure 2.15. The relationship between dynamic bulk modulus and Bond work index for sedimentary and volcanic rocks. Data extracted from dataset of Deniz and Ozdag (2003).

## 2.6. Concluding Remarks

Review of the published literature provides encouragement that comminution parameters can be related to deformational strength (e.g. P-wave velocity). Grindability parameters (e.g. BMWi) and deformational strength can both be related to measures of breaking strength (e.g. UCS).

Based on a limited number of samples compiled from published data, it was shown that Bond mill work index increases with an increase of P-wave velocity. The results suggest the potential use of P-wave velocity for characterisation of ore grindability. P-wave velocity alone, or in combination with density (P-wave modulus,  $M$ , and acoustic impedance,  $Z$ ) can provide a basis for estimation of crushability attributes if they are calibrated against direct measures of crushability (e.g.  $A^*b$ ).

Results presented here demonstrate that comminution behavior can be related to destructive and non-destructive rock strength parameters (e.g. Young's modulus). However non-destructive measurements are quicker and easier than destructive measurements. The most efficient and convenient way to measure dynamic Young's modulus is via downhole logging.

Strictly speaking, calculation of dynamic Young's modulus requires measurements of density, compressional and shear wave velocity. However, when shear wave velocity measurement is not possible, P-wave modulus has proven to be a good estimator of dynamic Young's modulus and hence other dynamic elastic parameters (e.g. dynamic bulk modulus). Acoustic impedance is also a potentially useful parameter that can be used as an alternative to dynamic Young's modulus in rock mass strength estimation and ore breakage characterisation.

Correlations exist between petrophysical properties and a measure of ore crushability and grindability (i.e.  $A^*b$  and BMWi) however, such correlations are not necessarily strong for every ore deposit. The main reason is that the particles used for JKRBT tests are survivors at a specific small size range after conventional crushing. At smaller size there are fewer defects and samples become harder in terms of comminution. More importantly though it should be noted that the petrophysical properties are measured on intact rock samples while BMWi is measured on composite ground samples from 2m of core. Therefore establishing a relationship between comminution attributes and petrophysical properties can be difficult.

Petrophysical measurements have potential to provide rapid, cheap and more detailed (continuous) characterisation of rock mass which could be used at early stage of investigation during mine design to assess rock mass condition and ore breakage behavior.



# CHAPTER 3

---

## Automated Multi-Sensor Core Logger

### 3.1. Introduction

Geophysical borehole logging is routinely applied for formation evaluation at oil fields and coal mines (Hearst et al, 2000). It is rarely performed at metalliferous mines. There are many reasons for the low utilisation of downhole logging in metalliferous deposits. Density and nuclear logging are often restricted owing to concern over use of probes with radioactive sources. Moreover borehole access, both in terms of equipment/crew logistics and in terms of borehole integrity, is another issue which limits the use of wireline logging in these environments.

Given the generally low historical utilisation of down-hole geophysical logging at metalliferous mines, there are a number of reasons why automated logging of drill core has merit in the context of mineral exploration and geometallurgical research. Measuring the properties of drill core samples removes the logistical problems noted above, while assaying and detailed metallurgical testing performed on the same core samples permits direct correlation of data sets. Most fundamentally, in many cases the archived core represents the only material available from mined portions of ore bodies. Core logging is the only option for petrophysical characterisation in these cases. Nevertheless, whenever practicable, downhole logging offers major advantages in terms of efficiency and, often, in terms of data quality (Fullagar, 2005). Core logger data quality is of course poor over intervals of broken core. This is a fundamental limitation of core logging, and another potential advantage of downhole geophysical logging.

Non-destructive measurement of petrophysical properties of drill cores has become routine in soft sediment studies or ocean drilling programs. Logging of soft sediment cores commenced in the 1960s, with measurement of bulk density using gamma ray attenuation (Evans, 1965; Preiss, 1968). Continuous compressional wave velocity logging (PWL) of soft sediments within cylindrical plastic core tubes was introduced in the mid-1980s (Schultheiss and McPhail, 1989). This provided data which were useful for seismic and stratigraphic correlation in ODP (Ocean Drilling Program) and other sedimentological research.

The first fully automated and integrated multi sensor core logging system (MSCL) included sensors for P wave velocity, gamma attenuation density and magnetic susceptibility (Schultheiss and Weaver, 1992). Automated core logging enables a number of parameters to be recorded simultaneously along each core section. The merging of data from successive core sections then provides the user with a virtually continuous petrophysical log.

It has been a common practice in mineral industry to interpolate and extrapolate ore density measured on discrete intervals of drill cores. However, the development of automated logging systems permits rapid collection of high-resolution petrophysical measurements. However in order to record meaningful data with such systems, systematic calibration of the sensors is required (Gerland and Villinger, 1995; Weber et al. 1997).

The GEOTEK Multi-Sensor Core Logger (MSCL) is one of the commercially available “instrumented bench” systems for multi-parameter core measurements. It allows simultaneous measurements of several petrophysical parameters on soft-sediment and rock cores. It is a portable bench-scale system, which is commercially available in a variety of configurations for work in the field, at sea, or in the laboratory.

Prior to its use in the AMIRA P843 project (as described here), the GEOTEK MSCL system had not been used for petrophysical characterisation of metalliferous deposits. One of the key aims of the P843 project was to ‘map’ geometallurgical attributes throughout an orebody. In order to achieve this goal, development of drill core scale proxies that can be linked to physical testing was required. This entailed direct comparison of petrophysical properties recorded along drill core section using MSCL system with processing indices conducted on the same drill cores.

This chapter presents protocols that have been developed for acquisition and processing of petrophysical data using a GEOTEK MSCL system on diamond drill cores from metalliferous mines. The GEOTEK system described in this chapter is installed in a 20ft (~6m) mobile containerized laboratory for use on mine sites. To accommodate the change from soft sediment to hard rock cores, significant modifications to a number of the sensors were required. The configuration of the logging system, its capabilities and issues of data precision, accuracy and repeatability are described in following sections.

### 3.2. Geotek System

The system is comprised of four main elements: a sensor array, an automatic motorized track which carries core sections past the sensors, an electronic interface, and a computer to control the sensors and record the data. A schematic diagram of a Geotek multi-sensor core logger system and sensors is illustrated in Figure 3.1.

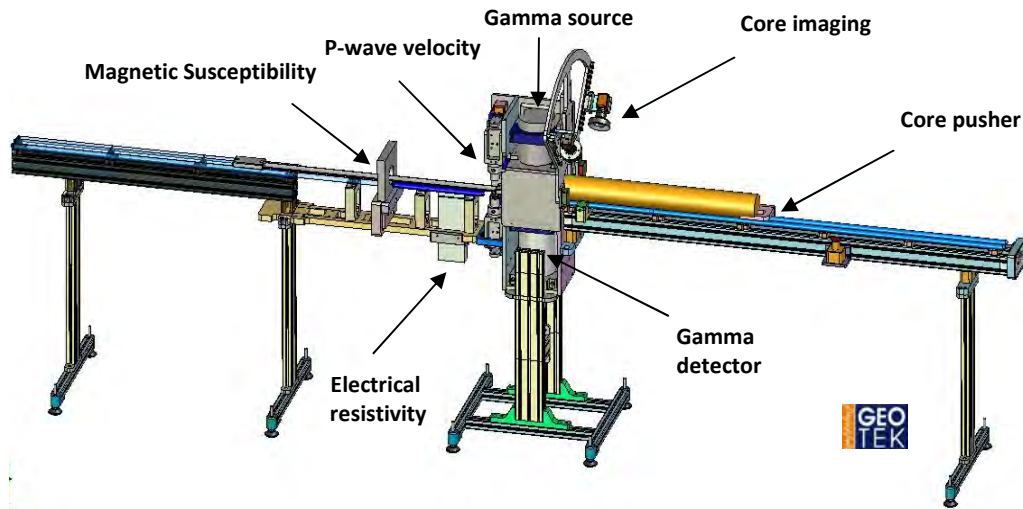


Figure 3.1. Schematic diagram of a Geotek Multi-Sensor Core Logger (MSCL).

Plastic core boats (normally cut into one meter length) are used during core logging. Core pieces are loaded in the plastic core boat and the automatic core pusher pushes the plastic core boat past the sensors at user defined intervals.

### 3.3. Geotek Sensors

A range of petrophysical properties can be recorded using a Geotek MSCL system. These properties include gamma attenuation density, compressional wave velocity and its amplitude, electrical resistivity, magnetic susceptibility and natural gamma. However, the Geotek system used in this research does not include a natural gamma sensor. High resolution core imagery can also be captured simultaneously with petrophysical measurements.

In addition the system records core thickness (which is required for sonic velocity, density and susceptibility calculations) and ambient temperature. The imaging system and petrophysical sensors are described in turn below.

### 3.3.1. Digital Imaging System

The Geotek imaging system was originally designed as a single camera system. The University of Tasmania MSCL system is equipped with three 4Mega pixel CCD cameras for capturing core imagery. A camera is positioned vertically above the track for half-core imagery (Figure 3.2) while the other cameras at 45° use for imaging whole core. All cores from the Cadia East and Ernest Henry study sites described in this thesis were split half cores.

Rock texture was clearly visible when the flat surface of the core was wet, but direct illumination with the ring flash units resulted in specular reflection. To avoid this problem the core was initially illuminated with one light at an inclination of 45°, resulting in reasonable imagery but slightly variable illumination across the cut surface. All core imagery at first case study site (Cadia-East) were captured with this setting (i.e. one camera and one light at an inclination of 45°), however the quality of images were not good enough for quantitative textural analysis. Therefore an additional light source was installed in order to achieve more uniform illumination. Imagery of second case study site (Ernest Henry) was captured with dual lights on either side of the track, at 45° inclination and upgraded software. When logging whole core, two cameras at 45° inclination, with lights, capture images of the core that are stitched in software to cover up to 220 degrees of the core surface.

The imaging camera produces high resolution (40 µm pixel) RGB colour imagery. Core imagery is being utilized in the AMIRA P843 project for automated classification of modal mineralogy (Figure 3.3) and for assessment of ore textural types (Leigh, 2009; Bonnici et al, 2008). Classified core images (Berry, 2009) can also be used for prediction of petrophysical properties (Chapter 7).

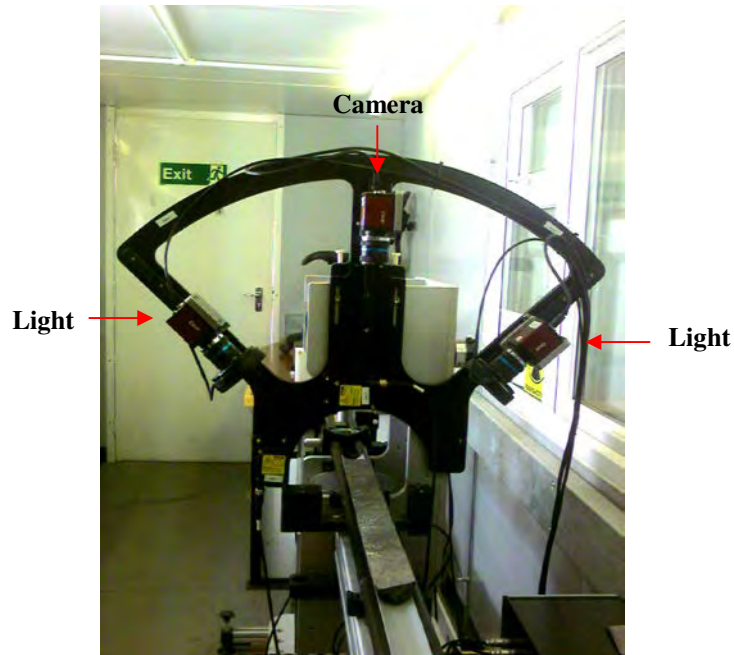


Figure 3.2. Geotek MSCL camera system for capturing half core imagery.

Structural orientations can be interpreted from images of (oriented) whole core. Images of core recorded at 9cm interval as part of the protocol (see section 3.4.4) which produced a generous overlap as each single image covered about 13cm. Individual images are stitched together into 1m intervals by Geotek software. Each stitched image occupies about 40 MB of digital storage.

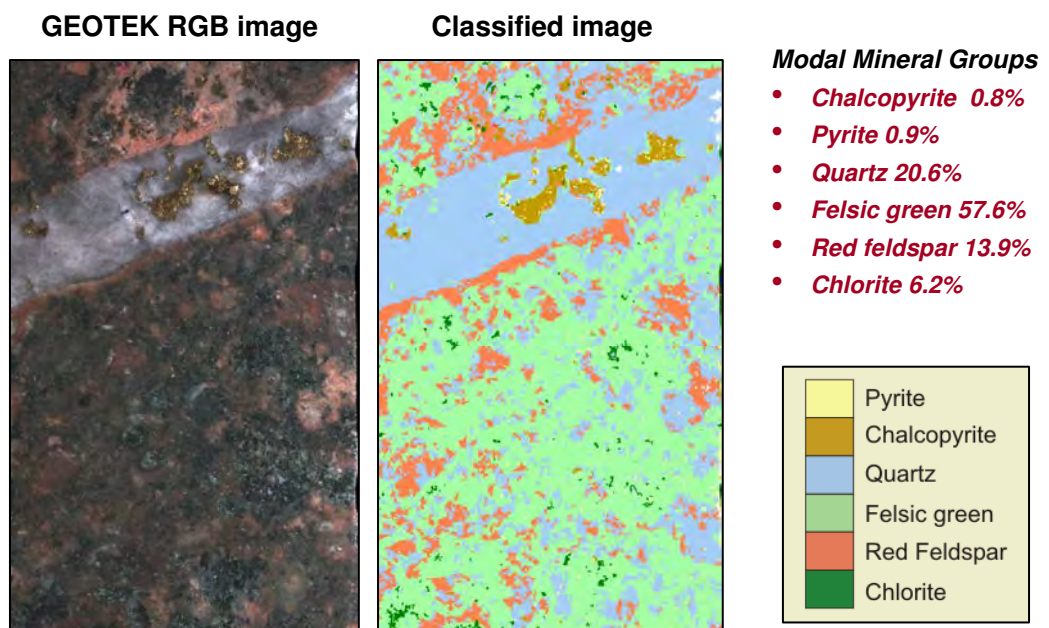


Figure 3.3. Geotek RGB raw image and classified image (Berry, 2008a)

### 3.3.2. Core Thickness Sensor

Knowing the correct thickness of the drill core is crucial for density and velocity calculation. It is also important for volume correction of magnetic susceptibility. The MSCL can measure thickness to 0.01mm precision using a laser range finder. Drill core that has been sawn in half is measured with a single vertical laser. The thickness of whole-core is measured by two horizontal lasers. In each case the thickness is measured relative to a reference thickness. The reference value is determined by placing a NQ/HQ test piece with known thickness directly in the path of the laser(s).

In many cases when logging half core, the core was not evenly split and there was significant variability (up to 0.5cm) in the thickness of each core stick. The accuracy of the thickness measurement can be affected by core rotation (when the P-wave transducer piston is applied). There is also a significant difference between the footprint of the laser (approximately 1mm diameter) and the footprint of the transducer piston (approximately 2cm diameter) and the footprint of gamma density (i.e. 10mm). Thicknesses are also subject to small random errors. The error produced with thickness measurement propagates through calculation of P-velocity, density and magnetic susceptibility.

In order to assess the accuracy of core thickness measured by the MSCL system, the thickness of a meter length of half NQ cores was measured by the logger and compared with the measurements using a digital calliper with 0.01mm precision. As represented in Figure 3.4 the Geotek logger thickness agrees closely with the calliper measurements. The root mean square error of measurements is 0.15mm.

Given that the NQ half-cores are about 2.2cm in radius, so an error of  $\pm 0.15$ mm equates to a relative error of  $\pm 0.7\%$ . Error in core thickness accounts for the bulk of the uncertainty in density and susceptibility, and is one of the two main sources of error in P-wave velocity (the other being the delay time, discussed in section 3.3.5.1). Therefore, when accuracy in core thickness deteriorates, the quality of all the Geotek logging data is adversely affected.

In some cases when NQ half was positioned on the logger below the level of horizontal laser beam, observed spikes in the thickness log were found to be due to interference between the two lasers (horizontal and vertical).

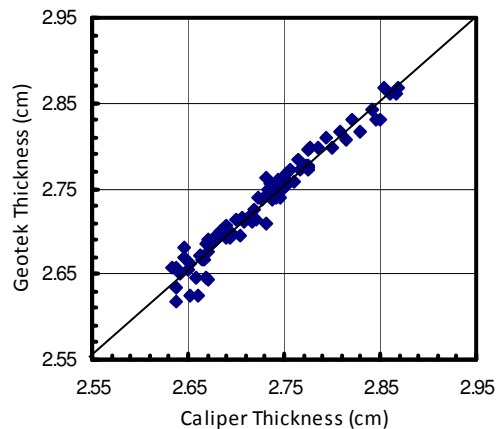


Figure 3.4. Comparison of core thickness measurement with Geotek thickness sensor and a digital hand held calliper.

### 3.3.3. Ambient Temperature

Temperature inside the containerized laboratory is measured with a standard platinum resistance thermometer probe with 0.01°C precision. As far as possible, the temperature was maintained between 20 and 21°C during core logging by an air conditioner installed inside the container.

### 3.3.4. Gamma Ray Attenuation Density

On the MSCL a low activity gamma ray source (10 milli-curie Cs-137) and a sodium iodide detector are used to measure the attenuation of gamma rays passing through the core. Density can be inferred from the count rate, given the core thickness. The radioactive source is enclosed in lead shielding. Operator dose rates are only marginally above background and well below OH&S allowable limits (ARPNSA, 2005). The system works by passing a collimated beam of gamma rays through the drill core (Figure 3.5).

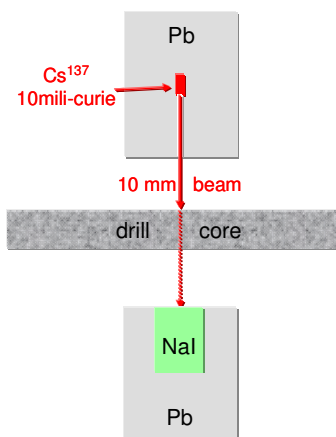


Figure 3.5. Schematic diagram of gamma density operating system.

### 3.3.4.1. Basic principle of measurement

The attenuation of a gamma ray passing through a material is governed by two phenomena, Compton scattering and the photoelectric effect. A caesium source emits gamma rays with energy of 0.662 MeV and at this energy the Compton scattering dominates (Ellis, 1987).

The gamma ray photons are scattered by the electrons in the core. The attenuation is related to the concentration of electrons in the rock. The density of the core can be determined by measuring the number of unattenuated gamma photons that pass through the core. Gamma ray attenuation is exponential with distance, i.e.

$$I = I_0 e^{-\mu \rho d} \quad (3.1)$$

where  $I_0$  represents the incident intensity of gamma rays (counts per second),  $I$  is the intensity after passing through the sample,  $d$  is the thickness of the sample (centimetres),  $\mu$  is the mass absorption coefficient (square centimeters per gram) of the material, and  $\rho$  (grams per cubic centimeter) is the electron density. Rewriting the equation (1), density can be calculated by equation (2) if all parameters on the right-hand side of are known.

$$\rho = \frac{1}{-\mu d} \ln \frac{I}{I_0} \quad (3.2)$$

The mass attenuation coefficient of a specific material depends on the ratio of the atomic number  $Z$  to the mass number of an atom  $A$ . For most minerals this ratio is close to 0.5 with a value of  $\mu = 0.0774 \text{ cm}^2\text{g}^{-1}$  (Gerland and Villinger, 1995). However for hydrogen the  $Z/A$  is about 1, resulting in a value of  $\mu = 0.085 \text{ cm}^2\text{g}^{-1}$  (Grasty, 1979) hence allowing the porosity to be estimated from density measurements.

### 3.3.4.2. Gamma Density Precision

There is a statistical fluctuation in count rate at the gamma detector, so precision increases with increasing count time. Gunn and Best (1998) reported that detector count times of 2 or 5 seconds proved to be the best compromise between logging time and count rate stability for a MSCL system used for sediment core logging.

In the current research, in order to assess precision and optimum count time, a half core sample was positioned in the path of the beam and 100 density determinations were

conducted at each of several integration times between 1 and 32 seconds (Roach, 2006). The density precision is measured by the standard deviation of the data which decreases rapidly as integration time increases.

The best compromise between precision and productivity is achieved for integration times of 8 to 10 seconds (Figures 3.6 and 3.7). For an 8 second integration time and a 5mm collimated beam the precision of the system is  $0.01 \text{ t/m}^3$ . This precision was deemed to be adequate for the purpose of this project.

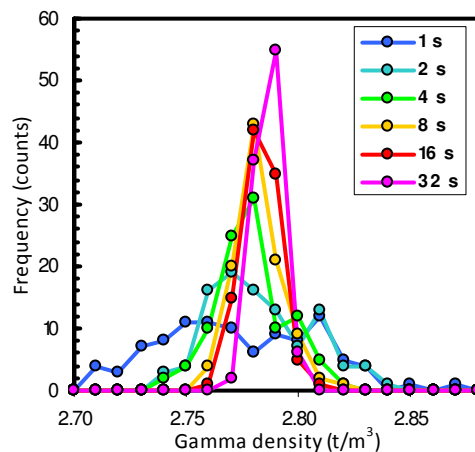


Figure 3.6. Gamma density histogram for a 5mm diameter collimated beam, illustrating the improvement in precision afforded by longer integration times.

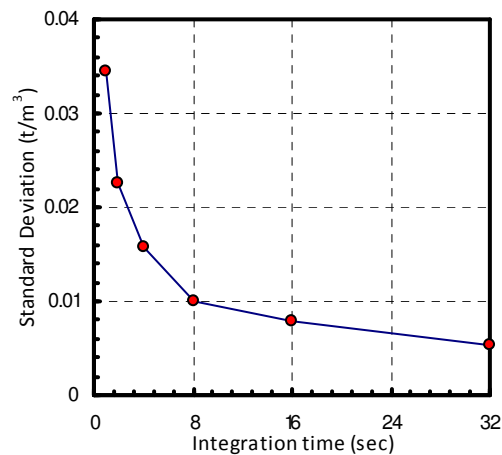


Figure 3.7. Gamma density precision versus integration time for a 5mm diameter collimated beam. An 8 second integration time provides the best compromise between data precision and system productivity.

The aperture for the collimated beam was originally 5mm in diameter, but in an effort to reduce the measurement time and hence increase throughput, the collimator size was increased to 10mm. This change was effected after the Cadia East core logging but before the Ernest Henry core logging. The larger beam size results in a slight loss of

spatial resolution but this is not significant for the current research. The increase in the beam size produced a modest improvement in integration time from 8 seconds to 6 seconds for 0.01 t/m<sup>3</sup> precision.

### 3.3.4.3. Gamma Density Calibration

A cylindrical aluminium test piece (Figure 3.8), machined to different thicknesses, was used initially for calibration of both half and full core samples. The diameter of the aluminium cylinder ranges from 10 mm to 60 mm in 5 mm increments. Gamma count rates are measured twice on the 55, 45, 35, 25 and 15 mm diameter sections and then averaged. One reason for using aluminium cylinder for calibration is because the aluminium density is 2.7 (typical rock density) and it has Z/A of 0.482 i.e. close 0.5 value for most minerals.



Figure 3.8. An aluminium cylinder used for gamma density calibration

The gamma count rate,  $I$ , is related to the electron density,  $\rho_e$ , and thickness,  $x$ , according to

$$I = \beta e^{-\alpha \rho_e x} \quad (3.3)$$

where  $\alpha$  and  $\beta$  are constants and where background gamma radiation is assumed negligible. Taking the natural logarithm of both sides,

$$\ln(I) = \ln(\beta) - \alpha \rho_e x = B - \alpha \rho_e x \quad (3.4)$$

Given the thickness and density of the aluminium, the constants  $\alpha$  and  $B$  can be determined via linear regression of  $\ln(I)$  against  $\rho_e x$ , as shown in Figure 3.9. The linear regression coefficients and sample thicknesses are then used to transform raw count rates to electron density. Small variations in the slope and intercept of the calibration line can result in significant differences in calculated density. In production logging, the gamma count rate is converted to density using

$$\bar{\rho}_e = \frac{B - \ln(I)}{\alpha x} \quad (3.5)$$

where  $\bar{\rho}_e$  denotes the average electron density along the path of the beam. Bulk density,  $\rho_b$ , is related to electron density as follows,

$$\rho_b = 0.5 \left( \frac{Z}{A} \right)^{-1} \rho_e \quad (3.6)$$

where  $Z$  is atomic number and  $A$  is atomic weight. The regression line in Figure 3.9 relates bulk density for aluminium ( $2.70 \text{ t/m}^3$  as measured by water immersion) to gamma counts. In fact the regression is against  $\rho_e$  (electron density) times thickness. The core density inferred from gamma counts using this line of best fit is a bulk density provided the (average)  $Z/A$  of the rock sample is 0.482, i.e. equal to  $Z/A$  for aluminium. Therefore the inferred density as reported in this thesis should more correctly be reported as a bulk density referenced to aluminium.

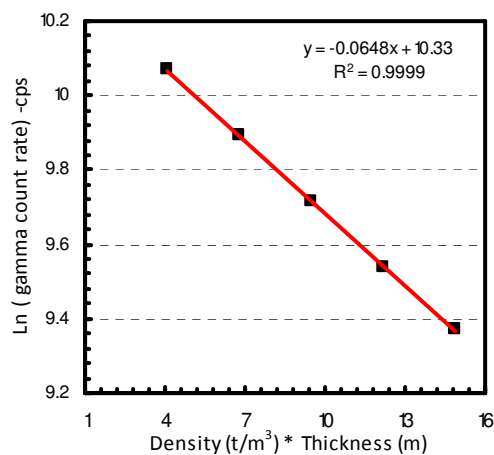


Figure 3.9. Gamma density calibration regression line for a cylindrical aluminium calibrator, relating count rate to aluminium bulk density.

For relatively high density (i.e. more than  $3 \text{ g/cc}$ ) core samples, it would be better that gamma calibration to be carried out with a calibrator that has a density close to the density of the cores. A brass calibrator was also tested in this research however the density of the brass is quite high ( $8.36 \text{ g/cc}$ ) and this causes an over estimation of the density of the core samples.

The geometry of the calibrator should ideally represent the core geometry in order to record accurate core density. In this research for both whole core and half core logging a full cylindrical aluminium calibrator was used (Figure 3.8). However it was found that the increase in collimator aperture from 5 to 10mm diameter affected the density measurement through errors due to calibration using the cylindrical aluminium calibrator

(Figure 3.11). This was mainly due to differences in the beam path for small diameters. For this reason a stepped aluminium calibrator was fabricated (Figure 3.10). The steps were cut into an aluminium cylinder to represent HQ half core with different thicknesses. The thickness of this calibrator varies from 20 to 55mm in 5mm increments.

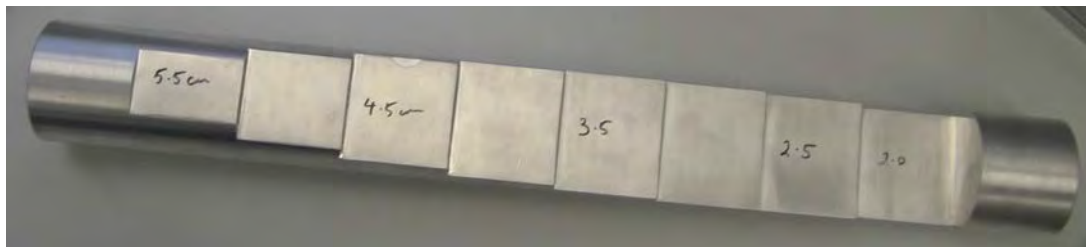


Figure 3.10. An aluminium cylinder machined into steps for gamma density calibration of half cores.

Comparing the calibration graph for the two calibrators (Figure 3.12), the slope of regression line for the half calibrator is less than that for the full cylinder calibrator resulting in a decrease in calculated density for identical gamma count rate and thickness. Conversely calibration using the cylindrical calibrator tends to increase the inferred density for half cores by about 5%.

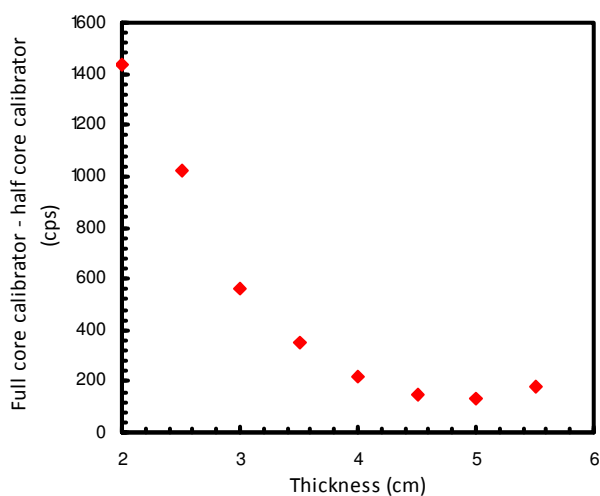


Figure 3.11. Variation of gamma count differences for each calibrator thickness. Note that at small thicknesses (close to the size of most archival half cores) the variation is larger.

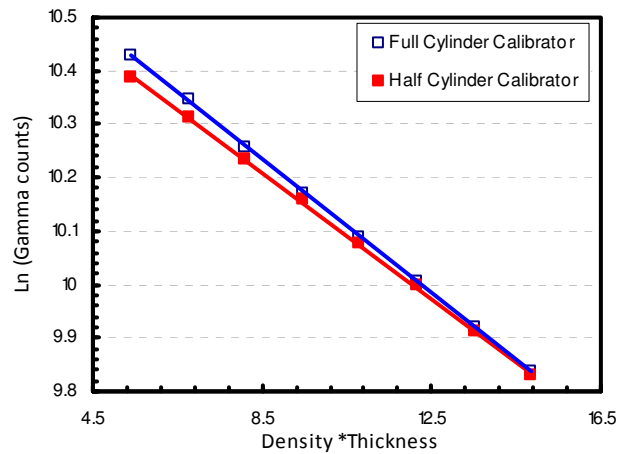


Figure 3.12. Gamma density calibration regression line for two aluminium calibrators

#### 3.3.4.4. Gamma Density versus Temperature

Daily variations between readings on the aluminium calibration piece revealed an inverse correlation between gamma count rate and ambient temperature. Variation in measured gamma count rate is attributed to temperature sensitivity of the gamma ray detector system. To assess the effect of temperature on gamma counts, the half aluminium calibrator with 5cm thickness was placed between the source and the detector and gamma counts were logged with 60seconds integration time. When all measurements for this thickness of aluminium were plotted against temperature, it was evident that count rate generally decreases as temperature increases (Figure 3.13a). Consequently the calculated density increases (Figure 3.13b). This is consistent with the expected behaviour of NaI(Tl) crystal (Hearst et al., 2000).

Prolonged exposure of the sensor to high count rates may also contribute to drift (Geotek, 2000). To account for these effects the containerised laboratory is maintained within a narrow temperature range (~ 1 degree if possible) and density calibration is performed each day prior to commencement of logging.

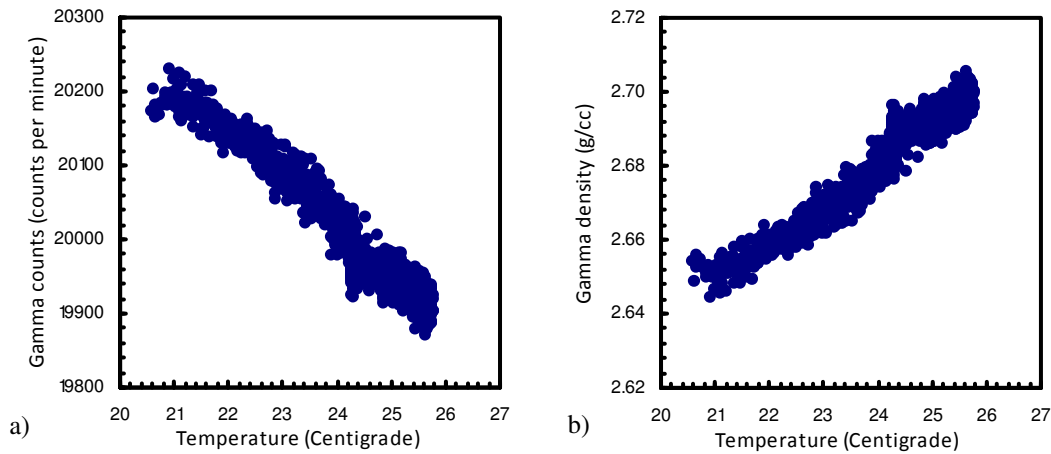


Figure 3.13. Gamma-density temperature sensitivity curve for 60 second integrations through 50mm of aluminum (a) and gamma density variation with temperature for a 50mm diameter aluminium calibration piece (b). Variation is attributed to temperature sensitivity of the gamma ray detector system.

### 3.3.4.5. Gamma Density Accuracy

The accuracy of gamma ray attenuation density compared to standard water immersion density measurement (bulk density) was reported as 0.01 g/cc (Vatandoost et al, 2008a). However the accuracy of gamma density in this study was tested at the time where the gamma source collimator aperture size was 5mm.

As mentioned in section 3.3.4.3 the increase in collimator aperture from 5 to 10mm diameter affected the density calibration using the cylindrical aluminium calibrator. Figure 3.14a and Figure 3.14b illustrate comparison of gamma density measurement versus water immersion density for series of core pieces from Ernest Henry using the cylindrical and half core aluminium calibrators respectively. Gamma attenuation density was measured by MSCL along the two sections of half NQ size drill core at an interval of 1 cm. The cores pieces were selected from different drill holes at Ernest Henry and included mafic and felsic volcanic rocks mineralized with chalcopyrite, pyrite and magnetite. The average gamma density over each length of core piece was computed and compared with the standard water immersion density.

Calibration of gamma densities with the cylindrical calibrator resulted in a bias in density calculation when compared with relative water immersion densities. However as represented in Figure 3.14b there is a much better agreement between gamma densities calibrated with the half core calibration piece and the immersion densities.

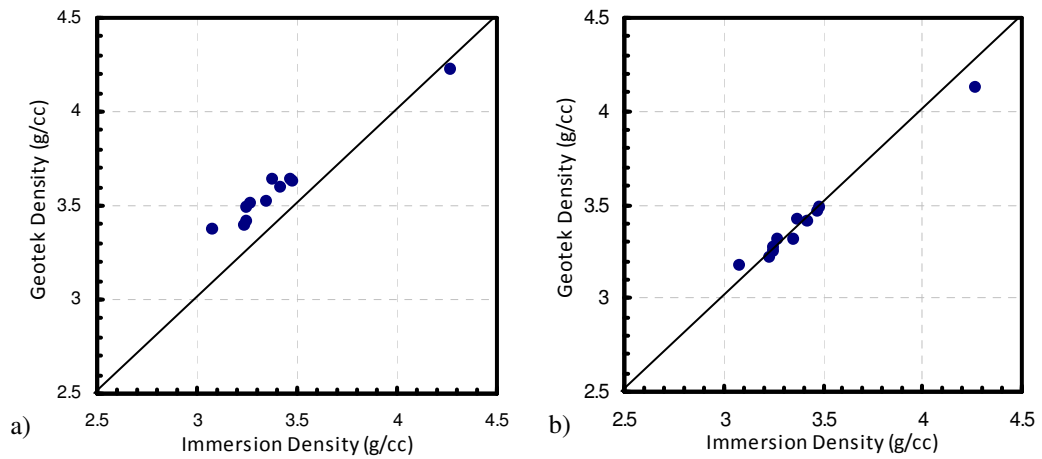


Figure 3.14. Comparison of average gamma density measured by the Geotek MSCL versus water immersion density. Gamma densities are calibrated with the cylindrical calibration (Figure 3.8) piece (a) and the half core calibration (Figure 3.10) piece (b).

### 3.3.5. Acoustic Velocity

Ultrasonic transducers (250 kHz) are used to measure the velocity of compressional waves in the core. P-waves are generated at one transducer, travel across the core sample, and are received at the other transducer. The quantities measured are travel time, in  $\mu\text{s}$ , and signal strength. Travel time is measured with a precision of  $0.01\mu\text{s}$ . The configuration for measurement of half core is illustrated in Figure 3.15. The upper piston transducer is automatically brought to the surface of the core while the lower rolling transducer remains in constant contact with the core boat beneath the core. This enables the core to move freely past the lower transducer before the next measurement is made.

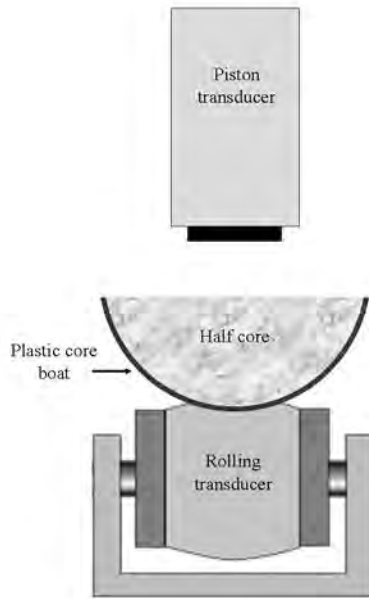


Figure 3.15. Schematic diagram of P-wave velocity transducers in half core mode of acquisition

For whole core measurement two piston transducers are mounted horizontally opposed across the core axis (Figure 3.16). A full measurement cycle takes approximately 5-6 seconds. The velocity through the core can be determined from core thickness and travel time. An automated system is used to detect and measure the travel time of the zero crossing after the first negative excursion of the received waveform that falls within preset amplitude thresholds. The travel time through the rock then is derived from the measured total travel time after correction for transducer delay and for the travel time through the plastic core boat and sonic gel used to improve sensor coupling.

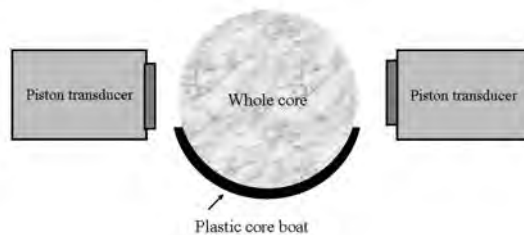


Figure 3.16. Schematic diagram of horizontally opposed P-wave velocity transducers in whole core mode of acquisition

During a measurement the motorised transducers clamp the core. In whole-core mode, the horizontal opposing pistons directly contact the core and there are few problems with coupling. For half-core measurements the coupling between rolling transducer and plastic core boat is less reliable. Moreover, signal is lost at the core-boat interfaces.

When logging half core, total travel time is largely insensitive to the pressure applied by the upper transducer. However, the P-wave amplitude is somewhat sensitive to the applied pressure. For consistency the piston is adjusted so that it travels a standard 30mm from a known rest position. As a result, the pressure applied to the core is expected to be invariant. However in logging operation, the variation in pressure is somewhat dependent on the variation in core thickness.

The amplitude of the signal is sensitive to coupling. Coupling is one of the important factors influencing the transmissibility of P-waves from the sensor into the sample and viscous liquids are normally used during P-wave measurement in laboratory. However water could also be an alternative if samples are saturated fairly well with water. The signal strength and repeatability improved when the flat surface of the half core was thoroughly wetted and when acoustic gel was smeared between the core and core boat (Figures 3.17a and 3.17b). It should be noted that just a sheen of gel is needed in order to couple the core to the core boat and hence to achieve adequate signal strength.

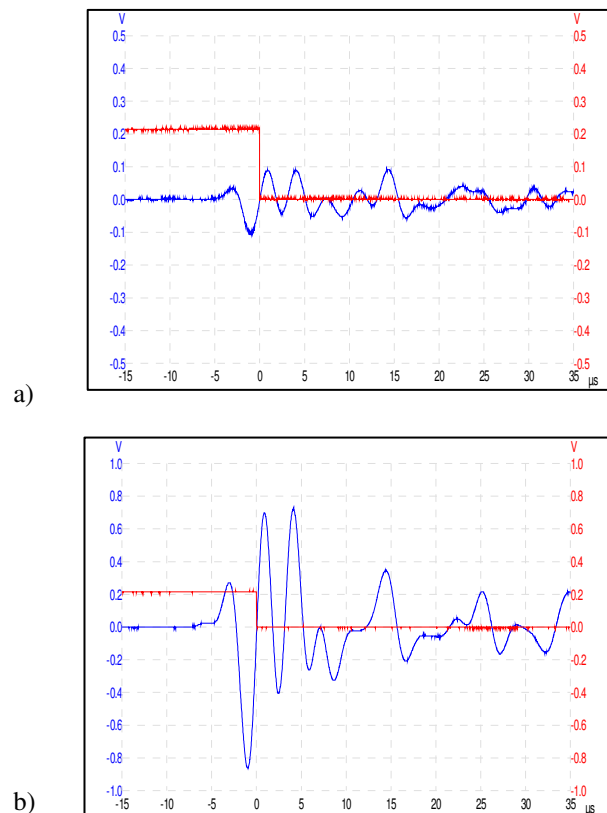


Figure 3.17. P-wave signal recorded on a half NQ size core sample. (a) without acoustic gel between the core and core boat. Signal amplitude is significantly attenuated. (b) with acoustic gel between core and core boat. Note the significant improvement in amplitude when compared to (a) and also the subtle differences in the waveform.

### 3.3.5.1. Sonic System Delay Time

The intrinsic delay of the P-wave system has been established by comparing Geotek travel times with times recorded independently with a model 6 Pundit (Portable Ultrasonic Non-destructive Digital Indicating Tester) using transducers with the highest available frequency (80kHz). The Geotek travel times are recorded in transverse propagation (across core) whereas the Pundit travel times are normally measured in axial propagation (along core). However, the Pundit travel time on the test sample was measured for transverse propagation in order to be comparable with the Geotek travel time.

The intrinsic GEOTEK transducer delay in half-core mode was determined to be  $15.10 \pm 0.25 \mu\text{s}$  with additional delays due to sonic gel ( $\pm 0.2 \mu\text{s}$ ) and of  $0.6 \pm 0.1 \mu\text{s}$  and  $0.8 \pm 0.1 \mu\text{s}$  due to NQ and HQ core boats respectively. Nevertheless the intrinsic delay time is variable during operation. The large intrinsic delay is due to the control software triggers on the positive-trending zero crossing rather than the first break (Figure 3.17).

### 3.3.5.2. Accuracy of Sonic Velocity

A plexiglass sample (half core shape, with a radius of 2.1cm) was used to assess the accuracy of P-wave velocity. The plexiglass has a stated velocity of 2650 m/s (Hung and Goldstein 1983). However the P-wave velocity that was measured for the plexiglass sample using the Pundit was 2750 m/s. The accuracy of the MSCL P-wave velocity for a homogeneous plexiglass sample was determined to be about  $\pm 150$  m/s when compared with the velocity measured by Pundit. However in production mode, the accuracy of velocity measured by MSCL P-wave transducers may decrease mainly due to coupling issues.

To compare the Geotek P-wave velocity measurements in operational logging with Pundit measurements, four sections of half NQ size drill cores selected from Ernest Henry drill hole EH446. P-wave velocity was recorded with the Geotek logger across the core samples at 1cm intervals and then the average of the 1cm velocity measurements along the length of each sample was compared with average of two measurements across the same cores using the Pundit with 80 kHz transducers. Great care was required during measurement of P-velocity both with Geotek and with Pundit as coupling of Pundit transducers with half core is problematic. Sonic gel was also used during P-velocity

measurement with Pundit. As represented in Figure 3.18a, the Geotek and Pundit average velocities are in good agreement, with an RMS difference of 155 m/s (~3%).

The sonic velocity accuracy experiment was also conducted for whole core samples. The mode of measurement by Geotek was kept the same (i.e. vertical transducer motion instead of horizontal) to compare the velocity of Geotek for whole core with that of Pundit. Four sections of NQ size whole cores were logged at 1cm intervals with the Geotek. The average of velocity along the length of each sample was compared with average of two measurements across the same cores using the Pundit with 80 kHz transducers. Figure 3.18b shows that both measurements have a good correlation, however Geotek P-velocity for most of the samples are lower than the P-velocity measured by Pundit. One reason for the low Geotek P-velocity calculation may have been errors in core thickness measurements.

It should be noted that a perfect match between P-velocity measurement with Geotek and Pundit is not necessarily desirable due to different factors that affects the measurements. Pundit travel times are normally measured in axial propagation (along core). Moreover sample size, frequency of transducers and the instrumental precision are also critical factors. ISRM (1981) recommends the minimum lateral dimension should not be less than ten times the wave length while ASTM (1978) stipulates five times the wave length. Thus considering an average velocity of 5000m/s for most hard rocks, the minimum frequency of Geotek transducers should be 1MHz for HQ core size to meet the requirement of ASTM (1978). This criteria is clearly not met by the current Geotek system with 250kHz transducers.

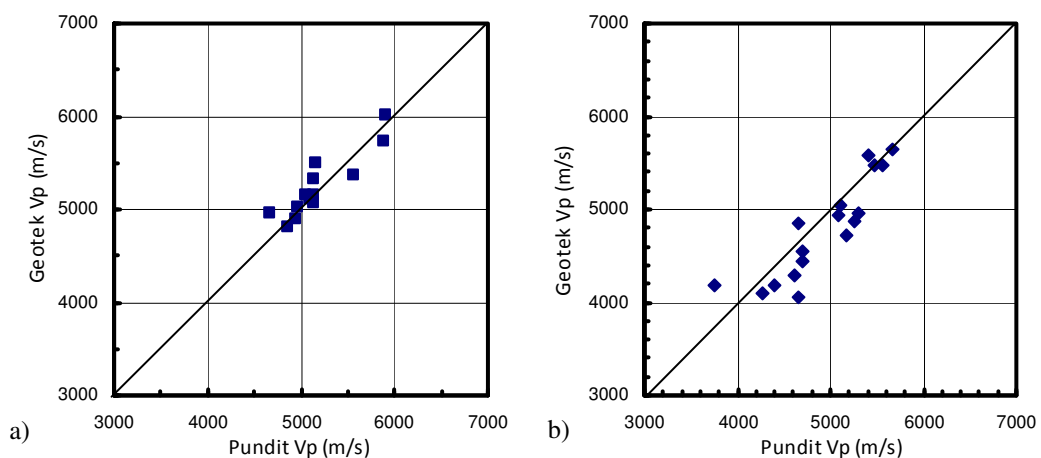


Figure 3.18. Comparison of average Geotek P-velocity versus average Pundit P-velocity for a series of half cores (a) and for a series of whole cores (b). Note that the vertical mode of measurement was conducted by Geotek MSCL.

#### 3.3.5.3. Sonic Full Waveform

The Picoscope virtual oscilloscope software allows visual quality control on velocity measurement during core logging. The P-wave waveform can be recorded only manually but is not routinely acquired by the system. An example of a full waveform P-wave measurement is shown in Figure 3.17. The digitally recorded data from a full waveform P-wave measurement needs to be processed. Waveform analysis can be much more detailed than that inferred from a simple transit time but some effort is required to produce the results. Spectral analysis (Fourier domain) can provide useful information such as attenuation.

#### 3.3.5.4. P-wave Amplitude

Measurements of P-wave amplitude were unreliable until the core surface was wetted thoroughly and acoustic gel was smeared between core and core boat. It is also essential to maintain a good acoustic coupling between the lower transducer roller and the core boat. This is achieved by putting a few drops of water (or gel) onto the top of the roller, where it makes contact with the core boat.

At this stage the GEOTEK MSCL system only records a relative measure of signal level, and does not digitise the full acoustic waveform. However, the amplitude appears in many cases to be a useful indicator of fracture density in rock masses as also suggested by Barton (2007). The acoustic waveform is currently displayed during data collection for quality control purposes and there are clear variations in sonic waveforms between different materials. However this observation has not been followed up in detail in this research since the logger cannot currently automatically capture this information. Implementation of full waveform recording in the MSCL could provide additional information on rock strength. Full waveform sonic recording would permit spectral analysis and hence better assessment of attenuation.

#### 3.3.5.5. Redesign of the Acoustic Velocity System

Coupling issues associated with the lower rolling P-wave transducer in half core mode were a major issue affecting accuracy and precision of P-wave velocity and amplitude measurement in the original Geotek configuration. The system was reconfigured to enable P-wave measurements to be made in a vertical orientation using the piston transducers in a reciprocating mode in the same way as can be achieved in the horizontal

mode. This mechanical arrangement of transducers (Figure 3.19) was believed to improve the transducer coupling and enables more consistent measurements. However the presence of the core boat and sonic gel still introduces uncertainties in accurate travel time and amplitude measurement.

In order to determine the intrinsic delay of the transducers, a reference cylindrical sample piece of aluminium with known travel time of  $26\mu\text{s}$  commonly used for calibration of the Pundit sonic tester used in this experiment. The travel time recorded by Geotek MSCL when the cylindrical sample placed between transducers in vertical position was  $37.10\pm 0.1\mu\text{s}$ . This means that the Geotek transducers in this mode have a delay of  $11.1\pm 0.1\mu\text{s}$ . However when transducers were opposed face each other the travel time was  $12.25 \pm 0.1 \mu\text{s}$ . This may mean that the actual travel time of Pundit reference sample is  $37.1-12.25= 24.85$  (i.e.  $1.15\mu\text{s}$  lower than the stated value).

In another experiment a cylindrical sample of plexiglass with a length of 10cm was tested for travel time. The total measured travel time with Geotek was  $48.35\mu\text{s} \pm 0.1 \mu\text{s}$ . The travel time through plexiglass after correcting the Geotek intrinsic delay was  $48.35-12.25 = 36.1 \mu\text{s}$ . The travel time of the same sample measured by Pundit was  $36.7\mu\text{s}$ . This means that recorded travel time by Geotek based on intrinsic delays of transducers ( $12.25\mu\text{s}$ ) will be underestimated by  $0.6\mu\text{s}$  when compared with Pundit measurement. Therefore a delay of  $12.25\mu\text{s}$  was assumed for this setting of transducers. However to assure repeatability it is recommended that this delay is measured daily prior to core logging.

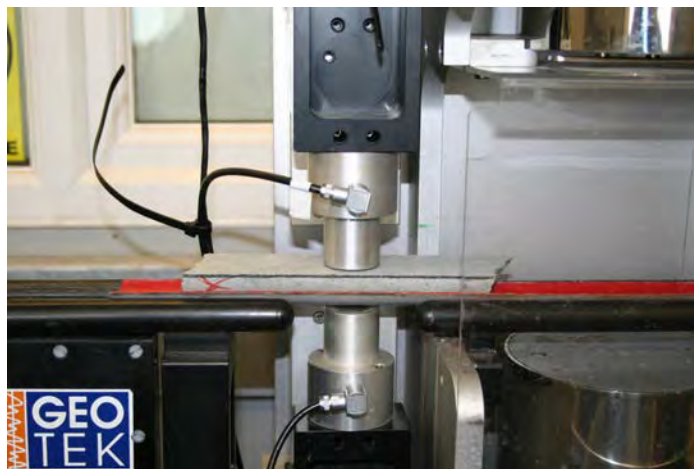


Figure 3.19. Geotek P-velocity transducers in vertical mode for both half and whole core acquisition.

**3.3.6. Non Contact Resistivity (NCR)**

The standard non-contact resistivity (NCR) system on the MSCL employs small horizontal coplanar coils in a slingram configuration. It has a dynamic range of 0.1-100  $\Omega$ m. The NCR sensor was originally designed to measure the resistivity of relatively homogenous water-saturated sediment cores in which resistivity is moderate and varies comparatively slowly with depth (Figure 3.20a).

Electrical conductivity in rocks occurs by one of two mechanisms: ionic conductivity electronic conductivity. The connectivity of pore spaces (i.e. permeability) is critical in determining ionic conductivity. However tests conducted in ODP research on dry and saturated cores of olivine-bearing gabbro, which were very conductive showed that there was little variation in conductivity measurement suggesting that ionic conductivity was not the dominant mechanism (Searle, 2008).

For a heterogeneous zone of conductive material with large conductivity contrast (e.g. thin sulphide veins and aggregates), the response of the standard Geotek NCR system is affected by the geometrical distribution of the minerals in addition to their conductivity. The secondary electric currents that are induced in a single vein can produce both positive and negative responses. Consequently the overall response from mineralised cores can be very complicated and confusing (Figure 3.20b). For this reason a different conductivity sensor with a co-axial loop configuration and with a larger dynamic range was interfaced to the MSCL.

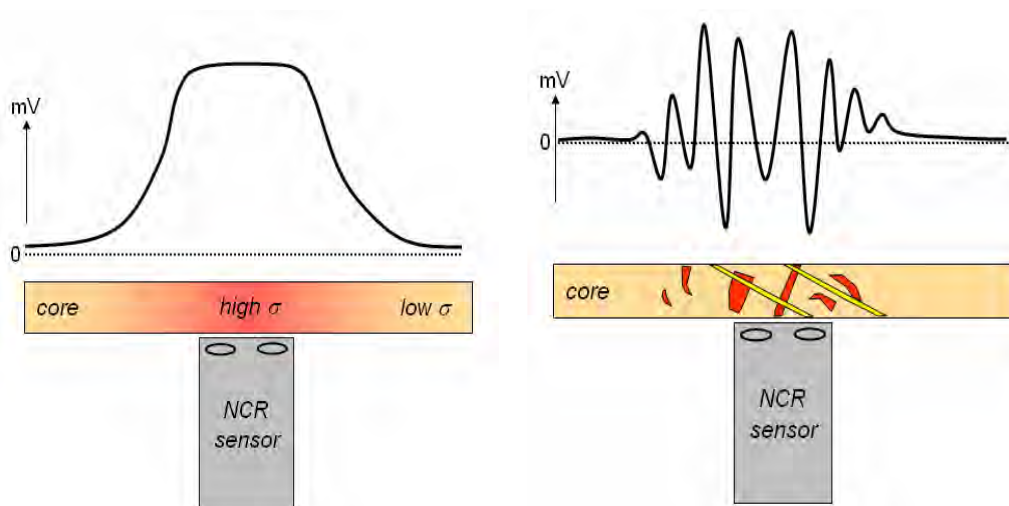


Figure 3.20. Non-contact resistivity response schematic. (a) for a thick zone of homogenous conductive material. (b) for a heterogeneous zone of conductive material.

### 3.3.7. Loop Conductivity Meter

A hand-held GCM-2 inductive coil conductivity meter designed by Geo Instruments was incorporated into the Geotek MSCL (Figure 3.21). Incorporation of GCM-2 into the logger was carried out after Ernest Henry core logging. The GCM-2 measures the inductive conductivity of drill-core inserted into the coil. The GCM-2 nominally has a wide dynamic range, from  $10^{-1}$  to  $10^5$  S/m although experience shows that its sensitivity at low conductivity is quite poor. There are sensor coils available with different internal loop diameters such as AQ (27mm), BQ (36.5mm), NQ (47.6mm), HQ (63.5mm) and PQ (85mm). The sensor operating frequency ranges from 15kHz to 2 MHz. An automatic frequency option in GCM-2 automatically assigns the appropriate frequency for the selected loop sensor. The sensor should be zeroed in free air before operation. Geo Instruments suggest a fluctuation of  $\pm 2$  S/M after zeroing. However zeroing of the system inside the Geotek container was problematic (i.e.  $\pm 10$  S/M). An attempt was made to cover the loop sensor with aluminium foil in an effort to shield the system, but the readings were still high (5-10 S/M).

In order to assess the precision of measurement with different frequencies, the conductivity of a BQ size massive sulphide core sample was measured with a loop of 63.5mm diameter using four different frequency range (62, 125, 250 and 500kHz). 100 conductivity measurements were conducted (one every second) while the sample was placed fixed in the loop sensor. As the frequency increases the conductivity decreases (Figure 3.22).

The variability of conductivity at 500 kHz is  $\pm 0.25$  S/M. However the system showed quite strong fluctuation at 250 kHz. This phenomenon is not yet understood. This experiment was repeated in the same manner but using a smaller loop size (i.e. 47.6mm). The measurement with 250 kHz was more stable ( $\pm 20$  S/M) compared with 62.5mm loop size ( $\pm 90$  S/M), but this variability is still very high. Again at high frequencies, the precision of conductivity was relatively higher. However at 500 kHz the variability of conductivity measurement was  $\pm 5$  S/M. These tests show that the operation of the GCM-2 conductivity sensor is problematic.

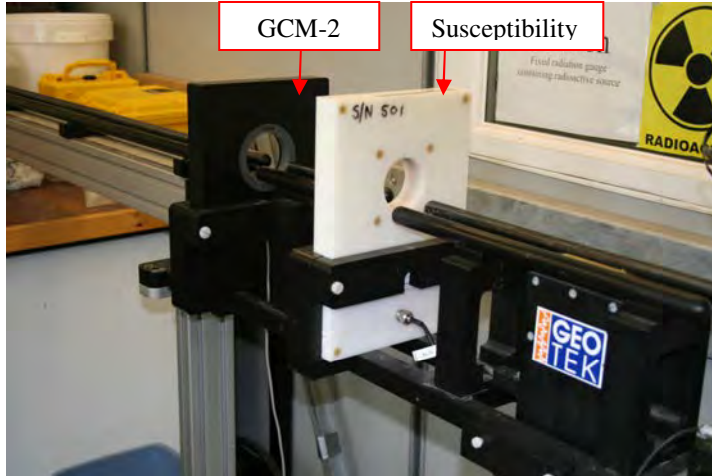


Figure 3.21. Loop Conductivity meter incorporated into the Geotek logger.

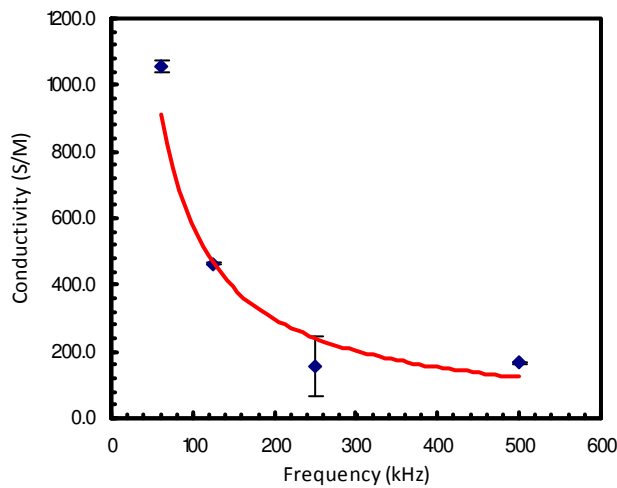


Figure 3.22. Conductivity of a core sample recorded using a 63.5mm diameter loop with different frequencies. Note that the vertical bar indicates the calculated standard deviation.

### 3.3.7.1. Loop Conductivity Meter Calibration

The half cylinder aluminium calibrator (used for gamma density calibration) was used for calibration of conductivity. Ideally it would be best to assess the conductivity measurement on individual pieces of aluminium with different thicknesses. A 63.5mm coil sensor was used in order to accommodate measurement on all thicknesses of aluminium calibrator. A frequency of 125 kHz selected in this experiment as the conductivity readings at this frequency were more repeatable. Averages of 10 conductivity measurements in each thickness (step) of aluminium calibrator were computed. However readings that were affected due to adjacent steps were eliminated before averaging. Figure 3.23a shows that the measured conductivity of aluminium calibrator increases as the calibrator thickness increases. The variability of conductivity

as calculated by standard deviation of measurements also increases slightly with increase of aluminium thickness.

In another experiment and in order to assess the effect of temperature on conductivity logging, the massive sulphide core sample was placed fixed within the conductivity loop sensor (47.6mm) with 500 kHz frequency and 1000 conductivity measurement conducted. Figure 3.23b shows that with an increase of temperature the conductivity increases as well. This is a large variation of conductivity with small change in temperature. The variation in conductivity is most likely due to sensitivity of the sensor to temperature and also sensor's temporal drift. The tests on the GCM-2 conductivity sensor indicate that a number of factors potentially affect the measured response and that this instrument is not ideally suited for routine logging.

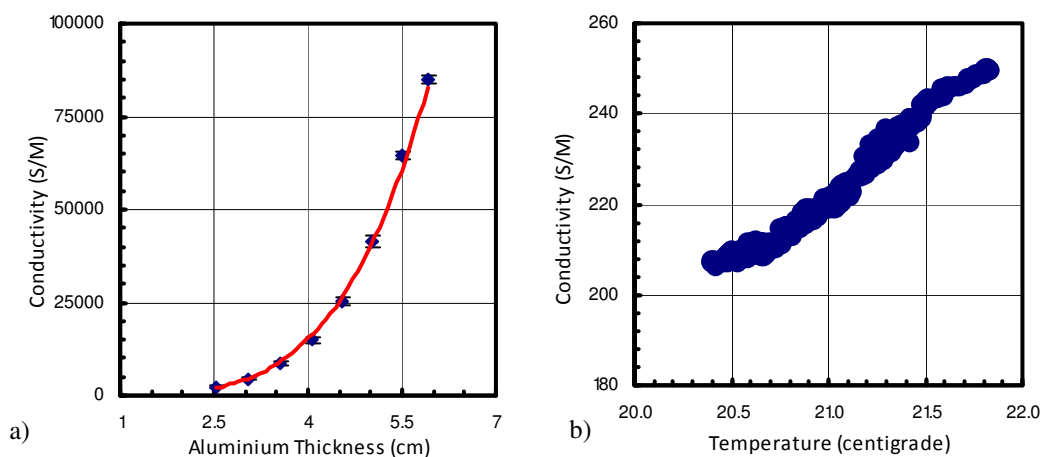


Figure 3.23. Conductivity of aluminium calibrator versus its thickness for 125kHz frequency and 63.5mm loop sensor (a). The vertical bars on data indicate the standard deviation for each thickness. Conductivity versus temperature for a sample fixed in place (b).

### 3.3.8. Magnetic Susceptibility

The MS2C Bartington meter incorporated into the logger measures magnetic susceptibility by recording the variation in inductance of the sensor coil when core is placed within it. Magnetic susceptibility is widely used in MSCL systems for studies of sedimentology, paleoclimate, bottom-water flow conditions and regional stratigraphy.

Two types of susceptibility sensors can be installed on the logger: a point-sensor which provides high spatial resolution, and a loop sensor which has poorer spatial resolution but a higher signal to noise ratio and so is better for measuring sediments with low magnetic

susceptibility (Gunn and Best 1998; Ortiz and Rack 1999). For heterogeneous volcanic rocks with high magnetic susceptibility (i.e. Ernest Henry drill cores), the sensitivity and smaller depth of investigation of the point sensor compared with loop sensors makes loop sensors more suitable. Moreover point sensors are more sensitive to temperature fluctuation (Geotek, 2000). For these reasons the loop sensor was used within this research.

The loop sensor was installed on the GEOTEK logger in such a way that no magnetic or metallic components are close to it. The MSCL software automatically zeros the sensor prior to the first measurement. However in order to remove sensor drift during acquisition it is recommended to zero the sensor after about 10 meters of core logging. As originally installed, the meter had a high sensitivity ( $1 \times 10^{-6}$  SI) but limited upper range (maximum 0.1 SI). The upper range of the system was often exceeded during initial logging trials so the sensor was modified by Bartington Ltd to accommodate susceptibilities up to 1 SI. Using a larger loop diameter than recommended for a particular core diameter enables measurement of susceptibility up to approximately 3 SI. This upgrade was carried out after Cadia East core logging but prior to Ernest Henry core logging.

Three test pieces were provided by Bartington Ltd with true susceptibilities of  $249 \times 10^{-4}$ SI,  $54 \times 10^{-4}$ SI and  $6 \times 10^{-4}$  SI for loop diameters of 60, 72 and 150mm respectively. The test pieces have a diameter of 41.1, 55.6 and 56.1mm. Two of these test pieces (41.1mm and 55.6mm in diameter) were used for recording susceptibility with different loop sizes. As represented in Figure 3.24 as the ratio of loop sensor diameter to sample diameter increases the measured susceptibility decreases. This observation suggests the need to correct the measured susceptibility measurement for sample volume.

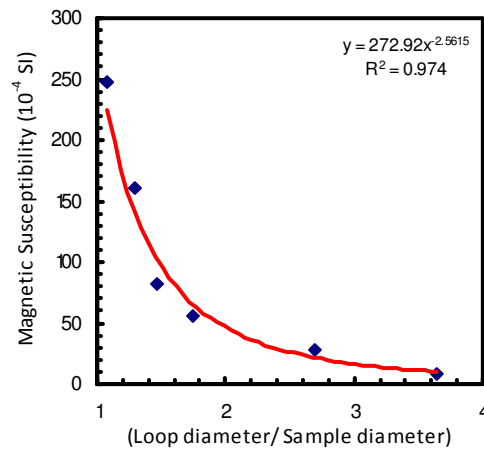


Figure 3.24. The relationship between apparent susceptibility and ratio of loop sensor diameter to sample diameter.

#### 3.3.8.1. Sample Volume Effect

Because measured susceptibility depends on sample volume, measurements on pieces shorter than the loop diameter will be underestimated. Such samples (less than loop diameter) need to be tested carefully. However in production logging where core pieces are placed end to end this should not be an issue unless a considerable gap between core pieces is present.

#### 3.3.8.2. Loop Size Correction

The maximum susceptibility that can be recorded increases with sensor coil diameter, so with appropriate volume correction higher magnetic susceptibility measurement can be achieved by using a bigger loop size. Susceptibility tests were conducted on three sections of half cores from Ernest Henry (drill hole EH635) with loop diameters of 60, 72 and 150mm. Each section was one meter long and all cores were altered mafic volcanic breccia and were mineralized with chalcopyrite and pyrite. The core pieces were positioned end to end in the core boats. Magnetic susceptibility was recorded in 1cm intervals with each loop sensor. As shown in Figure 3.25a, there is a linear relationship between measurements with 60 and 72mm loop sizes. The slope is 1.45 close to the ratio of the areas of the two coils (i.e. 1.44).

The readings with 60mm and 150mm diameter coils are compared in Figure 3.25b. 15 point (15cm) moving averages were computed for the 60mm coil data in an attempt to “resolution match” the profiles: the 60mm coil will resolve finer details than the 150mm coil. The susceptibility for the 150mm coil shows a good correlation with 15 point moving averages of readings with the 60mm loop size (Figure 3.25b). The ratio of coil areas  $(150/60)^2$  is 6.25 which is comparable with 6.57, the slope of the regression line. The comparison between magnetic susceptibilities recorded with the 72mm and 150mm diameter coils also revealed a good correlation (Figure 3.25c). A 15 point moving average has been applied to the 72mm coil data. The readings with 72mm and 150mm diameter coils are compared in Figure 3.25c. The ratio of coil areas is 4.34 in this case, which is comparable to the 4.58 slope of the regression line.

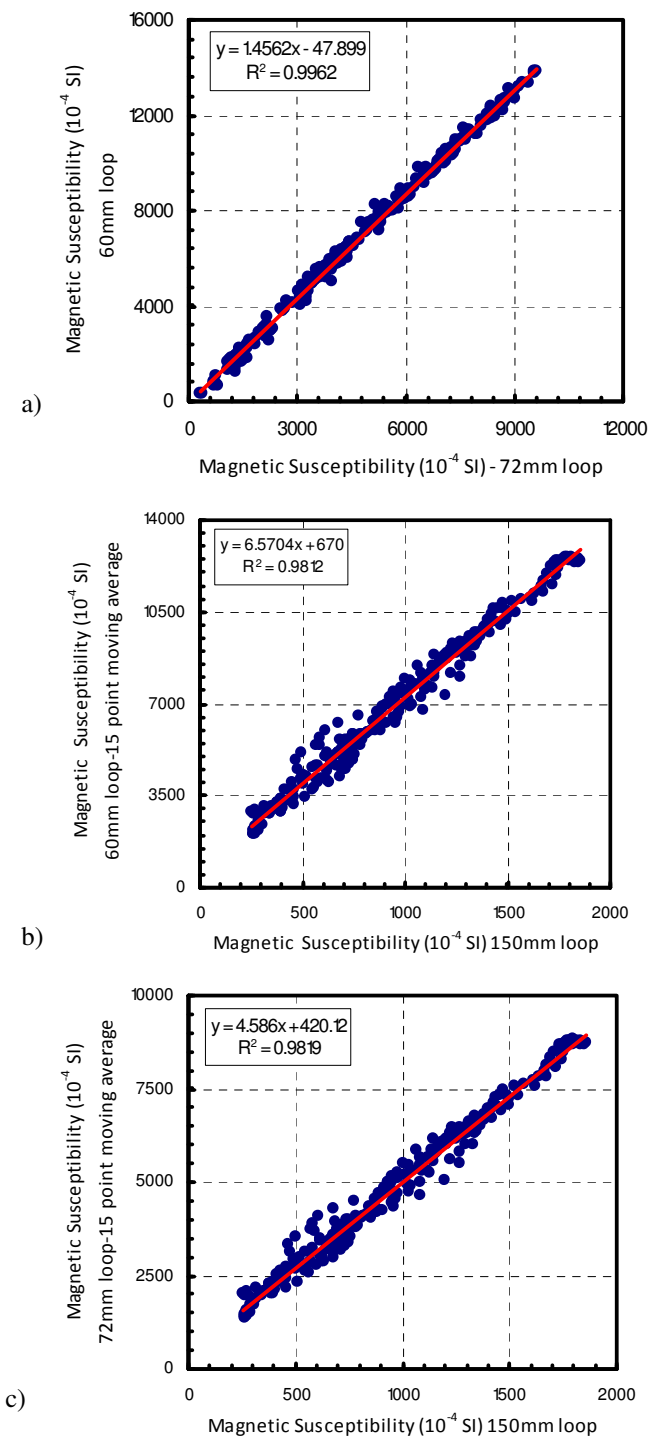


Figure 3.25. Correlation between apparent magnetic susceptibility as measured using 60mm and 72 mm (a) 60mm and 150mm (b) 70mm and 150mm (c) loop sensors. A 15 point moving average has been applied to the 60mm (b) and 70mm (c) loop data to account for the difference in spatial resolution of the two sensor.

### 3.3.8.3. Susceptibility Volume Correction

The MS2C coil sensors were developed for whole core measurements. Empirically, it has been established that the measured susceptibility value decreases by approximately a factor of two when a whole core is split in half. In this experiment eight sections of whole core from Cadia East was selected in which half of the sections were HQ size and the rest were NQ size. The core samples were volcanoclastic rocks with potassic and propylitic alteration. The susceptibility of these samples was checked with a hand held susceptibility meter to ensure that they were mineralized with magnetite. Each section was one meter long and was logged with Geotek MSCL at 1cm intervals with loop sensors of 60mm and 72mm for NQ and HQ cores respectively. Then the whole cores were split in half and the above measurements were repeated. As represented in Figure 3.26 there is a good correlation between measured susceptibility of whole (NQ/HQ) size core and measured susceptibility of half (NQ/HQ) size core derive from it. However the measured susceptibility value of whole (NQ/HQ) size core is higher by approximately a factor of two when compared with measured susceptibility of half (NQ/HQ) size core derived from it. Therefore half-core readings need to be corrected according to sample cross-sectional area.

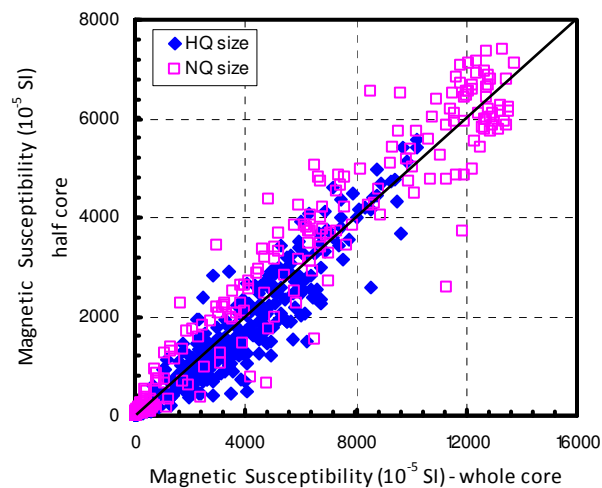


Figure 3.26. Magnetic susceptibility of whole core versus magnetic susceptibility of half cores derived from it.

For imperfectly split half-core, with thickness differing from the notional core radius,  $R$ , by an amount  $\Delta$ , the cross-sectional area of the remaining core (shaded section in Figure 3.27) controls the sample volume (Fullagar, 2006). The area of the blue zone is given by

$$A = \frac{\pi R^2}{2} \left[ 1 - \frac{2}{\pi} \left( \theta + \frac{\Delta}{R} \cos \theta \right) \right] \quad (3.7)$$

where  $\Delta$  is positive for thin half-core and negative for thick half-core. The volumetric correction factor then becomes

$$K_{rel} = \frac{2}{1 - \frac{2}{\pi} \left( \theta + \frac{\Delta}{R} \cos \theta \right)} \quad (3.8)$$

Therefore  $K_{rel}$  ranges from 1 for a complete core, to 2 for a perfect half-core, to larger values for thin sections of split core.

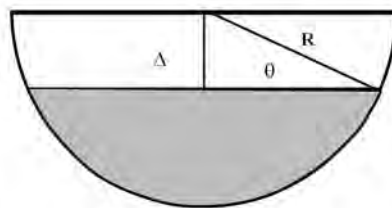


Figure 3.27. Schematic section through (half) core.

#### 3.3.8.4. Temperature Effect

Although Geotek Ltd suggests that magnetic susceptibility measurements are temperature sensitive, in practice temperature variation in the container did not affect the susceptibility measurements significantly. As illustrated in Figure 3.28, for a five degree increase in temperature, the susceptibility only increased by  $5 \times 10^{-4}$  SI which for the mineralized samples measured in this study is not a significant variation. The susceptibility sensor is not really affected by temperature variations but the sensor is subject to occasional random fluctuations. The experiment presented in Figure 3.28 was conducted on a piece of core with high magnetic susceptibility placed in a fixed position within between the loop, then susceptibility and temperature recorded by Geotek MSCL every minute. Using the same procedure, the experiment was repeated for a sample with low magnetic susceptibility. As represented in Figure 3.29 the susceptibility recordings are not significantly affected by temperature variations but the sensor is subject to random fluctuations that are usually readily identified in the data.

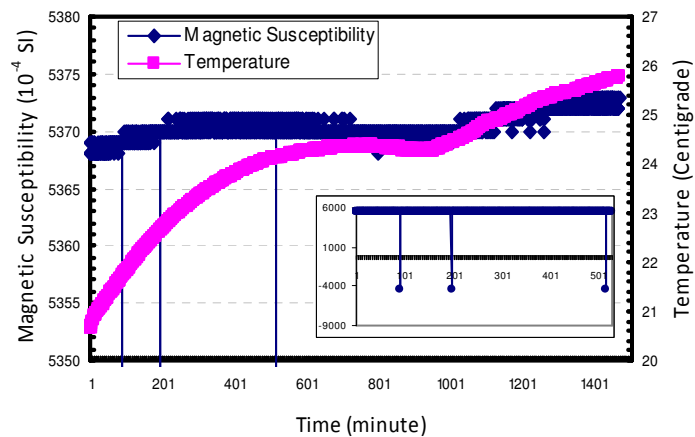


Figure 3.28. Magnetic susceptibility versus temperature recording for a sample with high susceptibility fixed placed within a loop sensor for about 24hours. The recording has not affected by temperature variations but sensor subject to random fluctuations.

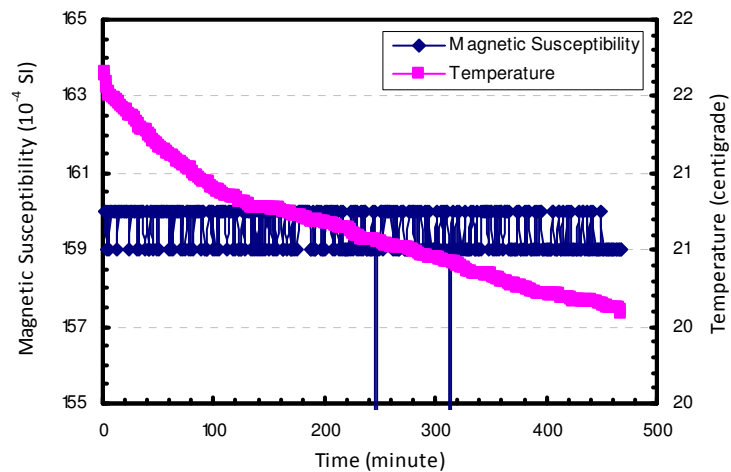


Figure 3.29. Magnetic susceptibility versus temperature recording for a sample with low susceptibility placed within a loop sensor for about 24hours. There is no evidence of temperature sensitivity but random negative spikes in the data are apparent.

### 3.3.8.5. Comparison of Measurements

Magnetic susceptibility measurement with the Geotek MSCL loop sensors were compared with a hand held KT-9 kappameter which is the most common instrument used in the mineral industry for magnetic susceptibility measurement. This test was conducted prior to upgrade to the MSCL susceptibility sensor. Both KT-9 and Geotek susceptibility sensor can record up to 0.1 SI however the nominal sensitivity of the loop sensor is  $10^{-6}$  SI while KT-9 has a sensitivity of  $10^{-5}$  SI.

In this experiment magnetic susceptibility was recorded at 1cm intervals using MSCL on about 4.5m half NQ size drill cores from Cadia East (CE098). The 60mm loop diameter was used for susceptibility measurement with MSCL. Then susceptibility was recorded

using a KT-9 every 10cm for the same drill cores. Two readings were recorded on kappameter and the averages of readings were used for comparison with the measured values of the MSCL. As represented in Figure 3.30, both dataset are in a good agreement. It should be noted that the drill cores selected in this experiment were low in susceptibility to allow comparison of measurement on loop sensor with KT-9.

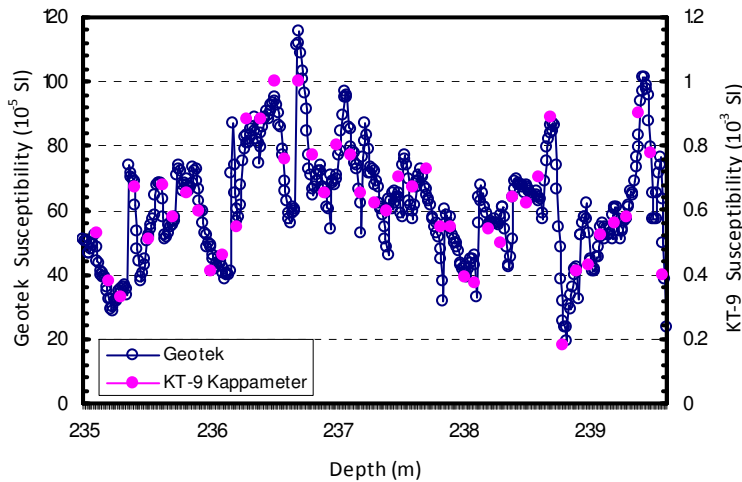


Figure 3.30. Comparison of Magnetic susceptibility recorded by Geotek and KT-9 Kappameter.

### 3.4. Core Logging

Prior to commencement of core logging procedures for core preparation need to be considered. This will be presented in following section.

#### 3.4.1. Core Preparation

Core preparation for logging is a key aspect of data acquisition. Drill core should be cleaned and completely wet on the surface. By wetting the surface of the core, the core imagery is improved, and the P-wave amplitude is also enhanced. Ultrasonic gel is smeared on the plastic core boat in order to achieve good acoustic coupling between the core and core boat. In order to log core in a continuous fashion, plastic clips are used to join the core boats together. If the core boats are not joined in this fashion, they may ride over one another as the core is pushed through the logger.

In general, measurement of drill core petrophysical properties involves the following steps:

1. Core trays are moved into the shipping container and stored on shelves for at least 2-3 hours prior to logging in order to attain temperature equilibration.
2. A core tray is lifted from shelf to bench and the core top section depth is checked
3. Wet sponges are placed on top of the core in the core tray to hydrate the surface of the sample.
4. Acoustic gel is smeared on the core boat
5. Core pieces are cleaned before being transferred to the core boat
6. Core pieces from the core tray are transferred to the core boats – severely broken core can not be logged
7. The top section depth is entered into the Geotek software.
8. After the core boat with the core is positioned on the track, plastic clips are used to join the core boat to the preceding one.

During measurement, the flat surface of half core is kept wet for imaging and sonic coupling. It is important that the core is kept wet in order to obtain good quality images but not too wet as this makes the surface too reflective and results in poor quality images.

When logging of a section of core is finished, the core pieces are transferred from the core boat back to the core trays and steps 4 to 9 are repeated until a tray of core is completed. Core trays in which logging is finished are shifted from the bench back to a shelf.

### **3.4.2. Data Acquisition and Processing**

During acquisition, the GEOTEK software displays raw data (core thickness deviation, P-wave travel time, P-wave amplitude, attenuated gamma counts, magnetic susceptibility, temperature and electrical resistivity) as illustrated in Figure 3.31 and imagery is displayed in real time. The spikes in some logs (Figure 3.31) are due to the broken core or a gap. There is also a processing window available which permits basic processing of data in real time. However the large amounts of data produced by MSCL require efficient software processing tools. The MSCL software is very limited in terms of processing and interpretation options, but some suitable commercial software is available. LogTrans software, developed by CMTE for multi-parameter log interpretation (Fullagar et al, 1999), has been used for data processing and interpretation in the current research. Although developed in the context of geophysical logs, LogTrans can be applied to any type of multi-parameter data.

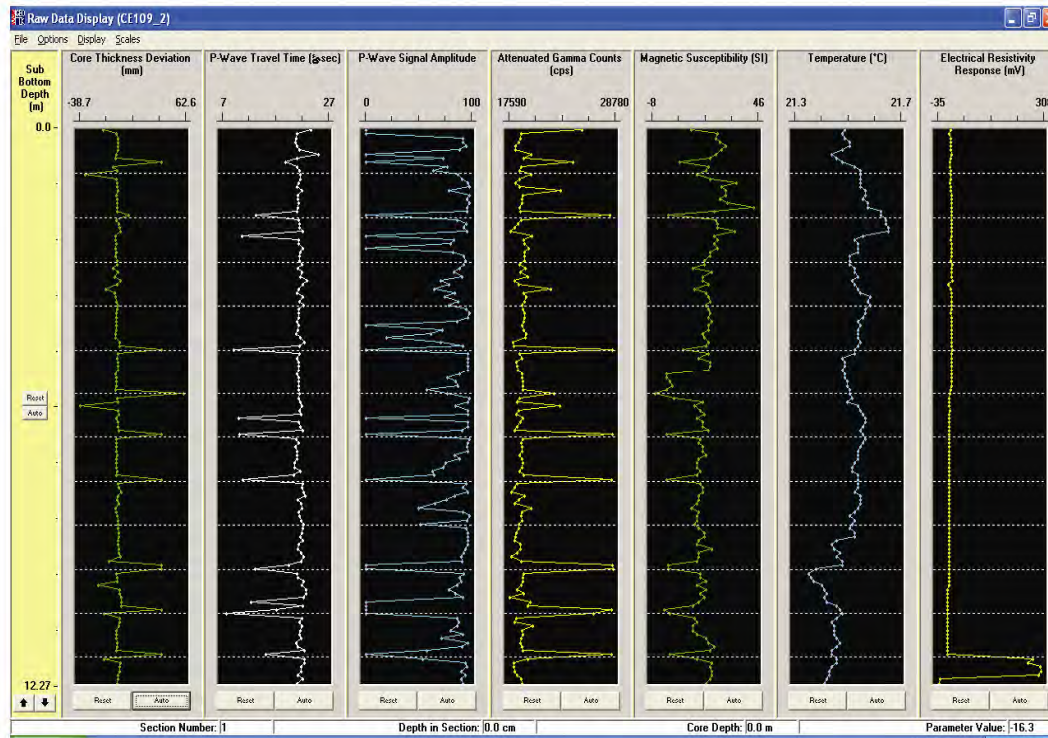


Figure 3.31. Geotek raw data displayed by MSCL software during core logging

### 3.4.3. Repeatability and Reproducibility

There are different ways to evaluate performance of a system. Accuracy and precision are important consideration in this context. Accuracy of a measurement involves comparison with a standard. While precision refers to the repeatability of measurements.

Repeatability refers to the variability of measurements conducted with the same device by the same person in a single experiment. Reproducibility on the other hand normally refers to measurements recorded in separate experiments with different machines (sometimes different method) and by different operators (Fullagar et al, 2005). Figure 3.32 shows reproducibility of Geotek gamma density when compared with water immersion densities conducted on the same cores by a different operator at JKMRC (University of Queensland). Geotek gamma densities were recorded on Ernest Henry cores at 9cm intervals and were averaged over 2m intervals to be comparable with JKMRC measurements. Water immersion densities were conducted only on a few pieces of core samples from each 2m intervals. Given the condition of experiments, both measurements are in good correlation.

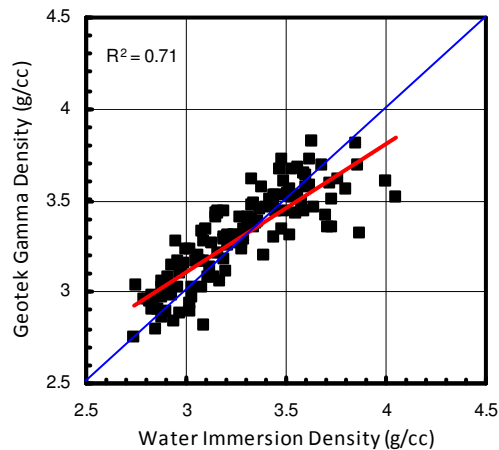


Figure 3.32. Reproducibility of Geotek MSCL Gamma density

In order to test operational repeatability of MSCL system, 5 repeat runs were conducted on four pieces of NQ half core (~1m total length) selected from Ernest Henry (EH633). There were three breaks in core over 1m. The core pieces were altered mafic volcanic rocks that contained variable proportions of magnetite, chalcopyrite and pyrite mineralisation. This testing involved setting up the logger for each run and repositioning the core boat in the logger. Petrophysical properties were recorded with 9cm sampling interval for each run.

Variation in position is the single most important factor affecting repeatability of the MSCL results, not only because rock properties can vary over short distances, but more especially because core breaks and changes in core thickness can influence the measurements.

The P-wave velocity was generally repeatable within about  $\pm 7\%$  (Figure 3.33a) if the coupling between core and core boat, and between core boat and the lower transducer, was maintained constant during all runs. P-wave amplitude was repeatable within about  $\pm 10\%$  (Figure 3.33b) but it is very sensitive to coupling. Gamma density exhibited good repeatability within about  $\pm 2\%$  (Figure 3.33c) and magnetic susceptibility was repeatable within about  $\pm 2\%$  (Figure 3.33d).

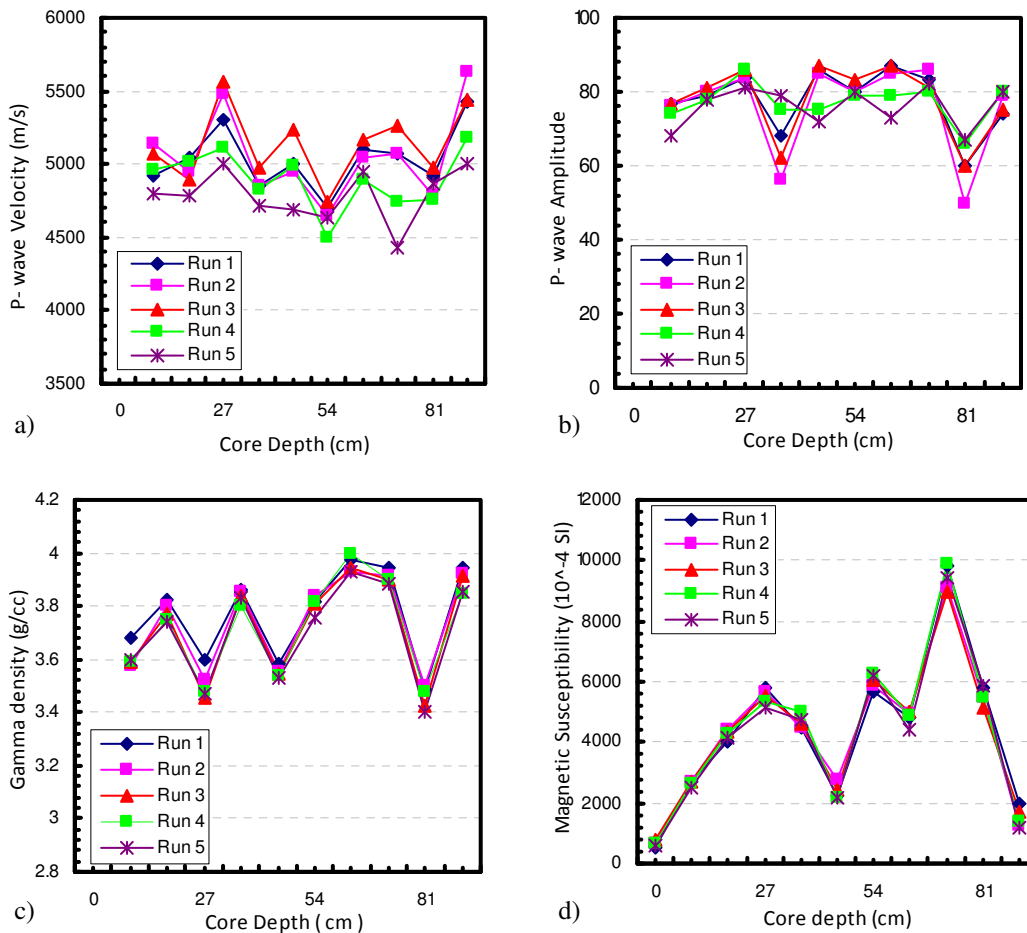


Figure 3.33. Repeatability of Geotek P-wave velocity (a) P-wave amplitude (b), gamma density (c) and magnetic susceptibility (d) on NQ half-core test pieces.

### 3.4.4. Sampling Intervals

In addition to the time taken for each sensor to acquire data, another factor that affects the productivity of the logger is the relative sensor spacing along the track. Each sensor has to take measurements at the same locations on the core and the process is fastest if multiple sensors can take measurements simultaneously. This can only happen if the sampling interval is a factor of the sensor spacing.

On the University of Tasmania MSCL system, if the imaging camera is at position zero, the core thickness laser is 6 cm along the track, the gamma density beam is at 22 cm, the P-wave sensor at 40 cm, the inductive resistivity at 56 cm, and susceptibility coil at 86 cm. Density, P-velocity and imaging are the slowest measurements, and density and sonic velocity are separated by 18 cm. Therefore, considering time optimization, factors of 18 cm are the most efficient. An 18 cm interval would of course be fastest, but some resolution would be lost and, more importantly, given the 13cm width of field for the

photography, the imagery would not be continuous. Another consideration is under-sampling (aliasing). Inherent variability of some cores over short distances demands a dense spatial sampling. In practice, it is accepted that in some cases the logs will sometimes be aliased. Mineralised samples are inherently and variously heterogeneous.

In order to assess the variability of petrophysical measurement based on sampling intervals, about 20m of typical core from the Cadia East drill hole CE098 was logged in 1cm intervals and then one dimensional semi-variograms of gamma density, P-velocity and magnetic susceptibility were analysed. The range in semi-variogram represents the maximum distance for which there is a degree of spatial correlation. As represented in Figures 3.34 the range of the semivariogram in each case was 10-15cm. As a rule of thumb the sampling interval should not exceed 2/3 of the range. A 9cm sampling interval was chosen for petrophysical measurement at Cadia East and Ernest Henry as a compromise between spatial resolution and logger throughput.

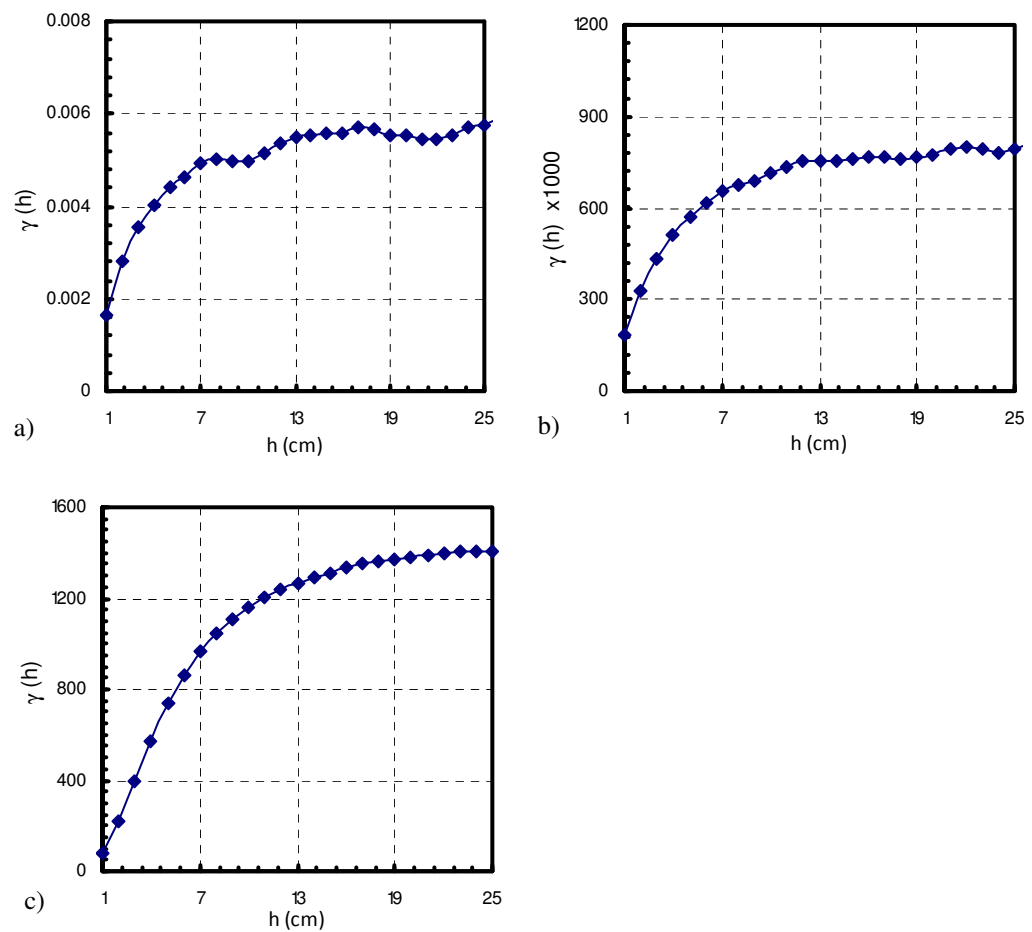


Figure 3.34. Semivariogram of gamma density (a), P-Velocity (b) and magnetic susceptibility (c) for 20m of cores from Cadia East. Note that the range for density and susceptibility is about 15cm and for P-velocity is about 12cm.

### 3.4.5. Geotek Core Logging Throughput

The logging production rate is a function of sampling interval and times taken for measurements of a set of sensors. Figure 3.35 shows logging throughput as a function of sampling intervals when only petrophysical measurements are recorded. Core imaging adds approximately another minute per meter of core for capturing imagery at 9cm sampling interval.

The logging rate depends on a range of different factors, including operator skill (setup and control of the logger), core preparation, time required for core section depth checking and system pauses e.g., time required to zero magnetic susceptibility or conductivity to avoid sensor drift. Data quality is affected by all of these factors. Production is also affected by the need to identify and remedy any problems and by the need to maintain a stable temperature inside the container.

Core imagery and petrophysical logging of 1m of half core takes about 5 minutes with a measurement spacing of 9 cm and an 8 seconds gamma density integration time. Logging time for 1m of whole core with the current configuration is about 6 minutes owing to the additional time required to acquire and process the images from the two cameras.

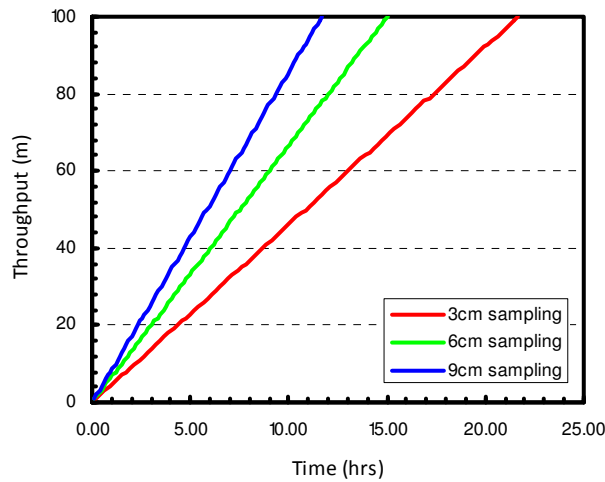


Figure 3.35. Geotek logging production rate without core imagery. Note that throughput is a user defined function of sampling interval and time required to take a set of measurements.

### 3.5. Concluding Remarks

The Geotek MSCL system can provide good quality and quasi-continuous petrophysical data on archival drill cores, both whole core and half core. The system can be deployed at a mine site or off site in a laboratory.

Core logging is the only alternative for petrophysical characterisation at established mine sites, if the boreholes through key sections of the ore body are not accessible or no longer exists. However, when practicable, downhole geophysical logging is a much more efficient option for acquisition of petrophysical data.

The University of Tasmania MSCL system is configured to record high resolution digital imagery of the core, and to measure density, P-wave velocity, P-wave amplitude, magnetic susceptibility, and conductivity. It delivers data with acceptable accuracy and precision if care is taken in system operation and calibration. One important factor affecting data quality is the size of the core and core condition.

Although a new conductivity meter with higher dynamic range compared with original sensor was incorporated to the logger, however the sensor is very sensitive to temperature. Also zeroing of conductivity sensor inside the container is problematic. The conductivity sensor thus is not reliable for quantitative interpretation of drill core samples.



# CHAPTER 4

---

## Geometallurgical Modeling Methodology

### 4.1. Introduction

Methodologies for assessing relationships between the petrophysical and processing characteristics of ores are introduced in this chapter. The automated MSCL system described in Chapter 3 provided petrophysical data and optical imagery for core samples from Cadia East and Ernest Henry. Magnetic susceptibility, density, P-wave velocity and P-wave amplitude were measured directly. A subset of 2m core samples from Cadia East and Ernest Henry were selected for small scale physical testing within the AMIRA P843 project. These tests provided values for “crushability” ( $A^*b$ ) and “grindability” (estimated Bond mill work index, BMWi) as explained in Chapter 2. The BMWi and  $A^*b$  are comminution attributes. The challenge in this chapter is to develop effective methodologies and models for prediction of comminution attributes on the basis of petrophysical properties.

Geometallurgical modeling is a cross-disciplinary approach incorporating geological, petrophysical, and metallurgical information to simulate processing behaviour of ore deposits mathematically. A geometallurgical model can be developed and used in two different ways. Model development is based on establishment of a statistical relationship between petrophysical and comminution attributes. The model can then be used either to estimate a value for a comminution attribute or predict a class that has certain comminution behavior.

In order to effectively characterize ore processability, alternative measurements which can act as proxies for processing indices are required. The major advantage of proxies is the increase in volume of data when compared to sparse large scale metallurgical sampling which then allows spatial modeling of processing indices throughout an ore deposit.

During mine development, decisions need to be taken in regard to design and operation of the ore processing plant (i.e. process planning). Design of a processing plant is optimal if processing behavior of ore can be characterized by a sufficient number of comminution tests on representative samples. Thus an effective geometallurgical modeling approach at the feasibility stage can provide a basis for a long term process planning. A

geometallurgical approach can also be implemented at later stages during the life of an operating mine to optimize current ore processing performance. Process optimization normally is required when issues such as ore variability and changes in metal prices arise. This chapter attempts to address these issues and to describe a number of effective geometallurgical approaches for process planning and optimization.

It is a common practice in the petroleum industry to establish an empirical model relating a quality parameter such as permeability, i.e. processing attribute, to an independent property like porosity (e.g. Balan et al, 1995). In the metalliferous mining industry there are cases such as the Red Dog mine, Alaska, where empirical geometallurgical models have been developed for both throughput and recovery (Kojovic, 2008a). The success of such empirical models is generally a result of long term practice during mine operation.

However, due to heterogeneity and variability of rock types in most mineral deposits, establishment of a reliable “universal” geometallurgical model is usually problematic. A universal model here refers to a statistical model developed empirically so that it could be applied reliably within an entire deposit. For this reason it is highly desirable to divide the deposit into domains and identify groups of rocks that have similar properties. The identified groups should reflect the ore processing behavior. Thus “class” definition is usually the first step towards geometallurgical modeling. A geometallurgical class can broadly be defined as a group of rock samples that have similar geological, petrophysical, geochemical, geotechnical and metallurgical characteristics.

If after creation of geometallurgical classes, a reliable statistical model can be established between comminution attributes and petrophysical properties, then the model(s) can be used for prediction of comminution behaviour in intervals of core where no comminution data are available.

This chapter presents four approaches for definition of geometallurgical classes for development of predictive comminution models. There are many different statistical techniques for data classification and it is beyond the scope of this thesis to investigate the efficiency of each. More details on a range of statistical approaches, including the advantages and disadvantages of each method, can be found in the literature (e.g. Tan et al, 2006; Witten and Frank, 2005). In this thesis a cluster analysis approach has been used to create geometallurgical classes.

Neural networks and conventional statistical techniques for model building will be reviewed. The application of these approaches is illustrated in the context of comminution modeling in Chapters 5 and 6, but the methodologies could be applied for prediction of other processing performances such as recovery.

## 4.2. Classification Schemes

The ultimate aim in geometallurgical modeling within this research is to relate petrophysical properties to comminution attributes. In this section, data classification schemes are explained and in the following section, statistical methods for performing such classifications are described.

In this thesis “data classification” refers to classification of geological, petrophysical and comminution attributes for geometallurgical modeling purposes. A total of four classification strategies have been devised primarily for two geometallurgical purposes within two different stages of mining: “process planning” and “process optimization”. The choice of each classification strategy for any of the two applications depends on ore comminution variability (Section 4.5).

Process planning here refers to practices during mine development for processing plant design and equipment selection while process optimization refers to refinements made during mining operation to optimize the processing plant performance.

A reliable classification can only be achieved when there are a representative number of samples for an orebody. The quality of data is also of great importance. Each classification approach has its own pros and cons which are discussed in the following subsections. The focus here is primarily on prediction of comminution parameters for each class on the basis of petrophysical properties. However, in the absence of petrophysical properties, the classification and model building could be based on other available data, e.g. assays.

In order to assess the distinctiveness of determined classes, statistical characterisation of each class is required. This normally involves determination of statistical parameters (e.g. mean and standard deviation) within each class for every variable that is used in the class definition. For example there might be cases where the mean value of a variable within two different classes is similar however they could be characterized by different standard

deviations. Other statistical tests (e.g. t-test) could also be used to statistically identify the similarity of two classes.

#### 4.2.1. Geological Classes (GC)

Geological observations can provide substantial information. At mine sites it is logical to test the geological classification approach before applying statistical algorithms. Geological classes (e.g. lithology, alteration) which are defined via visual logging of drill cores may provide a convenient means for separating samples according to their metallurgical behaviour. However, although geological logs are categorical rather than quantitative, they often record a wide range of attributes, and include detailed descriptive text, that makes a classification approach very difficult. Moreover visual core logging is subjective; experience based and often suffers from inconsistency due to high turnover of personnel.

Potential geometallurgical classes are defined from existing geological information (e.g. lithological classes or determined “ore type”). The statistical variability of metallurgical attributes within each class is then assessed in order to gauge the suitability of the geological class as a geometallurgical class. Geometallurgical class definition similar to GC approach has been practiced in most Chilean copper mines (Cardenas, 2009). Examples of such approaches from Chile are documented by some researchers (Scott et al, 1998; Alruiz et al, 2009). A similar approach for geometallurgical modeling has also applied to Highland Valley Copper, Canada (Simkus and Dance, 1998).

One advantage of this method is the availability of geological logs for virtually all drill holes. In some cases “ore types” at mines are determined based on a number of composite factors such as rock type, mineralogy and grade. Ore types if available could also provide a basis for geometallurgical investigations. However, classification based on geological observations may be imperfect (i.e. uncertainty in visual logging) and geological classes might not fully explain the metallurgical behaviour of orebody. For example differences in lithology may not capture the differences in comminution behavior. Nevertheless, a convenient starting point for geometallurgical modeling is to explore the link between existing geological units and boundary definitions with processing performance

Finally, formulae relating petrophysical properties to comminution attributes are derived. For this purpose, first the intervals that are assigned to similar geological classes on the basis of the visual logs are grouped to make a potential geometallurgical class; then

petrophysical-based comminution models are developed within each geometallurgical class using the regression analysis technique (Section 4.4.1). This is a novel modeling approach compared with the approach used by researchers (e.g. Scott et al, 1998; Alruiz et al, 2009) in the way that regression comminution models are developed in each class. The developed models can then be used in each geometallurgical class for prediction of comminution attributes in intervals of core where petrophysical properties have been measured but no comminution tests were conducted. This approach is illustrated at Cadia East, as presented in Chapter 6.

#### **4.2.2. Petrophysical Classes (PC)**

Potential geometallurgical classes can be created using petrophysical properties if such data are available at mine sites. The statistical variability of comminution attributes within each class is then assessed in order to gauge the suitability of the petrophysical class as a geometallurgical class. The approach is novel in a way that has not previously reported by any researcher.

Creation of petrophysical classes requires a sufficient amount of data to be representative of an orebody. An advantage of using petrophysical properties in creation of geometallurgical classes is that petrophysical properties are quantitative and objective. One approach for “objective” classification of petrophysical properties is cluster analysis (Section 4.3.2). The underlying hypothesis here is that each cluster should correspond to a certain rock type with a different physical response. Validation of defined classes is also a required task. This means the petrophysical classes should explain the comminution behaviour of orebody. Distinctiveness of created classes can be explored using statistical techniques (e.g. radar diagram). Geological information (e.g. lithological logs) can also help in assessing the validity of created classes. For example certain rock types may belong to a petrophysical class.

Once the classes are created, then petrophysical based comminution models are developed within each petrophysical class using the regression analysis technique (Section 4.4.1). The aim of regression modeling is to develop a formula for prediction of comminution attributes based on petrophysical properties in each class.

The developed models are based on the number of comminution tests that are available within each class. When accurate models are built, then models from each class can be

used only at the same class for prediction of comminution attributes in intervals of core where petrophysical properties have been measured but no metallurgical tests were conducted.

If the correlation between attributes is poor for a particular class, then this might suggest that either there is no clear relationship or that the classification should be revised. It is important to recognize that correlations will also be affected by the uncertainties involved in both measurements of petrophysical properties and comminution parameters.

A disadvantage of this approach in common with the GC method is that for each comminution attribute a separate model should be built for each individual class. For example, given three geometallurgical classes and two comminution attributes, six models need to be developed and considered. However, greater accuracy normally can be achieved when compared to global models if formulae are developed separately for each class. The petrophysical class approach (PC) has been applied to Ernest Henry data, as presented in Chapter 5.

#### **4.2.3. Comminution Classes (CC)**

One approach for definition of geometallurgical classes could be on the basis of comminution parameters, namely  $A^*b$  and  $BMWi$ . David (2007) has also recommended analyzing the metallurgical data set for determination of patterns or clusters as part of a geometallurgical investigation. However he has not explained the procedure for class definition and subsequent modeling.

The attraction of such a classification method is due to the fact that mill behaviour is mainly governed by ore comminution characteristics. Therefore creation of geometallurgical classes based on comminution parameters is a direct approach for geometallurgical modeling of an orebody.

Statistical techniques such as cluster analysis (Section 4.3.2) can be used for creation of classes. The variation of comminution attributes should be statistically characterized in order to assess the reliability and distinctiveness of the created classes. Statistical characterization of classes can be carried out using measures such as the mean and standard deviation of comminution variables within each class while class distinctiveness can be assessed visually using methods such as radar diagrams.

The created classes might not be consistent with geological data (e.g. lithology). However, a metallurgist needs to know mainly about the processing behavior of feed materials to a mill for comminution purposes rather than the lithology of the feed. An advantage of this method compared with GC and PC is that comminution parameters are considered in class definition i.e. expected variability of comminution behavior is identified with created classes. The real limitation of the CC approach is that for effective prediction of comminution classes in a practical case, a sufficient number of comminution tests is required to represent the processing behavior of the orebody.

This approach has been illustrated at both case study sites, Ernest Henry (Chapter 5) and Cadia East (Chapter 6).

#### **4.2.4. Comminution and Petrophysical Classes (CPC)**

On the basis of limited number of small-scale comminution data it may not be possible to achieve statistically distinctive geometallurgical classes; in such cases potential geometallurgical classes are determined through integration of petrophysical and comminution attributes. Cluster analysis (Section 4.3.2) can be conducted on a combination of petrophysical and comminution data for objective creation of the classes. The approach has the same advantages of the CC method. This approach is illustrated at Ernest Henry, as presented in Chapter 5.

### **4.3. Classification Methods**

Data classification can be carried out in subjective or objective fashion. Visual definition of classes from cross-plots of variables using methods such as data point density distribution is an example of subjective class definition. Clustering data based on intrinsic statistical similarity can be regarded as an objective method. There are numerous classification methods, some of which involve advanced statistical techniques (e.g. Kohonen, 1982).

#### **4.3.1. Geological Classification**

Potential geometallurgical classes can be defined from existing geological information. For example lithology, alteration or combination of lithology and alteration can be regarded as a potential geometallurgical class. For this purpose, the intervals that are

assigned to similar geological classes on the basis of the visual logs are grouped to make a potential geometallurgical class. This is a very simple approach for definition of potential geometallurgical classes. A more complex approach for definition of potential geometallurgical classes from geological information is explained by Williams and Richardson (2004).

#### 4.3.2. Cluster Analysis

Cluster analysis is an objective multivariate statistical method for data classification, well established for definition of petrophysical classes (Moss, 1997). Cluster analysis seeks to subdivide the multivariate data into a number of groups that are similar to each other. Dissimilar data are assigned to different clusters. There are a large number of clustering algorithms to choose from, but the K-Mean (McQueen, 1967) and Hierarchical (Ward, 1963) clustering techniques are probably the most commonly applied.

In K-Mean clustering the number of clusters,  $K$ , must be specified at the outset. The data are divided into  $K$  clusters such that some metric relative to the centroids of the clusters is minimized. Therefore K-Mean is regarded as a supervised clustering approach, although the only real user input is the number of classes. Hierarchical clustering can be considered as a tree, in which the branches of the tree are combinations of clusters. The trunk of the tree contains all clusters. The Hierarchical clustering method begins by grouping the most similar clusters together, then proceeds by grouping the next most similar clusters until all clusters are assigned to one of two groups. Ultimately all the clusters are linked as a hierarchy (i.e. dendrogram). There is no completely satisfactory method for determining the number of clusters for any type of cluster analysis (Hartigan, 1985; Bock, 1985). However, descriptive statistics can be used in order to characterize the groups defined by cluster analysis. Statistical analysis such as t-test and graphical techniques such as radar diagrams can then provide some confidence regarding the number of clusters. There are different algorithms for Hierarchical clustering that differ on the basis of the method for defining proximity between clusters. In this thesis Ward's Hierarchical clustering method (Ward, 1963) is used.

Cluster analysis does not guarantee the best data classification. In cases where cluster analysis does not yield a meaningful classification, alternative methods (e.g. difference relative to data mean) can be tested and applied. This approach is presented in Chapter 6.

### **4.3.3. Relative Average Approach**

The relative average approach is a simple method to data classification. The data are classified primarily based on variability of the parameters of interest around their respective mean values for the entire population. The data for each parameter is subtracted from total mean value. Those higher than the total mean value will be positive and vica versa. The transformed data are then classified based on their negative and positive signs. This approach is illustrated in Chapter 6.

## **4.4. Modeling and Prediction**

Once the geometallurgical classes have been created, then comminution models need to be developed within each class. There are different statistical methods for model building. Details on a range of model building statistical techniques can be found in Davis (1986). In the following sub-sections, regression analysis, minimum distance algorithms and artificial neural network techniques that can be used for building geometallurgical models are briefly reviewed.

It should be noted that both petrophysical properties and comminution attributes are subject to errors. The uncertainties in the measurements of these attributes will affect development of an accurate model. Moreover petrophysical properties alone may not have a strong correlation with comminution attributes; however their combination with other data (e.g. assays) can present satisfactory outcomes. Such issues are addressed in Chapter 5 and 6 where integrated modeling has been applied to data from Ernest Henry and Cadia East respectively.

### **4.4.1. Regression**

The most widely used statistical methods for numerical modeling are single or multiple linear (or nonlinear) regressions. This method is regarded in this thesis as one way of prediction of comminution parameter values. In simple linear regression the variations in the dependent variable are attributed to changes in only a single independent variable. However in some cases several factors simultaneously affect a dependent variable. Multiple regression analysis is a method for combining the effects of several factors concurrently. In this thesis the dependent variables are comminution attributes (i.e.  $A \cdot b$

and BMWi) and independent variables are petrophysical properties (density, magnetic susceptibility, P-wave velocity and P-wave amplitude).

When relating petrophysical properties to comminution attributes, a linear model can provide a good benchmark against which to judge more complex techniques. When several petrophysical variables must be combined to estimate the comminution parameter, it may become necessary to extend the regression model to account for nonlinear effects.

The coefficient of determination ( $R^2$ ) is a parameter in regression analysis that reflects the degree of variability and correlation between two parameters. It varies from 0 to 1 depending upon the degree of correlation between variables. The closer the value to 1 the higher the correlation. The coefficient of determination ( $R^2$ ) is simply the square of the correlation coefficient and it is incorrectly interpreted by many researchers as a reliable parameter in statistical modeling. There are cases where  $R^2$  between a dependent and an independent attribute based on a nonlinear function is higher than a linear one, but the nonlinear regression formula is not necessarily more accurate function than a linear one in terms of prediction. The root mean square (RMS) error a commonly used measure of error can be applied as a guide in selection of appropriate regression function. The RMS error is a measure of difference between values that are known and the values that have been predicted by regression equation. Figure 4.1 shows correlation between two attributes (X and Y) using a nonlinear and linear regression fit. Although a nonlinear regression fit (a power function) has a higher coefficient of determination ( $R^2=0.67$ ) than the linear regression fit ( $R^2=0.45$ ), however the root mean square error of the linear regression fit is 4% less than nonlinear one. It is therefore desirable to calculate the root mean square error as a supplementary parameter for judging the accuracy of a model.

In model building using regression analysis it is highly desirable to simplify a multiple regression equation where possible for better understanding and ease of use. Simplification of a regression equation is normally conducted by reducing the number of parameters in the model. However, selection of the most important attributes for a model is an issue. Stepwise regression analysis (Tan et al, 2006) which takes into account statistical criteria for attribute selection can be used for such purposes. The stepwise process can be carried out in two ways namely Backward and Forward regression.

In the Backward method, all of the input parameters (i.e. predictors) are included in the model initially. The variable that is least significant based on p-value (Brownlee, 1960) is then removed and the model is refitted. Normally a p-value less than 0.05 would be

significant and a p-value more than 0.05 is considered insignificant during regression analysis. This parameter is automatically calculated by most statistical software e.g. Statistica. Forward regression starts with an empty model. The variable that has the most significance based on p-value when it is the only predictor in the regression equation is placed in the model. Then each subsequent step adds the variable that has statistically relatively greater significance in comparison with the remaining variables.

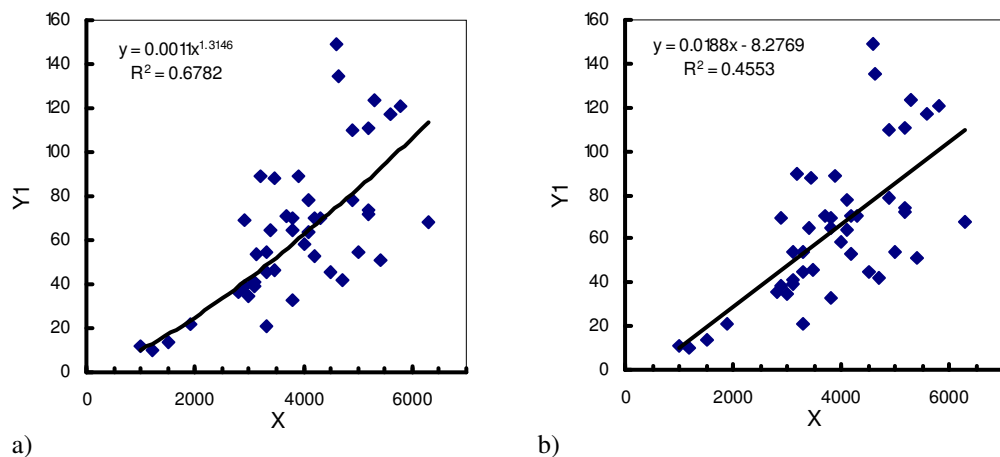


Figure 4.1. Correlation between X and Y dataset showing a nonlinear (a) and linear (b) regression fit. Note that although the correlation coefficient between the dataset (a) is higher than the dataset (b) but the accuracy of regression model for the dataset (b) is better than (a). RMS error value for dataset a and b is 25.11 and 24.15 respectively.

For the geometallurgical class definition methods described in this chapter, the stepwise regression has been applied for both GC and PC approach (Chapter 5 and 6). Firstly all petrophysical properties (including parameter averages and their standard deviations) are included in standard multiple regression analysis.  $R^2$  and RMS error are considered when all parameters are included. Then Stepwise regression (using the forward and backward approach) is conducted to assess the most significant parameters in the regression. The selection of significant parameters is based on p-value. For each approach (forward and backward),  $R^2$  and RMS error are considered and compared with standard multiple regression analysis including all variables. Finally the ‘best’ model is selected on the combined basis of smallest number of parameters and lowest RMS error value. It should be noted that in some cases two models may have only very small differences in RMS value. In such cases the preferred model is the one with smaller number of parameters in the regression model.

#### 4.4.2. Minimum Distance Algorithm

The minimum distance algorithm is embedded in LogTrans program. LogTrans is an automatic interpretation program originally developed for predicting lithological units based on geophysical logs and other downhole data. However, the program can be used for other applications such as geotechnical characterization (Zhou et al, 2001). A comprehensive explanation of the LogTrans algorithm is given by Fullagar et al. (1999) and a summary is given here.

The LogTrans procedure entails two major steps, known as statistical characterisation and discrimination. A rock type classification is presumed to exist at the outset. During the statistical characterization step the program computes representative statistics for each parameter in each class, specifically the means and standard deviations or medians and “spreads”. The lower and upper spreads are defined as the differences between the median and the 16<sup>th</sup> and 84<sup>th</sup> percentile values respectively. During discrimination, data points are assigned to the ‘nearest’ class in multi-parameter space. As the name suggests, the “discrimination” step is analogous to discriminant analysis.

Basically LogTrans assumes that various rock types have different petrophysical signatures so that they can be discriminated from each other as illustrated in Figure 4.2. LogTrans can operate on any number of petrophysical parameters simultaneously, but the concept is most easily explained in two dimensions. Figure 4.2 is a cross-plot of training data for two parameters, density and gamma ray, measured in five rock types. Different colours identify the data points for the different rock types. The training data for each rock type are clustered in a certain area or domain. The parameter mean or median value in each domain is adopted as the representative value while the standard deviation or spread is an indicator of the statistical dispersion (hence size of the domain).

During discrimination, new measurements are in effect compared with the training data in order to identify the class to which they belong. For example the point A will be unambiguously classified as quartz rhyolite (purple), while the measurement point B could be either Turbidite (green) or rhyolite porphyry (light blue). The measurement point C is too far away from any of the classes encountered in the training data. This point belongs to an unclassified new class.

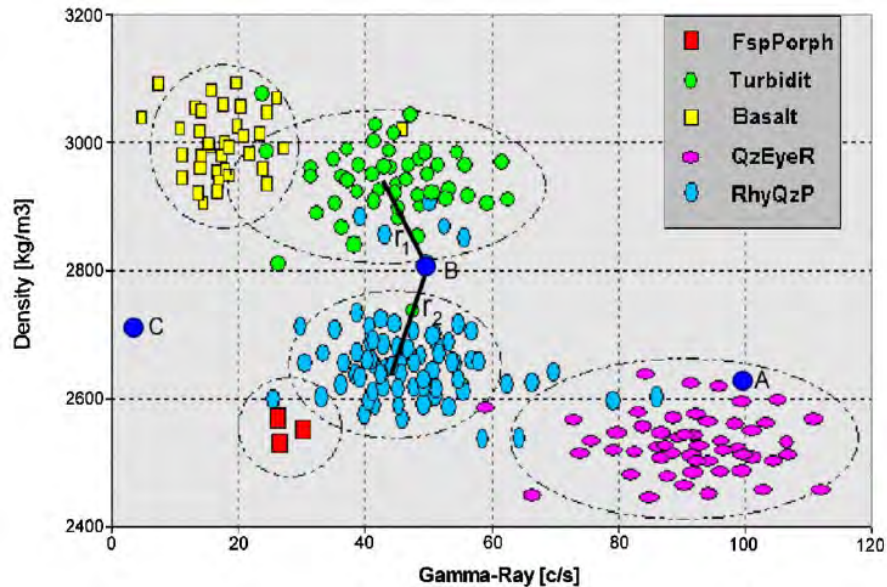


Figure 4.2. Scatterplot of density and gamma ray (after Emilsson, 1993) to illustrate operation of LogTrans algorithm (Fullagar et al., 1999). Coloured dots represent data from control holes. Points A, B, and C represent measurements to be interpreted. Classes are assigned to these points according to their normalised distance from the centre of each lithological “domain”.

The LogTrans program (Fullagar et al., 1999) has been used in this study for both processing of the petrophysical data collected using the Geotek MSCL and for automatic interpretation of alteration classes at Cadia East (Vatandoost et al, 2008b). LogTrans can also be used for automatic characterization of comminution behaviour. Geometallurgical classes that are determined via either CC or CPC can be characterized in terms of petrophysical properties using the LogTrans algorithm. As with any supervised classification technique, the success or failure of the LogTrans interpretation depends on the extent to which the training set can truly distinguish one class from all the others. Application of the minimum distance algorithm using the LogTrans program for prediction of comminution classes at Ernest Henry and Cadia East is presented in Chapter 5 and Chapter 6.

#### 4.4.3. Neural Networks

An artificial neural network (ANN) is a processing unit with a design inspired by the neural structure of human brain (Huang and Wanstedt, 1998). Neural networks have been applied in a wide range of geoscience applications (e.g. Baan and Jutten, 2000). The major reason for the popularity of neural networks is their good performance in non-linear multivariate problems. A complete description of neural networks algorithms has

already been prepared by many researchers (e.g. Hassoun, 1995). A summary is given here.

A neural network is comprised of three different layers, namely input, output and the middle (hidden) layer (Figure 4.3). Each layer consists of neurons (nodes) and the neurons are connected by weighted links which pass signals from one neuron to another. The weights in the network structure are determined by back-propagating the errors between the inputs and the outputs. Neural networks trained with the back propagation method have been applied successfully as prediction tools in a wide range of engineering fields (Garrett, 1994; Baudu, 1995; Annandale et al., 1996; Huang and Wanstedt, 1998; Sonmez et al, 2006).

An artificial neural network can be used for both supervised and unsupervised learning. In the supervised learning approach, the network learns from existing examples. This requires the existence of sufficient number of examples for optimum performance (Hassoun, 1995). These examples form a set of known “input-output pairs”, usually called a training set, and the task is to learn the input-output rules from these examples. Once the network has learned the relationship between the input and output for the training dataset, then this relationship can be applied to predict output values for other data sets.

In an unsupervised learning approach, only the inputs are known and there is no information of corresponding outputs. In this case the network seeks for specific features of the data, such as clusters. The unsupervised neural network approach has not been investigated in this research.

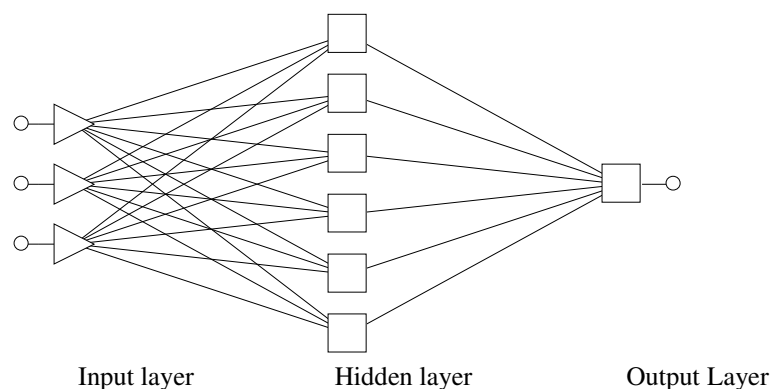


Figure 4.3. Structure of an artificial neural network showing three layers. Note that there is no connection between nodes of a given layer.

In a typical neural network training procedure, the data set is divided into three separate portions called training, validation and test sets. The training set is used to develop the desired network while the validation set is allocated for the purpose of controlling the network training. The validation set sometimes referred as testing set, is not included in the training set during training of the network. The validation set only enables the user to adjust the network training process for the best outcome. The test dataset which is not involved in network design and training is then used to test the performance of the trained network.

A number of factors such as training time, training error and network structure should be considered during design and training of neural networks. The training time for the network is an important factor. Basheer and Hajmeer (2000) proposed the optimum time to stop training a network would be the time that the prediction error for the testing dataset (here validation set) starts to increase (Figure 4.4). The training error (root mean square error) typically decreases with increase in training time at first, but over-training usually degrades the network performance. In other words the network has memorized the examples and patterns rather than learning. A network that has memorized the examples could only be able to respond to the same examples and will not be able to perform well with examples outside those used in the training stage.

The complexity of the multi layered neural network structure increases by the addition of either extra hidden layers or an increase in the number of nodes in the hidden layer. The hidden layers are normally likened to a “black box” within the network system. However the invisibility of a hidden layer does not mean that the function of this layer can not be evaluated (Mohaghegh et al., 1995). In fact based on mathematical functions within each node in every layer the performance of network can be evaluated (Yang and Zhang, 1997).

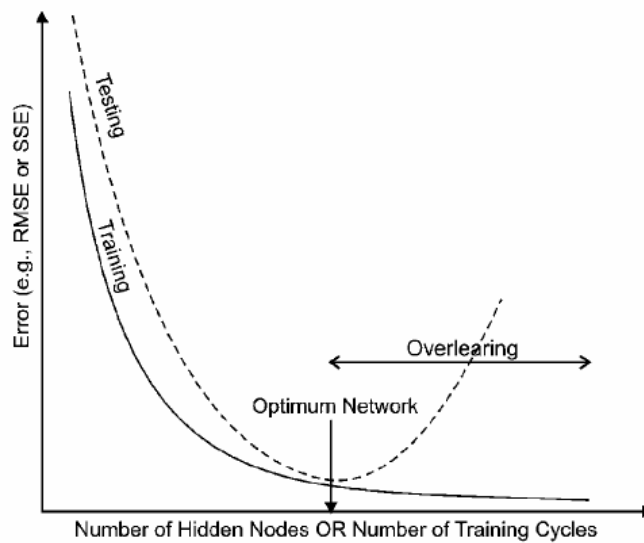


Figure 4.4. Criteria for selection of optimum network and training cycle (Basheer and Hajmeer, 2000). As the training cycles increases the prediction error reduces, however the prediction error for validation data (Testing) will start to increase after a certain training cycle known as optimum training point. This point that defines the optimum number of training cycles is regarded as the sufficient number of cycles for best performance of the network.

It is possible to assess the relative importance of each input variable in a neural net using the Yang and Zhang (1997) method. This approach enables the user to identify the most significant input variables that have an impact on output based on calculation of the derivative of output with respect to each input parameter. However, assessment becomes very complex when the number of nodes in a hidden layer (and number of hidden layers) increases. An alternative approach is to use the sum of the weights that can provide a quick way to evaluate the importance of each input parameter in a neural net. The sum of the weights is the sum of the absolute weights of the connections from the input node to all the nodes in the hidden layer.

A supervised learning approach has been used and implemented for prediction of comminution classes of Ernest Henry (Chapter 5) and Cadia East (Chapter 6) data. Comparison of neural network approach with minimum distance algorithm (LogTrans) for prediction of comminution classes has also presented in Chapters 5 and 6.

#### 4.5. Geometallurgical Modeling Applications

The geometallurgical models developed based on classification schemes (Section 4.2) can be applied during process planning or process optimization stage. These two process stages are briefly explained in the following subsections. However the choice of

classification scheme for geometallurgical modeling purposes (i.e. planning or optimization) depends primarily on ore processing variability. This can be identified by statistical analysis of comminution data and using statistical techniques (e.g. Histogram charts). Judgment on comminution variability is valid when a representative number of small-scale comminution tests are available.

A large processing variability explained by comminution attributes, suggests potential ore variability and hence a need for effective geometallurgical characterisation of orebody. In this case, the GC or PC method could be more appropriate than the CC or CPC for geometallurgical class definition and comminution modeling. This is because normally more geological and petrophysical data are available than comminution information that could provide a means for effective characterisation of ore variability. The GC approach should be exercised with great caution due to issues discussed in Section 4.2.1.

If there is only limited comminution variability defined based on statistical analysis it may suggest that it is highly unlikely that ore geological variability in a deposit can have a significant impact on comminution response. Thus it is highly likely that created classes based on GC or PC approach will reflect similar comminution behavior. Hence definition of geometallurgical classes based on the CC or CPC approach could better characterize ore comminution behavior and are more appropriate in this case.

#### **4.5.1. Process Planning**

The aim of process planning during mine development in general is to characterize processing behavior of an orebody prior to construction of a processing plant. Characterisation normally is carried out using a limited number of large scale metallurgical tests due to its high costs. There are cases where design of a Semi-Autogeneous (SAG) mill for a circuit was based on only two SAG tests (David, 2007), but these tests are often not representative of an entire orebody and never guarantee the lifetime success of the operation. Studies by many researchers (e.g. Bulled and McInnes, 2005) indicate that ore variability has caused serious daily challenges for process engineers in many processing operations. Hence effective characterisation of an orebody through application of a geometallurgical approach is beneficial.

Given the availability of petrophysical properties from exploration drilling, development of processing models based on petrophysical properties could provide an effective

approach for characterization of ore metallurgical behavior. Development of a universal geometallurgical model for process planning purpose would be ideal in terms of its simplicity. Thus it is worthwhile to assess the existence of a universal geometallurgical model during process planning stage. When such models do not exist or have poor accuracy then a class-based approach needs to be considered.

The potential advantage of a geometallurgical approach during process planning stage could lead to optimal selection of processing equipment that could be more cost effective than building a separate crushing plant after start-up (Starkey, 1997).

#### **4.5.2. Process Optimization**

Process optimization here refers specifically to optimization of a comminution circuit. It is a common practice in the mining industry to establish trends from metallurgical database information to forecast future mill performance. Identification of the quality of the mill feed material and its variation is vital. Since ore variability translates to mill throughput variability. Class-based geometallurgical approaches (Sections 4.2) can provide a “selective” treatment approach during ore processing. This means mining of ore blocks representing geometallurgical classes can be scheduled and consequently treated selectively in downstream processing operation. The potential benefit of this selective approach is that feed material variation will be reduced and subsequently the comminution process will be stable. Development of geometallurgical models can help to achieve optimal condition for ore processing.

#### **4.6. Concluding Remarks**

The ultimate aim of geometallurgical modeling is to provide constrained processing performance indices that could be used for spatial modeling of an orebody. Such indices are achieved either through direct measurements or prediction using proxy parameters. Prediction of processing attributes can provide an order of magnitude more data points than direct measurement, so that mining blocks could be populated more effectively with these attributes.

Investigation of a universal geometallurgical model needs to be considered as a first attempt in model development. However universal geometallurgical models generally have low accuracy since they do not account for geological variability. For this reason

predictive models of processing indices are developed and applied within geometallurgical classes. Four different approaches for geometallurgical class definition for development of predictive comminution modeling that can be used during process planning and optimization have been described in this chapter. The choice of classification scheme depends on ore processing variability explained by comminution attributes.

Cluster analysis is a useful and simple statistical technique for data classification suitable for use in the PC, CC and CPC approaches. The time required for cluster analysis varies depending upon the algorithm, number of variables and number of data. The K-mean method is faster than the Hierarchical algorithm, but it requires a prior knowledge of the number of classes to be effective.

Regression modeling is easy and simple in comparison to an artificial neural network. However a neural network is inherently a nonlinear algorithm and in comparison with linear regression, it normally enhances the modeling result. The predicted values from a regression model that are outside the range (maximum and minimum) of observed values should be treated with caution. The minimum distance classification (LogTrans) algorithm is more simple, intuitive and easy to apply to a data set than an artificial neural network. However, neural networks can outperform minimum distance classification technique. Although design and implementation of a neural network is a time consuming process, once they are designed then can be applied for future prediction quite easily.

Overall the choice of the most appropriate statistical technique for modeling purposes is a matter of simplicity, time, and accuracy. It is not possible to utilize a simple recipe for numerical modeling in all cases and the choice of the most appropriate method involves subjective choices. Moreover in many cases modeling may be considered as an art rather than a science.



# CHAPTER 5

---

## Characterization of Comminution Behaviour at Ernest Henry Iron-Oxide Cu-Au Mine

### 5.1. Introduction

The Ernest Henry mine is located approximately 40 km north of Cloncurry in the Mount Isa district, Queensland, Australia. The orebody is a member of the diverse iron-oxide-copper-gold (IOCG) class of deposit. It is the largest IOCG deposit within the Cloncurry district and the second largest within Australia behind Olympic Dam (Mark et al., 2006).

Ernest Henry was discovered in 1991 and identified as a mineral resource in July 1997. Mining commenced in May 1998. It is currently owned and operated by Xstrata Limited. The orebody is mined on 16m benches by conventional load and haul methods using large-scale mining equipment (Collier and Bryant, 2003). The July 2002 ore reserve as reported by Collier and Bryant (2003) was 88.7 Mt @ 1.0 percent Cu and 0.5 g/t Au. Ernest Henry currently produces 100,000 tonnes of Cu and 125,000 ounces of Au annually (Xstrata, 2008). Planning for an underground extension in order to extend the life of the mine is currently under investigation.

Metallurgical test works were carried out at Ernest Henry during feasibility studies. These tests were conducted on a large number of drill core samples mainly for the design of the concentrator (Strohmayr and Valery, 2001). The concentrator design at Ernest Henry primarily focused on the processing characteristics of the primary ore zone which was regarded as fairly homogeneous and resulting in a very few processing issues. However, the oxidized supergene ore zone, which provided a major component of the feed material for the first three years of the operation, created serious processing problems due to variable feed composition and physical characteristics hence poor recovery (Strohmayr and Valery, 2001).

The perceived relatively uniform comminution response of primary ore with very few processing issues in plant operation resulted in a limited metallurgical testing within the primary zone and the development of empirical models for mill performance. Rock type and alteration have an impact on comminution and mill throughput, with unbrecciated K-

feldspathic rich volcanic rocks proving harder to crush than the magnetite rich volcanic rocks (Strohmayr et. al., 1998).

Cu grade was recognised as the main proxy for mill performance (Tew et al, 2003). Higher grade Cu mineralisation (>1%) tends to be more brecciated and more magnetite rich. Such characteristics make the rocks soft for crushing and subsequently resulting in higher mill throughput. However the main issue at Ernest Henry is mill throughput prediction for low grade materials (<0.6%) which are much harder than high grade zones in terms of crushing and grinding. This issue will be more significant when mining is extended to underground operations. Thus the challenge in this research is to effectively characterize mill performance and to determine if more detailed class-based geometallurgical modeling can improve the mill throughput prediction for the primary ore zone.

The Geotek Multi Sensor Core Logger (MSCL) system was used to measure petrophysical properties on six drill cores from the primary ore zone of Ernest Henry mine in an attempt to characterise the rock type, alteration style and ultimately the ore crushing and grinding behavior. Gamma density, magnetic susceptibility, compressional wave velocity and its amplitude were measured along each length of half core. High resolution core imagery was also captured simultaneously. The merging of petrophysical data from successive core sections then provided a continuous log of core properties. The core logs provide a basis for research into the relationships between petrophysical and comminution parameters.

Small scale comminution tests ( $A \cdot b$  and estimated  $BMWi$ ) were performed on a subset of 2m-long drill core samples at JKMRC (Julius Kruttschnitt Mineral Research Centre, University of Queensland) after petrophysical data acquisition. These tests provided an opportunity to investigate directly the correlation between petrophysical properties and comminution attributes on the same core sections (Chapter 4).

This chapter is divided into ten sections. Section two presents briefly a review of geology of the Ernest Henry mine. It is followed by a summary of data collection from the six selected drill holes from Ernest Henry mine. Petrophysical data processing and discussion on quality of data are presented in sections four and five respectively. Petrophysical data interpretation in terms of lithology and alteration for each drill hole is presented in section six. The petrophysical signature for Ernest Henry based on combination of petrophysical data from six drill holes is given at section seven.

The relationship between petrophysical properties and corresponding small-scale comminution test results is investigated in section eight by applying different geometallurgical modeling methodologies as described in Chapter 4. Finally mill throughput modelling at Ernest Henry is presented in section nine followed by summary and conclusion for this chapter.

## **5.2. Geology of Ernest Henry Mine**

Ernest Henry mine has been recognised as an IOCG deposit. A comprehensive overview of the geology and mineralogy of Ernest Henry deposit can be found in Ryan (1998) and Mark et al. (2006). However a summary is given herein.

The mineralised zone at Ernest Henry is a pipe-like body with plan dimensions of approximately 250m x 300m, and is open at depth to at least 1000m (Ryan, 1998). The location of the ore-body is structurally controlled. Mineralisation occurs within felsic volcanic rocks that were brecciated during reverse fault movement along bounding shear zones (Mark et al., 2000). Breccia infill is made up predominantly of a magnetite-carbonate-chalcopyrite-pyrite assemblage, but also contains biotite, K-feldspar, hematite, garnet, barite, fluorite and quartz (Ryan, 1998; Mark et al., 2000).

The ore-body itself lies within a SE plunging breccia system within a sequence of porphyritic, intermediate volcanic rocks. The economic mineralisation is hosted by the breccia body which lies between a hanging wall sequence of altered volcanic rocks and a footwall sequence of carbonate-altered volcanic rocks and siltstones (Mark, et al., 2006). The major rock type is highly altered felsic volcanic (FV) with potassic, magnetite and carbonate alteration. Figure 5.1 shows representative digital images of the major alteration styles from Ernest Henry captured using the MSCL system.

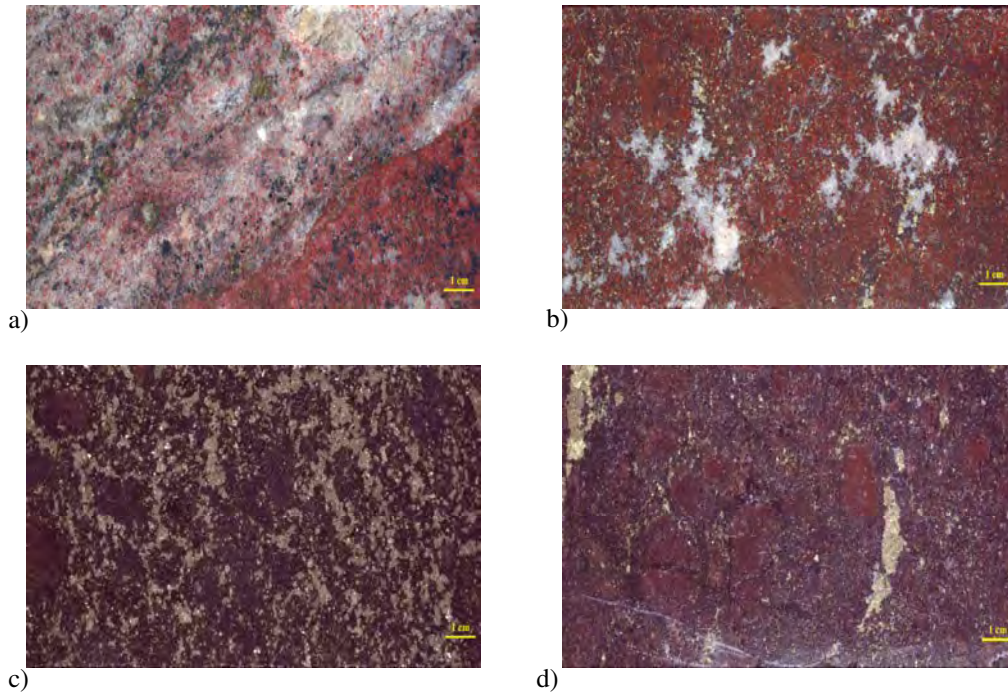


Figure 5.1. Photographs of drill cores from Ernest Henry captured using MSCL system. Felsic Volcanic (FV2) with carbonate (Calcite) alteration from drill hole EH446 - depth 430m (a), Felsic volcanic (FV3) with potassic (Kf) alteration from drill hole EH635 depth 1019m (b), Altered mafic volcanic rock (AMV2) with potassic (kf) alteration from drill hole EH635 depth 888m (c), and felsic volcanic rock (FV2) with magnetite (mt) alteration from drill hole EH635 depth 922m (d).

### 5.3. Data Collection Summary

Six drill holes (EH432, EH446, EH556, EH574, EH633 and EH635) were selected from the Ernest Henry deposit. Figure 5.2 shows the location of these drill holes. Drill holes and the respective depth ranges for detailed logging and analysis were chosen by GeM team members with the assistance of Ernest Henry site personnel to provide a cross-section through all parts of the known ore body. This included mineralisation in the open pit and potential underground areas of the deposit. EH512 was a PQ-size drill hole. Core from this hole was used in small scale comminution development test works at JKMR. Core from the remaining six drill holes was subjected to detailed petrophysical measurement and other testing procedures within the GeM project. A total of 1800m of half-NQ size core was logged from the six drill holes. The petrophysical measurements were recorded at 9 cm intervals using the Geotek MSCL. Continuous core images (40µm pixel size) were also captured by the system for all the logged core.

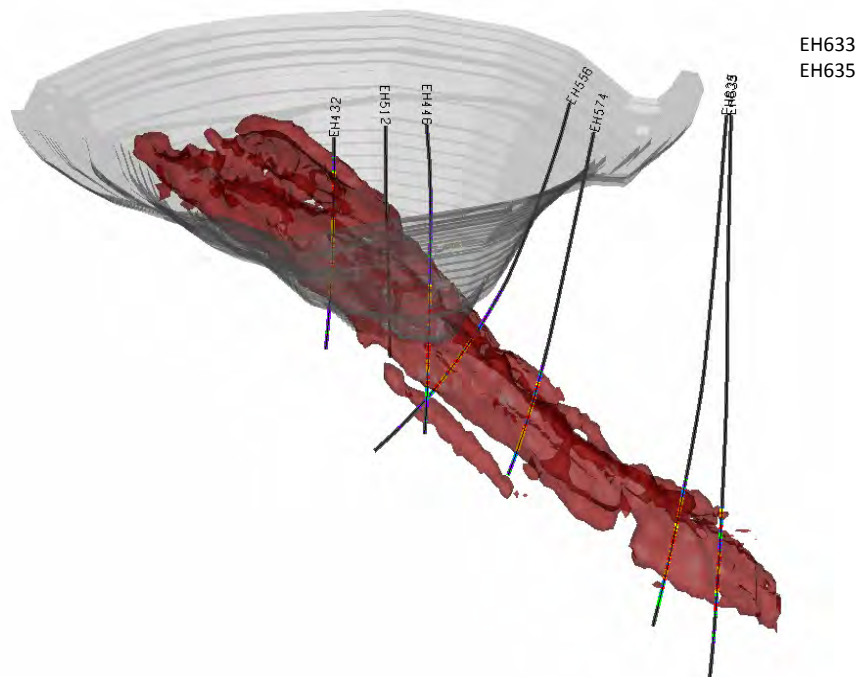


Figure 5.2. Perspective view of Ernest Henry showing the pit outline, the plunging pipe-like orebody and location of the six drill holes selected for this study (Walters, 2009).

A total of 142 Small scale comminution tests were conducted on a subset of the drill cores on which petrophysical measurements had already been recorded. The tests were performed on 2m assay intervals and yielded values for the comminution index (JKCi), impact hardness ( $A*b$ ) which is derived from JKRBT (JKMRC Rotary Breakage Tester) and batch ball mill operating work index (WI-5). The selected target grind size ( $P_{80}$ ) was  $212\mu\text{m}$ . The batch operating work index measurements and comminution index test results were used to estimate the Bond Ball mill work index (BMW<sub>i</sub>) for each 2m interval. These tests described in Chapter 2.

#### 5.4. Petrophysical Data Processing

In order to identify relationships between petrophysical data collected by the Geotek logger and comminution attributes, median values of petrophysical data over intervals for which comminution test data exist needed to be calculated.

The large amounts of data produced by the Geotek logger require efficient software processing tools. The Geotek software is limited in terms of processing and interpretation options, but some suitable commercial software is available. The LogTrans program (as

described in Chapter 4) was used for Geotek data processing and interpretation. Batch processing of raw data using LogTrans rendered the processing both faster and more consistent. Attaining the apparently simple objective of creating a single file with all petrophysical parameters sampled at common depths involved a large number of processing steps.

During processing of petrophysical parameters, new petrophysical attributes (Shear wave velocity, P-wave acoustic impedance i.e. product of density and P-velocity ( $\rho V_p$ ) and P-wave modulus) were also calculated. Shear wave velocity was estimated from P-wave velocity and density using Christensen's Equation (Entwisle and McCann, 1990). P-wave modulus and acoustic impedance are described in Chapter 2.

### 5.5. Quality of Petrophysical Data

As explained in Chapter 3 there are uncertainties involved with measurements of petrophysical properties. For instance factors such as core thickness, travel time measurement, delays due to sonic gel, delay of the transducer and delay due to core boat all add to uncertainties in P-velocity measurement. For gamma density, core thickness, calibrator and gamma fluctuation and temperature are influencing factors. For susceptibility the only factor that impacts the measurement is core thickness. Temperature had no effect on magnetic susceptibility measurement as shown in Chapter 3.

The intrinsic sensitivity of the Geotek density, velocity, and susceptibility sensors is quite high (Chapter 3). The precision and accuracy achievable in production logging are reduced by many factors. However the main factor contributing to the uncertainty in petrophysical measurement with the MSCL system is the core thickness. As it decreases, small errors in absolute thickness can be responsible for large relative errors in the measured parameter. Thus accurate measurement of petrophysical data on "NQ size" half-core becomes very difficult.

The Geotek laser can measure thickness with a precision of 0.01mm, but in production mode core logging of half-core the achievable accuracy in thickness is about  $\pm 0.2$ mm. The Ernest Henry NQ half-cores are about 2.2cm thick, so an error of  $\pm 0.2$ mm translates to a relative error of about  $\pm 1\%$ . Error in the core thickness propagates to density, susceptibility and P-wave velocity measurements. Therefore, when the accuracy in core thickness is affected, the quality of all the Geotek logging data is also being affected.

The intrinsic sensitivity of the Geotek gamma density system is approximately  $\pm 0.01$  g/cc, or  $\pm 0.31\%$  for Ernest Henry densities of 3.25 g/cc. When errors in thickness are also taken into account, the best-practice achievable accuracy for half NQ core is about  $\pm 1.31\%$ , i.e.  $\pm 0.04$  g/cc for Ernest Henry half-core.

P-wave velocity is determined by dividing core thickness by compressional wave travel time. The required time is the transit time across the core; however, the measured time is increased by a system delay and by the travel time through the silicon gel and plastic core boat (Chapter 3). Therefore a net delay of 16  $\mu$ s is subtracted from the measured times. Given the small radius of the NQ size half core ( $\sim 2.2$ cm) and the high velocities at Ernest Henry (average of  $\sim 5000$ m/s), the net delay is much larger than the actual transit time of interest ( $\sim 4.4$   $\mu$ s). The intrinsic sensitivity of the Geotek transducer system is approximately  $\pm 0.1$   $\mu$ s, or  $\pm 2\%$  for Ernest Henry velocities. When error in thickness is also taken into account, the achievable accuracy for half NQ core is about  $\pm 3\%$ , i.e. approximately  $\pm 165$  m/s for Ernest Henry half-core. When, in addition, the uncertainty in the net delay ( $\pm 0.25$   $\mu$ s) is considered, P-wave velocity accuracy in production logging on NQ half-core is  $\pm 6.5\%$ .

The magnetic susceptibility system was zeroed at regular intervals to avoid drift. Some intervals of drill core were relogged with a larger diameter of sensor coil to accommodate the high susceptibility of the cores, so loop size correction was applied. Volume correction, based on thickness has also been applied to the susceptibility data (Chapter 3). Increase in loop size slightly decreases the resolution of measurements.

Immersion densities measured on comminution samples at JKMRRC provided an independent check on the Geotek densities. During quality control of Ernest Henry data it was recognised that gamma density data were biased by about 0.2g/cc when compared with water immersion densities of core samples. It was later determined that the bias was introduced to gamma density measurement mainly as a result of the increase in gamma source aperture size and the full-core geometry of the aluminium calibrator during core logging (Chapter 3). Therefore an attempt was made to correct the measured densities using a new half-core aluminium calibrator as described in Chapter 3. To correct the densities, initially gamma calibration was conducted for five continuous days using both aluminium calibrators (Chapter 3). The calibration model derived based on two aluminium calibrators enabled conversion of previously recorded gamma readings with full cylinder aluminium for the period of Ernest Henry core logging to equivalent gamma readings on a new half-core aluminium calibrator.

The comparison of corrected gamma densities (averages over 2m assay intervals) with water immersion densities is represented in Figure 5.3 for all six holes. The correlation between Geotek densities and water immersion densities is moderate. The root mean square difference between gamma density and water immersion density is 0.16g/cc. The discrepancy between densities is a product of many factors including uncertainty in core thickness measurement by Geotek logger and the effect of Z/A (Chapter 3). Another very significant factor is random selection of pieces of cores from a combined sample of 2m intervals by JKMRC personnel for water immersion density.

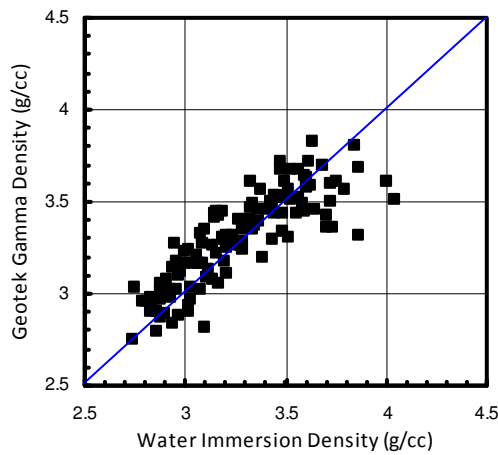


Figure 5.3. Comparison of gamma density and water immersion density measured on drill cores from five holes from Ernest Henry. The blue line represents a 1:1 line and the red line is the best regression fit.

Geotek P-wave velocity measurements (2m averages) on drill cores were compared with independent P-wave velocity measurements on small slabs derived from Ernest Henry drill cores using high frequency transducers (i.e.1MHz). High frequency P-wave velocity measurements were conducted at rock physics laboratory of Curtin University. A total of 35 slabs (3cm x 3cm x 1cm) derived from EH633, EH574, EH432 and EH446 drill holes. A minimum of five slabs derived from one meter interval of each drill hole. P-wave velocity measurements on slabs were conducted on two different directions; the smallest and longest length. ASTM (1978) recommends the minimum lateral dimension should not be less than five times the wave length, hence the measurements on the longest length were considered. Figure 5.4 illustrates the Geotek P-wave velocity and averages of P-wave velocity measurements on slabs. This comparison suggests that the high frequency P-wave velocity measurements are comparable to the Geotek P-wave velocities.

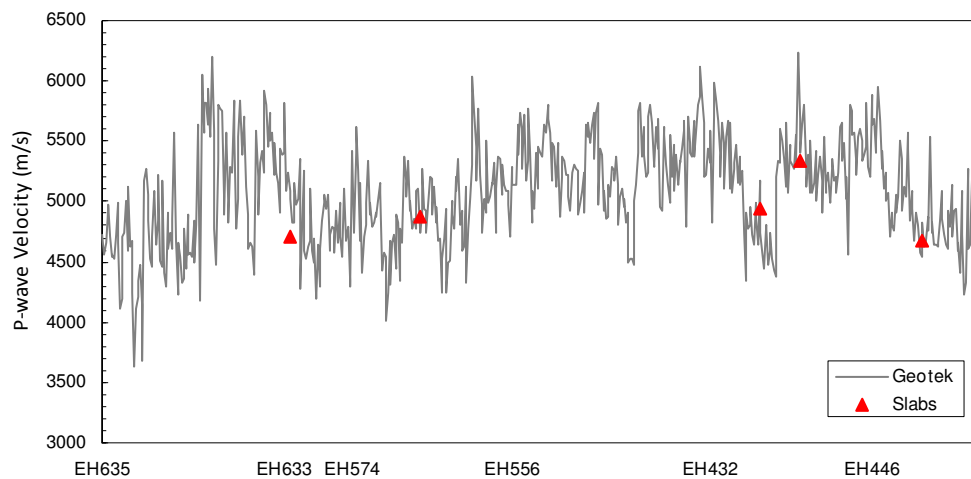


Figure 5.4. Comparison of the Geotek P-wave velocity measurements (2m averages) on drill cores from six holes from Ernest Henry with high frequency P-wave velocity measurements on slabs derived from drill cores. The samples originating from each drill holes are in depth order.

## 5.6. Petrophysical Data Interpretation

This section aims at exploring the relationship between petrophysical and comminution attributes for each drill hole at Ernest Henry. In order to identify relationships, the processed petrophysical logs for each drill hole have been plotted against geological, geochemical and metallurgical data using Logview software (Geological Survey of Canada). All variables have been plotted at the same scale in all drill holes for ease of comparison between drill holes. Petrophysical and comminution parameters, and geological and alteration codes appearing in the composite strip plots are defined in Tables 5.1 and 5.2 respectively. This section is divided into six subsections, one for each hole.

Table 5.1. Abbreviations for petrophysical and metallurgical parameters.

Measured Parameter	Description
Thick	Core Thickness (cm)
Density	Density (g/cc)
Vp	P- wave Velocity (m/s)
Vp-amplitude	P wave amplitude
MSUS	Magnetic susceptibility ( $10^{-4}$ SI)
Log(MSUS)	Logarithm of Magnetic susceptibility ( $10^{-4}$ SI)
PLI	Point Load Index (MPa)
Axb	Ore ranking hardness, a measure of ore crushability
BMWi	Bond mill work index (kWh/t)
Derived Parameter	Description
Vs	Estimated S-wave Velocity (m/s)
Young	Estimated Young's Modulus (GPa) $=0.8\rho V_p^2$
Impedance	P-wave acoustic Impedance ( $\text{Kg/m}^2\text{s}$ )

Table 5.2. Key for lithology and alteration

Lithology Code	Rock description
FV	Felsic Volcanics - not fractured, veined or brecciated
FV1	Fractured Felsic Volcanics - brittle fracturing, clast supported, can be an overprinting alteration
FV2	Mosaic Felsic Volcanics - matrix supported breccia with moderate to strong digestion of clasts
FV3	Felsic Volcanics - generally matrix supported with aligned clasts
MMB	Marble Matrix Breccias - Massive carbonate rock. Generally reserved for the footwall of mineralised zone, contains 'swirly' textures.
IV	Intermediate volcanics-massive to banded rock
IV1	Intermediate volcanics-brittle fracturing, clast supported
IV2	Intermediate volcanics-matrix supported breccia
SCH3	Weakly to moderate foliated schist
MV	Mafic Volcanics, generally phenocryst poor, very fine to fine grained, variably amygdaloidal, massive to banded volcanic rock.
AMV2	Altered Mosaic Mafic Volcanics - matrix supported breccia with moderate to strong digestion of clasts
AMV	Altered Mafic Volcanics, generally phenocryst poor, very fine to fine grained, variably amygdaloidal, massive to banded volcanic rock
AMV1	Altered Fractured Mafic Volcanics - brittle fracturing, clast supported, can be an overprinting alteration
Alteration Code	Alteration code description
ca	Calcite
kf	K-Feldspar
mt	Magnetite
dr	Dark rock
bt	Biotite
cb	Carbonate
hm	Hematite
py	Pyrite

### 5.6.1. Petrophysical Data from Borehole EH635

Petrophysical data were recorded on NQ-size half-core from drill hole EH635, for the depth range 800m to 1120m, using the Geotek MSCL. Two meter medians of petrophysical data were computed over assay intervals in order to facilitate direct comparison with metallurgical attributes and also assay data. Figure 5.5 shows strip logs of geological, geochemical, petrophysical and metallurgical parameters. There is no petrophysical data in some intervals (e.g. 850-865m) owing to core condition (i.e. quarter size core, fault zones). In addition, scatter in thickness readings was large ( $\pm 5$ mm) in some intervals (e.g. 944-946m). The source of the scatter is not known and the problem was not recognised immediately. These intervals of noisy thickness have been excluded from the composite plot and subsequent analyses.

Density and susceptibility measurements could assist both in visual core logging and definition of high grade ore zones. For example in the interval 916-920m where pyrite alteration is indicated, the density attains a peak value of about 4.1 g/cc and susceptibility is relatively low; both sulphur and iron content are high, as would be expected in the presence of pyrite. High grades of Cu and Au also correlates with high density and susceptibility. No strong correlation was found between susceptibility and P-wave velocity in this hole however in some intervals (e.g. 968-974m) a negative correlation was evident.

A positive linear correlation is evident between magnetic susceptibility and  $A^*b$ . This means with increase of magnetic susceptibility, the samples become softer in terms of crushing because magnetite acts as a crack initiator.

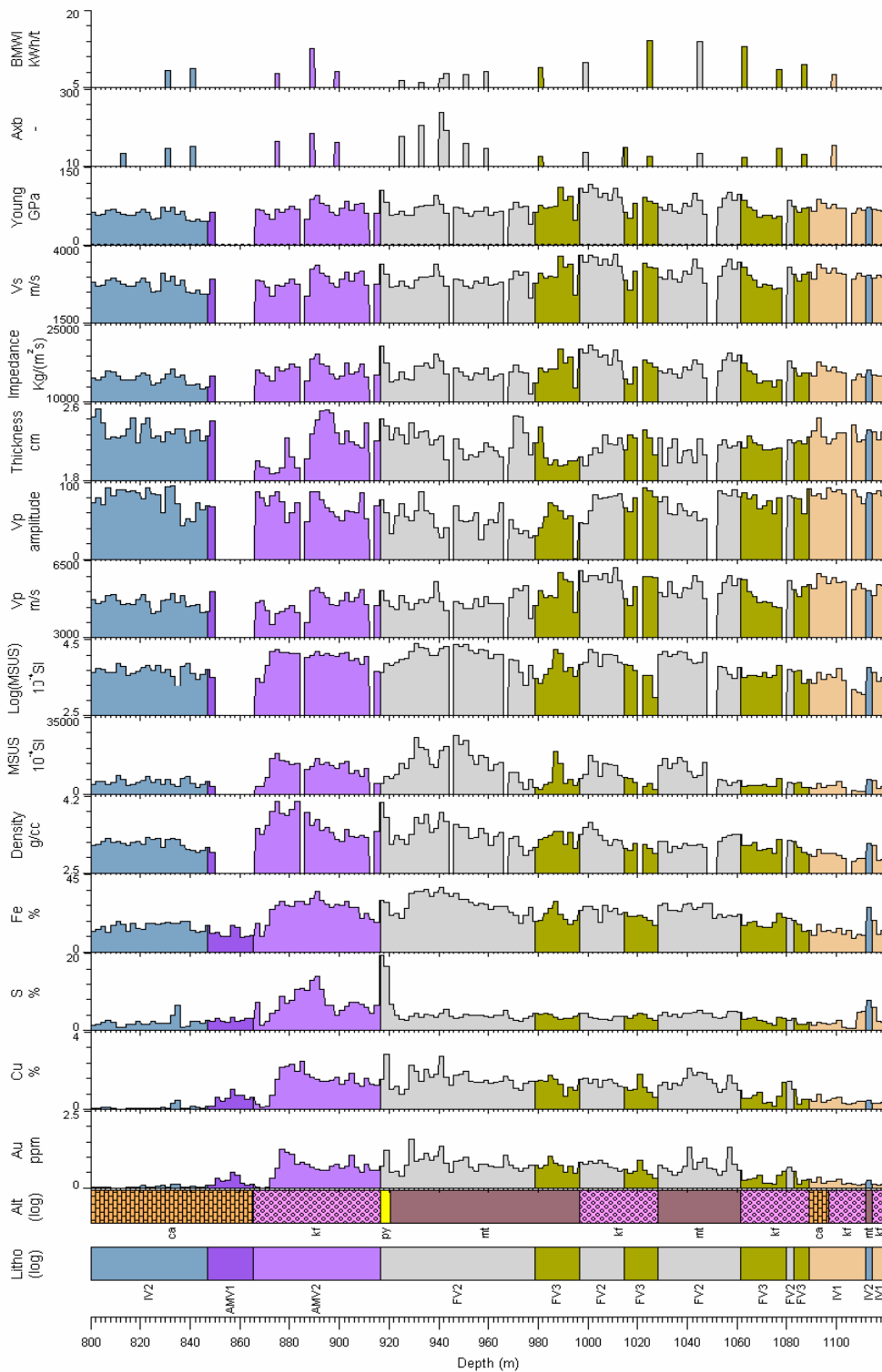


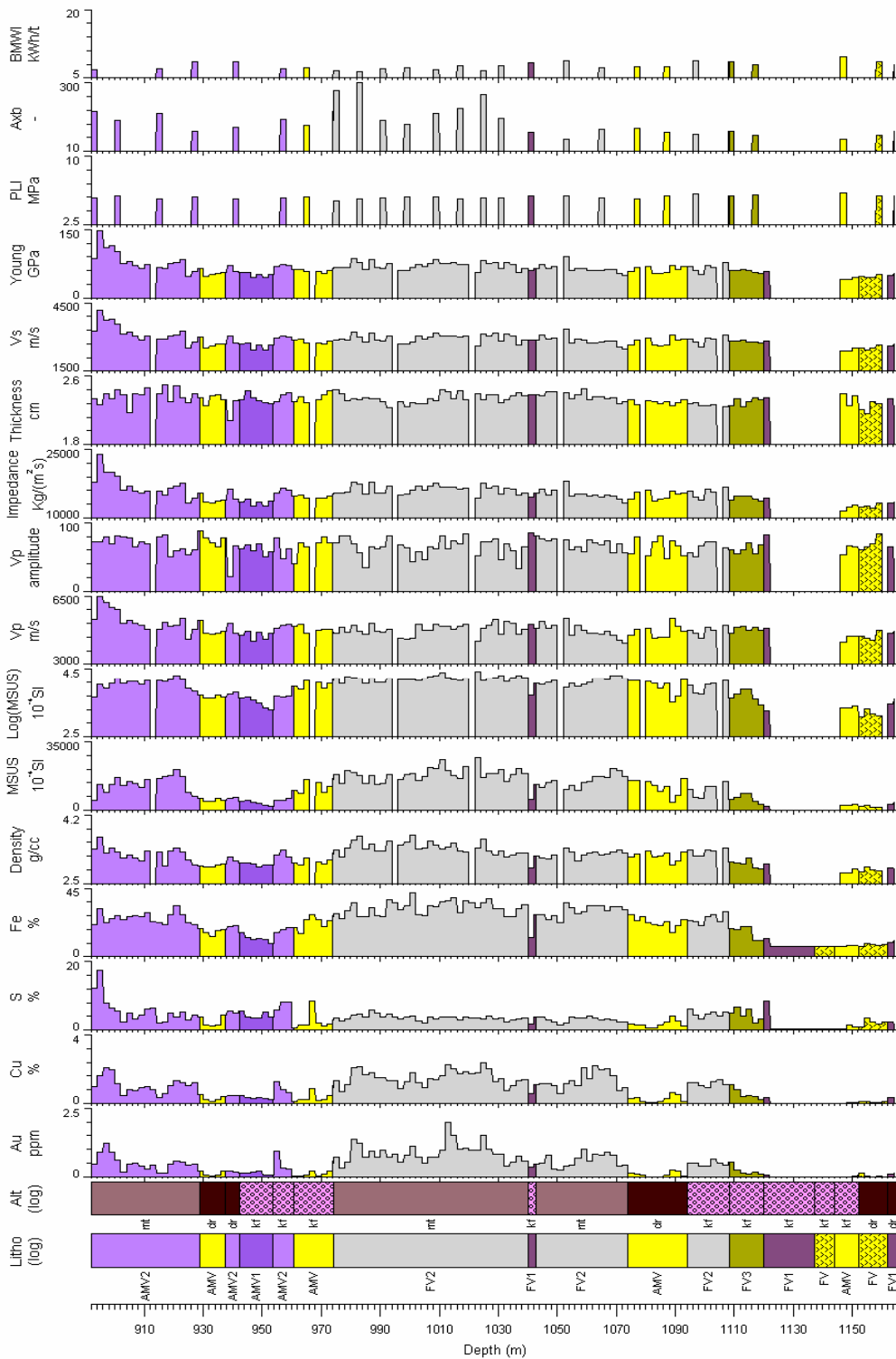
Figure 5.5. Strip logs of geological, geochemical, petrophysical, geotechnical and metallurgical composite for EH635

### 5.6.2. Petrophysical Data from Borehole EH633

NQ-size half-cores from EH633 were logged from 900m to 1165m depth. Two meter medians of petrophysical data were computed over assay intervals in order to facilitate direct comparison with metallurgical attributes and also assay data. Figure 5.6 shows strip logs of geological, geochemical, petrophysical and metallurgical data for this hole. There is no petrophysical data in some intervals owing either to core condition (i.e. quarter size core, fault zones).

High magnetic susceptibility clearly differentiates magnetite alteration intervals from potassic (kf) and “dark” (dr) alteration. A gradual decrease of susceptibility is evident from a maximum of 1.8 SI at 924m to 0.5 SI where dark alteration is present. Beyond this depth a gradual increase in susceptibility is apparent from 954m which continues until susceptibility reaches to maximum value where magnetite alteration is present.

As evident from strip logs in Figure 5.6, there is a positive correlation between susceptibility and  $A^*b$ . Also a positive correlation between density and  $A^*b$  is evident while the correlation between density and  $BMWi$  is negative. Estimated Young’s modulus and acoustic impedance both show a positive correlation with  $A^*b$  in EH633.



F Figure 5.6. Strip logs of geological, geochemical, petrophysical, geotechnical and metallurgical composite for EH633

### 5.6.3. Petrophysical Data from Borehole EH574

NQ-size half-cores from EH574 were logged from 543m to 810m depth. Two meter medians of petrophysical data were computed over assay intervals in order to facilitate direct comparison with metallurgical attributes and also assay data. Figure 5.7 shows strip logs of geological, geochemical, petrophysical and metallurgical composites. There is no petrophysical data in some intervals (e.g. 622-636m) due to core condition (i.e. quarter size core, fault zones). There is a positive correlation between density and Fe% and between susceptibility and Fe% (Figure 5.7). There is no obvious strong correlation between petrophysical and comminution parameters in this hole.

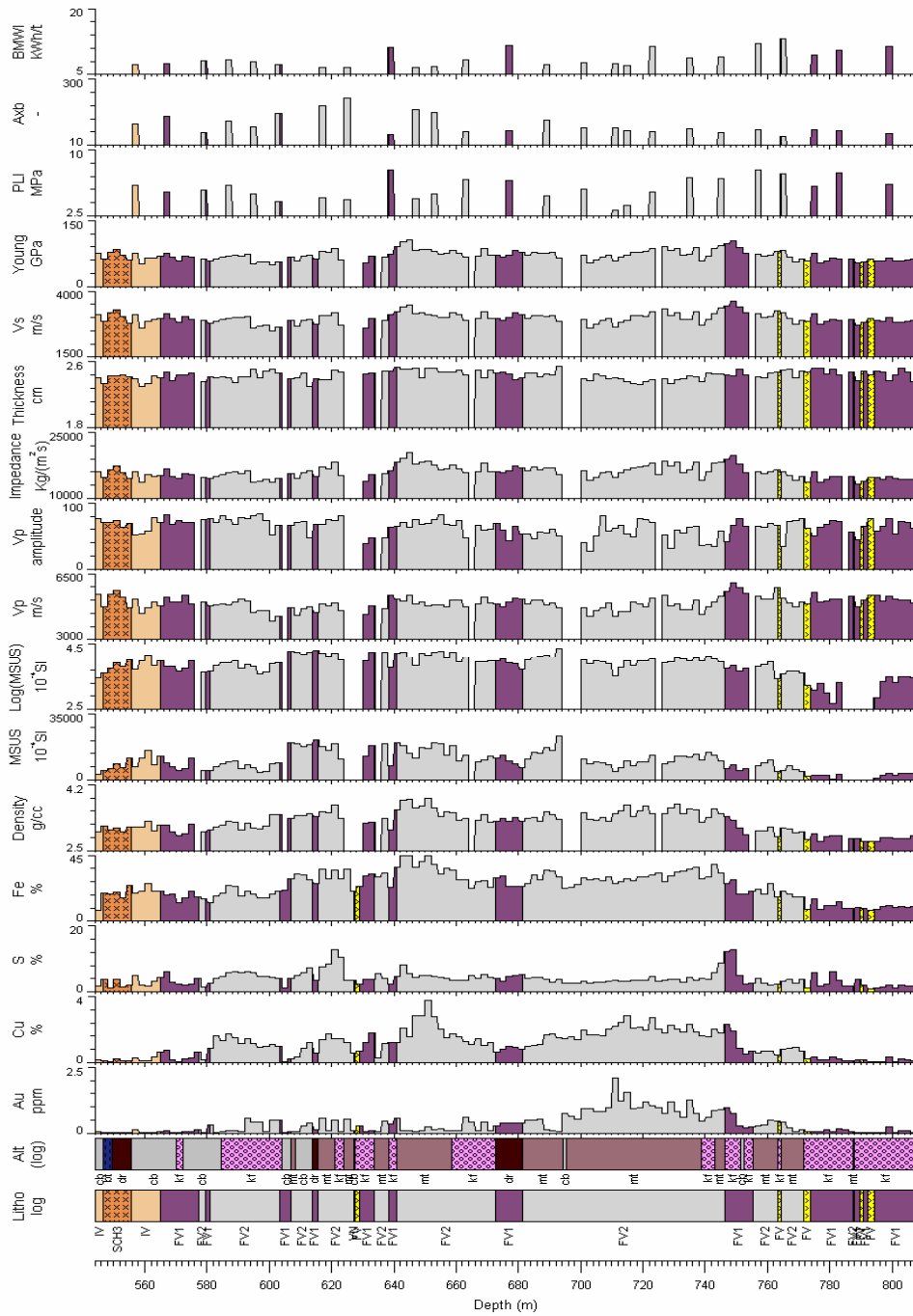


Figure 5.7. Strip logs of geological, geochemical, petrophysical, geotechnical and metallurgical composite for EH574

#### 5.6.4. Petrophysical Data from Borehole EH556

Petrophysical properties were recorded at 9cm intervals on drill cores of EH556 from a depth of 450m to 795m. Two meter medians of petrophysical data were computed over assay intervals in order to facilitate direct comparison with metallurgical attributes and also assay data. Figure 5.8 shows strip logs of geological, geochemical, petrophysical and metallurgical composites for this hole. There is no petrophysical data in some intervals owing either to core condition (i.e. quarter size core, fault zones).

Susceptibility data were recorded using the biggest loop size (150mm loop diameter) for depths below 690m to accommodate high susceptibility values. There is relatively low magnetic susceptibility (less than 0.5 SI) in the interval 450-548m, even though it is logged as magnetite altered. Normally a susceptibility of 0.5 SI is considered high, but in this case there is a possibility that either the alteration has been mis-logged or this interval is characterised by only very low intensity magnetite alteration. Susceptibility is higher from 548-564m where magnetite alteration is indicated in lithology "FV".

Density decreases significantly below the depth of 730m. This change in density corresponds to changes in Fe, Cu and S content. Magnetic susceptibility also decreases below this depth.

In the interval 569-731m, where high susceptibility is evident, the alteration appears to be incorrectly logged as K-feldspar. From 731m to 755m there are zones of hematite and K-feldspar alteration where susceptibility is very low, as expected.

Density decreases significantly below the depth of 730m. This change in density corresponds to changes in Fe, Cu and S content. Magnetic susceptibility also decreases below this depth and consequently  $A^*b$  decreases while  $BMWi$  and  $PLI$  increase. Density exhibit a positive correlation with  $A^*b$  while P-wave velocity has a weak negative correlation with  $A^*b$ .

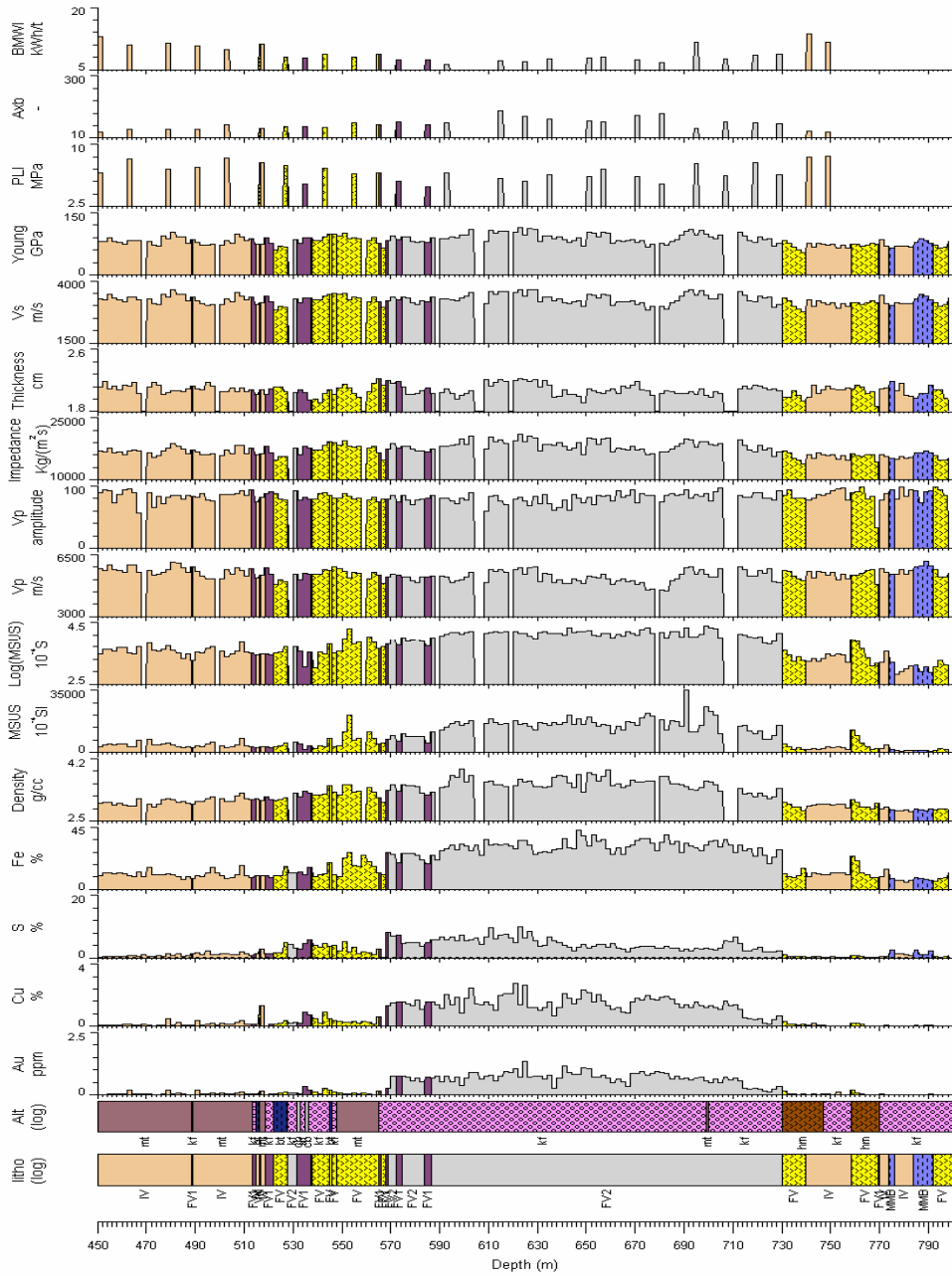


Figure 5.8. Strip logs of geological, geochemical, petrophysical, geotechnical and metallurgical composite for EH556

### 5.6.5. Petrophysical Data from Borehole EH446

Half NQ-size core from EH446 was logged from 299 to 633m. Two meter medians of petrophysical data were computed over assay intervals in order to facilitate direct comparison with metallurgical attributes and also assay data. Figure 5.9 shows the geological, geochemical and petrophysical logs for this hole. All susceptibility data were recorded using the biggest loop size (150mm loop diameter) to accommodate the high susceptibility of the cores.

The dominant rock type in this hole is felsic volcanic material (FV2) with magnetite alteration. Susceptibility is well correlated with the alteration log, since high susceptibility corresponds to magnetite alteration and low susceptibility to K-feldspar (kf) or dark (dr) rock alteration. There is a step change at 351m, at the transition from “kf” to “mt” alteration, where susceptibility increases (Figure 5.9). Susceptibility remains generally high until 604m, except between 427m and 449m where the dominant alteration is carbonate (ca). Below 604m the alteration style is k-feldspar and dark rock.

A\*b shows significant variability within magnetite alteration intervals. This high variability is attributed to the effect of alteration intensity. Magnetic susceptibility shows a moderate positive correlation with A\*b for all comminution tests samples at this hole. There is also a positive correlation between density and A\*b. P-wave velocity gradually decreases from 302m to 340m in “kf” alteration class where A\*b is relatively low.

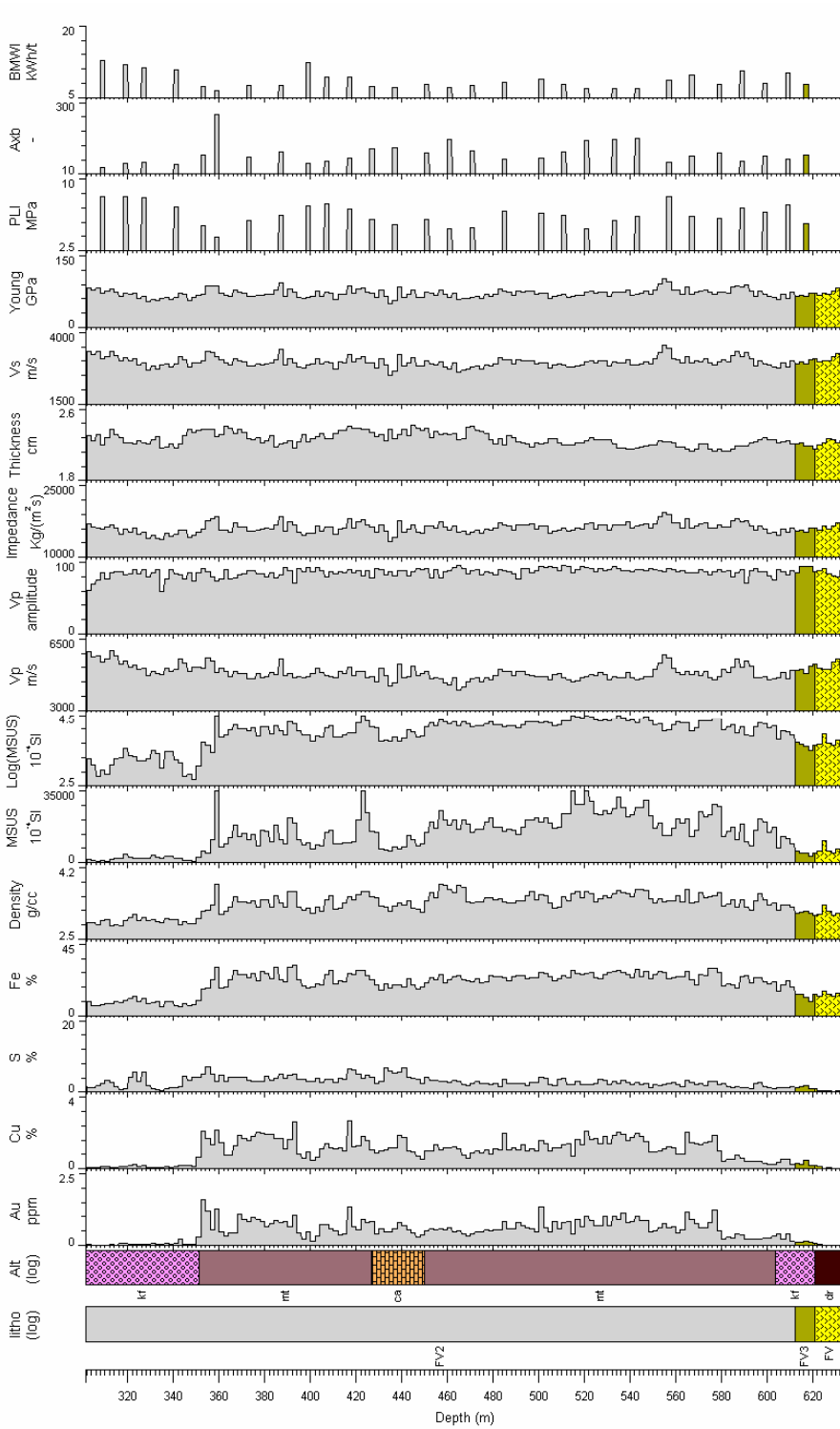


Figure 5.9. Strip logs of geological, geochemical, petrophysical, geotechnical and metallurgical composite for EH446

### 5.6.6. Petrophysical Data from Borehole EH432

NQ-size half-cores from EH432 were logged from 139m to 399m depth. Two meter medians of petrophysical data were computed over assay intervals in order to facilitate direct comparison with metallurgical attributes and also assay data. Figure 5.10 shows the geological, geochemical, petrophysical and metallurgical composites for this hole. There is no petrophysical data in some intervals (e.g. 180-182m) owing to core condition (i.e. quarter size core, fault zones). All susceptibility data were recorded using the biggest loop size of susceptibility sensor (150mm loop diameter) to accommodate the high susceptibility of the cores.

The susceptibility log in most intervals shows high susceptibility which does not correspond well with alteration logging. For example from 214-240m there is a peak of susceptibility (~2.5 SI) within a zone of carbonate alteration. There is only 10m within this hole (300-310m) where alteration logging (mt) matches with high susceptibility measurements. Therefore it appears likely that most of the visual core logging is incorrectly recorded.

A gradual decrease in P-wave velocity from 190m to 240m suggests a decrease in strength of rocks that conforms to the BMWi variation. There is also a step change increase in P-wave velocity at 240m where K-feldspar alteration is apparent. The increase in P-wave velocity conforms to decrease in A\*b and an increase in point load index and BMWi in this interval. A moderate positive correlation also exists between P-velocity and BMWi (Figure 5.10). The density log shows a decrease in density from 3.6g/cc to 3.2g/cc in the interval from 244-262m where "FV1" rock type with k-feldspar alteration exists. This unit represents a very hard rock in terms of comminution as is evident by A\*b, PLI and BMWi values.

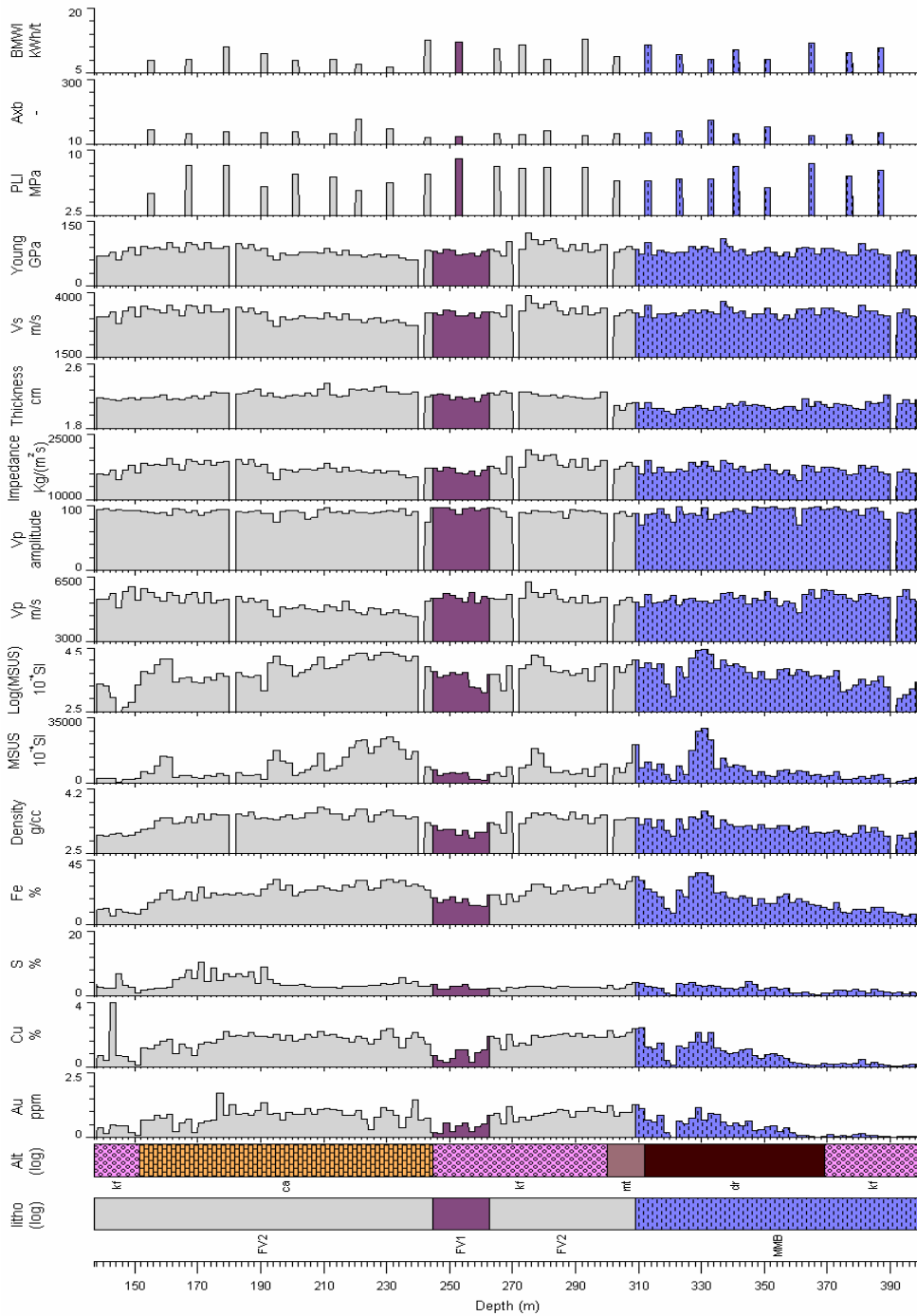


Figure 5.10. Strip logs of geological, geochemical, petrophysical, geotechnical and metallurgical composite for EH432

### 5.7. Petrophysical Signature of Ernest Henry

The relationship between petrophysical properties, assays, geological and metallurgical attributes has been considered in the combined data set for all six drill holes from Ernest Henry.

Overall there is a moderate positive correlation ( $R^2=0.57$ ) between density and magnetic susceptibility in all holes (Figure 5.11). While density follows a Normal distribution magnetic susceptibility follows a log Normal distribution (Figure 5.12). The density of the majority of samples varies from 2.75 to 4.1 g/cc, while variation in magnetic susceptibility is from 0.1SI to ~ 4SI. Anomalous high values of magnetic susceptibility (i.e. 4.0 SI) are mainly due to the magnetite-enriched samples. P-wave velocity has a normal distribution while P-wave amplitude measurements are skewed (Figure 5.12). P-velocity of the samples varies from 3000m/s to a maximum of 7000m/s.

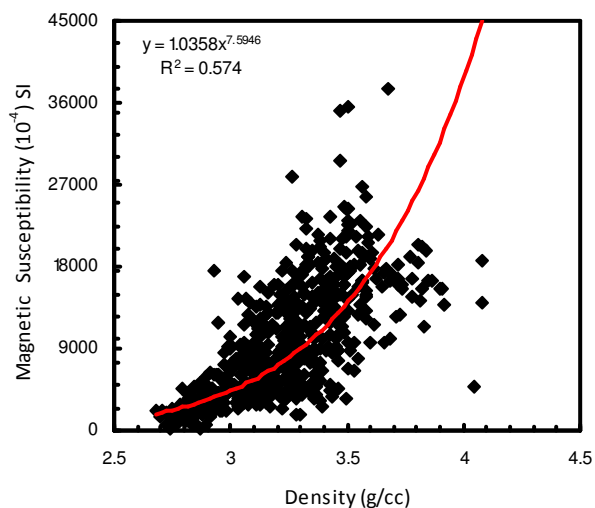


Figure 5.11. Scatter plot of gamma density versus magnetic susceptibility from all the six drill holes of Ernest Henry.

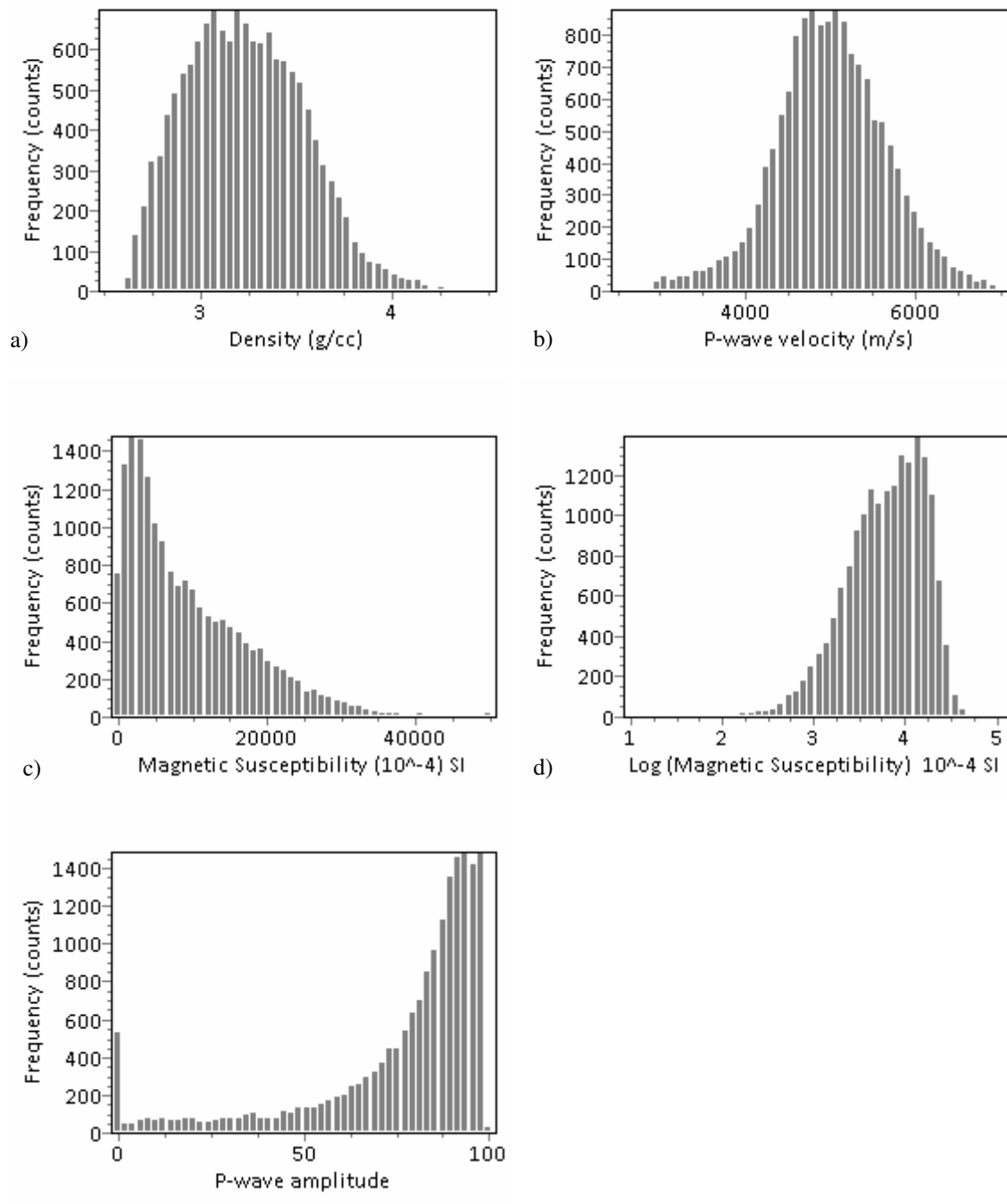


Figure 5.12. Histograms of (a) density, (b) P-wave velocity, (c) magnetic susceptibility (d) logarithm of magnetic susceptibility and (e) P-wave amplitude from drill holes EH633, EH635, EH574, EH432, EH556 and EH446.

Medians and spreads of density, P-wave velocity, P-wave amplitude and magnetic susceptibility in 2m intervals from drill holes EH633, EH635, EH574, EH432, EH556, and EH446 are calculated for each visually logged litho-alteration class (Figure 5.13). For any one parameter there is considerable overlap of property ranges between litho-alteration classes. Many litho types with “kf”, “ca” and “cb” alteration are highly magnetic (Figure 5.13b). This suggests that alteration in some samples have been either classified incorrectly by mine geologists or “kf” alteration class is a compound of two population (i.e. with low and high proportion of magnetite). Further investigation of relationships between petrophysical properties and geology is difficult given concerns about the veracity of the visually logged litho-alteration classes. It may be possible to refine and redefine the alteration classification using magnetic susceptibility as a proxy but this case has not investigated in this research.

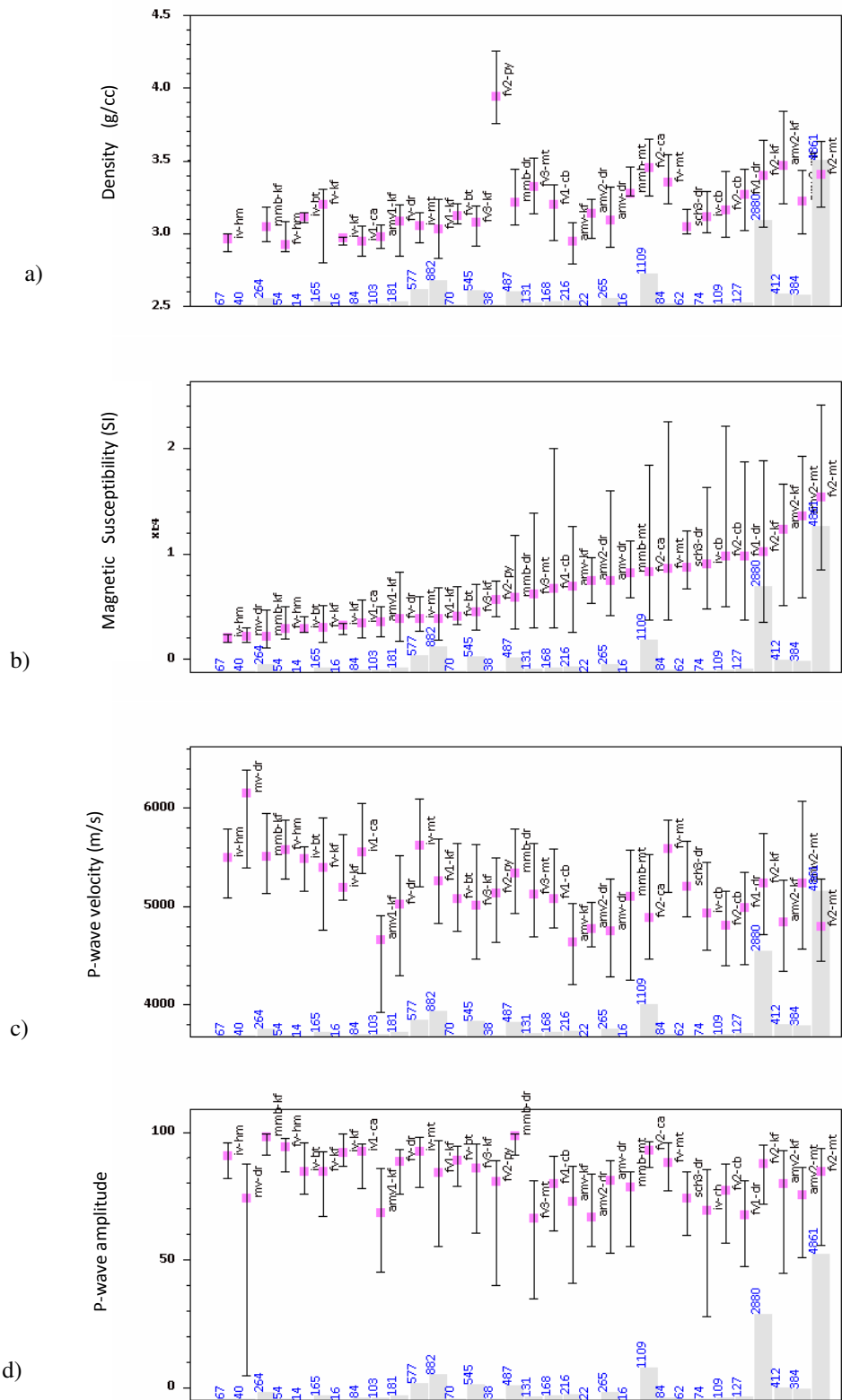


Figure 5.13. Medians and spreads of (a) density, (b) magnetic susceptibility (c) P-wave velocity and (d) P-wave amplitude in 2m intervals from drill holes EH633, EH635, EH574, EH432, EH556, and EH446, classified by litho- alteration classes. Pink square = median, black bar = range (16<sup>th</sup> – 84<sup>th</sup> percentile), gery histogram = number of samples for each litho- alteration class. Abbreviations as defined in Table 5.2.

The relationship between susceptibility and grade and between density and grade was examined in all drill holes. It is possible to estimate grade reasonably well from these physical properties. Zones of high Fe, Cu and Au grades are generally coincident (Figure 5.14). Density and susceptibility correlate well with Fe (Figure 5.15). Therefore high density and susceptibility translates to high Au and Cu grades. Density appears to have a linear correlation with Fe grade while susceptibility is related to Fe in nonlinear form. A simple density model based on Fe grade has been developed and used at Ernest Henry mine (Collier and Bryant, 2003). The model is a linear regression of Fe versus water immersion density using 2m composite drill hole data from Ernest Henry. The model has the form:

$$\text{Density} = 0.0287 * \text{Fe} + 2.5764 \quad (5.1)$$

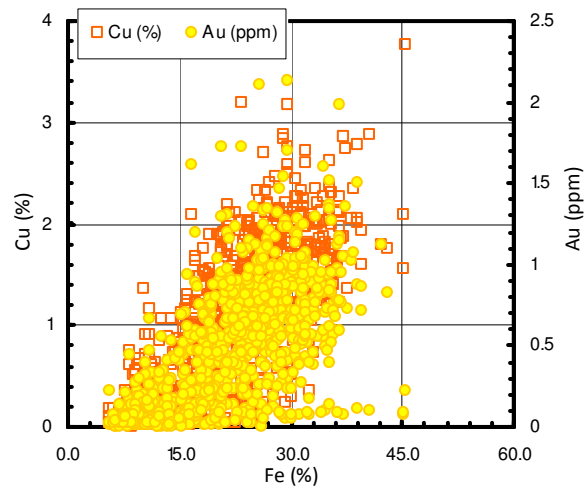


Figure 5.14. Correlation of Fe with Au and Cu in all six holes of Ernest Henry.

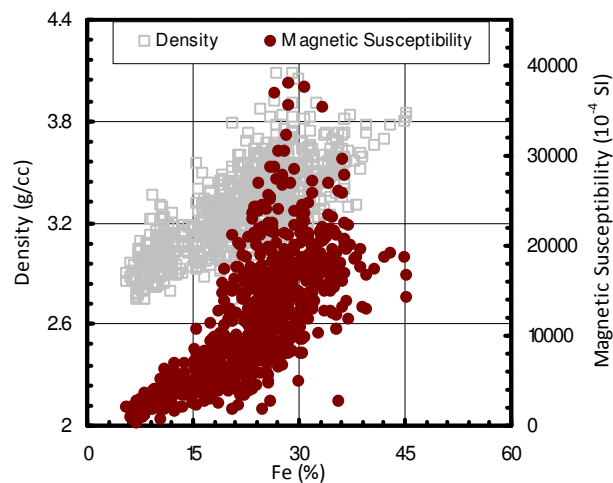


Figure 5.15. Cross plot of Fe with density and susceptibility in all six holes of Ernest Henry. Note that the relationship between Fe and density is effectively linear while the relationship between Fe and susceptibility is nonlinear.

### 5.8. Comminution Modelling

Comminution behaviour for Ernest Henry is depicted in Figure 5.16. There is a negative correlation between  $A^*b$  and  $BMWi$  that suggests samples that are hard to crush (low  $A^*b$ ) are also hard to grind (high  $BMWi$ ) as well. Therefore the harder the materials are for crushing and grinding, the lower is the mill throughput. Figure 5.16 shows a large dynamic range for  $A^*b$  and  $BMWi$  values. The large variation in comminution behaviour translates to high mill throughput variability (Section 5.9). A high throughput of ~2700 t/h can be predicted for soft materials in terms of crushing and grinding, whereas a low throughput (~1100 t/h) is expected for hard materials (Figure 5.16). This shows that the ore comminution behaviour at Ernest Henry is not uniform as claimed by Strohmayer et al (1998).

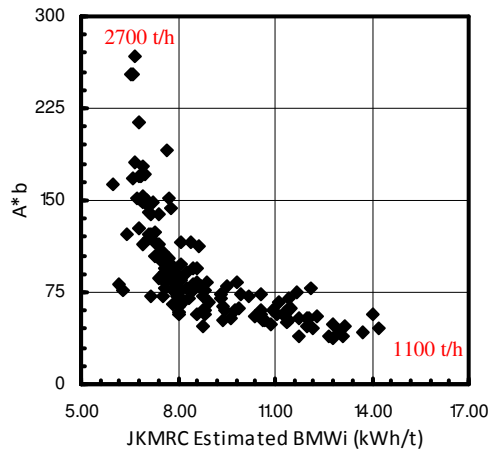


Figure 5.16. Cross plot of  $A^*b$  and JKMRC estimated Bond mill work index for all comminution test samples of Ernest Henry.

The relationship between petrophysical properties and  $A^*b$  and  $BMWi$  are investigated for all comminution test samples (Figures 5.17 and 5.18). Averages of petrophysical properties (2m assay intervals) were calculated for comparison to comminution attributes. Overall the correlations between petrophysical properties and comminution attributes are weak. Linear regression was only applied to the data as nonlinear regression did not result in significant improvement in prediction. Magnetic susceptibility shows a weak positive correlation with  $A^*b$  and a negative correlation with  $BMWi$ . Density shows similar correlations with  $A^*b$  and  $BMWi$ . Higher susceptibility and density are both general indications of high concentration of magnetite. The higher magnetite content makes the rocks softer in terms of crush and grind, hence high  $A^*b$  and low  $BMWi$ .

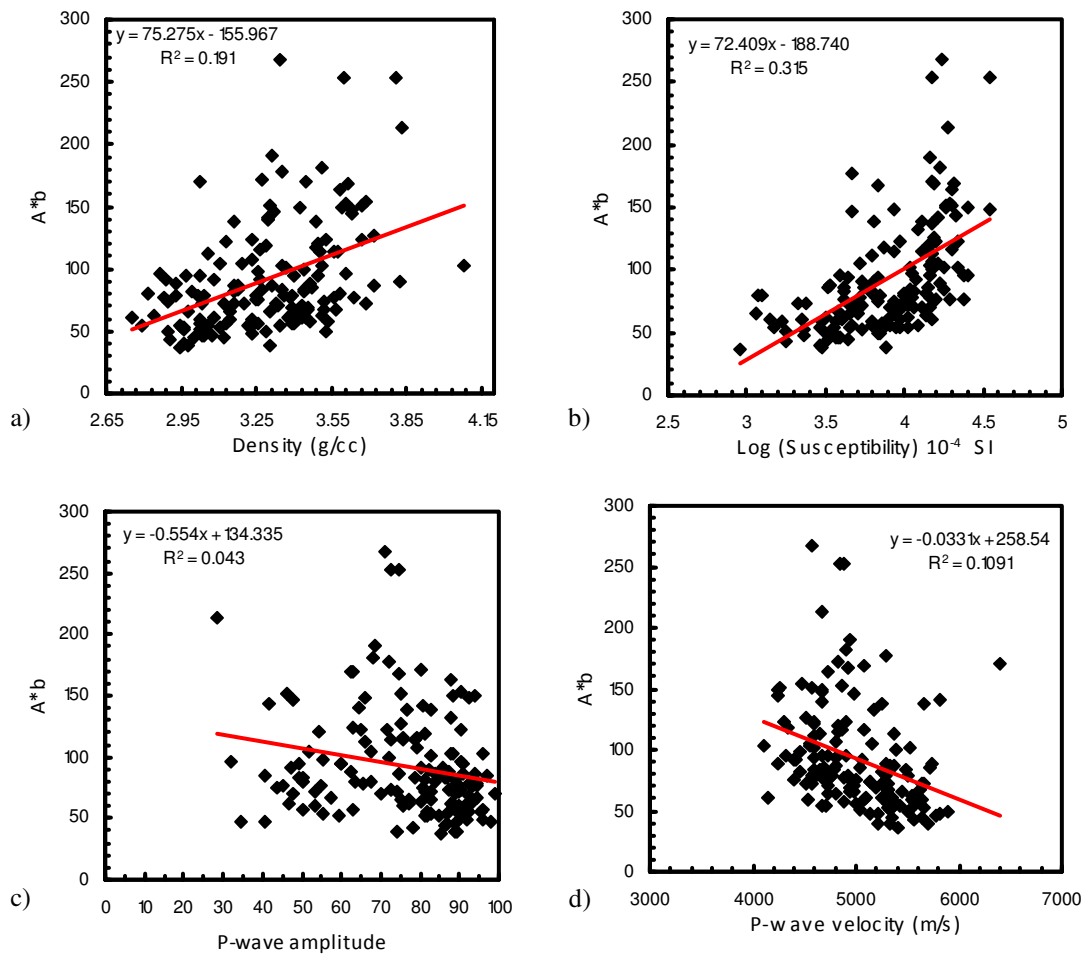


Figure 5.17. Cross-plots of  $A^*b$  versus 2m averages of (a) density, (b) logarithm of magnetic susceptibility, (c) P-wave amplitude, and (d) P-wave velocity for all comminution test samples from all drill holes. The red line in each case is the linear regression fit to the data which has been shown for comparative purposes even when correlations are very poor.

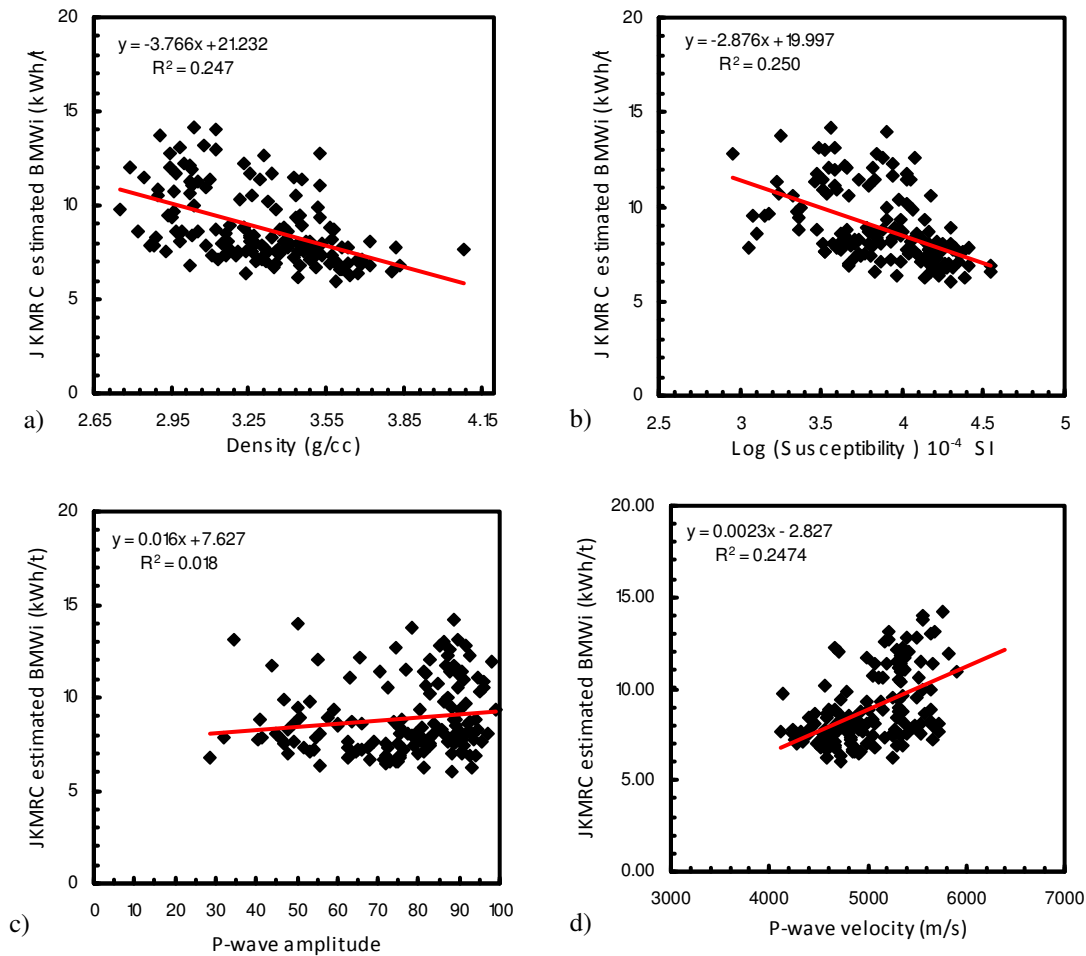


Figure 5.18. Cross-plots of JKMRC estimated BMWi versus 2m averages of (a) density, (b) logarithm of magnetic susceptibility, (c) P-wave amplitude, and (d) P-wave velocity for all comminution test samples from all drill holes. The red line is the linear regression fit to the data.

The results of multiple regression of four petrophysical properties (P-velocity, P-amplitude, gamma density and magnetic susceptibility) against all 142 available A\*b and BMWi determinations are represented in Figure 5.19a and Figure 5.19b respectively. The relative error of prediction (REP) for A\*b and BMWi is 26.3% and 14.5% respectively. As evident from Figure 5.19a soft materials for crushing were poorly predicted. Hard materials for grinding were poorly predicted (Figure 5.19b).

Stepwise regression analysis (Chapter 4) suggests that the most important input variable for prediction of A\*b and BMWi is magnetic susceptibility (Figure 5.17b and Figure 5.18b). The relative error of prediction for A\*b and BMWi using magnetic susceptibility alone is 28.4% and 18.7% respectively. Such models are not accurate enough to be used as a universal model for future prediction of comminution parameters. Prediction of A\*b

from the JKMRC developed “destructive” test (crushing index; JKCi) only marginally improved the prediction (relative error of 22%).

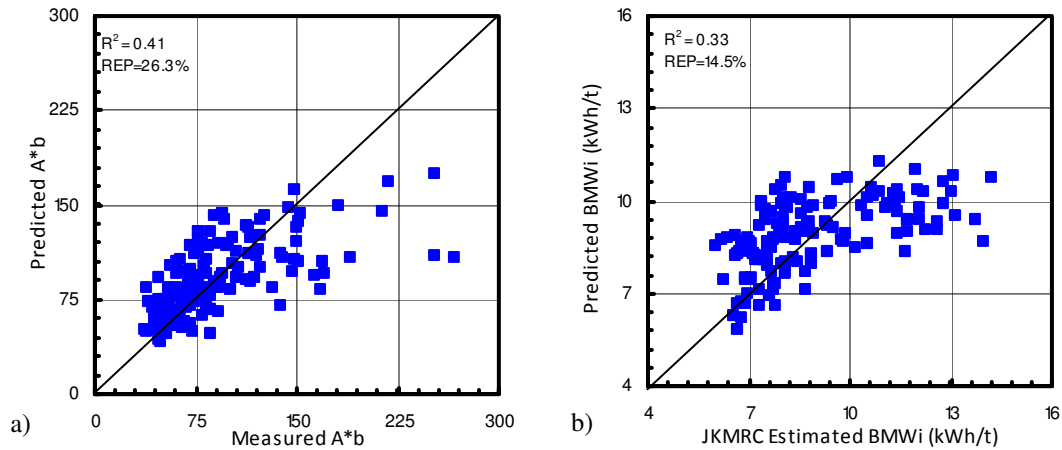


Figure 5.19. Measured versus predicted A\*b (a) and JKMRC estimated versus predicted BMWi (b) for all 142 test samples using multiple regression of four petrophysical parameters (P-velocity, P-amplitude, gamma density and magnetic susceptibility).  $R^2$  is regression correlation coefficient and REP is relative error of prediction. The RMS error values for A\*b and BMWi universal models are 34.3 and 1.61kWh/t respectively.

It was envisaged that classification of data could improve the accuracy of the comminution models. As stated in Chapter 4, the choice of appropriate data classification for geometallurgical purpose depends on ore comminution variability. Given the significant variability of comminution parameters at Ernest Henry (Figure 5.16), definition of geometallurgical classes based on the petrophysical (PC) or geological (GC) approaches was postulated as effective methods for development of models as discussed in Chapter 4. In the following subsections this idea is further investigated. The application of other approaches (CC and CPC) for geometallurgical data classification and comminution modelling (Chapter 4) are also illustrated in the following subsections.

### 5.8.1. Comminution Modelling : GC Approach

The aim of “GC” approach as discussed in Section 4.2.1 is to investigate the relationship between petrophysical properties and comminution attributes within geological classes (e.g. litho types). A database of visual alteration and lithology logs compiled by site geologists was available from Ernest Henry. The combination of lithology and alteration could potentially provide effective geometallurgical classes for subsequent geometallurgical model development. However, using this information resulted in more than 30 different classes thus making investigation of the relationship between petrophysical and comminution parameters rather difficult. This was mainly due to the

fact that in some classes there were no comminution tests or the number of tests was so small to develop a model.

Investigation of relationships between petrophysical properties and comminution attributes within the brecciated felsic volcanic classes (FV2) which are the host rocks of mineralization and respective alteration styles was undertaken. Figure 5.20 is a box and whisker plot showing mean values of A\*b and BMWi together with standard deviation for each litho-alteration class. The comminution properties overlap in all classes. Moreover visually logged alteration classes at Ernest Henry are inconsistent in some drill holes (Section 5.7) hence geometallurgical class definition based on GC approach is not effective at Ernest Henry.

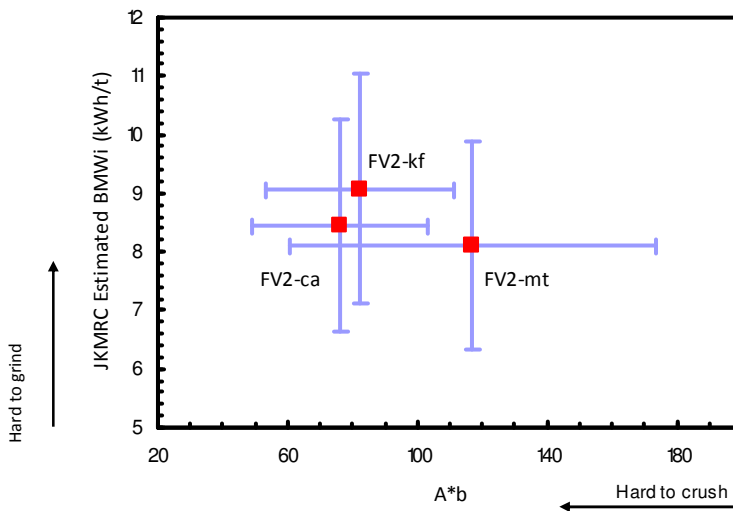


Figure 5.20. Scatter plot of mean A\*b and Bond mill work index for litho-alteration classes at Ernest Henry. The red squares and the blue bars indicate the mean and standard deviations of comminution attributes respectively.

### 5.8.2. Comminution Modelling : PC Approach

The geometallurgical modelling based on the PC approach (section 4.2.2 of Chapter 4) has been documented by Vatandoost et al (2009). Petrophysical data were grouped into four classes using cluster analysis techniques and then predictive comminution models for  $A^*b$  and  $BMWi$  were developed within each cluster for the subset of samples for which comminution parameters existed. The performance of the PC based models was better than universal models (Vatandoost et al., 2009). Thus they were used to estimate  $A^*b$  and  $BMWi$  for intervals of drill cores where comminution tests were not available. However, such models were verified only against samples used for analysis. In order to ensure that the regression models adequately represent the general population of the dataset and whether they are appropriate enough to be applied for future prediction, the models should be validated using samples drawn from the general population to ensure representativeness.

In this section a review of the approach conducted by Vatandoost et al (2009) is presented and the comminution models are rebuilt using petrophysical properties based on samples from five drill hole (EH635, EH633, EH556, EH432 and EH446). The developed models then are tested for samples from EH574 (randomly selected drill hole) to predict comminution attributes and to assess the validity of the comminution models.

As presented in section 5.8 the universal models of  $A^*b$  and  $BMWi$  are not very accurate. In order to better predict the comminution behavior using petrophysical properties it is advantageous to divide the core samples into groups or classes. The underlying hypothesis here is that each petrophysical cluster should correspond to certain comminution behaviour. Four clusters were defined as a result of cluster analysis using four petrophysical properties (i.e. density, susceptibility, P-velocity and P-amplitude). The statistical distance was used to select the number of clusters (Section 4.3.1 of Chapter 4). Moreover the petrophysical properties of the classes were statistically analysed to establish whether they are well discriminated. Principal component analysis provides a useful framework for visualizing clusters. In Figure 5.21 the Ernest Henry data, coloured according to cluster, are projected onto the plane defined by the first two principal components. As can be seen the clusters are fairly well separated in this representation.

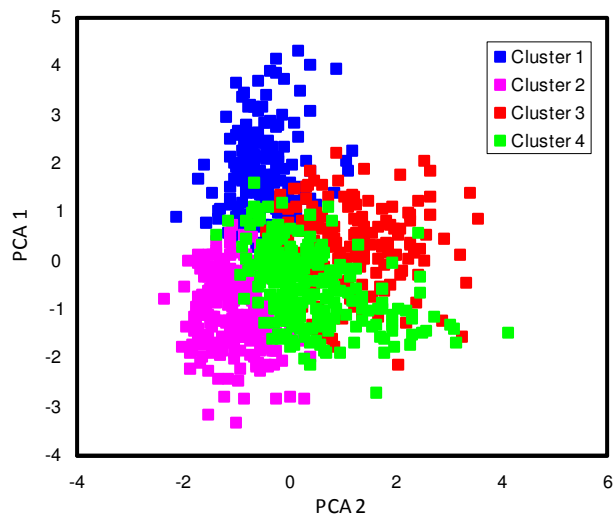


Figure 5.21. Cross-plot in principal component space, with data points differentiated according to petrophysical cluster.

A radar chart offers another way to assess the individuality of the selected classes (Figure 5.22). Each parameter on the radar chart was normalized based on the minimum and maximum of each parameter using equation 5.2 so that all four petrophysical properties to be in the same scale.

$$Z = \frac{X - X_{Min}}{X_{Max} - X_{min}} \quad (5.2)$$

where Z is the normalized value, X is the value to be normalized,  $X_{Min}$  and  $X_{Max}$  are minimum and maximum value of X in a given dataset respectively. If the quadrilaterals representing the different clusters differ in shape and size, the clusters are distinctive. Conversely, if the quadrilaterals are similar in shape and size, the existence of separate clusters is questionable.

As can be inferred from Figure 5.22, Cluster 1 is well separated from others by virtue of higher density and susceptibility and lower velocity. Qualitative assessment suggests that Cluster 1 material should be soft to crush and easy to grind, given its greater magnetite content. Cluster 2 is characterized by low magnetic susceptibility and low density but high velocity. Therefore, Cluster 2 may likely represent rocks that are more competent or harder to crush. Cluster 3 is separated from other clusters mainly due to low P-wave amplitude. Cluster 4 is fairly similar to Cluster 2 but has lower P-velocity.

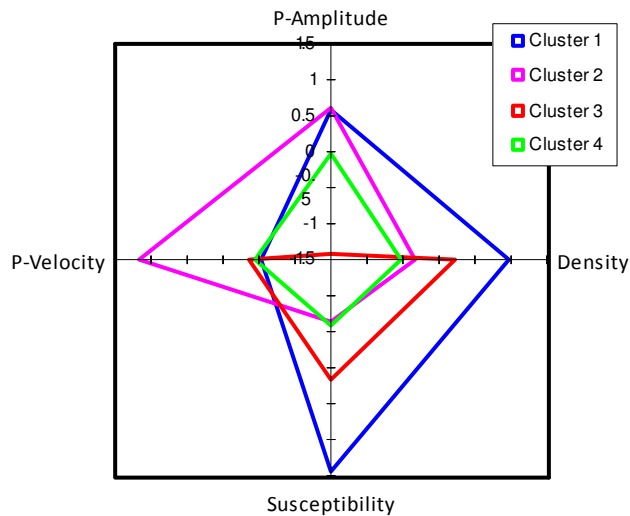


Figure 5.22. A radar diagram of petrophysical parameters for four-cluster solution

Table 5.3 shows the mean and standard deviation of comminution test results within each cluster. There is a clear difference between comminution response in Clusters 1 and 3 when compared with Clusters 2 and 4: the samples in Cluster 1 and 3 are soft to crush and relatively easy to grind while samples in Cluster 2 and 4 are relatively hard to crush and hard to grind. Although Clusters 2 and 4 are both hard to crush it appears that the samples in Cluster 2 may be harder to grind (a difference of 1.3 kWh/t) and relatively harder to crush when compared to samples in Cluster 4.

Table 5.3. Mean and standard deviation of comminution parameters ( $A^*b$  and  $BMWi$ ) in each cluster for test samples from all holes.

Comminution Parameter	Cluster 1 (31 samples)	Cluster 2 (41 samples)	Cluster 3 (30 samples)	Cluster 4 (40 samples)
$A^*b$	112 (44)	64 (20)	120 (56)	83 (32)
$BMWi$	7.8 (1.09)	10.3 (1.86)	8.1 (1.69)	9.0 (2.00)

In order to geologically characterise the created clusters, the distribution of visually logged litho-alteration classes was constructed for each cluster. The histogram of litho-alteration classes for each cluster (Figure 5.23) reveal that the majority of samples with magnetite alteration (FV2-mt) report to clusters 1 and 3 while the majority of samples which have K-feldspar alteration are found in clusters 2 and 4. This breakdown is consistent with the observation that unbrecciated K-feldspar rich volcanics are harder to crush or more competent than the magnetite rich rocks (Strohmayr et al, 1998).

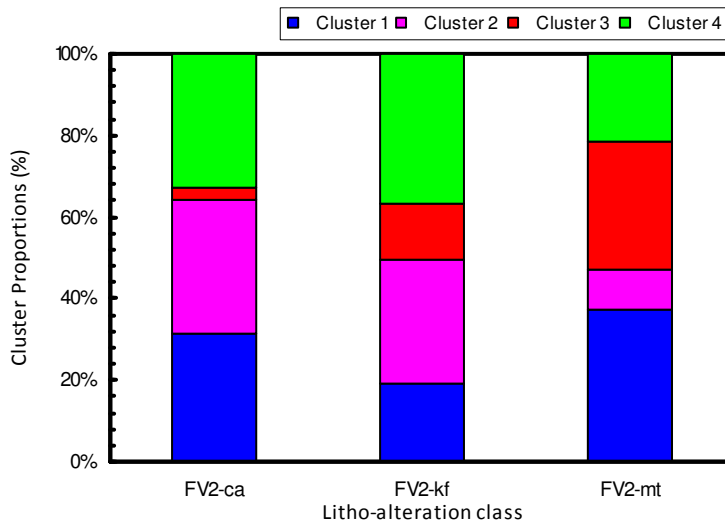


Figure 5.23. Cluster proportions for litho-alteration classes.

In order to investigate the correlation between petrophysical parameters and comminution attributes, multiple regression was applied to the 2m samples for which comminution test data existed. Comminution parameters ( $A^*b$  and  $BMWi$ ) were modeled separately for the four clusters. Averages and standard deviations of the four petrophysical properties over 2m assay intervals were considered during the multiple regression analysis. The optimal number of input parameters was selected based on stepwise regression technique (Chapter 4). The maximum number of parameters in each regression model was one fifth of the number of data after stepwise regression.

Figure 5.24a and Figure 5.24b show the predicted versus actual  $A^*b$  and estimated  $BMWi$  for each cluster. The regression model for  $BMWi$  in Cluster 1 is better than those for the other clusters. The accuracy of the model is judged according to average relative error of prediction. Table 5.4 summarizes the results of regression in each cluster. If the root mean square error is interpreted as the predictive error of the computed relationships, it can be deduced that it is possible to calculate  $BMWi$  from petrophysical properties with an accuracy of about 0.57kWh/t and 1.74kWh/t in Cluster 1 and Cluster 2 respectively. The overall  $R^2$  and RMS error values between predicted and measured  $A^*b$  are 0.63 and 27.3 respectively. The overall  $R^2$  and RMS error between predicted and measured  $BMWi$  are 0.51 and 1.39 kWh/t respectively.

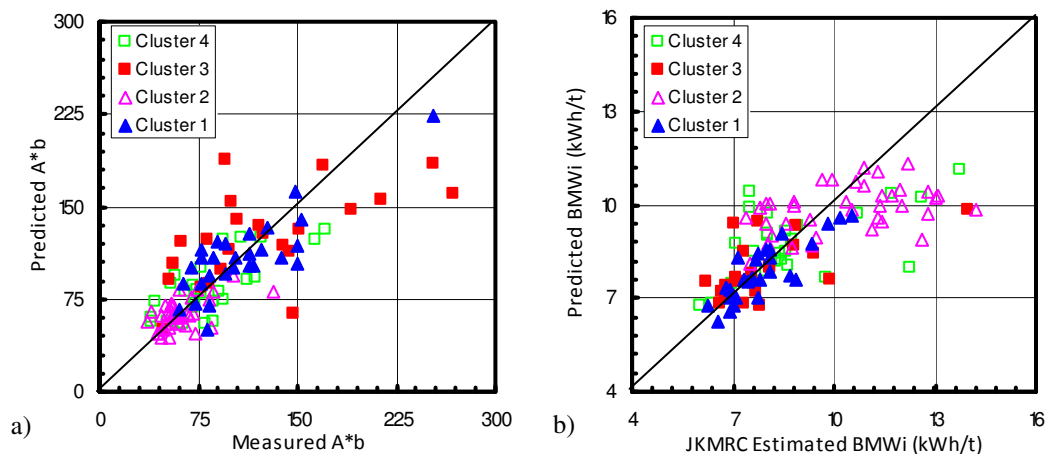


Figure 5.24. Measured versus predicted  $A^*b$  (a) and Estimated versus predicted BMWi (b) in four petrophysical clusters. Predicted values are derived from petrophysical parameters.

Comparison of  $A^*b$  between DWT and JKRBT test results for a hard ore ( $A^*b < 35$ ) suggests an uncertainty of about 7.5% for the JKRBT results (Kojovic, 2008). For softer ore samples there would be more variability, therefore the uncertainty in  $A^*b$  values would likely be even greater. Given that most of the samples from Ernest Henry are soft ( $A^*b > 30$ ), a 10% error of prediction for  $A^*b$  could reasonably be expected. Estimated BMWi carries uncertainty due to crushing index and batch grinding test results. As for  $A^*b$ , the uncertainty in estimated BMWi is greater for the softer ore samples. An uncertainty of 10% for softer ore samples (less than 10kWh/t) and 5% for harder ore samples (e.g. 15kWh/t) in estimated BMWi is assumed. Considering the uncertainty in BMWi, it is evident that the prediction accuracy of the models in Cluster 1 and Cluster 3 is better than the prediction accuracy of BMWi in other clusters.

Table 5.4. Results of multiple regression of  $A^*b$  and BMWi vs petrophysical properties for each cluster. Quality of fit indicated by average relative error of prediction (REP) in percent and root mean square error (RMSE).

Comminution Parameter	Cluster1	Cluster2	Cluster3	Cluster4
$A^*b$ (REP, RMSE)	16.71, 21.90	16.97, 14.73	30.10, 47.58	22.25, 21.89
BMWi (REP, RMSE)	6.12, 0.57	13.66, 1.74	10.79, 1.29	12.43, 1.52

Invoking the regression models for prediction of comminution attributes of all available 2m samples is justifiable if the comminution test samples are representative of the entire set of core samples. Figure 5.25 shows the comminution test samples, colored by cluster, projected onto the plane defined by the first two principal components. Comparing with Figure 5.21, it is evident that each cluster has approximately the same number of

comminution test samples with a minimum of 30 samples. Therefore, the test samples can be considered representative of the population as a whole.

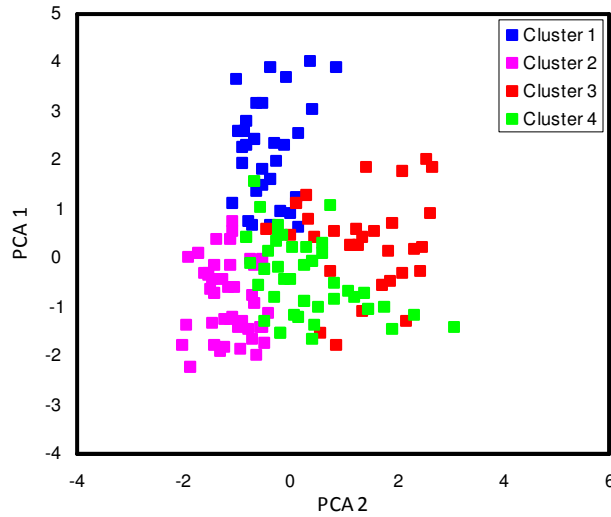


Figure 5.25. Comminution test samples (EH556, EH574, EH635, EH633, EH432 and EH446) for each cluster projected onto principal component space, c.f. Figure 5.21.

When the representivity criterion is met, the models (Figures 5.24a and 5.24b) can be applied to the entire dataset for prediction of comminution behaviour with a higher level of confidence. However in order to assess the predictability of each regression model developed within each cluster, the regression was tested for the samples of EH574 which was not initially used in model building. The overall RMS error for  $A^*b$  and  $BMWi$  are 35.2 and 1.87 kWh/t respectively. As represented in Figure 5.26 predicted values of  $BMWi$  for most samples of EH574 (except sample with  $BMWi > 10$  kWh/t) are within the range of  $BMWi$  variability while prediction of  $A^*b$  is not very accurate. Although the  $A^*b$  and  $BMWi$  models (Figure 5.24a and 5.24b) are not very accurate, however they can still characterise ore comminution variability by prediction of comminution attributes in intervals were no tests are available.

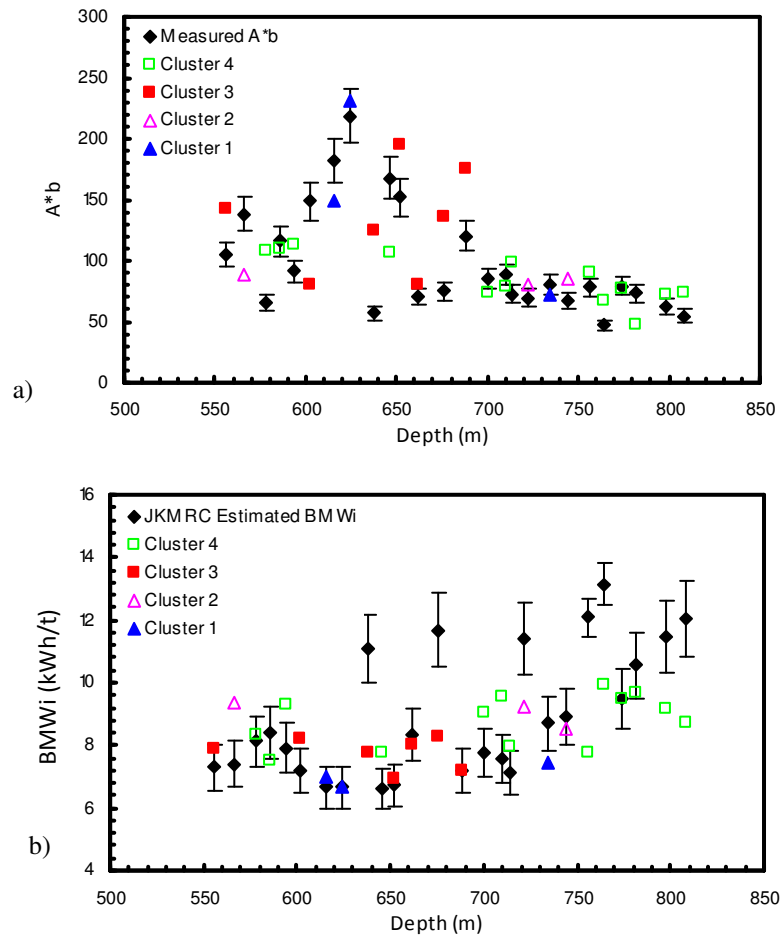


Figure 5.26. Predicted  $A^*b$  and measured  $A^*b$  (a) versus depth in four clusters for test samples of EH574 using regression model presented in Figure 5.24a and predicted Bond mill work index and JKMRC estimated Bond mill work index versus depth in four clusters for test samples of EH574 using regression model presented in Figure 5.24b.

Predicted and measured  $A^*b$  and Bond mill work index for all 2m core samples are presented in Figure 5.27a and Figure 5.27b respectively. The predictions are based on the models in Figures 5.24a and 5.24b. The predicted values lie within the range of measured values, and there is good qualitative agreement in terms of trends with depth. This suggests that the petrophysically-based prediction of comminution performance may have potential for delineating geometallurgical domains. Although the derived models appear promising for the drill holes involved, analysis of a much larger data set would be necessary in order to develop predictive models for the entire orebody.

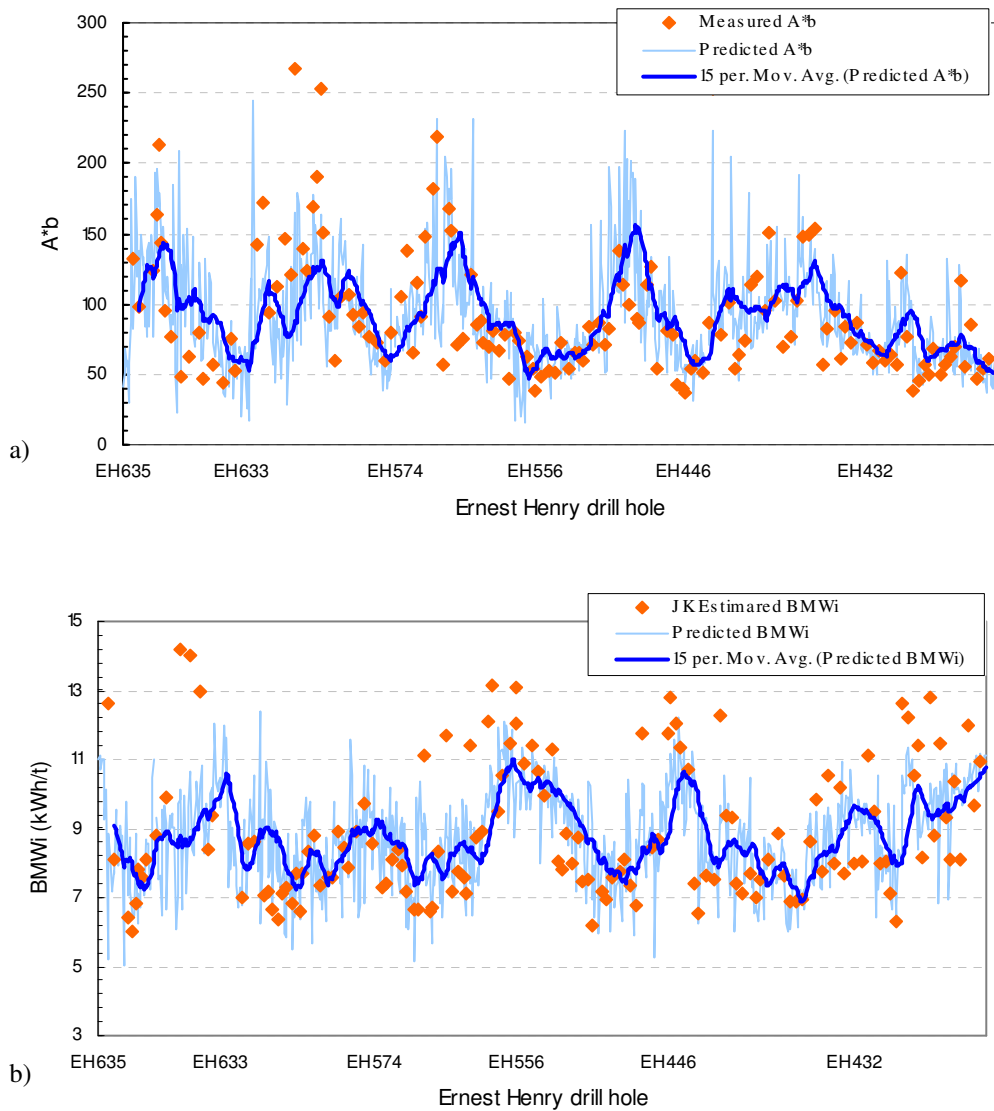


Figure 5.27. Predicted A\*b (a) and predicted BMWi (b) for the entire dataset (~800 2m intervals). The measured A\*b and JKMRc estimated BMWi are also plotted for comparison. The samples originating from each drill hole are plotted in depth order.

Given that these comminution attributes (A\*b and BMWi) can be derived from petrophysical measurements, then the mill throughput may be estimated through an alternative characterisation approach based on petrophysics. This idea has further investigated in Section 5.9.

### 5.8.3. Comminution Modelling : CC Approach

The aim of this section is to create geometallurgical classes purely based on comminution test results at Ernest Henry and then investigate the relationship between petrophysical properties and created classes. Cluster analysis techniques were used in order to create the

comminution classes objectively. Three classes based on  $A^*b$  and  $BMWi$  were defined (Figure 5.28).

Class 1 is low in  $A^*b$  and high in  $BMWi$ , i.e. both hard to crush and hard to grind, while Class 2 is comparatively easy to crush and grind. Class 3 is located between these two clusters and can be regarded as medium to crush and medium to grind. The variability of  $A^*b$  in Class 2 is approximately five times greater than the variability of  $A^*b$  in Class 1; conversely, the variability of  $BMWi$  is far greater in Class 1 than in Class 2.

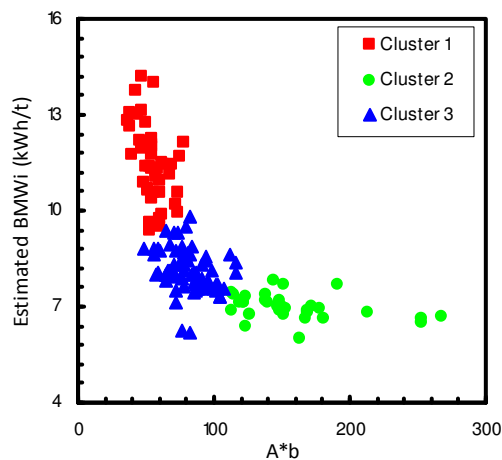


Figure 5.28. Crossplot between  $A^*b$  and Bond mill work index ( $BMWi$ ) for all 142 comminution test samples determined by cluster analysis.

Once the classes of comminution have been identified, then such classes can be characterised using petrophysical properties. The LogTrans program (Fullagar et al., 1999) was used for this purpose. Statistics (medians and spreads) for petrophysical parameters (P-wave velocity, density and susceptibility) and assay data (Cu, Fe, S, Au) in comminution classes were computed by LogTrans. All input attributes (petrophysical and assay) were used during training and testing in each individual hole. However the optimum number of input variables was selected based on the prediction performance of groups of variables in a trial and error fashion. The best suite of input parameters that predict comminution classes in control holes (EH633, EH635, EH556, EH432, and EH446) are susceptibility, P-wave velocity and Cu grade. The performance of the prediction was judged based on the number of correct test sample class assignments by LogTrans. The LogTrans result for EH633 is presented in Figure 5.29. Comminution class has been predicted continuously down the hole. As can be seen, LogTrans successfully predicted the comminution test sample classes with an overall performance

of 76% for EH633. In order to assess the prediction in a blind hole, drill hole EH574 was treated as an independent hole and training was conducted on the other five holes. Figure 5.30 shows the predicted comminution classes for the test samples from EH574 as an independent hole, using statistics based on EH633, EH635, EH556, EH432 and EH446. The performance of prediction in EH574 is reasonably poor at only 60%. The effect of errors both in Geotek data and comminution measurements could be reasons for this poor performance in addition to geological differences between drill holes. Availability of a larger dataset for training would likely further improve the performance of the prediction.

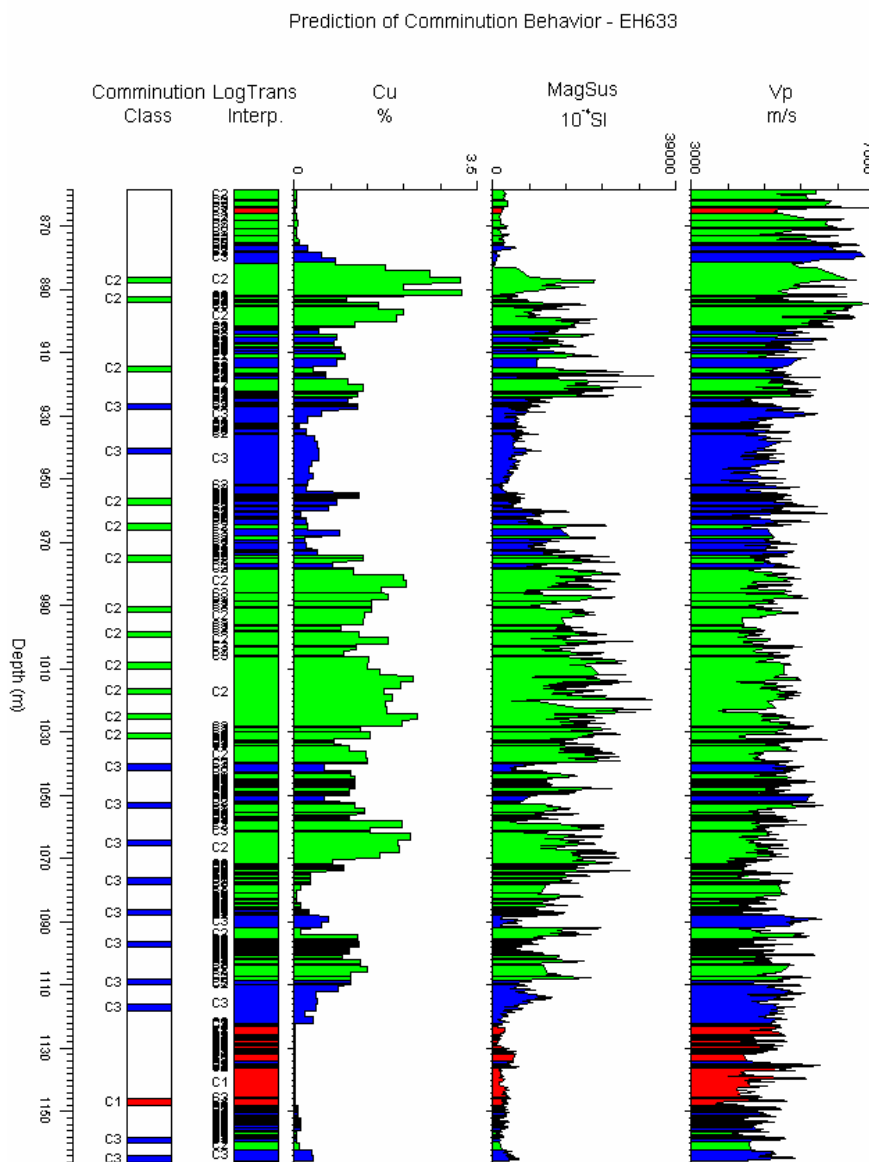


Figure 5.29. Prediction of comminution classes in control drill hole EH633 using LogTrans. First column shows the comminution classes. The second column is predicted comminution classes based on magnetic susceptibility (MagSus), P-wave velocity (Vp) and Cu grade. LogTrans window length during fluster analysis was 0.25m.

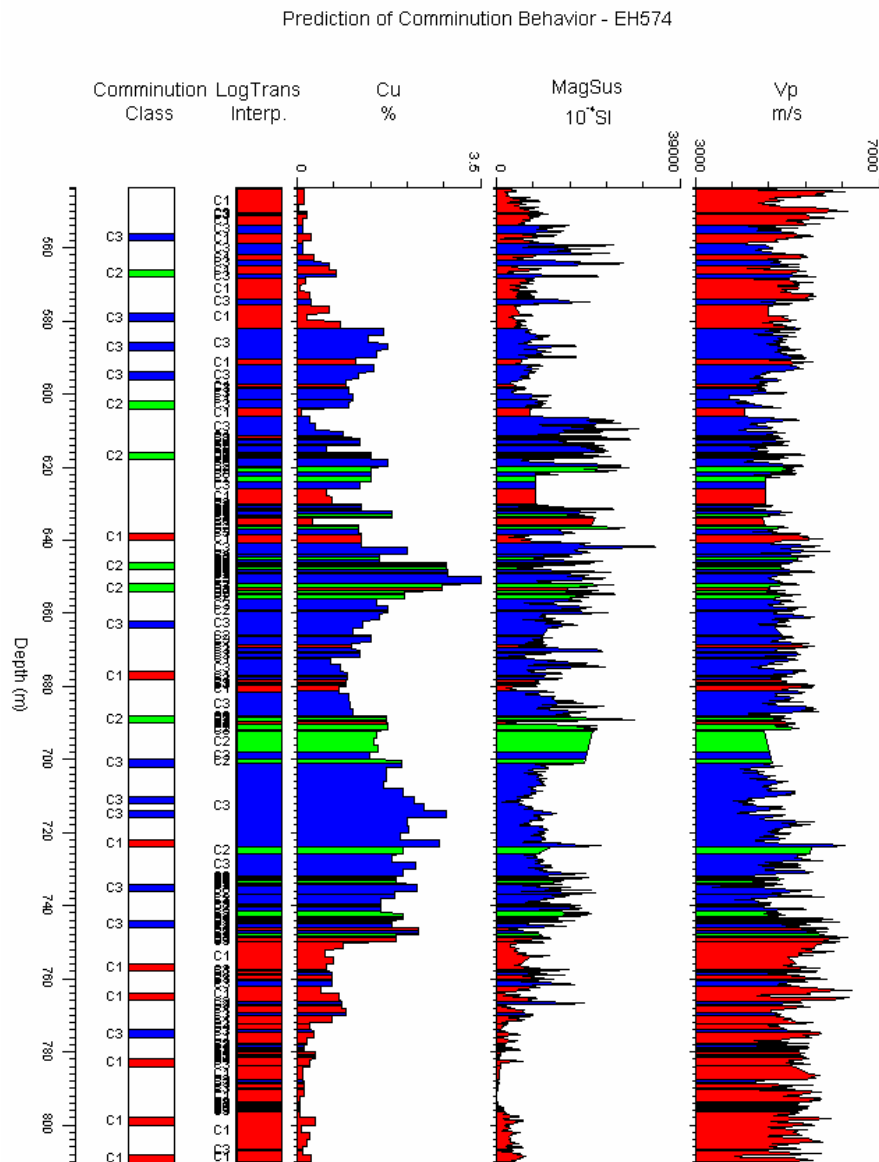


Figure 5.30. Prediction of comminution classes in independent drill hole EH574 using LogTrans. First column shows the actual comminution classes. The second column is predicted comminution classes based on magnetic susceptibility (MagSus), P-wave velocity (Vp) and Cu grade. LogTrans window length during fluster analysis was 0.25m.

A neural network structure of with three nodes in hidden layer, three input parameters (P-wave velocity, magnetic susceptibility and Cu%) and three outputs for three clusters was designed and trained. Statistica neural network software was used here in order to train, verify and test petrophysical properties for prediction of defined clusters. Neural network modelling is described in Chapter 4. The same input as used for LogTrans interpretation was used here. The number of nodes in hidden layer was defined based on performance of network when compared with other structures. Training of the network was based on

data from EH633, EH635, EH556, EH432 and EH446. The samples from EH574 were then used to assess network performance for data that was not used during training. Table 5.5 summaries the results. The “Total” number represents the number of clusters that belong to a certain cluster. The “Correct” number is the number of clusters that the network has predicted correctly and similarly the “Wrong” number is the number of incorrect predictions. The overall performance of network for testing set (EH574) can be judged based on total number of correct predictions. The prediction performance of network is 72% (18/25\*100). Neural network prediction is thus relatively better than minimum distance algorithm employed in LogTrans.

Table 5.5. Statistics of prediction performance of neural network for training data (EH635, EH633, EH432, EH446, EH556) and testing (EH574) data.

	Training			Testing		
	Cluster 1	Cluster 2	Cluster 3	Cluster 1	Cluster 2	Cluster 3
Total	34	28	59	8	6	11
Correct	28	22	30	5	3	10
Wrong	6	6	29	3	3	1
Unknown	0	0	0	0	0	0
Cluster 1	28	1	15	5	0	1
Cluster 2	1	22	14	0	3	0
Cluster 3	5	5	30	3	3	10

**5.8.4. Comminution Modelling : CPC Approach**

In this approach the classes here are defined based on petrophysical properties and comminution attributes. The rationale for this approach is that creation of classes based on combined properties may better explain the geometallurgical behaviour. In fact from a practical perspective classes that have distinctive behaviour both in terms of petrophysics and metallurgy are of interest.

An attempt was made to classify objectively all comminution test samples according to their A\*b and BMWi values and their associated petrophysical properties (density, susceptibility and velocity) using cluster analysis. A hierarchical clustering approach was used to classify the data automatically. This analysis resulted in three clusters. A radar diagram of comminution and petrophysical properties shows the composition of the clusters (Figure 5.31). Cluster 1 is high in P-wave velocity, but low in susceptibility and density. This characteristic generally corresponds with rocks that are hard in terms of crushing and grinding. Average values of A\*b (low) and BMWi (high) for Cluster 1 conform to such characteristics.

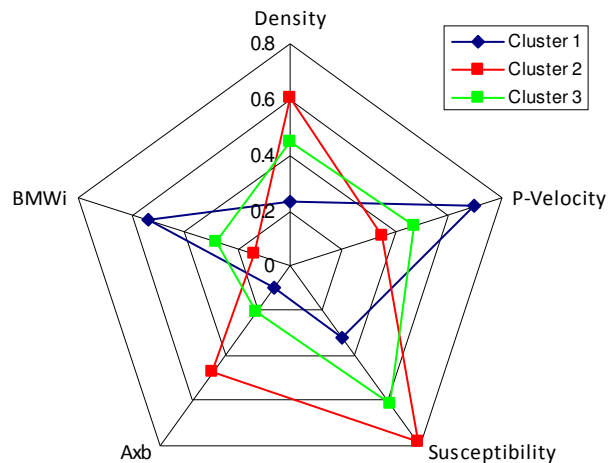


Figure 5.31. Normalized data means for clusters, three-cluster solution.

The created classes are only known for intervals of drill core where both comminution and petrophysical properties are available. It would be advantageous if such classes could be predicted for other intervals of drill cores using petrophysical properties. For this purpose a neural network was trained for the created clusters using the petrophysical properties in such a way that it could be used for prediction. The selection of the neural network technique for this purpose was due to its better performance than minimum distance algorithm presented in the previous section.

Petrophysical properties (P-velocity, density and susceptibility) and the created clusters for five drill holes (EH635, EH633, EH446, EH432 and EH556) were used for design and training of the neural network. Petrophysical properties were used as input and three created clusters as output of the network. After training and testing of the neural network, the data from EH574 were used to assess the network prediction performance. During network design data from five drill holes were randomly assigned by the software into training and verification datasets. Ten different neural network structures were tested. A network structure with 14 nodes in the hidden layer performed better than other structures. The performance of the neural network for each dataset is represented in Table 5.6. The performance of the network in prediction of clusters for the training and verification datasets are 86% and of 93% respectively. Test data for EH574 shows prediction performance of 76%. This was not a significant improvement compared with MC approach (Section 5.8.3).

Table 5.6 Statistics of prediction performance of neural network for three sets of data, training set (black), validation (blue) and testing (red).

	Training			Verification			Testing		
	Cluster 1	Cluster 2	Cluster 3	Cluster 1	Cluster 2	Cluster 3	Cluster 1	Cluster 2	Cluster 3
Total	45	22	40	5	5	5	10	7	8
Correct	36	21	35	5	4	5	8	4	7
Wrong	9	1	5	0	1	0	2	3	1
Unknown	0	0	0	0	0	0	0	0	0
Cluster 1	36	0	4	5	0	0	8	0	1
Cluster 2	1	21	1	0	4	0	0	4	0
Cluster 3	8	1	35	0	1	5	2	3	7

### 5.9. Mill Throughput Modelling

Cu head grade at Ernest Henry Mine is regarded as a good indicator of expected mill throughput (Tew et al, 2003). Comminution attributes can be used for prediction of mill performance (Bearman et al, 1996). However, for the 142 small scale test samples a polynomial regression of Cu with an order of four against both A\*b and BMWi showed a very poor correlation. The use of four terms in the regression was only for comparison with models based on four petrophysical properties (Figures 5.19a and 5.19b). The predicted versus measured A\*b and estimated BMWi using Cu is represented in Figure 5.32a and Figure 5.32b respectively. The relative error of prediction (REP) values for A\*b and BMWi after regression against Cu% are 34% and 16% respectively. Comparison of models (Figure 5.32a with Figure 5.19a and Figure 5.32b with Figure 5.19b) suggest that petrophysical properties are more sensitive to underlying rock properties than Cu% alone. Thus development of comminution models based on petrophysical properties could be more reliable at Ernest Henry than models based on assays alone (Vatandoost et al, 2009).

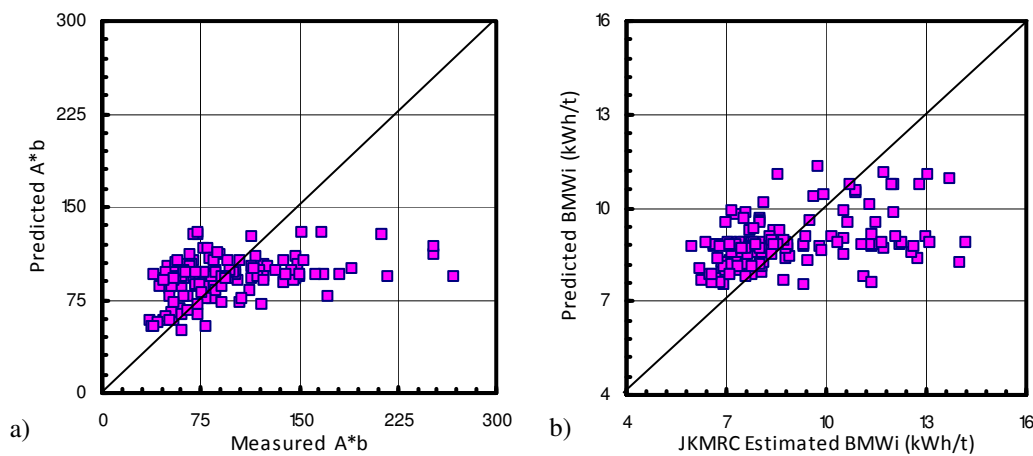


Figure 5.32. Measured versus predicted A\*b (a) and Estimated versus predicted BMWi (b) for all 142 test samples derived from a 4<sup>th</sup> order polynomial regression of Cu%.

The Ernest Henry mill throughput can be estimated using a set of engineering equations (GeM model) developed by Kojovic (2008) from 28 operating mills (closed and open circuit), covering a range of diameters, lengths, speeds, ball loads, grate designs, ore characteristics and feed size distributions. These models are similar to the models developed by Morrell (2004) for scale-up, design and optimisation. The equations have the form:

$$SP(\text{kWh/t}) = f'(F80, P80, SG, DWSP, BMWi, BL, CS, D, D/L) \quad (5.3)$$

$$P80 = f''(SP, F80, SG, DWSP, BMWi, BL, CS, D, D/L) \quad (5.4)$$

where

SP = AG/SAG specific power required for given set of operating conditions

F80 = SAG mill feed 80% passing size

P80 = SAG Mill product 80% passing size (or transfer size)

SG = ore specific gravity

DWSP = Drop Weight specific power required to break feed to transfer size, which is dependent on ore A and b parameters, feed size distribution and transfer size.

BW<sub>mi</sub> = Bond ball mill grindability index

BL = ball charge (%)

CS = mill speed (% of critical)

D = mill diameter

D/L = aspect ratio = mill diameter/mill length (EGL)

In comparison, the mill throughput model currently used by Ernest Henry is based solely on Cu headgrade developed using historical data on shift assays and actual throughput. Figure 5.33, compares the mill throughput prediction for the 142 GeM 2m core intervals using the mine site (EH) model based on Cu% head grade and GeM model based on A\*b, estimated BMW<sub>mi</sub> and ore density (measured by the Geotek MSCL).

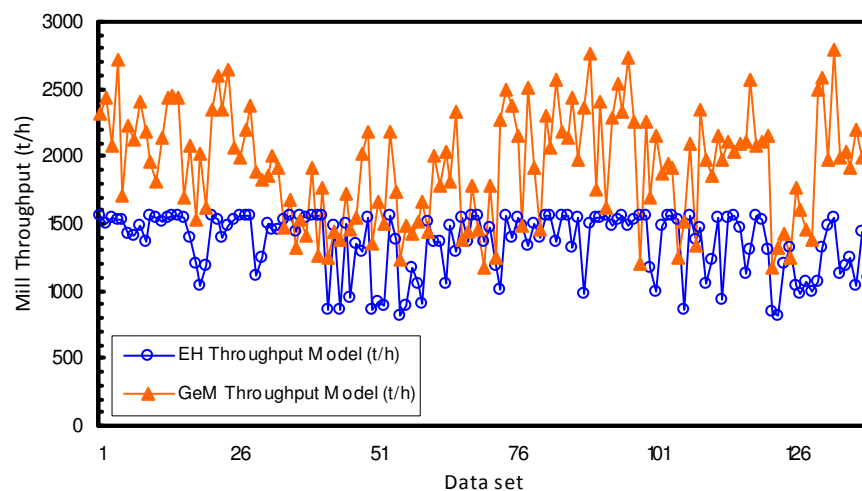


Figure 5.33. Comparison of throughput predictions for 142 GeM 2m samples. The current mine site (EH) model is based on Cu-grade; the GeM model is based on actual A\*b, estimated BMW<sub>mi</sub> and gamma density.

The GeM estimated throughput is based on the existing Ernest Henry circuit (Figure 5.34), consisting of an open circuit Semi Autogeneous (SAG) mill (34 ft x 16.5 ft, 11MW installed power) followed by a closed-circuit Ball mill (20 ft x 27.5 ft, 5.5MW installed power). The GeM throughput estimates were based on a fixed target grind size ( $P_{80}$ ) of 220 microns and fixed feed size ( $F_{80}$ ) of 93mm.

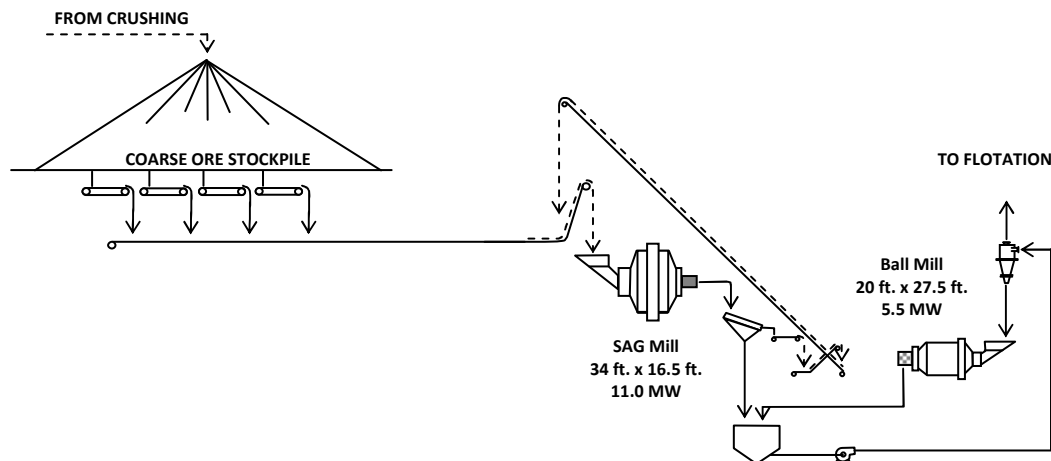


Figure 5.34. Schematic diagram of Ernest Henry comminution circuit (Kojovic, 2008)

As can be seen (Figure 5.33), there is a clear difference in throughput estimation between the EH and GeM models. The GeM model is more sensitive than the current Ernest Henry throughput model, which is limited to a maximum of approximately 1575 tons per hour (t/h). This limit is consistent with the physical capacity of the cyclone feed pumps in the ball mill circuit (Peaty, 2008). As the assay range used in the EH model development was 0.6 to 1.5% Cu, the accuracy of the EH model for lower grade samples included in the GeM study is questionable. To provide a more realistic comparison of the two models, the GeM intervals were filtered to only include the samples which conform to the typical assay range and ore hardness measured in previous studies. The comparison using the remaining 12 intervals, shown in Figure 5.35, suggests the two models are broadly consistent (relative error of  $\sim 7\%$ ), and indicates the GeM model based on the comminution parameters is valid. If the comminution attributes (i.e.  $A*b$  and  $BMWi$ ) or comminution classes can be derived from petrophysical measurements, then the mill throughput can be estimated through an alternative characterisation approach based on petrophysics.

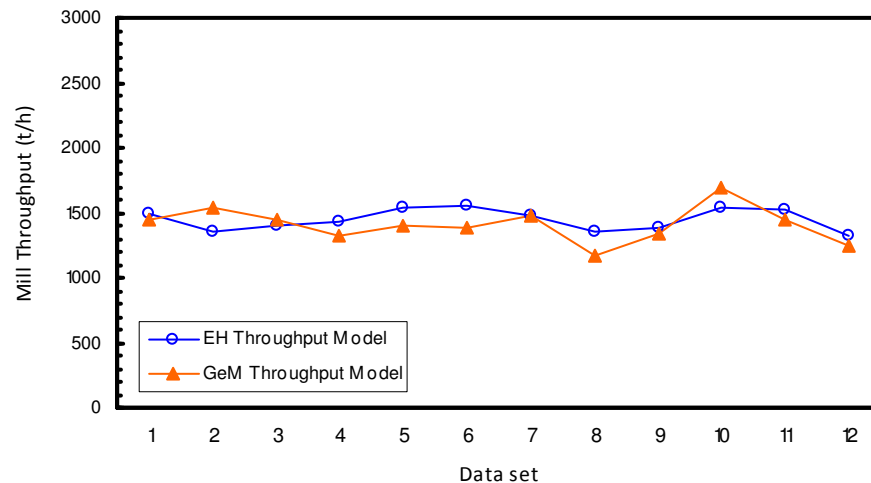


Figure 5.35. Comparison of throughput predictions for subset of GeM 2m samples. The current EH model is based on Cu-grade; the GeM model is based on actual A\*b, estimated BMWi and gamma density. Only samples which conform to the typical assay range and ore hardness have been included.

In order to visualise throughput variability with depth in the drill holes, predicted throughput for all 2m core samples are plotted in depth order in each drill hole in Figure 5.36. Throughput predictions were generated in the same fashion, based on the existing Ernest Henry SAB (SAG and Ball mill) circuit. Mill throughput was predicted from A\*b, estimated Bond mill work index, and ore density (measured by the Geotek logger). The estimates were based on an assumed fixed target grind size ( $P_{80}$ ) of 220 microns and fixed feed size ( $F_{80}$ ) of 93mm.

From examination of the figure, low throughput is expected in the upper part of EH556, but throughput increases with depth most probably due to magnetite mineralization which renders the samples soft to crush and easy to grind. The same trend is evident in EH446. The throughput in EH432 is expected to decrease in deeper parts of the borehole. Predicted throughput is almost constant in EH633 and EH574.

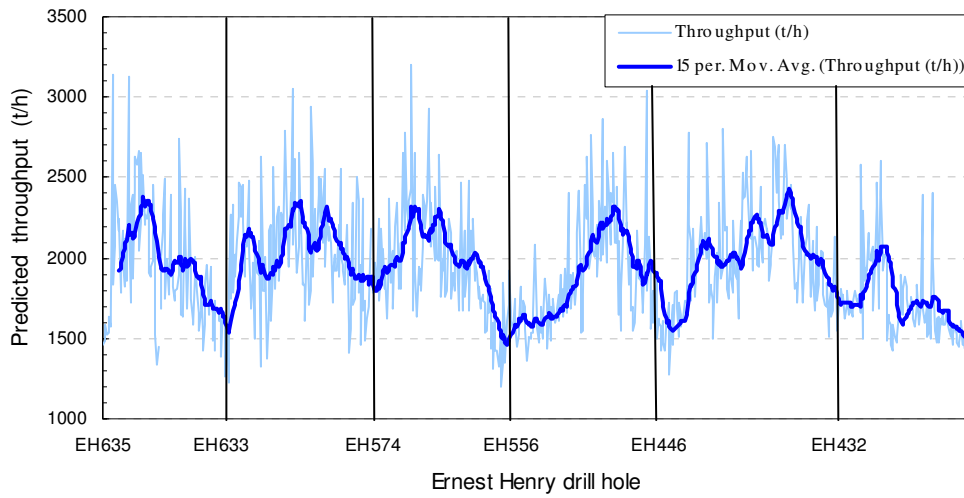


Figure 5.36. Predicted mill throughput for a larger dataset. The blocks of samples originating from each drill hole are plotted in increasing depth order.

In practice the materials transported to the processing plant are from ore blocks extracted after blasting, not from the individual drill holes. This means that a mixture of materials as a result of blasting should be treated in the processing plant. Thus the throughput prediction presented in Figure 5.36 is an illustration of how petrophysics can predict mill throughput behaviour but actual mill performance will be affected by material mixing.

An effective approach for optimization of grinding circuit of Collahuasi Cu-Mo porphyry mine, Chile is documented by Alruiz et al (2009). Their approach for representation of mill throughput variability within geometallurgical classes is adopted here. Separate throughput predictions for the each drill hole were generated. The results are summarized in Figure 5.37. The drill holes here are assumed as a proxy to mineable volumes (mining blocks) and the four petrophysical clusters (Section 5.8.2) representing different ore types with certain comminution ( $A*b$ , BMWi, and TPH) characteristics. As represented in Figure 5.37, throughput for almost all holes (except EH432) varies over a small range from 1860t/h to 1950 t/h. The EH432 composite is associated with a low throughput mainly because Cluster 2 (which is very hard in terms of crushing and grinding) accounts for the highest proportion. In order to reduce the mill throughput variability it might be useful to blend materials of clusters appropriately before processing. For example a small proportion of materials from Cluster 2 from drill hole EH432 should be mixed with high proportion of materials from Cluster 1. This illustration, although based on drill holes could be used as an effective approach for plant optimization.

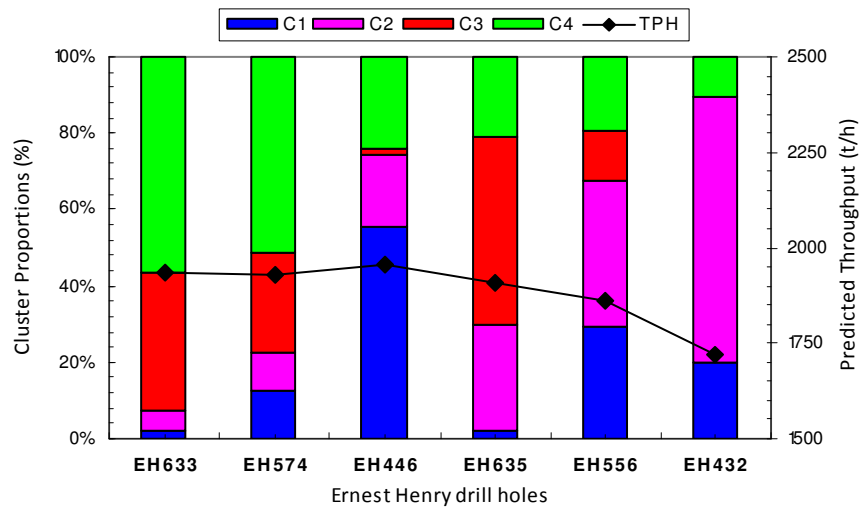


Figure 5.37. Mill throughput estimate for clusters defined using PC approach (section 5.8.2). The drill holes are sorted according to proportion of Cluster 2 (C2) which is relatively hard material. As the proportion of C2 increases, the estimated mill throughput decreases.

### 5.10. Concluding Remarks

A Geotek multi-sensor core logger has been used to measure density, susceptibility, P-wave velocity, and P-wave amplitude of drill core from six Ernest Henry holes. A total of 1800m of petrophysical data at 9cm intervals and high resolution imagery were recorded using the procedures described in Chapter 3. After processing, the petrophysical data were averaged over 2m assay intervals in order to correlate with comminution attributes measured on a subset of assay intervals.

The quality of the Geotek logger data from Ernest Henry with respect to both accuracy and repeatability was satisfactory. The main determinant of data quality is the size of the core. Variability in the “feed material” for the logger translates into greater uncertainty in the petrophysical data. All of the material presented to the logger from Ernest Henry was NQ-size half-core; this size is marginal for obtaining reliable velocity, density and susceptibility determinations. In addition, the cutting of the core was imperfect over many intervals, with the result that the logger was commonly measuring wedges of core, rather than half-core of consistent size.

Magnetite alteration is associated with high susceptibility and density due to abundance of magnetite. As copper enrichment is spatially related to magnetite alteration, elevated susceptibility can be a good indicator of high grade Cu zones. Overall the susceptibility ranges from less than 0.1 SI to more than 4 SI (massive magnetite). Density also exhibited a wide range, varying from 2.7 to 4.3 g/cc. Density and susceptibility showed a

good correlation with copper and gold assays in all holes. However the relationship is not sufficiently accurate to be used for routine prediction of copper and gold grades.

The relationship between petrophysical properties and comminution attributes at Ernest Henry has been investigated. Generally a positive correlation exists between susceptibility and  $A^*b$ , while a negative correlation between susceptibility and  $BMWi$  is evident. The magnetite acts as crack initiator and renders the rocks soft in terms of crush and grind. Therefore the higher the magnetite content, the higher the susceptibility and the softer the rock for crushing i.e. high  $A^*b$ . Density is also positively correlated with  $A^*b$  and negatively correlated with  $BMWi$ . The correlations between P-wave velocity and comminution attributes ( $A^*b$  and  $BMWi$ ) were weak except in some localized intervals of drill holes.

Although the global models for comminution attributes ( $A^*b$  and  $BMWi$ ) based on multiple regression of petrophysical properties (i.e. density, susceptibility, P-velocity and P-amplitude) are not very accurate, they are potentially better than the models based purely on Cu grade alone. Comparison of these models provided a degree of confidence in estimation of mill throughput from petrophysical properties.

Comminution modeling based on the petrophysical classification (PC) approach provided a means for “quantitative” prediction of comminution attributes and subsequently characterisation of mill throughput performance. Comminution modeling based on comminution classes (CC) or integration of petrophysical and comminution classes (CPC) provides a “qualitative” prediction of comminution behaviour and can be used as an alternative approach to petrophysical classification (PC).

The Ernest Henry mill throughput was estimated using a set of engineering equations developed from 28 operating mills (closed and open circuit), covering a range of diameters, lengths, speeds, ball loads, grate designs, ore characteristics and feed size distributions. The validity of GeM throughput model was assessed based on subset of samples available in GeM database which represented the typical ore hardness and Cu assay range at Ernest Henry. Comparison of Ernest Henry throughput model with GeM throughput model for a wide range of data showed that GeM throughput model is more sensitive to comminution properties (i.e.  $A^*b$  and  $BMWi$ ). This showed that GeM throughput model can be useful for better prediction of mill performance at Ernest Henry. Throughput prediction based on petrophysical properties showed a clear variation in terms of trend with depth. Therefore, mill throughput can also be estimated from

petrophysical properties. Moreover petrophysical classes represent a potential application for mill throughput optimization based on selective treatment of petrophysical clusters.

Automated prediction of comminution behaviour at Ernest Henry derived using minimum distance classification approach (LogTrans) and neural networks technique was also presented. The results suggest that neural network has better performance (72%) in prediction of comminution behaviour than the minimum distance algorithm (60%). An integrated approach for comminution class definition and model development also tested. In order to improve the prediction performance of comminution behaviour in independent holes using either technique, more control holes would be advantageous in the training set.

Geological logging for the selected Ernest Henry drill holes is not entirely consistent particularly for alteration assemblages. This uncertainty has retarded investigation of the relationship between petrophysical properties and geological observations. Measurement of magnetic susceptibility along the sections of drill core could significantly assist geologists during visual core logging. Availability of petrophysical parameters could significantly enhance the reliability of geological classification and hence geometallurgical characterisation.

Only four petrophysical parameters were recorded at Ernest Henry. Additional parameters, e.g. natural gamma activity, could be very useful for discrimination of alteration style (e.g. potassic alteration). Hence natural gamma has the potential to be used as a proxy for characterisation of comminution behaviour at Ernest Henry.



# CHAPTER 6

---

## Characterization of Comminution Behavior at Cadia East Au-Cu Porphyry Deposit

### 6.1. Introduction

The Cadia East deposit is a porphyry Au-Cu system characterized by large tonnage and low grade of ore. The Cadia district is located near Orange, New South Wales, Australia and is a host of many Au-Cu porphyry systems (e.g. Ridgeway, Cadia East). The Cadia East deposit is one of the world's largest gold deposits and has a resource of 2,347Mt containing 33.2Moz of Au and 6.59Mt of Cu (Newcrest, 2010). The mineralized system is about 600m wide and extends 1900m below surface. The mining operation at Cadia East was initially planned as a large open pit but the decision has recently been made to mine the resource as an underground panel caving operation with an expected mine life of at least 30 years (Newcrest, 2010). The mining lease is currently owned and operated by Newcrest Mining Ltd.

The ore characteristics (e.g. hardness and copper grade) of Cadia East are different from the currently mined Cadia Hill deposit (Clement, 2004) and this introduces a challenge for processing of ores at Cadia Hill processing plant. Cadia East ore is clearly recognized as hard material in terms of both crushing and grinding and is harder than Cadia Hill ore (Clement, 2004). Newcrest Mining has investigated the possibilities for Cadia East ore treatment and has planned to process Cadia East ore at the Cadia Hill processing plant. Clearly introduction of new feed material may necessitate optimization of the current plant configuration at Cadia Hill. Hence the existing Cadia Hill processing plant will be upgraded and the ore processing rate will be increased from the existing 24Mtpa rate to approximately 26Mtpa (Newcrest, 2010).

Comparison of ore comminution behavior (Figure 6.1) indicates that ore grindability at Cadia East is much harder ( $BMWi > 14$  kWh/t) than Ernest Henry. Ore grinding behavior at Ernest Henry is regarded as soft to medium hard (Chapter 5) whereas Cadia East material is very hard to grind. Moreover  $A^*b$  values at Cadia East indicate a very hard ore in terms of crushing with a small dynamic range of variability. Thus design of processing plant and effective selection of comminution equipment at Cadia East is a real challenge. Given that in the underground operation it is planned to process of ~26Mtpa of

ore at Cadia Hill processing facilities, effective characterization of comminution behavior at Cadia East is highly desirable.

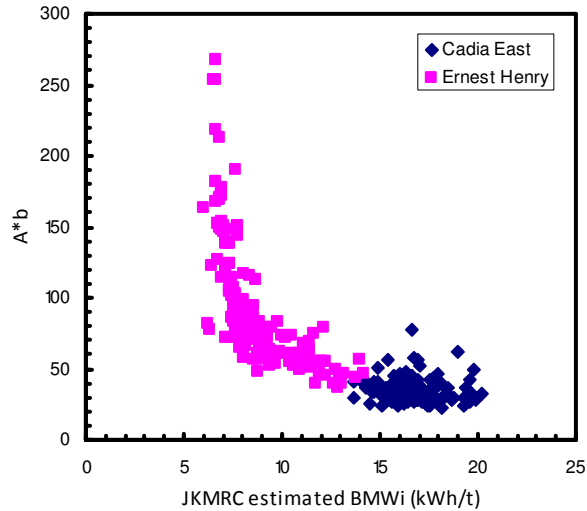


Figure 6.1. Scatter plot of  $A^*b$  versus  $BMW_i$  for Cadia East and Ernest Henry data.

It is not the intent of this thesis to investigate the characteristics and configuration of the processing circuit but rather to characterize the ore processing behaviour effectively using petrophysical properties. In particular, the challenge for this research is to investigate whether petrophysical properties can serve as proxies for comminution attributes and hence assist in improved modelling of comminution variables. Cadia East was the first study site in the AMIRA P843 Project. As such it played a key role in method development and establishing protocols for petrophysical core logging and petrophysical characterization within the context of this research.

The Geotek MSCL system was used to measure petrophysical properties on five drill cores from the Cadia East deposit in an attempt to characterise the rock type, alteration style and ultimately the ore processing performance. Gamma density, magnetic susceptibility, P-wave velocity and its amplitude were measured along each length of (both NQ and HQ) half core. High resolution core imagery was also recorded simultaneously with petrophysical measurements. The merging of petrophysical data from successive core sections then provided virtually continuous logs of core properties. The core logs provide a basis for research into the relationships between petrophysical and metallurgical parameters.

Small scale comminution tests ( $A^*b$  and estimated  $BMWi$ ) were performed on selected 2m Cadia East drill core intervals at JKMRC (Julius Kruttschnitt Mineral Research Centre, University of Queensland) after petrophysical data acquisition. These tests provided an opportunity to investigate directly the correlation between petrophysical properties and comminution attributes on the same core sections.

This chapter is divided into ten sections. Section two presents briefly the geology of Cadia East deposit. It is followed by a summary of data collection from the five selected drill holes selected at Cadia East for the AMIRA P843 project. Petrophysical data processing and discussion on quality of data are discussed in sections four and five respectively. Petrophysical data interpretations for each drill hole and combined drill holes are presented in section six and seven respectively. The relationship between petrophysical properties and corresponding small-scale comminution test results is investigated in section eight. A neural network approach for prediction of  $A^*b$  from petrophysical properties is presented in this section. Then four different methods for geometallurgical class definition for comminution modeling are tested. Mill throughput modeling at Cadia East is presented in section nine. Also a strategy for approaching optimization of mill throughput is illustrated in this section followed by a summary and conclusion for this case study in section ten.

## 6.2. Geology of Cadia East Deposit

Detailed geological descriptions of the Cadia East ore-body have been documented by many researchers (Wilson, 2003; Kitto, 2005; Finn, 2006). The Cadia East ore is mainly developed within a sequence of volcanoclastic conglomerates and sandstones interspersed with massive volcanic flows. Monzonite porphyries are only developed towards the base of the system. The volcanoclastics are a very distinctive rock type with highly variable textures. Gold mineralisation is localized around a core of steeply-dipping sheeted quartz-calcite veins within an envelope of disseminated chalcopryrite, bornite, and pyrite (Holliday et al., 2002).

Porphyry deposits of the Cadia district are characterised by well developed potassic and propylitic alteration assemblages (Newcrest, 1998). Potassic alteration is associated with high grade porphyry gold copper mineralization (Wilson, 2003). Propylitic alteration overprints the core potassic alteration and the mineralization in all porphyry deposits in the Cadia district. The dominant gangue mineralogy at Cadia East is controlled by various

alteration stages and assemblages (Wilson, 2003). The main alteration stages are sodic (albite), potassic (magnetite-orthoclase-biotite), inner and outer propylitic (albite-actinolite-chlorite/biotite) and phyllic (Illite-muscovite-feldspar-pyrite). The dominant sulphide minerals are chalcopyrite, bornite, and molybdenite. Gold occurs as electrum or pure gold (Wilson, 2003).

The two major rock types recognized within the five selected holes at Cadia East are volcaniclastics (logging codes: G, B, V, Vc and U) and porphyry (logging codes: E, F, Pf, M and P). The diversity of lithological codes for these rock units suggests that visual core logging is often highly subjective. Volcaniclastics at Cadia East are characterised by rocks ranging from coarse conglomerate (G) to bedded sediments (B). The porphyry units comprise a range of intrusive rocks (e.g. dykes and stocks) including monzonite that appear in the lower part of the ore system. A phenocrystic texture is distinctive of the porphyritic rocks. The six alteration classes, as logged by Cadia East geologists, are inner propylitic (Pi), skarn peripheral (Sp), phyllic cap (Pc), albite pyrite/sodic (Ap), transitional sodic-propylitic alteration (Tr) and pervasive potassic alteration (Kp). Figure 6.2 represents a selection of MSCL drill core images that illustrate the different alteration styles at Cadia East.

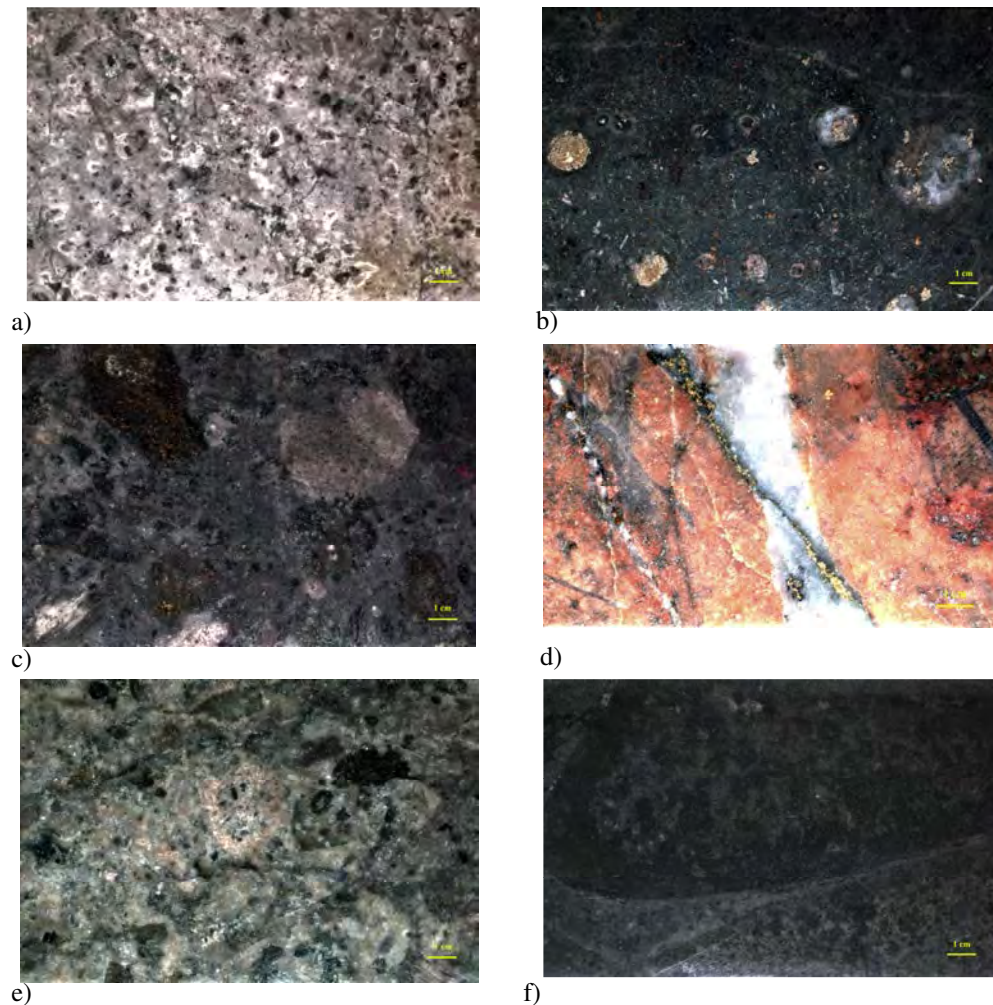


Figure 6.2. Images of drill cores from Cadia East captured using MSCL system. Volcaniclastic with phyllic alteration from drill hole CE082 - depth 150m (a), Volcaniclastic with propylitic alteration from drill hole CE082 at depth 195m (b), volcaniclastic with transitional sodic propylitic alteration from drill hole CE098 depth 245m (c), Monzonite porphyry with intense potassic alteration CE143 depth 1420m (d), Volcaniclastic with albite pyrite alteration from CE109 depth 338 (e) and volcaniclastic with skarn porphyry alteration from CE098 depth 368m (f).

### 6.3. Data Collection Summary

Due to the size and geometry of the Cadia East system no single drill hole penetrates the entire mineralised system or all of the alteration types. Cadia East site personnel identified five drill holes that intersect the range of associations and lithologies considered to be important. Four drill holes were from the upper section of Cadia East (CE082, CE098, CE109 and CE110) and one drill hole (CE143) was from the lower portion of the deposit. The location of the selected holes relative to the main mineralisation zones is indicated in Figure 6.3.

The Geotek MSCL system was deployed at the Cadia East site. Petrophysical data were collected with the MSCL system at 9cm intervals along selected mineralized intervals of drill core from the five boreholes. Core images were also captured along these sections. Altogether 1442m of core (half-NQ or half-HQ size) from these boreholes were logged at Cadia East.

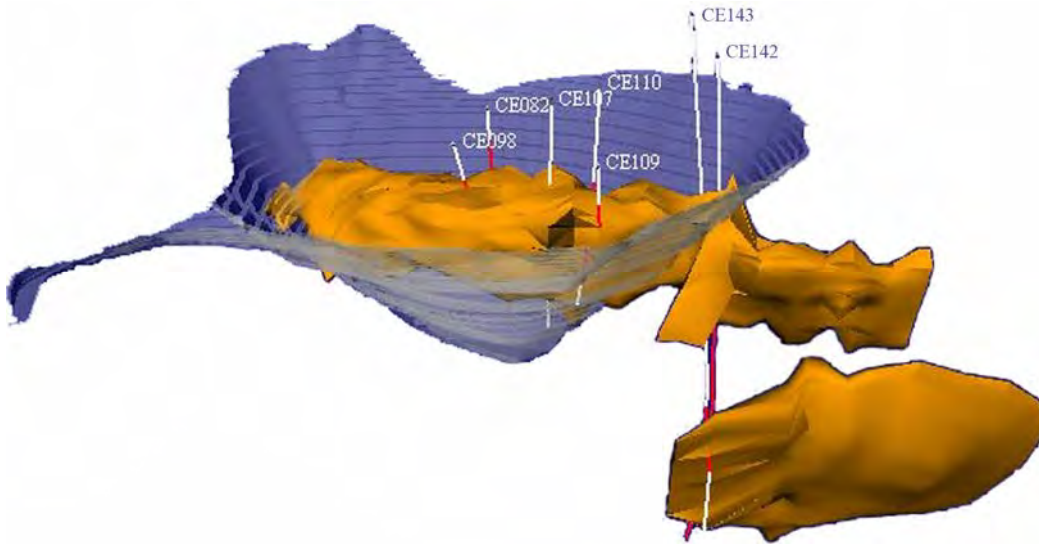


Figure 6.3. Isometric view of Cadia East showing the previously proposed open pit (blue), selected drill holes and their relationship to upper disseminated Cu zone and the lower veined Cu zone. Modified after Walters (2008).

In order to calibrate petrophysical properties directly against crushability and grindability, small scale comminution tests were conducted on a subset of the Cadia East drill cores at JKMR. Selection of samples for physical testing was conducted based on integration of core logging and existing geological data within the GeM project. There were no processing attributes available to help in sample selection, therefore a spatially and geologically representative spread of samples was selected. In each drill hole a series of 2m assay intervals at a nominal spacing of 10-15m downhole was selected.

A total of 148 small scale tests were performed on 2m core intervals of half NQ or HQ core, corresponding to assay splits. In some cases, depending on sample mass, two adjacent assay intervals were sampled. The comminution index (JKCi), batch grind ball mill operating work index (WI-5), and impact hardness ( $A*b$ ) derived from the JKRBT were measured. These quantities have been described in Chapter 2. The batch operating work index measurements and comminution index test results were used to estimate the Bond Ball Mill work index (BMW<sub>i</sub>) for each 2m interval. The selected target grind size

(P<sub>80</sub>) was 150 $\mu$ m. The large number of small-scale comminution tests conducted on drill cores from Cadia East during the P843 project provided a means for comminution characterization of the orebody.

#### 6.4. Quality of Petrophysical Data

As discussed in Chapter 3, the Geotek laser can measure thickness with a precision of 0.01mm, but in production mode core logging of half-core the achievable accuracy in thickness is about  $\pm 0.2$ mm. The Cadia East NQ half-cores are about 2.2cm thick, so an error of  $\pm 0.2$ mm translates to a relative error of about  $\pm 1\%$ . The Cadia East HQ half-cores are about 3cm thick, so an error of  $\pm 0.2$ mm translates to a relative error of about  $\pm 0.6\%$ . Error in the core thickness propagates to density, susceptibility and P-wave velocity measurements. Therefore, when the accuracy in core thickness is affected, the quality of all the Geotek logging data is also affected.

The intrinsic sensitivity of the Geotek gamma density system is approximately  $\pm 0.01$  g/cc, or  $\pm 0.35\%$  for Cadia East densities of 2.80 g/cc. When errors in thickness for half NQ size core are also taken into account, the best-practice achievable accuracy for half NQ core is about  $\pm 1.35\%$ , i.e.  $\pm 0.04$  g/cc for Cadia East half NQ size core.

For P-wave velocity measurements of half-core with the Geotek MSCL, the signal must travel through the plastic core boat and silicon gel as well as the rock itself. In addition, the Geotek transducer system introduces a delay. The intrinsic delay of the P-wave system has been established by comparing Geotek travel times with times recorded independently by a Portable Ultrasonic Non-destructive Digital Indicating Tester (Pundit) model 6 (Chapter 3).

Different plastic core boats were used for HQ and NQ core. The net delay for HQ half-core (radius approximately 3.0cm) and NQ half-core (radius approximately 2.2cm) measurements was 16.2  $\mu$ s and 16.0  $\mu$ s respectively.

In production logging, P-wave travel times for NQ half-core are inherently unreliable for several reasons:

- (i) the short path, hence small travel time, through the rock means that small absolute errors represent large relative errors;
- (ii) the core boats are narrow and do not always track truly along the rails of the Geotek system;
- (iii) the variation in thickness of lubricant (sonic gel) introduces an added uncertainty

- (iv) the sonic gel increases the likelihood of relative movement of core with respect to core boat, at right angles to the rails, i.e., the core boat can slide around the core as pressure is applied by the ram.

Given the small radius of the NQ size half core (~2.2cm) and the high velocities at Cadia East (average of ~5000m/s), the net delay is much larger than the actual transit time of interest (~4.4  $\mu$ s). The intrinsic sensitivity of the Geotek transducers system is approximately  $\pm 0.1 \mu$ s, or  $\pm 2\%$  for Cadia East velocities. When error in thickness is also taken into account, the achievable velocity accuracy for half NQ core is about  $\pm 3\%$ , i.e.  $\pm 165$  m/s for Cadia East NQ half-core. Therefore, achieving high P-wave velocity accuracy in production logging on NQ half-core is problematic.

### 6.5. Petrophysical Data Processing

In order to identify relationships between petrophysical data collected by the Geotek logger and comminution attributes, median values of petrophysical data over comminution test intervals were calculated in the same manner as described in Section 5.4.

After data reduction and processing, the petrophysical data were integrated with geological (lithology and alteration), geotechnical (RQD, fracture frequency) and assay (Au, Cu, S and Fe) data. Composite plots were generated, as discussed in Section 6.6 below. Shear wave velocity was estimated from P-wave velocity and density using Christensen's Equation (Entwisle and McCann, 1990). Dynamic Young's modulus is estimated from P-wave modulus, as presented in Chapter 2.

## 6.6. Petrophysical Data Interpretation

To investigate the relationships between petrophysical properties and metallurgical attributes, two meter medians of petrophysical properties for each drill hole at Cadia East were computed over assay intervals. Geological, geochemical, petrophysical, geotechnical and comminution data in each drill hole have been plotted as strip logs using Logview (Geological Survey of Canada) software. All variables in the strip logs for all drill holes have been plotted at the same scale for ease of comparison of variables between drill holes.

This section is divided into five subsections. Each subsection aims at exploring the relationship between petrophysical and comminution attributes for a specific drill hole at Cadia East. Geological and alteration codes appearing in the composite strip logs are defined in Table 6.1; petrophysical and comminution parameters are defined in Table 6.2.

Table 6.1. Listing of definitions for key geological parameters

<b>Lithology Code</b>	<b>Rock description</b>
E	Porphyry pyroxene feldspar
F	Porphyry feldspar
Pf	Porphyry
M	Porphyry monzonite
P	Porphyry pyroxene
G	Volcaniclastics - conglomerate
B	Volcaniclastics - bedded
V	Volcaniclastics - massive
Vc	Volcaniclastics
U	Volcaniclastics - angular
Fb	Fault breccia
Fc	Fault cataclasite
Ft	Fault - structure
Fv	Fault vein
Bx	Breccia
A	Altered not identifiable
K	Skarn
<b>Alteration Code</b>	<b>Alteration code description</b>
Pr	Regional propylitic
Pc	Phyllic cap
Ap	Albite-pyrite
Tr	Transitional sodic-propylitic
Pi	Inner propylitic
Kp	Potassic pervasive
Sp	Skarn peripheral
NC/?	Not coded

Table 6.2. Listing of abbreviations for petrophysical and other parameters.

Measured parameter	Description
Thick	Core Thickness (cm)
Density	Density (g/cc)
V <sub>p</sub>	P-wave Velocity (m/s)
Log(SUSC)	Logarithm of magnetic susceptibility 10-5SI
V <sub>p</sub> amplitude	P-wave amplitude
PLI	Point Load index (MPa)
Axb	Ore ranking hardness
BMW <sub>i</sub>	Bond mill work index (kWh/t)
Derived parameter	Description
YOUNG	Estimated Young's Modulus (GPa) = $0.8\rho V_p^2$
V <sub>s</sub>	S-wave Velocity (m/s)
Other parameter	Description
RQD	Rock quality designation
FFREQ	Fracture frequency (f/m)

### 6.6.1. Petrophysical Data from Borehole CE082

Petrophysical data were recorded on NQ size half cores (from 218m to 309m) and HQ size half cores (from 114m to 218m) from CE082 using the Geotek MSCL. Figure 6.4 shows strip logs of geological, geochemical, petrophysical, geotechnical and comminution parameters. 2m medians of petrophysical parameters over assay intervals are plotted

P-wave amplitude values are low and erratic from 114m to 218m in CE082 These measurements were taken from HQ half core and are affected by poor coupling between core and transducers due to dry cores and not using sonic gel between the core and the coreboat. P-wave amplitude measurements from 218m to 309m on NQ half core are higher and more consistent. The higher values are attributed to improved coupling and not to a change in lithology. Coupling was improved due to wetting of the core, and use of acoustic gel between the core and core boat and between the core boat and lower transducer.

It should be noted that the logging procedures were still being developed during Cadia East petrophysical core logging hence the improvement in coupling was achieved by means of wetting of the core and application of sonic gel. The effect of coupling on P-wave amplitude (Figure 3.17) was presented in Chapter 3. Unfortunately operational pressures dictated by comminution testing deadlines did not allow relogging of intervals for which petrophysical data are considered substandard.

There is a step change in S content starting at the depth of 172m which corresponds to the change from phyllic to propylitic alteration. Magnetic susceptibility increases sharply at 180m although there is no change in logged lithology. This increase corresponds with the change from phyllic alteration dominated by feldspar-pyrite to propylitic alteration that is characterised by the presence of magnetite and chlorite.

Susceptibility values at Cadia are relatively low, even below 180m the magnetic susceptibility is modest in absolute terms; approximately  $1900 \times 10^{-5}$  SI (Figure 6.4), corresponding to less than 1% magnetite equivalent.

Fe content also increases near 180m depth, albeit less markedly than the magnetic susceptibility values. A general correlation is evident between the logarithm of magnetic susceptibility and Fe grade (Figure 6.4).

There is no specific correlation between petrophysical properties and comminution attributes in this hole.

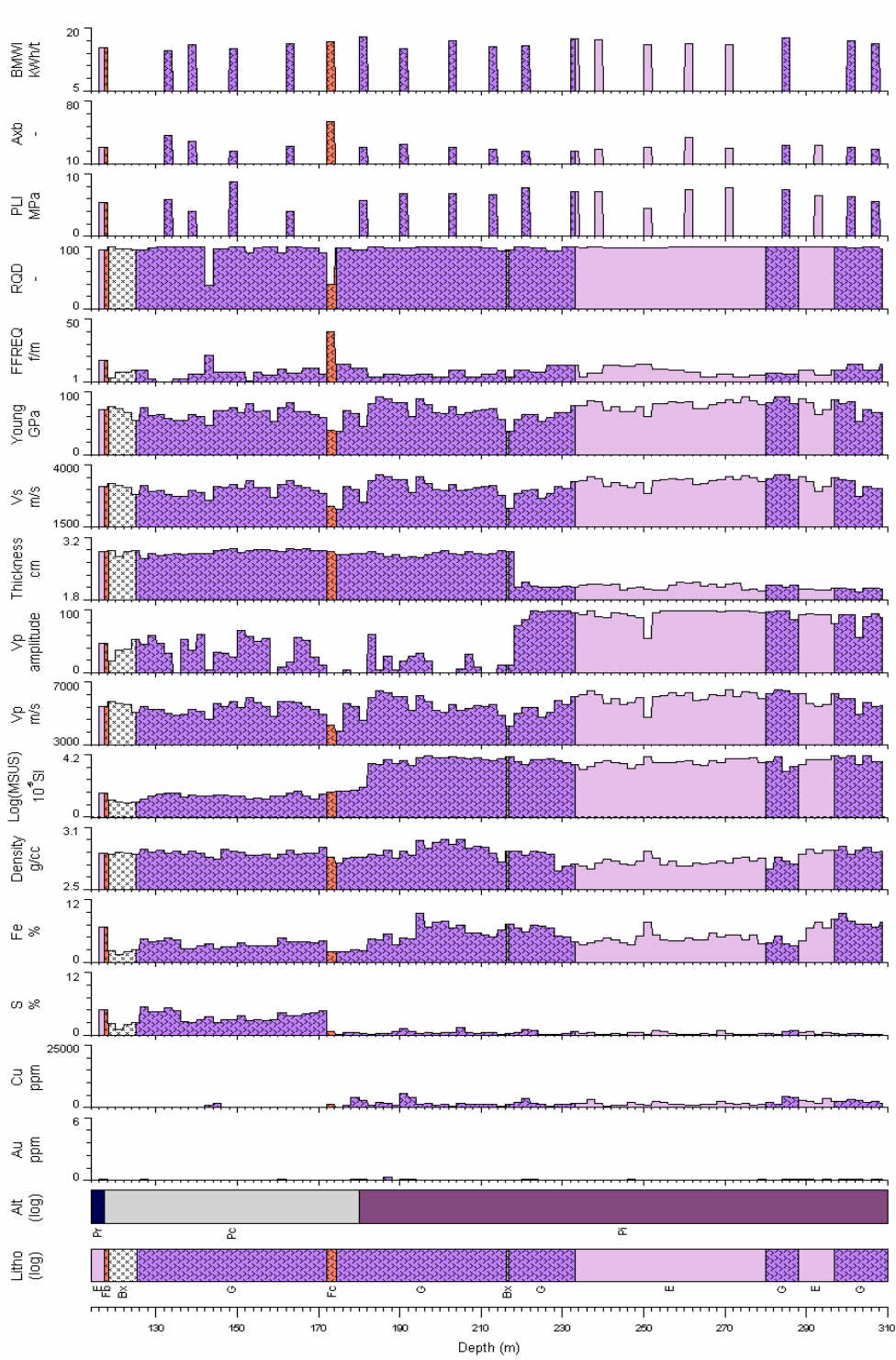


Figure 6. 4. Strip logs of geological, geochemical, petrophysical and geotechnical composite for CE082

The magnetic susceptibility histogram is bimodal (Figure 6.5), with high (approximately  $4200 \times 10^{-5}$  SI) and low (approximately  $25 \times 10^{-5}$  SI) magnetic susceptibility peaks. The low and high magnetic susceptibilities are characteristics of phyllic and propylitic alteration styles.

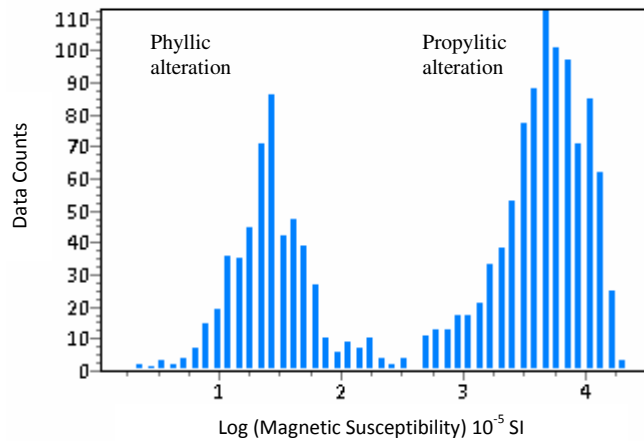


Figure 6. 5. Histogram of Logarithm of magnetic susceptibility for drill hole CE082

### 6.6.2. Petrophysical Data from Borehole CE098

Petrophysical data were collected from depth of 143 to 400m for drill hole CE098. All logged cores were HQ-size. Figure 6.6 shows strip logs of geological, geochemical, petrophysical, geotechnical and comminution data for this hole.

As in CE082, magnetic susceptibility is very low in the shallow phyllic zone, above 240m. Magnetic susceptibility is generally high in propylitically-altered zones, but the major transitions in magnetic susceptibility do not always coincide with the visually-logged locations of the changes in alteration style. For example, the magnetic susceptibility jumps at 275m, 20m below the logged transition to propylitic alteration. On the other hand, the interval 335-350m is logged as propylitic, but its magnetic susceptibility is relatively low.

Phyllic and transitional alteration classes can be characterised by low density and susceptibility while propylitic and skarn alteration have high density and susceptibility (Figure 6.6).

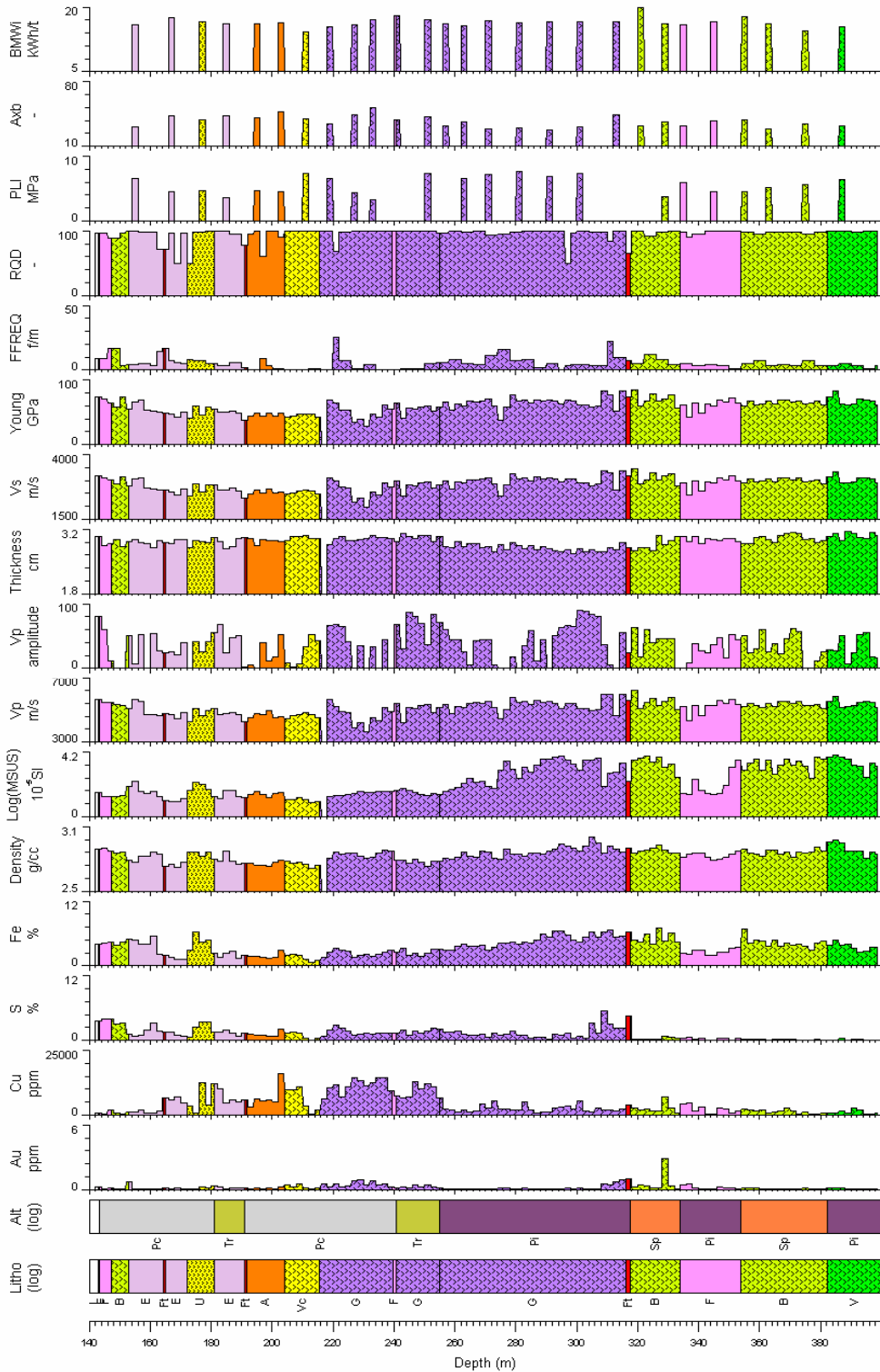


Figure 6. 6. Strip logs of geological, geochemical, petrophysical, geotechnical and comminution composite for CFE098

The histogram of magnetic susceptibility for drill cores from CE098 is bimodal, with high and low magnetic susceptibility peaks: from 143 to 275m values are about  $25 \times 10^{-5}$  SI and below 275m they are about  $2000 \times 10^{-5}$  SI (Figure 6.7).

Fe content is somewhat elevated between 270 and 330m, coinciding with an interval of high magnetic susceptibility. There is a step change in S content at 318m and S concentration is very low at greater depths.

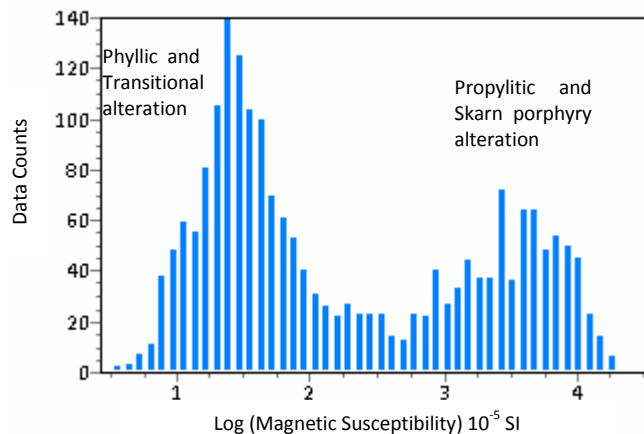


Figure 6.7. Histogram of Logarithm of magnetic susceptibility for drill hole CE098

$A^*b$  varies in a small range from a value of 27.5 to 52 suggesting that these rocks are very hard materials for crushing. P-wave velocity and logarithm of magnetic susceptibility show a moderate negative correlation with  $A^*b$ .

### 6.6.3. Petrophysical Data from Borehole CE109

CE109 is a central hole covering all alteration, lithology and mineralization styles. Petrophysical data were collected from a depth of 117m to 498m. All drill cores were HQ-size. Figure 6.8 shows strip logs of geological, geochemical, petrophysical and geotechnical logs for this hole. There is no petrophysical data in some intervals (e.g. 146-168m) owing to core condition (i.e. quarter size core, fault zones). During the logging of this hole (289-307m and 405-453.7m) an incorrect setting of the magnetic susceptibility sensor (point sensor instead of loop sensor) unfortunately resulted in the recording of many negative values which can not be interpreted. Operational pressures unfortunately meant that these intervals could not be relogged and for this reason there are gaps for magnetic susceptibility measurements in the mentioned intervals.

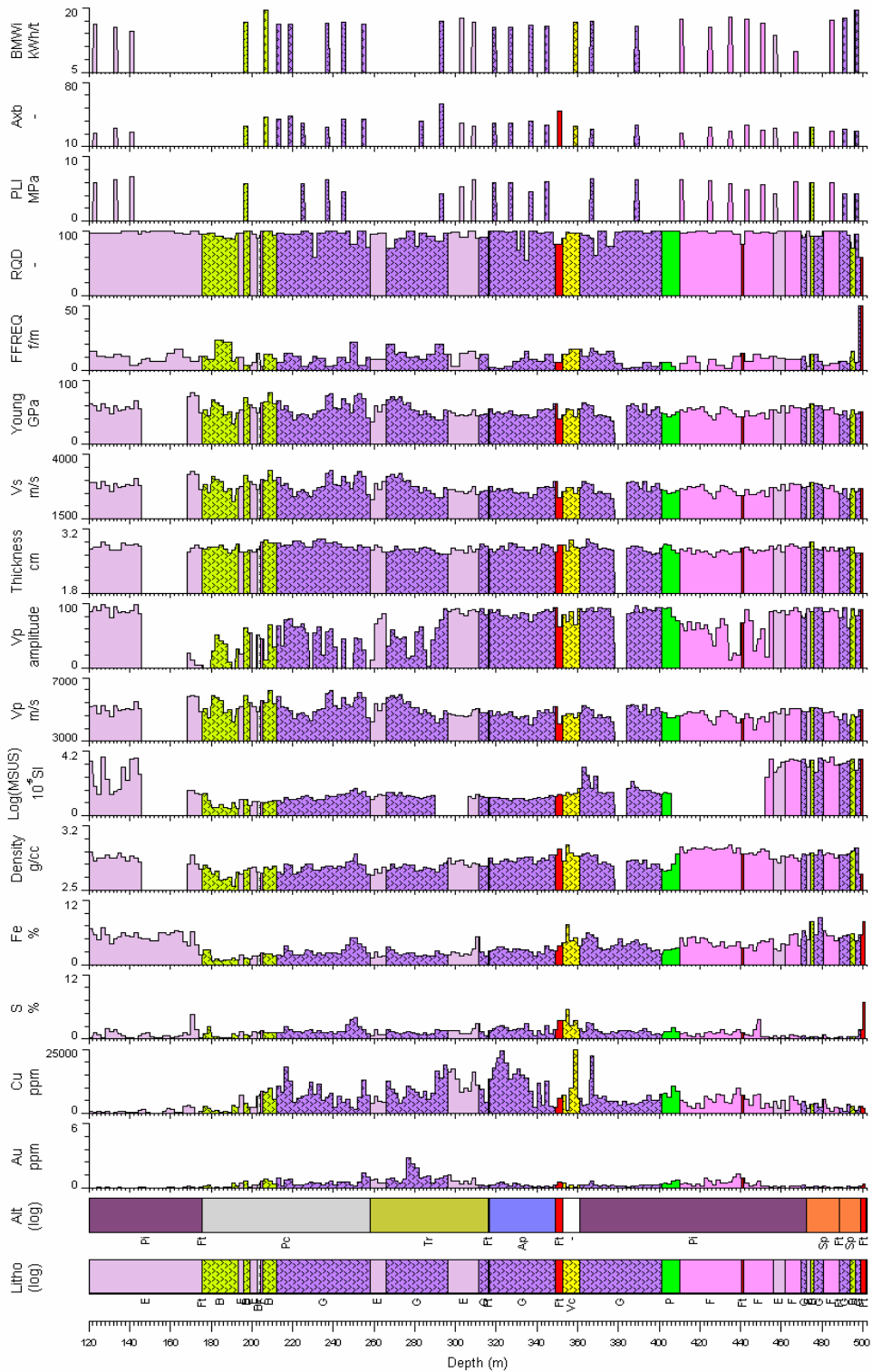


Figure 6. 8. Strip logs of geological, geochemical, petrophysical and comminution composite for CFE0109

The histogram of magnetic susceptibility is again bimodal in CE109, with high and low magnetic susceptibility peaks (Figure 6.9). High values of approximately  $4000 \times 10^{-5}$  SI occur from 118-146m and below 453m. The remainder of the hole has magnetic susceptibility values of about  $20 \times 10^{-5}$  SI. Although no magnetic susceptibility measurements were recorded between 146-170m, based on the increasing iron content and the logged prophylic alteration, the magnetic susceptibility values are likely to still be high up to 170m.

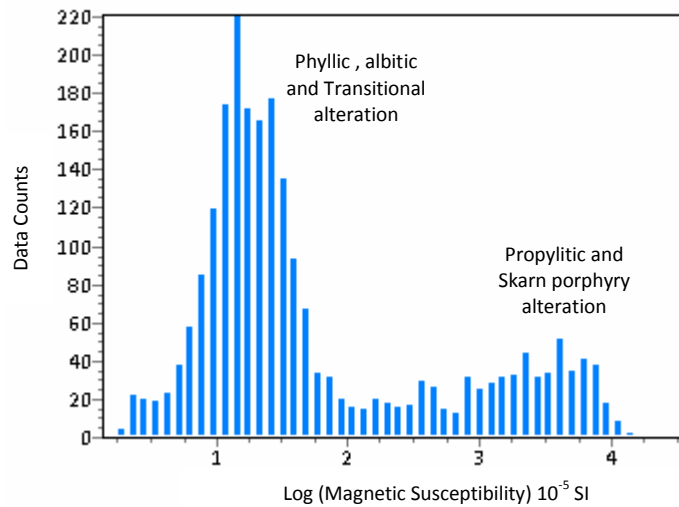


Figure 6. 9. Histogram of Logarithm of magnetic susceptibility for drill hole CE109

Bond mill work index generally does not vary in the entire drill hole.  $A^*b$  is relatively low in propylitic (Pi) and skarn porphyry (Sp) alteration zones suggesting hard materials for crushing in these intervals. The logarithm of magnetic susceptibility shows a moderate negative correlation with  $A^*b$ .

#### 6.6.4. Petrophysical Data from Borehole CE110

Petrophysical data were collected from a depth of 214 to 454m. Drill cores were HQ-size above 252m and NQ-size below 252m. P-wave amplitude is more reliable in this hole as better coupling was achieved during logging. Figure 6.10 shows geological, geochemical, petrophysical, geotechnical and comminution composite logs for this hole.

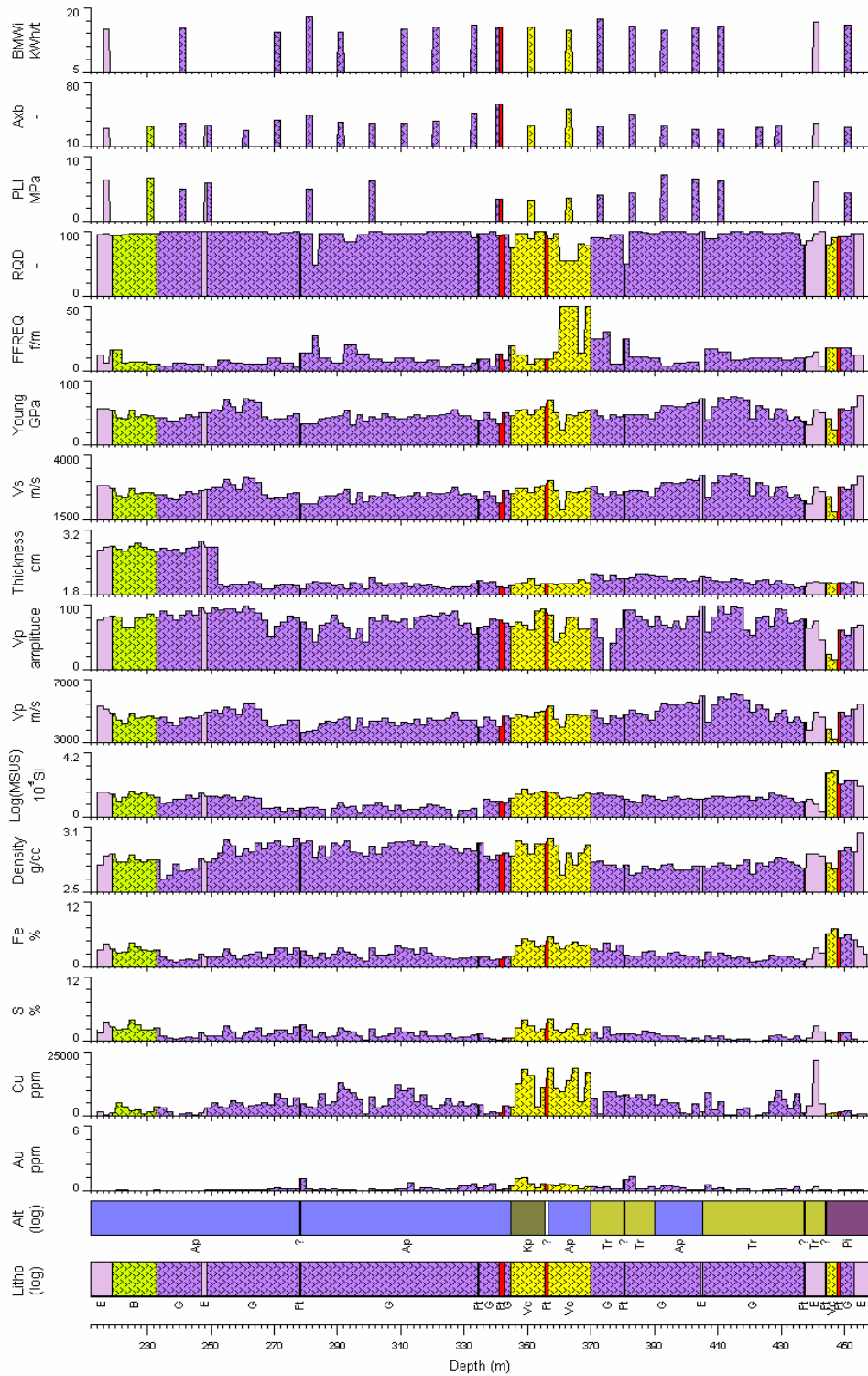


Figure 6. 10. Strip log of geological, geochemical, petrophysical and comminution composite for CE110

Density is slightly elevated between 250 and 360m with an average value of 2.91g/cc versus an average value of 2.78g/cc from 360 to 454m. This increase may be related in part to sulphide mineralisation in this interval, though sulphide mineralisation also occurs at depths greater than 360m. The same lithology, volcanoclastic conglomerate (G) is encountered between 370 and 437m, but its density is lower. The alteration style is different for these two intervals of G with albite-pyrite (Ap) for the shallower interval versus mainly transitional sodic-propylitic (Tr) for the deeper zone.

Magnetic susceptibility is characterized by a bimodal distribution (Figure 6.11). However propylitic alteration occurs only the lower portion of drill hole and in consequence the high magnetic susceptibility peak has only a low amplitude. Magnetic susceptibility values in this hole are only slightly elevated just below 445m, which is the depth at which propylitic alteration is first encountered.

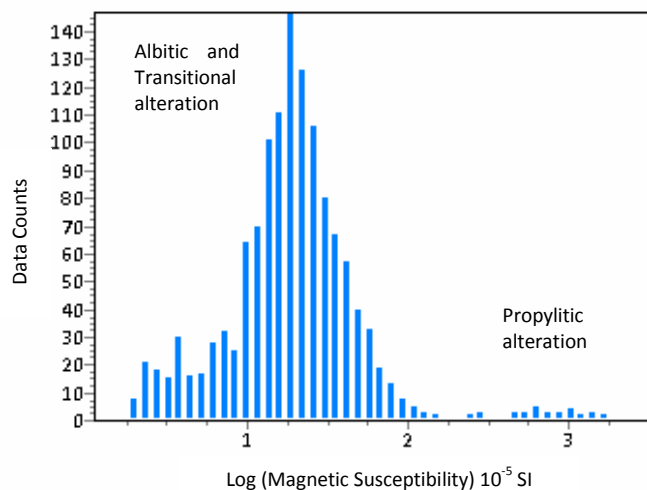


Figure 6. 11. Histogram of Logarithm of magnetic susceptibility for drill hole CE110

There is an increase in P-wave velocity from 390-425m. This increase corresponds with an increase in Point load index and a decrease in  $A^*b$ . Although P-velocity decreases below 425m but  $A^*b$  remains relatively invariant. Overall P-wave velocity shows a negative correlation with  $A^*b$ . The logarithm of magnetic susceptibility also shows a weak negative correlation with  $A^*b$ .

### 6.6.5. Petrophysical Data from Borehole CE143

This hole has a deep intersection of high grade Cu-Au mineralization associated with veining of monzonite and porphyry. CE143 represents a different mineralisation style from that intersected in the other four holes. The predominant alteration classes are propylitic and potassic. Petrophysical data were collected from 1103 to 1475m, transecting the high grade quartz vein Au mineralization. All logged core sections were NQ-size. Figure 6.12 shows the geological, geochemical, petrophysical and geotechnical logs for this hole.

Petrophysical properties are unreliable across the intensely fractured interval from 1140-1155m, where the core is badly broken. Therefore these sections of data are removed. During the logging of this hole, an incorrect setting of the magnetic susceptibility sensor (point sensor instead of loop sensor) resulted in the recording of many negative values which cannot be used. Thus, sections of this hole were re-logged for magnetic susceptibility. Magnetic susceptibility data is missing over two intervals: 1140-1165m and 1430-1465m.

Both Au and Cu grade increase in potassic alteration at 1313m. S is anomalous between 1324m and 1332m but the alteration style in this interval is not known, but is inferred to be potassic alteration.

Magnetic susceptibility is generally high in this drill hole, and reaches a maximum within the interval logged as volcanoclastics (V; 1260-1310m); the alteration type is not specified over most of this depth range but is logged as propylitic between 1260 and 1270m. However within these intervals magnetite mineralization was observed by the site geologist. Susceptibility has a moderate positive correlation with Fe% in this hole. Overall susceptibility in zones of propylitic and potassic alteration in this hole shows a wider range of variability (i.e. changes from 0.0001 SI to 0.1 SI) as represented in Figure 6.13.

Bond mill work index is generally high and invariant in entire hole and has no correlation with petrophysical parameters. P-velocity and density only show a weak negative correlation with A\*b

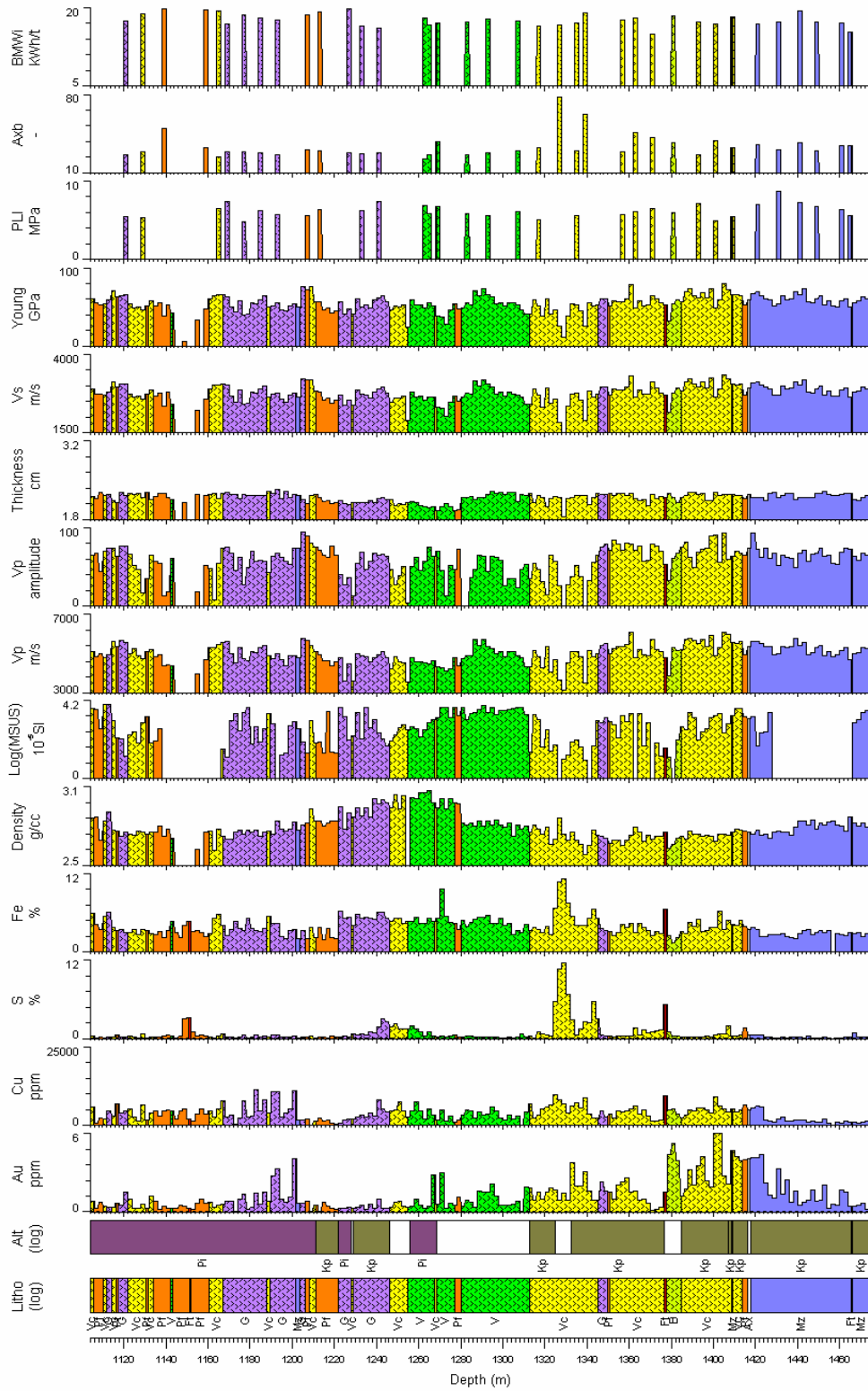


Figure 6. 12. Strip log of geological, geochemical, petrophysical, geotechnical and comminution composite for CE143

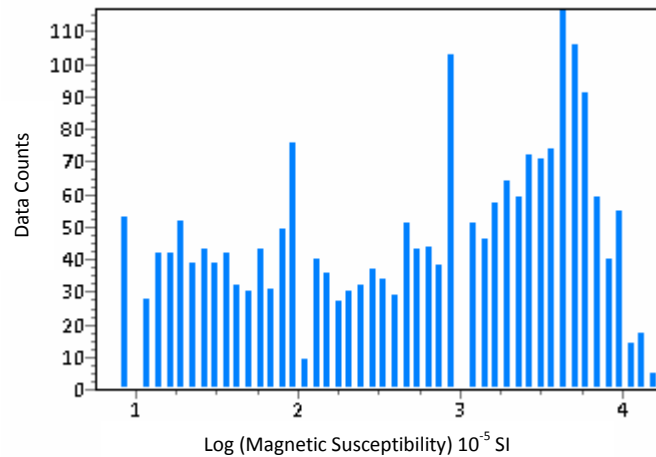


Figure 6.13. Histogram of Logarithm of magnetic susceptibility for drill hole CE143

### 6.7. Petrophysical Signatures of Cadia East

Given its geological characteristics (disseminated sulphide mineralization in Ordovician volcanoclastics), the Cadia East ore system is unlikely to produce consistent strong physical property contrasts. For any one parameter there is considerable overlap of property ranges between lithologies. Figure 6.14 shows medians and spreads for density, P-wave velocity and the logarithm of magnetic susceptibility within each litho-alteration classes from all five drill holes. The individual lithologies cannot be uniquely identified based on a single parameter.

However as presented in Section 6.6, magnetic susceptibility exhibited a bi-modal distribution in holes CE082, CE098, CE109, and CE110. The high and low susceptibility litho-alteration classes can be identified in Figure 6.14c, which shows the medians and spreads for the logarithm of susceptibility within each class. Elevated susceptibility at Cadia East is associated with inner propylitic alteration (Pi) and with skarn peripheral alteration (Sp). It should be noted that rocks with potassic alteration have shown both high and low susceptibility, but most of the samples with high susceptibilities were present in CE143 only.

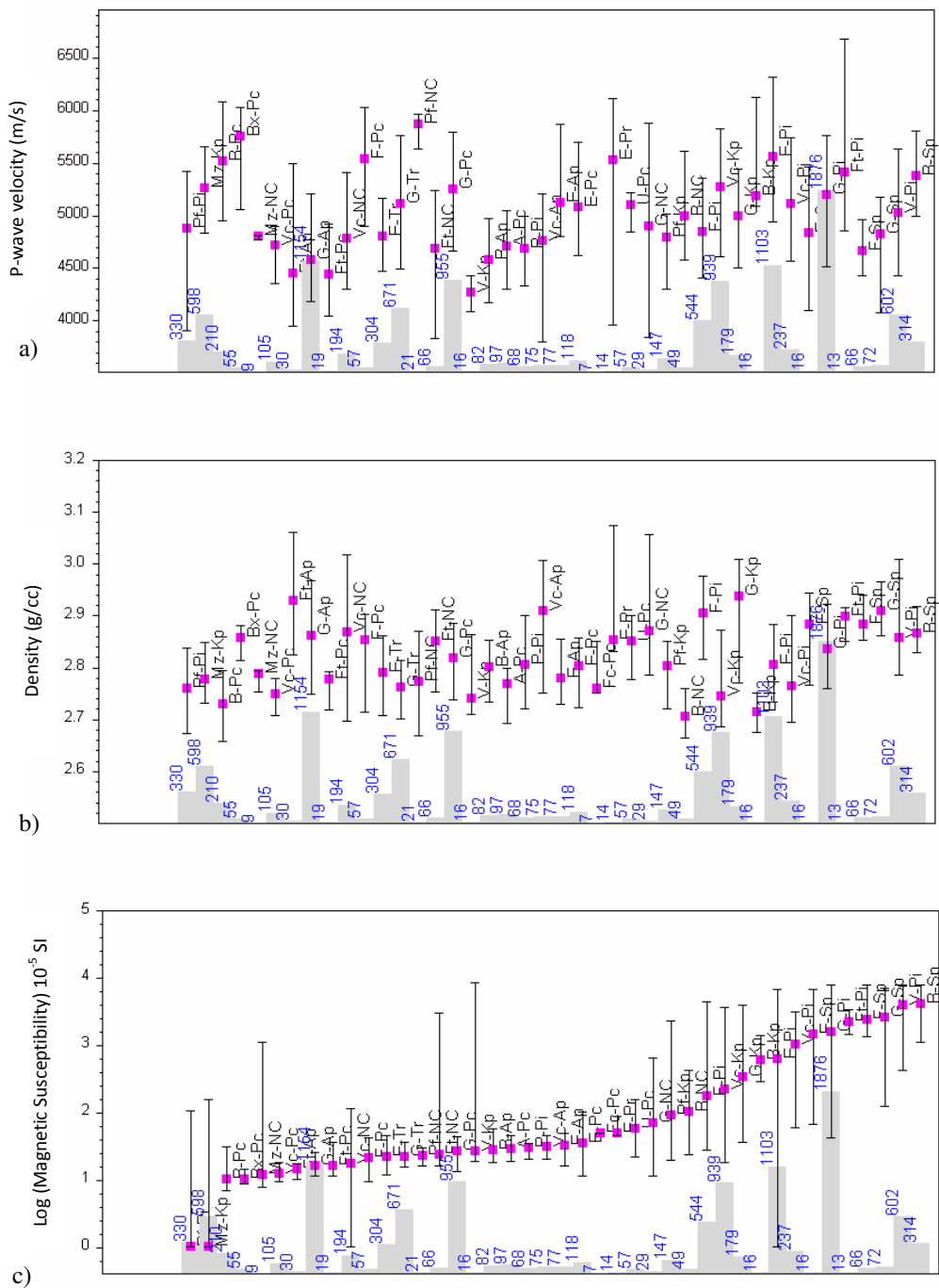


Figure 6. 14. Medians and spreads in average (a) P-wave velocity, (b) density and (c) magnetic susceptibility (log scale,  $10^{-5}$  SI) over 2m assays splits from drill holes CE082, CE098, CE109, CE110 and CE143, classified by litho-alteration type. Pink square = median, black bar = range (16<sup>th</sup> – 84<sup>th</sup> percentile), grey histogram = number of samples for each litho-alteration type.

There is a weak positive correlation between magnetic susceptibility and P-wave velocity in all holes. Likewise, a weak positive correlation exists between magnetic susceptibility and P-wave modulus (Figure 6.15). Magnetite has a high velocity of 7410 m/s and high

density of 5.18 g/cc (Schön, 1996) hence a high P-wave modulus of 284GPa. However due to low concentrations of magnetite in Cadia East drill core (at most 3%), the increase in P-wave modulus cannot be attributed to presence of magnetite only.

The increase in P-wave modulus is more likely due to minerals associated with magnetite such as calcite, chlorite and feldspar. Although the relationship between susceptibility and P-wave modulus is not strong a general trend is evident. Thus magnetic susceptibility might be useful both as an indicator of alteration style and as an indicator of elastic properties.

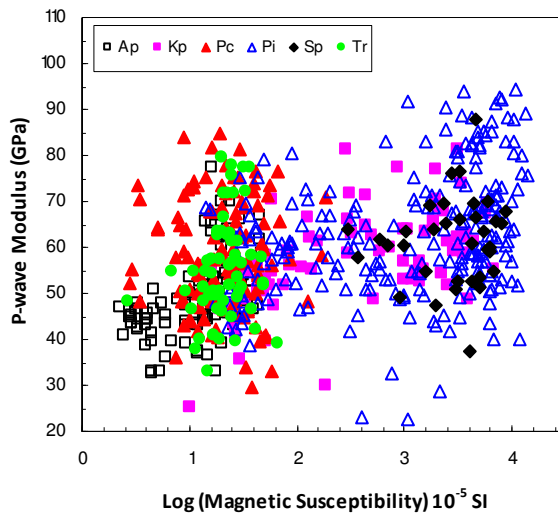


Figure 6. 15. Cross-plot of P-wave modulus and logarithm of magnetic susceptibility, grouped according to alteration styles in all five boreholes

### 6.8. Comminution Modeling

Different geometallurgical modeling approaches (as described in Chapter 4) are investigated in this section. As discussed in Chapter 4, it is worthwhile to investigate “universal” models as a starting point to determine if a simplistic approach has merit. Correlations between petrophysical properties and comminution attributes for 148 test samples from all drill holes were investigated. It should be noted that in some comminution intervals petrophysical measurements were not available due to issues explained in previous section (Section 6.6).

Figure 6.16 shows the scatter plots of petrophysical properties (P-wave velocity, density and susceptibility) against comminution attributes ( $A^*b$  and  $BMWi$ ) when all comminution dataset are considered. There is no clear relationship between any of petrophysical properties and  $BMWi$ . However, a general negative trend is evident between P-wave velocity and  $A^*b$  (Figure 6.16f). There is a tendency for an increase in P-wave velocity to correspond with a reduction in  $A^*b$  value and consequently for the rock to become harder to crush.

Figure 6.16e shows a weak negative correlation between magnetic susceptibility and  $A^*b$  for all comminution test samples. It should be noted that some susceptibility measurements in comminution intervals are absent as explained in Section 6.6. Magnetite content at Cadia is generally low in absolute terms, and certainly low in comparison to Ernest Henry.

Magnetite is normally associated with propylitic alteration and high susceptibility rock samples which are propylitically altered have low  $A^*b$  (i.e. hard to crush). This trend is the reverse of that observed at Ernest Henry (Chapter 5).

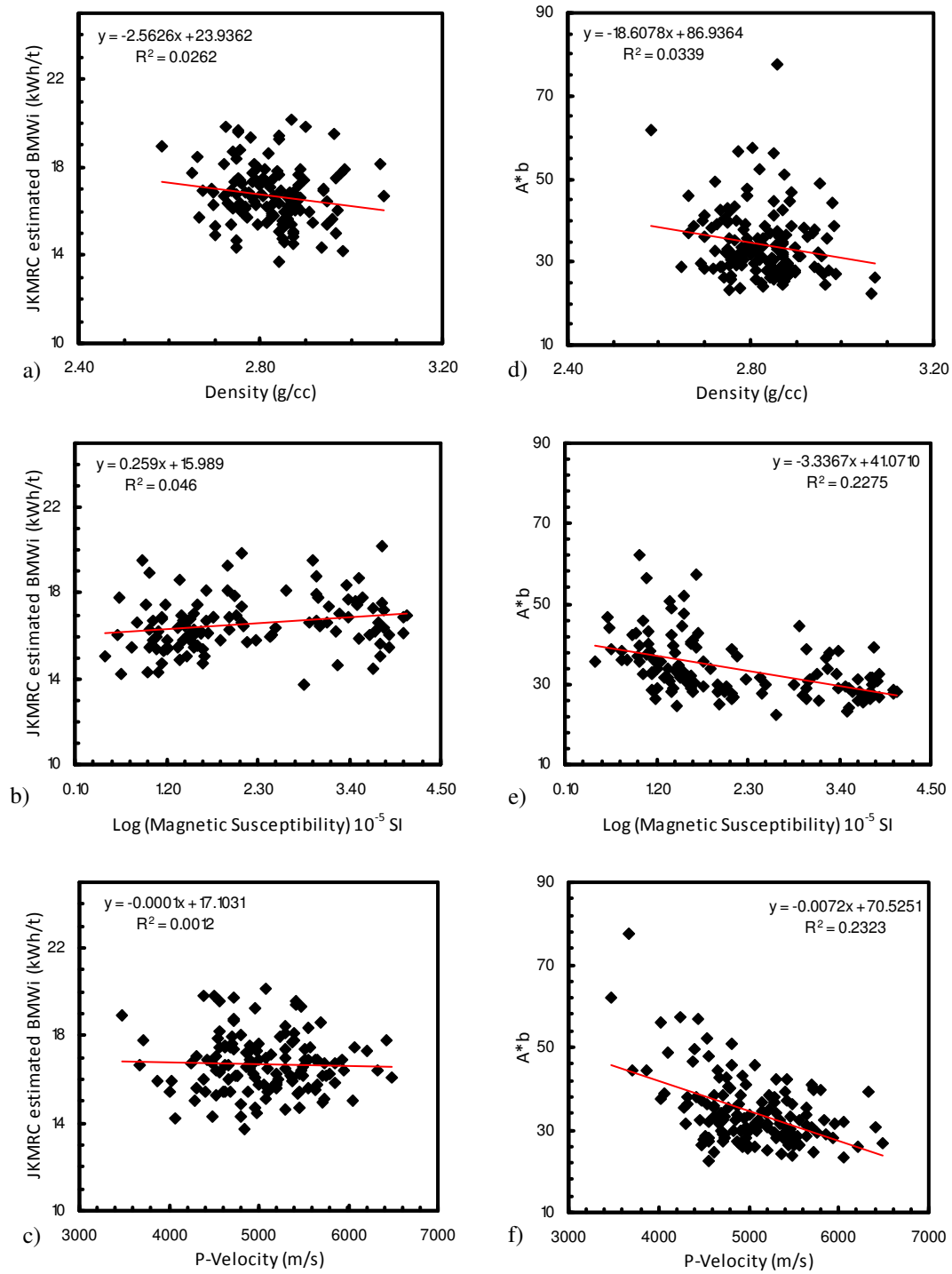


Figure 6.16. Scatter plot of JKMRC estimated BMWi versus medians of (a) density, (b) logarithm of magnetic susceptibility and (c) P-wave velocity for all comminution test samples. Also scatter plot of A\*b versus medians of (d) density (e) logarithm of magnetic susceptibility and (f) P-wave velocity for all comminution test samples. The red line in each panel is a linear regression fit to data which has been shown even when correlation coefficients are poor.

A nonlinear regression fit slightly increases the correlation between P-wave velocity and  $A^*b$  (Figure 6.17a). Correlation between P-wave modulus (as described in Chapter 2) and  $A^*b$  also investigated here. There is a weak negative nonlinear relationship between P-wave modulus and  $A^*b$  (Figure 6.17b). A reciprocal transformation of P-wave modulus slightly increases its correlation with  $A^*b$  (Figure 6.17c). The root mean square error (RMSE) between reciprocal of P-wave modulus and  $A^*b$  is 6.60, while the RMSE value between P-wave velocity and  $A^*b$  is 7.25.

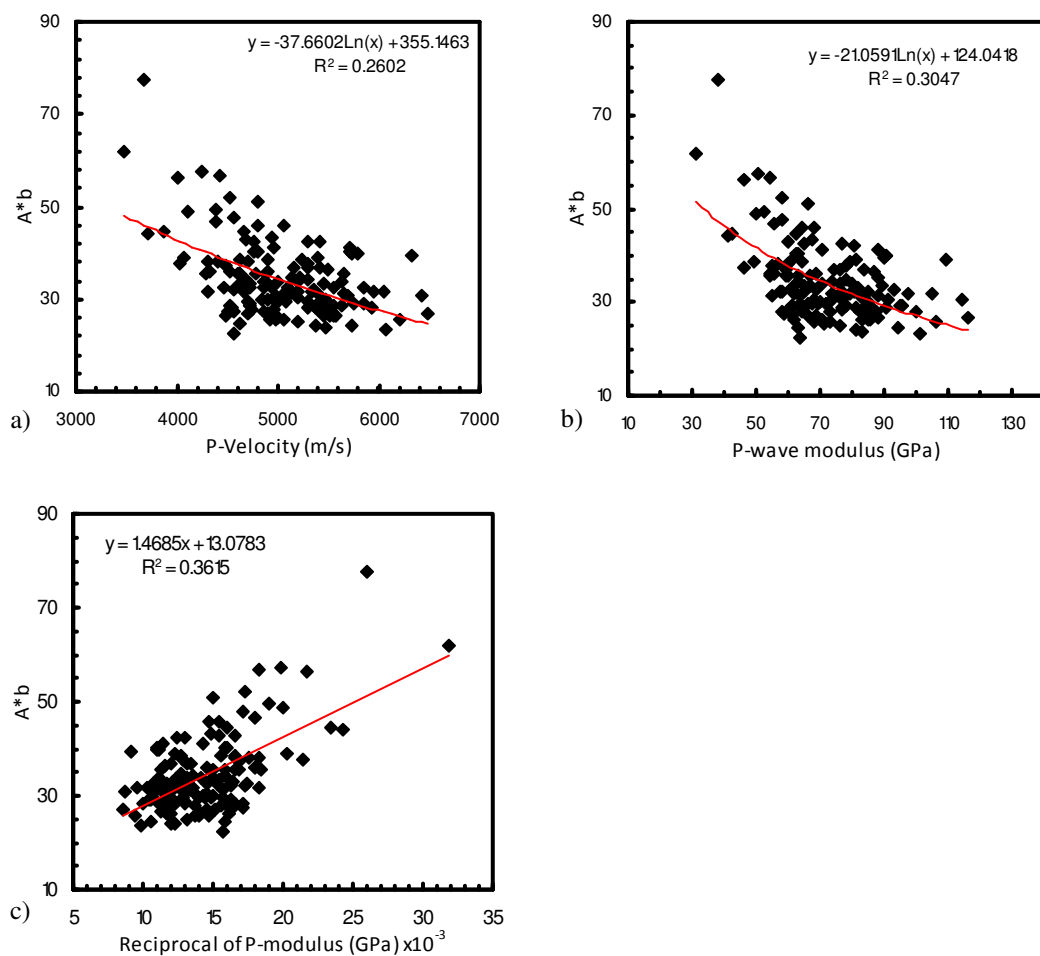


Figure 6. 17. Scatter plot of  $A^*b$  versus (a) P-wave velocity (b) P-wave modulus and (c) reciprocal of P-wave modulus for all comminution test samples. The red line is a regression fit to data

Detailed analysis of Figure 6.17a shows that although P-wave velocity in propylitic altered samples varies greatly (from 4000m/s to 6000m/s),  $A^*b$  is almost constant ( $30 \pm 5$ ). One explanation for small dynamic range of  $A^*b$  values at Cadia East is the fact that  $A^*b$  measurements are based on “survivor” particles after crushing the rock samples and that these materials are more competent at the crushed size.

The large variation of P-wave velocity can to some degree be attributed to factors such as variations in the elastic properties of the rock. Figure 6.18 explains the variability of P-wave velocity theoretically to some extent. For a given stress, the P-wave velocity will change according to the value of Poisson’s ratio (equation 6.1). Density can be assumed as invariant because even large variation of density does not greatly affect the velocity according to equation 6.1.

$$V_p = \sqrt{\frac{E(1-\sigma)}{\rho(1+\sigma)(1-2\sigma)}} \quad (6.1)$$

where  $V_p$  is the P-wave velocity,  $\rho$  is density,  $E$  and  $\sigma$  are Young’s modulus and Poisson ratio respectively.

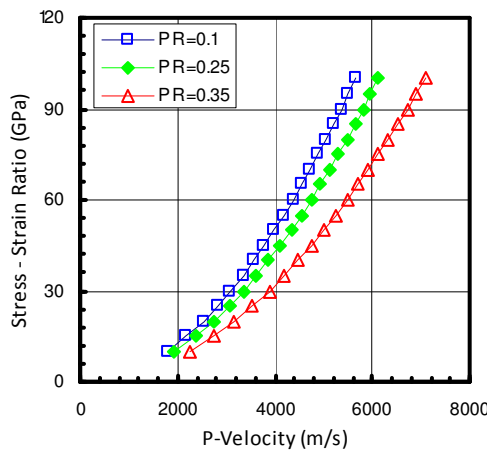


Figure 6.18. P-velocity versus the ratio of stress to strain (i.e. Young’s modulus) for different values of Poisson ratio (modified after Hatherly et al., 2003)

As presented in Figure 6.18 the materials with Young’s modulus of 60GPa, represent a wide range of P-wave velocity i.e. from 4000m/s to approximately 6000m/s. This large variation is attributed to variation of Poisson ratio from 0.1 to 0.35.

Medians and spreads of P-wave velocity, density, and susceptibility for 2m intervals of drill cores corresponding to comminution intervals were investigated. It is evident that petrophysical properties recorded at 9cm intervals have a high degree of variability within individual 2m section of drill cores (Figure 6.19). P-wave velocity in most 2m intervals varies by approximately 1000m/s (Figure 6.19a) which is a high level of variability for P-wave velocity and beyond the degree of variability that can be explained by issues associated with data acquisition. Density has also shows a high level of variability and in some intervals there is  $\pm 0.3\text{g/cc}$  variability (Figure 6.19b). Local variability of susceptibility is only significant within high susceptibility intervals (Figure 6.19c). The significant variability of petrophysical properties is representative of real small-scale interval variability within each comminution interval and could in fact be responsible for the poor correlation between petrophysical properties and comminution attributes.

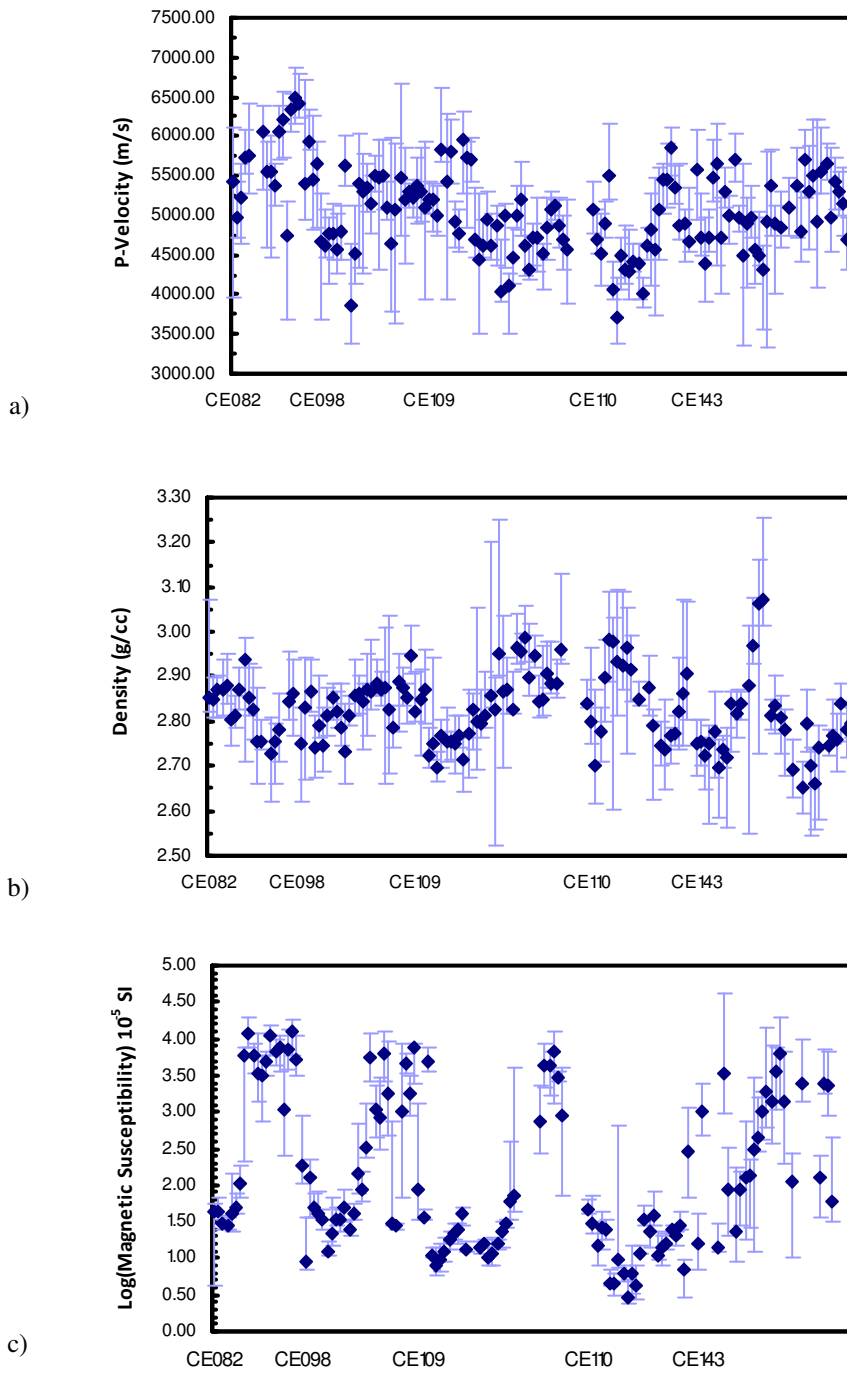


Figure 6.19. Medians and spreads of P-wave velocity (a), density (b) and logarithm of magnetic susceptibility (c) over comminution intervals for each drill hole from Cadia East. Note that susceptibility measurements were not recorded on some intervals.

In Figure 6.16 the general correlations between P-wave velocity, magnetic susceptibility and  $A^*b$  for all Cadia East comminution test samples were presented. The correlation between  $A^*b$  and P-wave modulus (or estimated Young's modulus) is relatively stronger than the correlation between  $A^*b$  and P-wave velocity (Figure 6.17). The following

formula (equation 6.2) for  $A^*b$  in terms of susceptibility and P-wave modulus was derived via multiple regression. The relative error of prediction is 13.2%.

$$A^*b = 23.96 - 2.14 \log(\text{susceptibility}) + 1017.68(\text{P-wave modulus})^{-1} \quad (6.2)$$

In order to assess the relative performance of neural network modeling for  $A^*b$  prediction, a neural network (as described in Chapter 4) was designed and trained for prediction using susceptibility and P-wave modulus. A network structure with two nodes in the hidden layer was found as the best structure in terms of performance when compared with ten different structures using Statistica Neural Network software. The relative error of prediction reduced by 1.4% in comparison to  $A^*b$  values estimated via multiple regression. Measured and predicted  $A^*b$  are compared in Figure 6.20. Although there are some large discrepancies on a point by point basis, the overall trends in the predicted and measured  $A^*b$  values are very similar for both predictions. A perfect match between measured and predicted attribute should not be necessarily expected, given the inherent uncertainty in the  $A^*b$  determinations and in the petrophysical measurements.

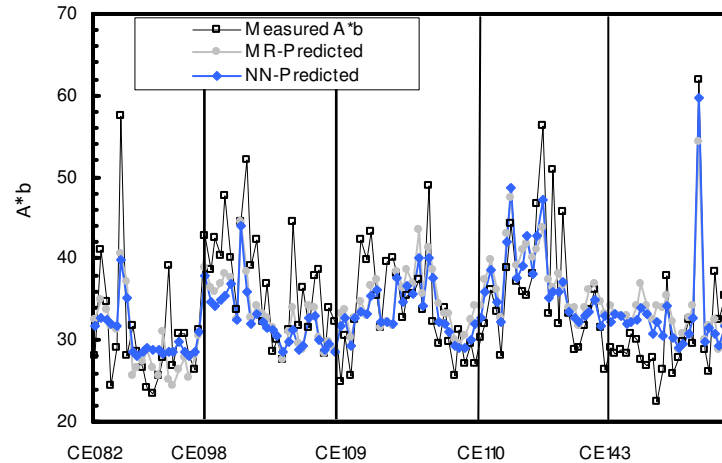


Figure 6.20. Comparison between measured  $A^*b$  and the  $A^*b$  values predicted using multiple regression (MR) of P-wave modulus and logarithm of magnetic susceptibility (equation 6.2) and  $A^*b$  predicted using neural network (NN). The samples originating from each drill hole are plotted in depth order.

Figure 6.20 indicates that  $A^*b$  can be predicted fairly well based on petrophysical properties. However similar global modeling of BMWi using petrophysical properties produced an unsatisfactory result. A multiple regression of magnetic susceptibility, density, P-wave velocity and P-wave modulus against BMWi produced a very poor correlation ( $R^2=0.03$ ).

Data classification schemes presented in Chapter 4 can be used to assess whether data classification can improve prediction of both  $BMWi$  and  $A^*b$ . As stated in Chapter 4, the choice of appropriate data classification for geometallurgical purpose depends on ore metallurgical variability. Given the small range in variability of comminution parameters at Cadia East (Figure 6.1), definition of geometallurgical classes based on the petrophysical (PC) or geological (GC) approach were not anticipated be effective methods for development of models. Nevertheless all four approaches for geometallurgical data classification and modeling presented in Chapter 4 are tested in turn in the following subsections.

### 6.8.1. Comminution Modeling: GC Approach

The relationship between petrophysical properties and metallurgical attributes of Cadia-East based on geological classes is presented here. There are too many litho-alteration classes defined by site geologists (Table 6.1) to enable effective litho-alteration classification using the available comminution sampling. Although amalgamation of lithological classes (i.e. all volcanoclastics in one class) may simplify the number of classes but does it not necessarily help in characterizing comminution behavior. For this reason alteration classes alone were tested here. The comminution test samples were grouped into alteration classes.

Table 6.3 records the mean and standard deviation of  $A^*b$  and  $BMWi$  within each alteration class. Overall there is little variability of  $A^*b$  and  $BMWi$  between the alteration classes. Figure 6.21 is a box and whisker plot showing mean values of  $A^*b$  and  $BMWi$  together with standard deviation for each alteration class. The comminution properties overlap in all alteration classes. This immediately suggests that there is no clear relationship between alteration classes and comminution attributes. Moreover Figure 6.24 reinforces the fact that a change in ore geological characteristics at Cadia East does not have a significant impact on metallurgical variability. If only mean values of properties for each class are considered then it might be possible to broadly characterize alteration classes based on comminution properties. However, the observed differences between class average for  $A^*b$  and  $BMWi$  are still very small and only marginally greater than the inherent uncertainties in the measured values.

The relationships between petrophysical properties and comminution attributes were investigated within each alteration class using regression analysis. A moderate negative

correlation ( $R^2=0.55$ ) between P-wave velocity and  $A^*b$  was found for samples of “Pc” alteration class (Figure 6.22a). Similarly a good negative correlation ( $R^2=0.79$ ) was also established between P-wave velocity and  $A^*b$  for samples of “Ap” alteration class after rejecting outliers (Figure 6.22b). Multiple regression analysis of P-wave modulus and the logarithm of magnetic susceptibility against  $A^*b$  for the remainder of alteration classes was not superior to the universal model (equation 6.2). BMWi showed no good correlation with petrophysical properties within any alteration class.

Table 6.3 Mean and standard deviation of comminution parameters ( $A^*b$  and BMWi) in each alteration class for test samples from all five drill holes of Cadia East.

Comminution Parameter	Pi Class (51 samples)	Ap Class (16 samples)	Sp Class (8 samples)	Tr Class (9 samples)	Pc Class (22 samples)	Kp Class (19 samples)
$A^*b$	29.8 (5.1)	38.6 (7.4)	31.6 (4.3)	39.2 (8.5)	39.4 (7.5)	34.5 (8.3)
BMWi	16.7 (1.6)	15.4 (0.8)	17.4 (1.8)	16.7 (0.6)	16.4 (1.1)	17.2 (1.3)

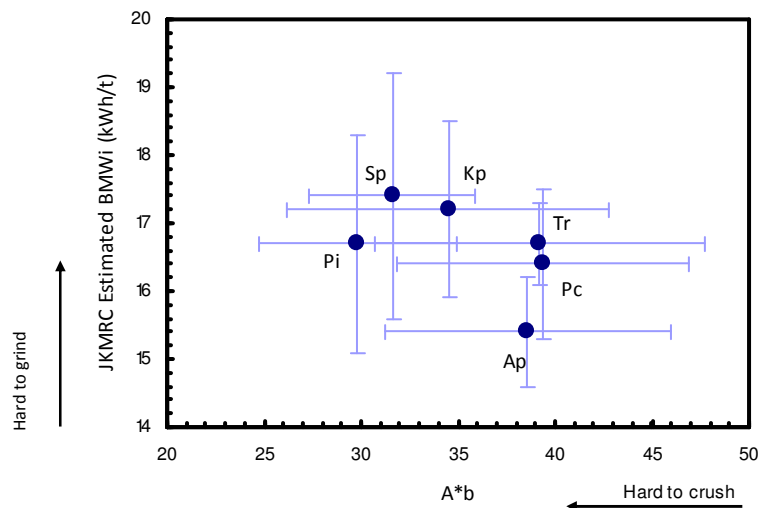


Figure 6.21. Scatter plot of mean  $A^*b$  and Bond mill work index for six different alteration classes at Cadia East. The blue bars indicate the standard deviation of comminution attributes.

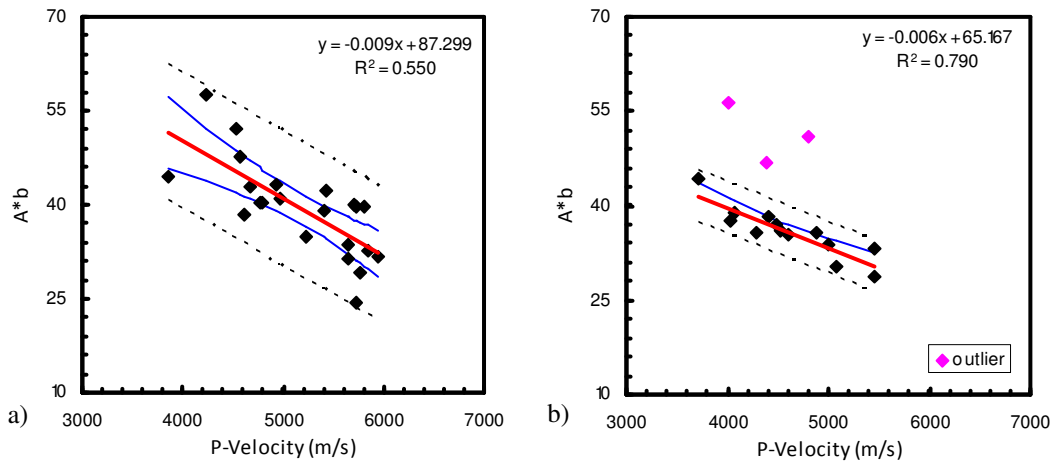


Figure 6.22. Scatter plot of P-wave velocity versus A\*b for phyllic cap (a) and albite-pyrite (b) alteration classes. The red line is a linear regression fit to data. The blue lines are 95% confidence intervals and the dashed lines are regression prediction limits. Outliers rejected during model development for the albite-pyrite alteration class are specifically highlighted in (b).

### 6.8.2. Comminution Modeling : PC Approach

In order to better predict A\*b and BMWi using petrophysical properties the samples were divided into groups or classes based on petrophysical properties. Three clusters were retained as a result of cluster analysis (described in Chapter 4) using three petrophysical properties (i.e. density, susceptibility and P-velocity).

A bar chart offers a way to assess the individuality of the selected clusters. The normalized mean values of each parameter within each cluster are presented in Figure 6.23. Each parameter was normalized based on its minimum and maximum using equation (5.2) so that all three normalized petrophysical properties range between zero and one.

As can be inferred from Figure 6.23, Cluster 1 is well separated from others by virtue of higher P-wave velocity and susceptibility and medium density. Therefore, Cluster 1 material is likely to be relatively hard to crush. Cluster 2 is characterized by high density and low P-wave velocity and medium susceptibility. Therefore, Cluster 2 should represent rocks that might be relatively softer to crush. Cluster 3 is separated from other clusters by low density and low susceptibility and medium P-wave velocity.

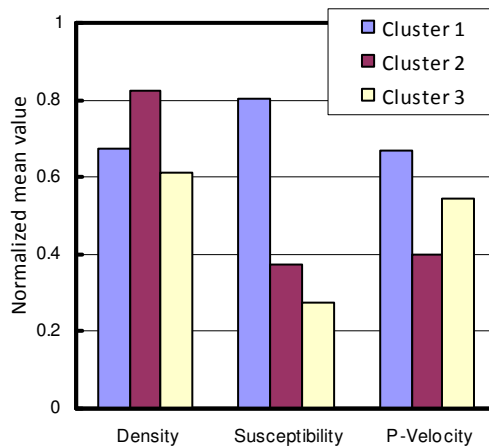


Figure 6. 23. Bar chart of normalized petrophysical property means for three petrophysical clusters

Table 6.4 shows the mean and standard deviation of comminution test results within each petrophysical cluster. The comminution parameters have little variability within each cluster. Mean BMWi in all classes is almost identical. Mean A\*b value for Cluster 1 is only slightly lower than the mean A\*b for the other two clusters. Multiple regressions of petrophysical properties against comminution parameters (A\*b and BMWi) within each cluster did not yield an improved prediction when compared with global models (Section 6.8). Multiple regression of the logarithm of magnetic susceptibility and P-wave modulus against A\*b within each class did not significantly improve the relative error of prediction of the A\*b model when compared with equation 6.2 except in Cluster 1 (relative error of 9.3% c.f. 13.2% for the global model).

Table 6.4 Mean and standard deviation of comminution parameters (A\*b and BMWi) for comminution test samples in each petrophysical cluster.

Comminution Parameter	Cluster 1 (38 samples)	Cluster 2 (22 samples)	Cluster 3 (62 samples)
A*b	29.8 (3.8)	36.8 (8.6)	35.5 (7.5)
BMW <sub>i</sub>	16.7 (1.3)	16.5 (1.5)	16.5 (1.1)

### 6.8.3. Comminution Modeling : CC Approach

At Cadia East, modelings based on GC (Section 6.8.1) and PC (Section 6.8.2) approaches were ineffective since they did not adequately discriminate distinctive comminution populations. The ineffectiveness of such approaches is mainly attributed to the small variability of ore comminution behavior. In this section comminution classes are created purely based on comminution test results (i.e. A\*b and BMW<sub>i</sub>) and then the relationships between petrophysical properties and created comminution classes are examined. Ideally

each comminution class represents a specific processing behaviour based on variability of ore crushing and grinding.

If a reliable relationship can be established between petrophysical properties and comminution classes, then petrophysical properties could be used for prediction of comminution behavior (classes) in intervals where no comminution tests were conducted.

$A^*b$  itself is an ore ranking parameter, the higher the value the softer the rock would be for crushing. Bond mill work index (BMW<sub>i</sub>) is a quantitative measure of ore grindability. A variation of 0.5kWh/t in BMW<sub>i</sub> could be significant for an operating mill. The mean values of  $A^*b$  and BMW<sub>i</sub> for Cadia East comminution test samples are 34.4 and 16.7 kWh/t respectively. When compared with many other mining operations (e.g. Ernest Henry) these values indicate that the ore at Cadia East is comparatively hard both in terms of crushing and grinding. Nonetheless for the purpose of this study, materials are classified on the basis of  $A^*b$  and BMW<sub>i</sub> as “hard” or (relatively) “soft”.

A scatter plot of  $A^*b$  versus BMW<sub>i</sub> for Cadia East samples shows no specific relationship between these two attributes and no obvious visual groupings of data points (Figure 6.24a). A cluster analysis approach based on  $A^*b$  and BMW<sub>i</sub> did not produce distinctive comminution classes due to the limited variability of BMW<sub>i</sub> and  $A^*b$ . In other words, automatic classification based on  $A^*b$  and BMW<sub>i</sub> is problematic at Cadia East. As an alternative a simple approach for data classification was adopted (Chapter 4). The data were classified based on variability of  $A^*b$  and BMW<sub>i</sub> around the respective mean values for the entire population.

Four classes were defined based on  $A^*b$  and BMW<sub>i</sub> (Figure 6.24b). These classes can be broadly interpreted as “hard to crush and hard to grind” (G2), “Soft to crush but hard to grind” (G3), “hard to crush but soft to grind” (G1) and “Soft to crush and soft to grind” (G4). “Soft” in the Cadia context should be interpreted as “relatively soft”. Table 6.5 represents the mean and standard deviation of comminution attributes ( $A^*b$  and BMW<sub>i</sub>) in each class.

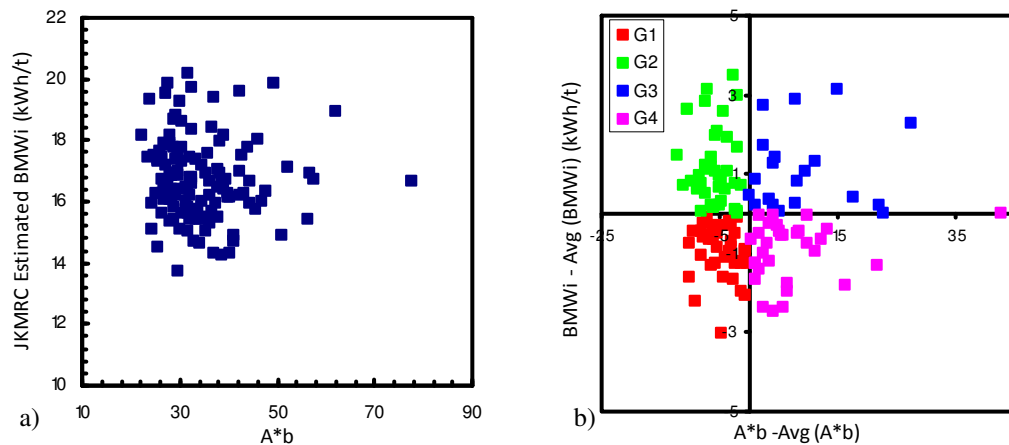


Figure 6.24. Cross-plots of A\*b versus Bond mill work index (BMWi) for all comminution samples from Cadia East (a) and a scatter plot of comminution data grouped by colors representing comminution classes (b) as defined in the text (G1 to G4). G1,G2,G3 and G4 are colored by red, green, blue and pink respectively

From Table 6.5, it is also evident that G1 and G2 classes are harder to crush (mean A\*b value of 29.2 and standard deviation of ~2.75) than G3 and G4 classes (mean A\*b value of 42.6 and standard deviation of 8.2). Likewise G2 and G3 classes are harder to grind (mean BMWi value 17.75 kWh/t and standard deviation of 0.95) than G1 and G4 classes (mean BMWi value of 15.7 kWh/t and standard deviation of 0.65).

Table 6.5 Mean and standard deviation of comminution parameters (A\*b and BMWi) in each class for test samples from all five drill holes of Cadia East.

Comminution Parameter	G1 (38 samples)	G2 (41 samples)	G3 (20 samples)	G4 (31 samples)
A*b	29.8 (2.9)	28.6 (2.6)	43.4 (8.1)	41.8 (8.3)
BMWi (kWh/t)	15.7 (0.6)	17.8 (0.9)	17.7 (1.0)	15.7 (0.7)

Means and standard deviations for petrophysical properties and geochemical assays were computed for the comminution classes using LogTrans software followed by prediction of classes for samples without comminution data. Selection of properties was based on trial and error during training to achieve the best suite of properties in terms of accuracy of prediction in individual control holes. Initially in each individual hole at Cadia, the prediction of classes was assessed based on training using data from the same hole to check whether parameters can be used for prediction. The population of each comminution class within each hole is something that needs to be carefully considered in each case as training classes with few members may significantly distort the prediction results.

Means and standard deviations of petrophysical parameters (P-wave Velocity, P-wave modulus, density and susceptibility) and geochemical attributes (Fe, S, Cu and Au) were calculated for comminution classes. There is considerable overlap of the spreads from one class to another, for all petrophysical and geochemical parameters. Therefore the individual class cannot reliably be uniquely identified on the basis of a single parameter but combination of parameters can increase the chance of correct prediction of the comminution classes. Although there is considerable overlap for P-velocity for all four classes, discrimination of two broad comminution classes (G1/G2 versus G3/G4) based on P-velocity is possible if the average in each class is considered (Figure 6.25a). This indicates potential for prediction of A\*b from P-wave velocity, as per Figure 6.16f. Classes G1 and G2 are characterized as hard to crush and have correspondingly higher P-wave velocity.

Statistics for density (Figure 6.25b) shows that the G4 class is relatively denser than other classes, this could be due to higher proportions of sulphide mineralization for G4 samples which is supported by the high sulphur content for these samples as well (Figure 6.25c). Geological information based on visual observations from drill cores supports the fact that G4 samples are mineralized with pyrite, hence higher density and sulphur content. Density separates G1/G4 from G2/G3, so density offers some potential for predicting BMWi.

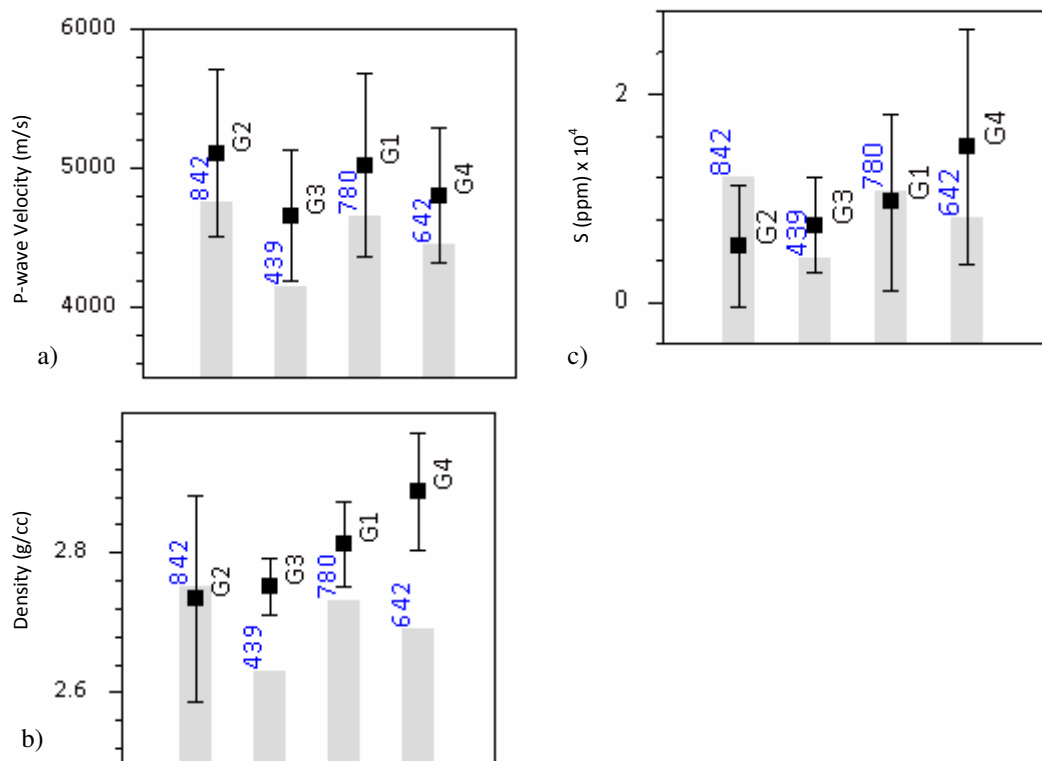


Figure 6.25. Averages and standard deviation of (a) P-wave velocity, (b) density and (c) sulphur content in comminution classes in five holes of Cadia East (CE082, CE098, CE109, CE110 and CE143). Black square = Average, black bar = standard deviation, grey histogram = number of samples for each comminution class.

The minimum distance algorithm (Chapter 4) was applied to petrophysical (P-wave velocity, P-wave modulus, density and susceptibility) and assay (Fe and S) data in order to predict the comminution classes using the LogTrans program (Fullagar et al, 1999).

In order to test the performance of the minimum distance classification technique in a “blind” hole, one hole was treated as an independent hole and interpreted based on a training set derived from the remaining holes.

The accuracy, based on the number of correct class predictions in each drill hole (CE082, CE098, CE109, CE110 and CE143) was greater than 60%. The classification results for CE082 and CE110 are presented in Figures 6.26 and 6.27 respectively. The comminution classes were predicted with an overall performance of 68% and 94% respectively. In addition to providing a prediction for the comminution test intervals, the algorithm predicts comminution classes in intervals between test samples. Thus comminution class is predicted continuously over depth ranges where petrophysical data and assays are available.

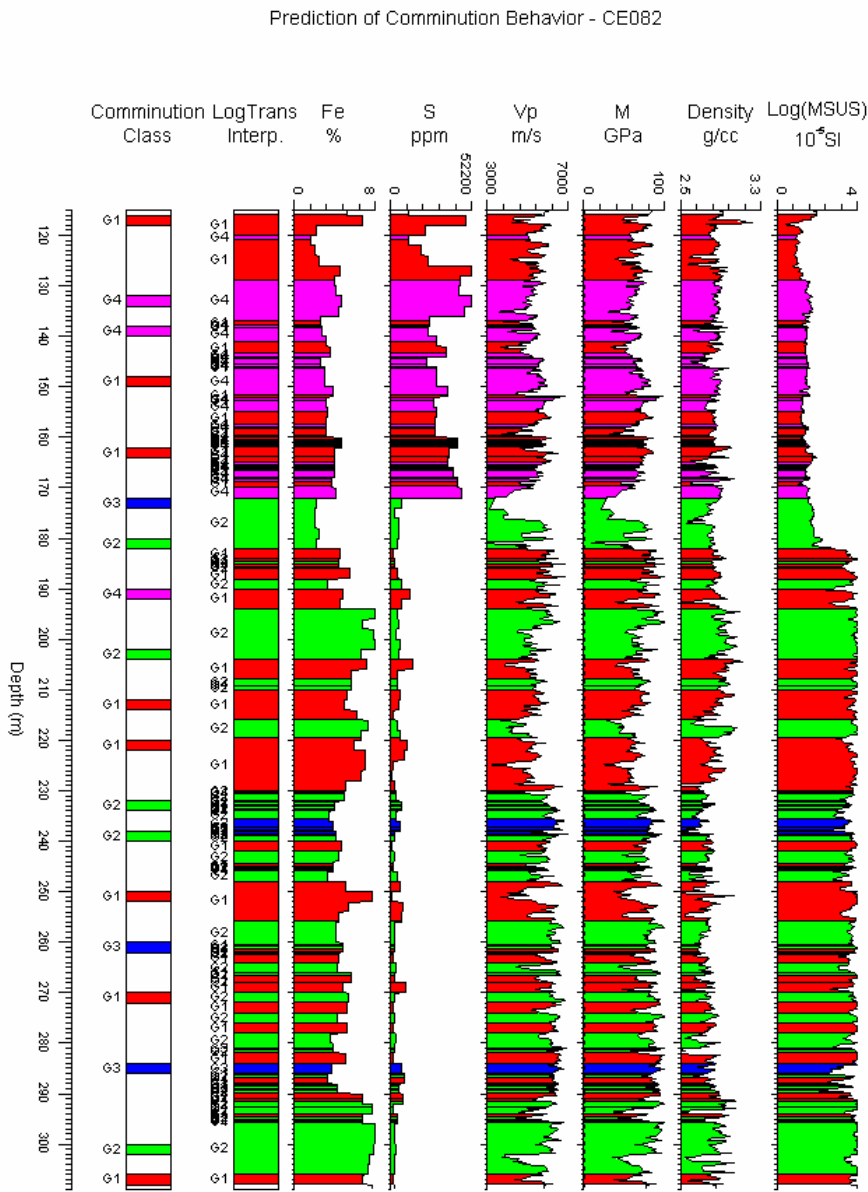


Figure 6.26. Prediction of comminution classes in drill hole CE082 (control hole) using LogTrans. The first column shows that comminution classes determined for training set. The second column is the predicted comminution classes based on petrophysical and assay data shown in the remaining logs. Note that P-modulus is denoted with M. LogTrans window length during fluster analysis was 0.25m.

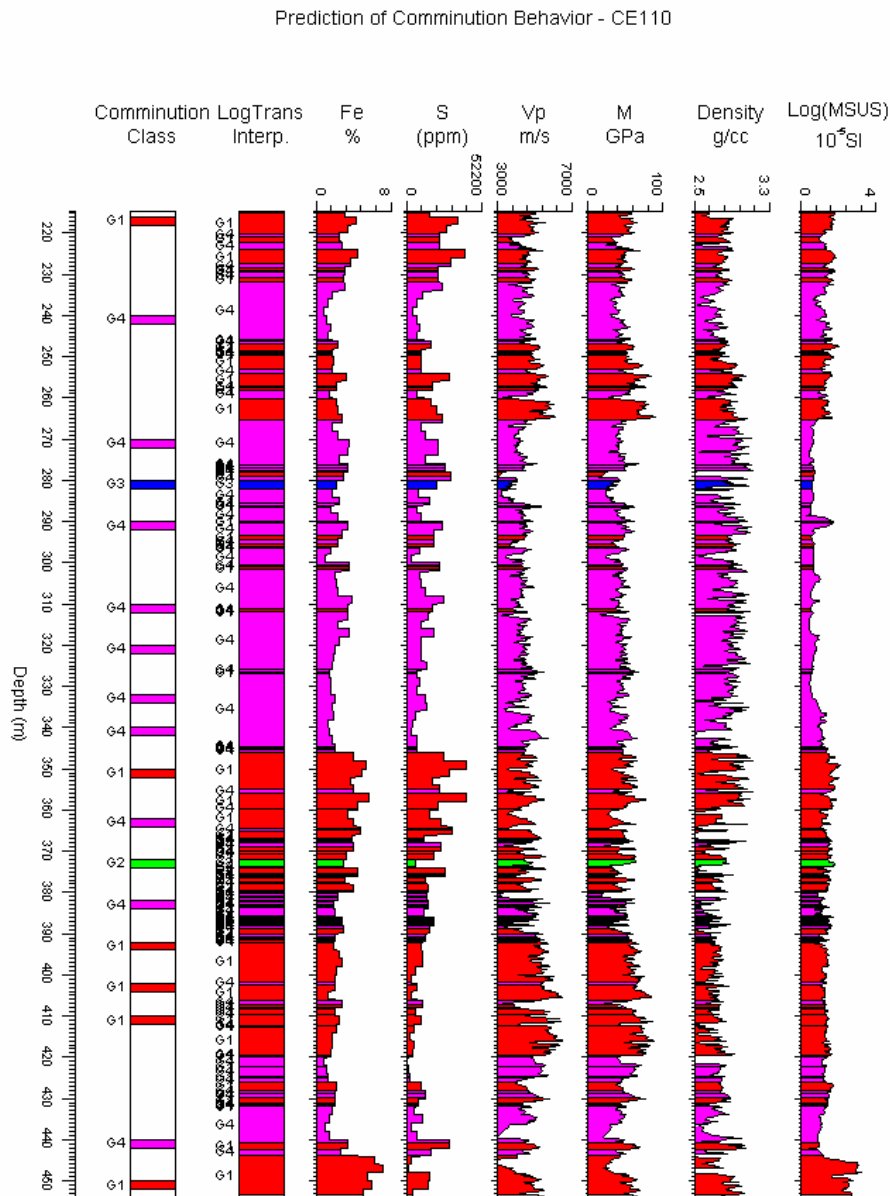


Figure 6.27. Prediction of comminution classes in drill hole CE110 (control hole) using LogTrans. The first column shows that comminution classes determined for training set. The second column is the predicted comminution classes based on petrophysical and assay data shown in the remaining logs. Note that P-modulus is denoted with M. LogTrans window length during fluster analysis was 0.25m.

In order to test the performance of minimum distance classification technique in a “blind” hole, one hole was tested as an independent hole and was interpreted based on a training set derived from the remaining holes. Each hole was treated as an independent hole in turn, and training was conducted on the other four holes. Table 6.6 shows the performance of prediction in each case. The performance of prediction for drill hole CE098 was poor. The main reason for this poor prediction is the fact that data from CE098 is very important in defining an effective training set.

Table 6.6. LogTrans performance in prediction of metallurgical classes in independent drill holes

Training Holes	Prediction Hole	Performance (%)
CE098, CE082, CE109, CE110	CE143	56
CE098, CE082, CE109, CE143	CE110	55
CE098, CE082, CE143, CE110	CE109	62
CE098, CE143, CE109, CE110	CE082	68
CE143, CE082, CE109, CE110	CE098	44

In order to assess the performance of the neural network technique for prediction of comminution classes, a similar approach to the minimum distance algorithm presented above was carried out.

Table 6.7 summaries the results of prediction of comminution classes in independent holes using neural network technique. The network in each case was developed based on data from training holes. In each case the best network structure was found when compared with ten different structures. A network structure of 6x2x4 indicates that 6 parameters are used as input to predict 4 comminution classes (output) based on 2 nodes in the hidden layer.

The number of node in hidden layer, although may improve the prediction performance of training set, however it does not necessarily have a better prediction performance for the test set. For example in prediction of CE143, a network structure of 6x3x4 showed a prediction performance of 74% for training set but a poor prediction for test set (24%).

Comparison of Tables 6.7 and 6.6 suggest that neural network performance for three holes (CE143, CE110 and CE098) is better than minimum distance algorithm. However given the time required for design and training of a network, application of minimum distance algorithm is significantly faster and less complicated than the neural networks approach. Neural networks can still be used as an alternative modeling approach for prediction of comminution classes. This comparison illustrates the trade-off that exists between the time available for data processing and the accuracy required in prediction of comminution behavior.

Table 6.7. Neural networks performance in prediction of metallurgical classes in independent drill holes

Training Holes	Prediction Hole	NN-Structure	Performance (%)
CE098, CE082, CE109, CE110	CE143	6x2x4	66
CE098, CE082, CE109, CE143	CE110	6x13x4	77
CE098, CE082, CE143, CE110	CE109	6x12x4	59
CE098, CE143, CE109, CE110	CE082	6x8x4	63
CE143, CE082, CE109, CE110	CE098	6x13x4	51

### 6.8.4. Comminution Modeling : CPC Approach

Integration of comminution parameters and petrophysical attributes and subsequent classification based on cluster analysis approach did not improve the classification conducted in section 6.8.3. This was mainly due to small variability of  $BMWi$  and  $A^*b$ .

### 6.9. Mill Throughput prediction

Estimates of  $A^*b$  and Bond mill work index enable prediction of mill throughput. An accurate universal prediction of  $BMWi$  was not possible for Cadia East samples. However comminution behaviour both in terms of crushing and grinding is characterized in section 6.8.3. Modeling based on comminution classes (Section 6.8.3) could therefore provide prediction of mill throughput for a given processing circuit.

The mill throughput model was developed by Kojovic (2009) using a set of engineering equations (similar to equations in Section 5.9). The equations for Cadia East is based on the existing Cadia Hill processing circuit (Figure 6.28), consisting of open circuit Semi Autogeneous Grinding (40 ft x 22 ft, 20MW installed power) followed by two closed-circuit ball mill (22 ft x 34 ft, 9MW installed power). The throughput model assumes a fixed target grind size ( $P_{80}$ ) of 150 microns and fixed feed size ( $F_{80}$ ) of 105mm. Studies by Kojovic (2009) indicated that mill throughput estimates based on engineering equations are consistent with actual throughput for Cadia Hill samples.

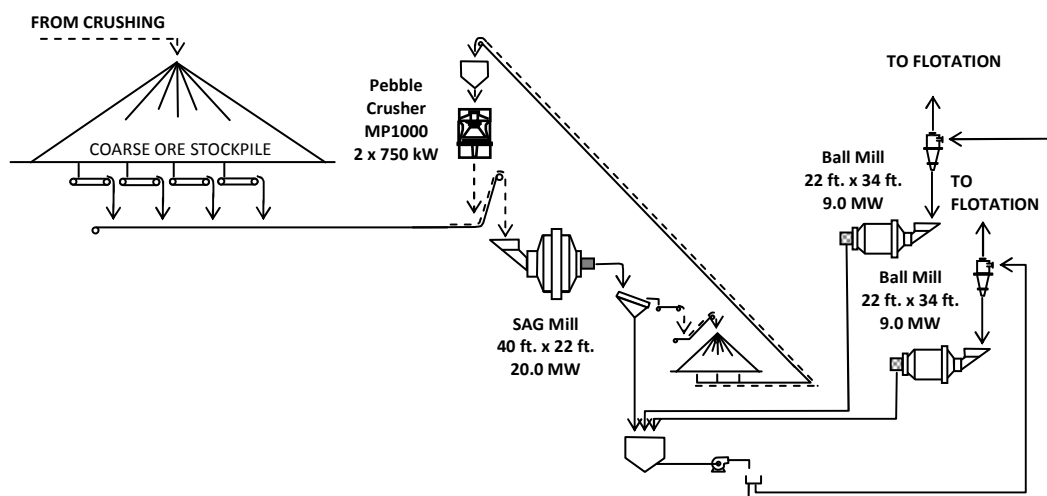


Figure 6. 28. Schematic diagram of Cadia Hill processing circuit (Kojovic, 2009)

Mill throughput was estimated for the comminution classes created in Section 6.8.3. The “G4” and “G1” classes have high throughput of 1884 t/h and 1828 t/h respectively. The samples of both “G1” and “G4” classes require relatively low energy for grinding (Table 6.5) and although “G1” samples are harder than “G4” in terms of crushing, the throughput estimation is not significantly affected. Also “G1” and “G2” samples both are hard in term of crushing whereas “G1” is easier for grinding than “G2”. “G2” and “G3” have lower throughput of 1626 t/h and 1696 t/h respectively because these classes require more energy for grinding (Table 6.5). Thus throughput is mainly governed by ore grindability, and little affected by crushability.

Given that the ores at Cadia East are hard both in terms of crushing and grinding, increasing the processing plant capacity to ~26Mtpa at Cadia Hill may be difficult. The relatively “soft” samples in terms of crushing and grinding are “G4” samples with average  $A^*b$  and  $BMWi$  values of 41.8 and 15.7 kWh/t respectively. Expected mill throughput for these samples is 1884 t/h and even if the processing plant operates continuously throughout the year, the ore processing rate will be ~16Mtpa. Estimated throughput is based on the existing Cadia Hill processing circuit (Figure 6.28). In reality not all Cadia East material will behave like “G4” samples and there are harder components (e.g. G2) as well. Moreover shutdown hours for maintenance of processing plant also need to be considered. Therefore in order to achieve the required capacity (26Mtpa), there will be a need for a major upgrade to current Cadia Hill processing plant to meet predicted throughput projections. Figure 6.29 represents predicted comminution classes in CE098 as an independent hole with statistics derived from other four holes (i.e. CE082, CE109, CE110 and CE143). Mill throughput (TPH) is predicted for CE098 for each inferred class using the class measured  $A^*b$  and  $BMWi$  presented in Table 6.5.

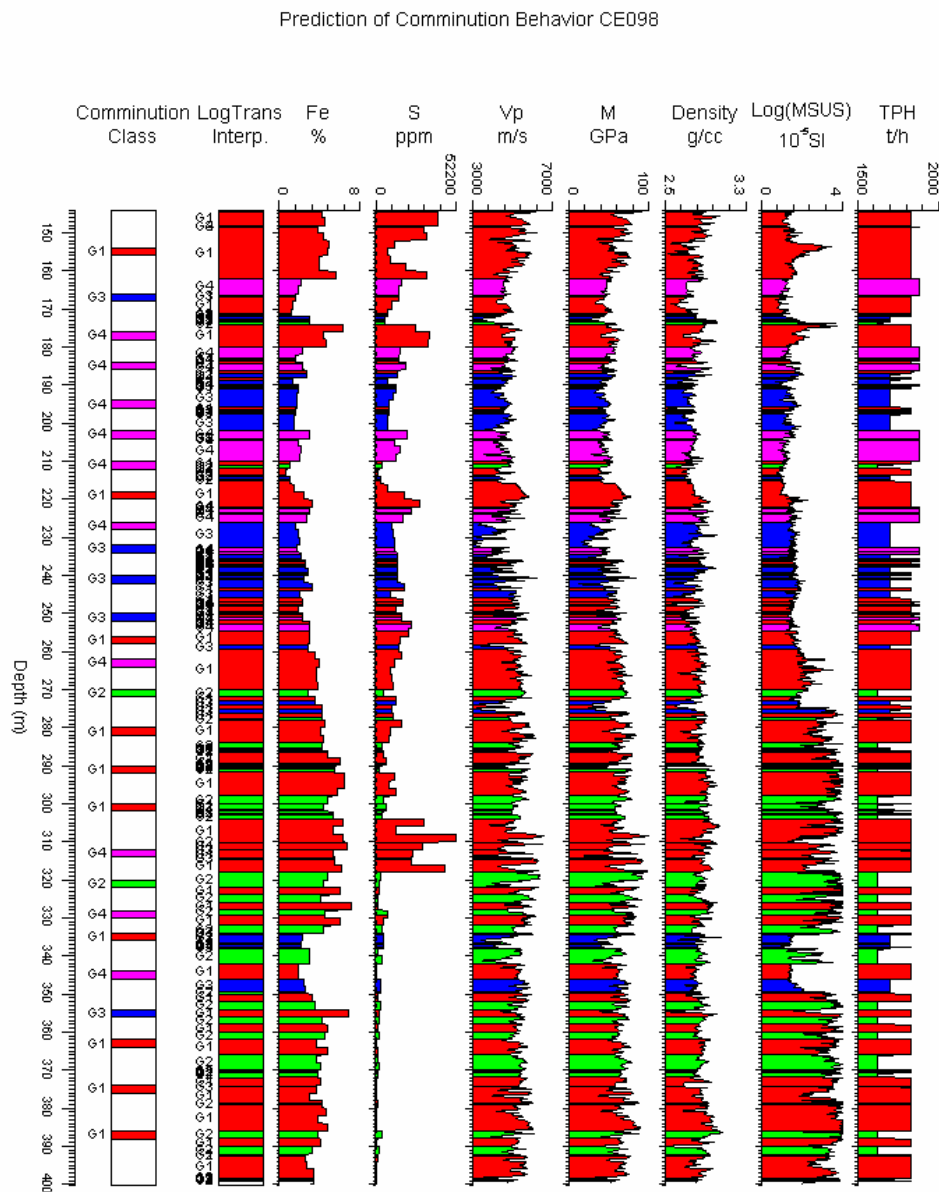


Figure 6.29. Prediction of comminution classes in independent drill hole CE098 using LogTrans. The first column shows the comminution classes. The second column is predicted comminution classes based on petrophysical and assay data. Note that P-modulus is denoted with M and estimated mill throughput is denoted with TPH.

In Chapter 5 mill throughput optimization using Alruiz et al (2009) approach was presented for Ernest Henry. Their approach for representation of mill throughput variability within comminution classes (Section 6.8.3) is applied here for Cadia East. Figure 6.30 shows the predicted mill throughput in all five drill holes of Cadia East. The drill holes here are assumed as proxy to mineable volumes and four comminution classes representing different ore types. The proportion of each comminution class that is assumed to be fed to the plant is shown for each analyzed drill hole. As can be seen from Figure 6.30, the predicted throughput at drill hole CE143 is lower compared to other

holes. At CE143 there is a high proportion of “G2” class which is hard to grind and crush (Table 6.5). One approach to reduce the mill throughput variability can be appropriate blending (Alruiz et al, 2009) of “clusters” before processing. As stated in Chapter 5, although this illustration is based on drill holes however it could provide a basis for effective plant optimization at mine sites.

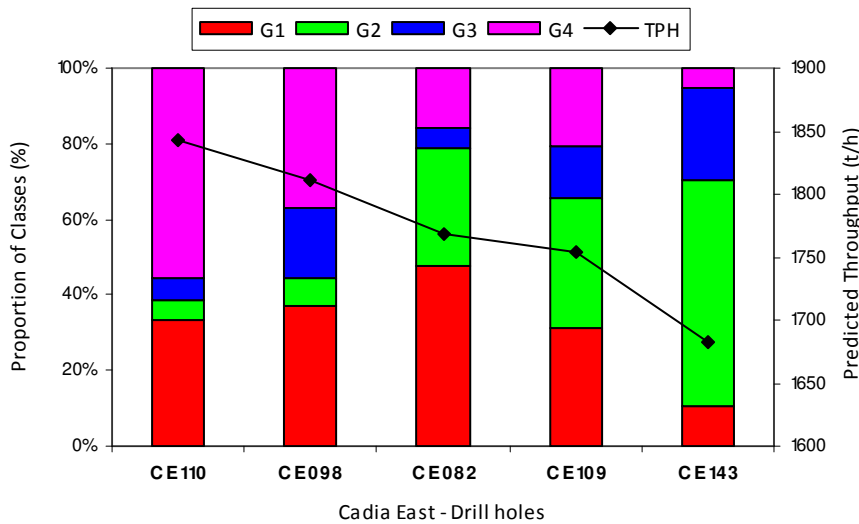


Figure 6.30. Proportions of comminution classes and predicted mill throughput. The drill holes are sorted according to proportion of G2 which is hard in terms of crushing and grinding.

### 6.10. Concluding Remarks

A Geotek multi-sensor core logger has been successfully deployed at Cadia East. After establishment of procedures and protocols, 1442m of high resolution core imagery and detailed petrophysical data were recorded over selected intervals from five drill holes.

The Cadia East ore is very hard both in terms of crushing and grinding also with very small dynamic range in  $A*b$  and  $BMWi$  values. Given the nature of the geological environment, and the relatively low sulphide contents at Cadia East, strong petrophysical contrasts were not expected. Therefore Cadia East is a challenging site for geometallurgical investigation and development of comminution models.

The single most important determinant of data quality is the size of the core. At Cadia East the bulk of the material presented to the logger was NQ half-core; this is marginal for reliable velocity and density determinations. In addition, the splitting of the core was poor over many intervals, with the result that the logger was often measuring wedges of

core, not half-core of consistent size. Variability in the “feed” for the logger translates into greater uncertainty in the petrophysical data.

Fundamentally, NQ half-core should be avoided if at all possible. If NQ half-core is the only material available, then the core boats should be re-designed, to prevent rotational sliding of the core, and preferably to permit direct contact between the fluid-filled roller and the underside of the core. The errors in production measurements across HQ half-core will probably be no larger than NQ half core, since the HQ core boat is wider and the core is heavier so there is less likelihood of significant rotation of one with respect to the other.

A number of interesting observations have been made on the basis of the Geotek data. For example a bimodal distribution of magnetic susceptibility is evident in holes CE082, CE098, CE109, and CE110. Magnetic susceptibility showed a negative correlation with ore crushability ( $A^*b$ ), this was the reverse of the trend observed at Ernest Henry. The high magnetic susceptibility samples at Cadia East are associated with propylitic or skarn alteration that have low  $A^*b$  (i.e. hard to crush). Magnetic susceptibility can be useful as a tool for geometallurgical domaining at Cadia East. Magnetic susceptibility measurement is cheap, fast, quantitative and non-destructive.

BMWi can not be modeled accurately based on petrophysical properties using multiple regression or neural networks. Although both petrophysical properties and BMWi are controlled to some extent by mineralogy, the lack of a clear relationship between BMWi and petrophysical properties may be explained by the way that these properties are measured. The petrophysical properties are measured on intact rock samples while BMWi is measured on composite ground samples from 2m of core. Errors in estimation of BMWi and petrophysical properties are factors which may contribute in poor correlation between these properties.

Several different comminution modeling approaches were investigated. First a universal model was sought, for all the data. A global correlation has been recognized between P-wave velocity and  $A^*b$ , a measure of crushability. Similarly, a weak global correlation has been observed between susceptibility and  $A^*b$ . A multiple regression of P-wave modulus and magnetic susceptibility based on all comminution test samples can be used for prediction of  $A^*b$  with a relative prediction error of 13.2%. A neural network technique for prediction of  $A^*b$  using the same parameters achieved a relative prediction error of 11.8%.

Geometallurgical class definition based on geological (GC) or petrophysical properties (PC) did not show a significant comminution contrast between the classes in terms of ore crushability and grindability. This was mainly attributed to small dynamic range of both  $A^*b$  and  $BMWi$ . To characterize comminution behavior more effectively, comminution classes were created based on  $A^*b$  and  $BMWi$  (CC approach). Four comminution classes were defined based on variability of  $A^*b$  and  $BMWi$  around the respective mean values for the entire population. Created classes were linked to petrophysical (P-wave velocity, density, P-wave modulus, magnetic susceptibility) and geochemical attributes (Fe and S).

The performance of the minimum distance algorithm and neural network approach for prediction of comminution classes were assessed. Neural network showed better performance (~10%) than minimum distance algorithm in prediction of comminution classes in three holes (CE143, CE110 and CE098). Given the time required for design and training of a network, application of the minimum distance algorithm is probably more productive than the neural networks approach. Nevertheless neural network technique can be used as an alternative to conventional approaches such as minimum distance algorithm.

Given that the ores at Cadia East are almost uniformly hard in terms of comminution, increase of processing plant capacity to ~26Mtpa at Cadia Hill can be difficult. Estimated mill throughput for “relatively” soft samples is 1884 t/h which translates to ~16Mtpa if shutdown hours for maintenance of equipments are not considered. Hence increasing the processing plant capacity to 26Mtpa as planned by Newcrest Mining, will certainly need an upgrade to current Cadia Hill processing plant.

# CHAPTER 7

---

## Prediction of Petrophysical Properties from Core Imagery

### 7.1. Introduction

Photographs and digital images of hand samples, core slabs and drill cores are often captured by geologists as a record of rock to which their observations of lithology, mineralogy, texture and alteration refer. Capturing and archiving core photographs have been adopted as an essential step during core material handling at most Chilean mines (Cardenas, 2009). This is especially helpful in cases where whole cores need to be destroyed for mechanical testing or assaying. The technology to acquire high quality digital core images is now available. The cost and logistics for deployment of core image acquisition systems at mine sites are very small compared with other costs in a mining operation (e.g. exploration drilling).

There are many applications for core image analysis, ranging from mineralogical to geomechanical studies. Lemy et al, (2001) have investigated the potential applications of digital core images for geomechanical purposes and have presented an image processing algorithm for determination of core recovery, and detection of breaks on drill cores, hence determination of RQD.

Core images can also be used for automatic classification of the volumetric proportions of minerals and rock texture using sophisticated image processing software e.g. Definiens (<http://www.definiens.com>). Automated estimates of mineral abundances and texture can be used to characterize ore processing behavior (Berry, 2009).

Within the AMIRA P843 project, core images from Cadia East and Ernest Henry were captured using the Geotek MSCL system (Chapter 3). The core images from Cadia East were not of sufficient quality for image analysis and classification, as discussed in Chapter 3. However, an upgrade to the MSCL camera system prior to the start of Ernest Henry core logging made it possible to acquire high quality images for image analysis and processing.

The Ernest Henry core images were analyzed and then classified via an object oriented approach (Berry, 2008a) to map occurrences of the key mineral phases. The classified

core images from Ernest Henry have been used extensively during the P843 project for textural analysis in an attempt to relate textural information to ore processing performances (Bonnici et al, 2009; Hunt et al, 2009; Leigh, 2009). Such information provides estimate of minerals grain size and their size distribution. Analysis of grain size distribution for the mineral of interest provides an estimate of the “target” grind size for mineral liberation. This enables effective planning and selection of comminution equipment.

Classified core images can also potentially be used to predict petrophysical properties continuously along the entire drill hole. Prediction of petrophysical properties from core images can be carried out in different ways. Oyno et al (1998) have applied a partial least square regression to calibrate ten different textural features derived from image analysis against measured petrophysical properties (porosity and gas permeability).

Prediction of petrophysical properties from core images can be conducted using the Voigt and Reuss bound models (Section 7.3) if volume estimates of minerals and their intrinsic property values (petrophysical properties) are known. In general the relationships between the intrinsic properties of the minerals, their volume fractions and the bulk properties of the rock are more complex than this simple assumption implies. The physical properties of minerals are not fixed but rather are bounded within certain limits. There is significant uncertainty owing mainly to the variability of chemical composition of mineral species. The Voigt and Reuss models are very simple and do not account for geometric distribution of the constituents of rock samples. If the uncertainties in mineral composition and associated physical properties can be recognized, then an upper and lower limit can be defined for prediction of petrophysical properties from core images.

Given that bulk density is mainly dependent on rock mineralogy, classified core images have good potential for prediction of density if accurate estimates of the volume fraction of each mineral and its density are available. Porosity is treated as a single mineral phase in this context.

Density is an important physical parameter due to its influence on ore resource and reserve estimation. Density is also an important parameter for mill throughput estimation. Nevertheless, it is surprising how little attention is paid to density variations at some mine sites. The most efficient form of density measurement is gamma-gamma logging. However, downhole density logging is rarely conducted in metalliferous mines. There are many reasons for low utilization of downhole density logging (Mutton, 1994), including

concerns over use of probes with radioactive sources at mine sites. Accurate prediction of density from core images could provide an alternative means for continuous density estimation. Prediction of density from core imagery would represent an important new method for density determination at some mines. In highly porous rocks, density prediction from core imagery can be difficult, however porosity can also be estimated from core imagery.

Core images are 2D representations of what is fundamentally a 3D system. This means that both estimates of mineral grade and prediction of petrophysical properties from images could suffer from a lack of three-dimensional information. The errors introduced in this way would be greatest when core materials are not isotropic. Given the generally non-directional character of the brecciated felsic volcanoclastics at Ernest Henry, such errors are unlikely to be significant (Leigh, 2009) and are regarded as a minor issue in prediction of physical properties. The main error in prediction of mineral grades is attributed to inaccuracy in mineral identification and the fact that mineral grains are often smaller than the effective resolution of the images (Berry, 2008b).

The core images are likely to be more representative of rock sample than local Geotek density and P-wave velocity measurements. This is because cores are imaged continuously whereas the Geotek gamma density and P-wave velocity measurements are conducted every 9cm along the core (Chapter 5) and are representative of only a 5 – 10mm column through the core.

Accurate prediction of bulk properties is difficult given the uncertainties in the underlying bound models, intrinsic properties of minerals and estimated volume fraction of minerals. In order to generate accurate bulk property prediction using simple bound models, either the intrinsic properties or volume fraction of mineral phases may need to be adjusted.

This Chapter describes prediction of density, P-wave velocity and susceptibility from classified core images from Ernest Henry. The mineral grade estimated from core images for prediction of comminution attributes ( $A^*b$  and  $BMWi$ ) is also illustrated. The work presented in this chapter is an initial exploration of potential for prediction of petrophysical properties from core images.

The challenge is to assess the validity of mineral grades estimated from core images. If the volume estimates of mineral phases are sufficiently accurate then they can potentially be used for prediction of physical properties. Unfortunately the optical estimates of mineral phase abundance were not comparable with assay data at Ernest Henry. As a

result the predicted density values based solely on the classified images were not directly comparable with measured values (average relative error of 8.9%).

A linear programming algorithm developed by Fullagar (2009) has been used to improve the volume estimates of mineral phases. The correlation between the volume fraction of mineral phases and geochemical assays improved after applying the linear algorithm. This approach improved the density prediction (average relative error of 3.5%) and encouraged attempts to predict magnetic susceptibility and P-wave velocity. However prediction of P-wave velocity is more difficult than susceptibility as will be discussed in Section 7.5.5.

The improved estimates of mineral phase volumes also provided an additional means for estimation of  $A^*b$  and  $BMWi$  from the classified images (Section 7.6) and enabled these parameters to be estimated in intervals of core where these measurements are not available. Continuous estimates of mill throughput can then be predicted from the comminution attributes.

## 7.2. Core Image Processing

Petrophysical properties (density, P-velocity, magnetic susceptibility) and core imagery were collected on drill cores from six selected drill holes from Ernest Henry as described in Chapter 5. Drill core images were captured continuously at 9cm intervals (optimum sampling interval) and then were stitched together by Geotek MSCL software into ~1m length (i.e. core section length). The imaging camera produces high resolution (40  $\mu\text{m}$  pixel) RGB colour imagery.

Core images were classified using Definiens Developer software in order to produce a classified mineral image (Figure 3.3). Details of image analysis and classification are described by Berry (2008b). The output data from image analysis of a one meter section of core is the area of identified mineral phases, ignoring gaps between core pieces, and writing or marks on core pieces (e.g. depth). The number of pixels for each mineral species is divided by the total number of pixels assigned to all mineral phases, to yield a fractional volume for each phase for each 1m intervals. Averages of these estimates over adjacent 1m intervals were then calculated for 2m assay intervals, in order to facilitate combined analysis of mineral grades with assay data. The predominant individual mineral phases identified for Ernest Henry drill cores are quartz, pyrite, chalcopyrite, magnetite, chlorite and K-feldspar. In addition, four mixed mineral phases were defined. Fine-

grained aggregates comprised predominantly of feldspar, magnetite and chlorite were present in drill cores. The grain size of the minerals in these aggregates was too small to be resolved by the Geotek logger cameras. Therefore two mixture classes, “magnetite/chlorite” and “magnetite/feldspar”, were defined during image analysis. Reliable separation of carbonate and quartz was difficult from core images as these two minerals are both light in colour. Therefore the two other mixture classes were “felsic” (consisting of quartz, feldspar and carbonate) and “quartz/carbonate”. Table 7.1 summarizes the identified mineral phases and mixtures from Ernest Henry drill core images.

Table 7.1. Summary of mineral phases and mixtures identified at Ernest Henry

Individual Mineral Phase	Mixture Phase
Quartz	felsic (Quartz, K-feldspar, carbonate)
K-Feldspar	magnetite/chlorite
Pyrite	magnetite/k-feldspar
Chalcopyrite	quartz-carbonate
Chlorite	
Magnetite	

### 7.3. Bound Models

Many models have been published, attempting to describe theoretically the effective physical properties and elastic moduli of rocks and sediments (Mavko et al., 1998). The simplest models are those proposed by Voigt (1910) and Reuss (1926) who developed averaging schemes to estimate the elastic constants (e.g. bulk modulus) of a mixture of material phases (Schön, 1996). Equations 7.1 and 7.2 define the Voigt and Reuss models respectively. The models are based on the physical property of rock phases and their corresponding volume fractions. In the Voigt estimate,  $K_V$ , for a mixture of  $n$  phases is defined by

$$K_V = \sum_{i=1}^n K_i V_i \quad (7.1)$$

and the corresponding Reuss estimate,  $K_R$ , is defined by

$$\frac{1}{K_R} = \sum_{i=1}^n \frac{1}{K_i} V_i \quad (7.2)$$

where  $V_i$  is the volume fraction of the  $i$ th component and where the total volume is 1.  $K$  can be any elastic constant or desired geophysical attribute. For density and, arguably, for

low values of susceptibility, the Voigt average *is* the bulk property. For other properties, the Voigt average represents an upper bound (maximum bulk property) and the Reuss average a lower bound (minimum bulk property). However such interpretation is not always true. For example, a small volume fraction of pyrrhotite can dramatically increase the conductivity of a sample because it tends to create pervasive networks. The Voigt estimate is not a maximum in such cases; the true maximum is close to the conductivity of pyrrhotite. The Voigt model does not account for the natural tendency of pyrrhotite to establish networks, i.e. its texture. “Percolation threshold” models attempt to capture this type of behaviour (Fallon, 2003). These simple models (Voigt and Reuss) do not consider the geometric distribution of the constituents of rock samples (i.e. texture). Hill (1952) introduced the arithmetic mean of the two estimates from Voigt and Reuss models as a best estimate for elastic properties.

Hashin and Shtrikman (1963) proposed an alternative model that has been widely used in petroleum research for elastic moduli estimation. The Hashin and Shtrikman (HS) model provides upper and lower bounds of bulk and shear modulus that are generally narrower than the Voigt (upper bound) and Reuss (lower bound) models. Upper and lower bounds derived from the HS model are discussed in detail by Mavko et al (1998). Estimates of bulk and shear modulus derived from the HS model and predicted bulk density from the Voigt model enable calculation of P-wave velocity. At Ernest Henry, the predicted upper and lower bounds for P-wave velocity using the HS model were generally very similar and close to the bounds predicted using the Voigt and Reuss models (within the range of experimental error). The Voigt and Reuss mixing models have been utilised for petrophysical parameter estimation throughout this study due to their simplicity and the fact that they provide values that agree closely with the more complex HS model predictions.

#### **7.4. Intrinsic Properties of Minerals**

Each mineral has a set of physical and chemical properties known as intrinsic properties. Intrinsic properties are usually not well defined discrete values, but are often irregularly distributed. There are three main reasons for the dispersion of intrinsic properties. Firstly, many minerals exhibit a range of compositions. For example “chlorite” does not have a unique chemical composition: chlorite composition depends upon relative abundance of Mg, Fe, Al, and F. Secondly, physical properties of chemically pure minerals provide a benchmark in most geophysical studies but they are not necessarily relevant to the natural

world since naturally occurring mineral samples are impure in almost all cases. Thirdly, direct measurement of naturally occurring mineral properties usually involves multiple mineral grains and hence is affected by mineral boundaries and texture.

The petrophysical properties of the minerals identified from classified core images of Ernest Henry were compiled from the published literature (Table 7.2). There is a wide range for physical properties of some minerals e.g. P-wave velocity of magnetite which varies from 4180-7400m/s or density of chlorite which varies from 2.6-3.3g/cc (Klein and Hurlbut, 1985). A common problem with published data is that the researchers have not fully documented the experimental procedures nor fully described the samples. In some cases the averages of measurements are reported (Rzevsky and Novik, 1971) but there is no indication of the number of measurements or their variability. Even the anomalously low P-wave velocity of 4180m/s and low density of 4.81 g/cc for magnetite (Mavko et al, 1998) has not been clarified.

Table 7.2. Physical properties of key Ernest Henry minerals as compiled from published literature.

Mineral	Density (g/cc)	Vp (m/s)	Vs (m/s)	Reference
Quartz	2.65	6050	4030	(Rzevsky and Novik, 1971)
	2.65	6060	4106	(Fallon,2003)
	2.65	6050	4090	(Mavko et al, 1998; Schön, 1996)
Calcite	2.71	6320	3500	(Rzevsky and Novik,1971)
	2.70	6260	3420	(Mavko et al, 1998)
	2.71	6640	3440	(Mavko et al, 1998)
	2.71	6540	3430	(Schön, 1996 )
	2.71	6607	3415	(Fallon, 2003)
K-Feldspar	2.54	5680	3090	(Rzevsky and Novik, 1971)
	2.57	5690	3260	(Schön, 1996)
	2.63	6460	3120	(Mavko et al, 1998)
	2.55	5590	3060	(Fallon,2003)
Pyrite	5.03	7300	4980	(Rzevsky and Novik, 1971 )
	4.81	7700	4780	(Mavko et al, 1998)
	4.93	8100	5180	(Mavko et al, 1998)
	5.01	8043	4972	(Fallon, 2003)
	5.01	7920	5060	( Schön, 1996)
Chalcopyrite	4.23	4530	2720	(Fallon, 2003)
	4.20	-	-	(Schön, 1996)
	-	5500	-	(Salisbury et al, 1998)
Chlorite	2.80	-	-	(Schön, 1996)
	3.07	4916	2700	(Fallon, 2003)
	2.6-3.3	-	-	(Klein and Hurlbut, 1985)
Magnetite	5.17	6820	4220	(Rzevsky and Novik, 1971)
	5.18	7390	4200	(Schön, 1996)
	5.18	7400	4190	(Fallon, 2003)
	4.81	4180	1970	(Mavko et al, 1998)
	5.20	7380	4190	(Mavko et al, 1998)

Given the uncertainties in intrinsic properties of minerals and in estimates of mineral grades, accurate prediction of bulk properties from core imagery is difficult. However if

estimated mineral grades correlate well with assays, then greater confidence in prediction of petrophysical properties is justified. Otherwise the uncertainty in mineral grades can be reduced by adjustment of volume fraction of phases (Section 7.5.2) using geochemical assays and the information in Table 7.3. To adjust mineral grades using geochemical assays, the weight percent (wt %) of major elements is required (Section 7.5.2). Fe, S and Cu are the major elements at Ernest Henry. The mineral densities in Table 7.3 were used to predict density of Ernest Henry drill cores from classified core images using equations (7.1) and (7.2).

Determination of the weight percent of Fe and Mg in chlorite is not easy due to the variable substitution of these of these elements in the chlorite lattice. The chemical composition for chlorite is not universally agreed. The chlorite formula of Whitten and Brooks (1972) was adopted in this study for determination of its wt% Fe (Table 7.3). The weight percent of Fe in chlorite was calculated based on assumed two chlorite end members (Fe free and Mg free). The Mg free and Fe free members are considered to represent the highest and lowest chlorite density (i.e. 3.3g/cc and 2.6g/cc) respectively. The weight percent of Fe calculated for Mg-free chlorite (3.3g/cc density) was 38.77%. The weight percent of Fe for chlorite with a density of 2.95g/cc was then estimated as half of the wt% for Mg-free chlorite.

Table 7.3. Elemental wt% and densities assumed for key Ernest Henry minerals

Mineral	Composition	Density (g/cc)	Fe (Wt%)	Cu (Wt%)	S (Wt%)
Quartz	SiO <sub>2</sub>	2.65	0	0	0
Calcite	CaCO <sub>3</sub>	2.71	0	0	0
K-Feldspar	KAlSi <sub>3</sub> O <sub>8</sub>	2.63	0	0	0
Pyrite	FeS <sub>2</sub>	5.03	46.7	0	53.3
Chalcopyrite	CuFeS	4.2	30.5	34.6	34.9
Chlorite	(Mg,Fe) <sub>10</sub> Al <sub>2</sub> (Si,Al) <sub>8</sub> O <sub>20</sub> (OH,F) <sub>16</sub>	2.95	19.38	0	0
Magnetite	Fe <sub>3</sub> O <sub>4</sub>	5.17	72.4	0	0

Whitten and Brooks (1972) have stated an approximate density of 3.0g/cc for chlorite. This corresponds well to 2.95 g/cc, the midpoint of the density range quoted by Klein and Hurlbut (1985). The published density values for quartz and calcite are constant at 2.65 and 2.71 g/cc respectively. Densities of other minerals in Table 7.3 were selected from Table 7.2 on a somewhat subjective basis due to the ranges and inherent uncertainties in published values.

## 7.5. Prediction of Petrophysical Properties

The following subsections illustrate prediction of petrophysical properties from core images. First density is predicted from the original classified optical mineral grade estimates from core images. The predicted values do not compare well with measured density. Then in order to improve the prediction accuracy of density, an algorithm is presented to adjust the volume fraction of mineral phases to accord with assay data. After assay-based volume adjustment, a good agreement between measured and predicted density is achieved. Prediction of magnetic susceptibility and P-wave velocity is then considered, using the adjusted mineral grade model. Finally, direct prediction of comminution attributes from mineral grade is illustrated.

### 7.5.1. Prediction of Density from Visual Mineral Grade Estimates

As stated in Section 7.2, six main individual mineral phases and four mineral mixtures were identified from image analysis of Ernest Henry drill core samples (Table 7.1). Initially, constituents of mixtures were assumed to be present in equal proportion (i.e. 50:50 for magnetite/chlorite, magnetite/feldspar, and quartz/carbonate and 33:33:33 for quartz/feldspar/carbonate in felsic). Under this assumption, and using the “best information” density estimates (Table 7.3), bulk density was computed from the original visually estimated fractional volumes using equation 7.1.

Medians of measured Geotek densities over 2m assay interval were computed in each drill hole from Ernest Henry for comparison with predicted densities. Measured densities have a Normal distribution (Chapter 5); hence medians or averages of density over 2m intervals were similar. The comparison of these initial calculated densities with measured densities (i.e. medians over 2m assay intervals) from all six drill holes is illustrated in Figure 7.1. The average relative error of prediction is 8.9%. In each drill hole the predicted densities were higher than measured densities and the correspondence was poor.

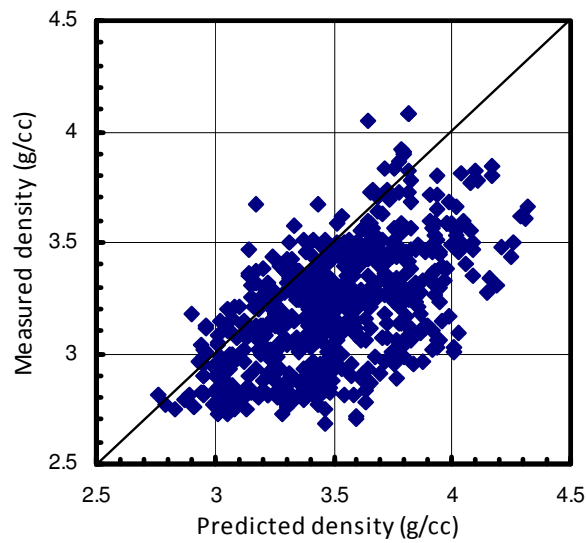


Figure 7.1. Predicted density from classified core images, based on original volume estimates, versus measured density (i.e. medians of 2m assay intervals) for samples from six Ernest Henry drill holes.

The large discrepancy between measured and predicted density might be caused by the assumption of uniform distribution of minerals in the mixed classes. Comparison of magnetic susceptibility with total volume fraction of magnetite estimated assuming 50:50 distributions for magnetite/chlorite and magnetite/feldspar showed a poor correlation (Figure 7.2a). Similarly, the total estimated volume fraction of magnetite showed no correlation with Fe grade (Figure 7.2b). Likewise, Figure 7.2c shows that there is no obvious correlation between estimated volumes of chalcopyrite and magnetite. This is in conflict with the observation (presented in Chapter 5) that Fe and Cu grade correlate well at Ernest Henry, assuming that volume fraction of magnetite correlates Fe grade. Finally, and perhaps the most compelling observation is that the volume fraction of chalcopyrite showed no correlation with Cu grade (Figure 7.2d). These observations reveal that the original estimated fractional volumes are inconsistent with assays and with measured density and susceptibility.

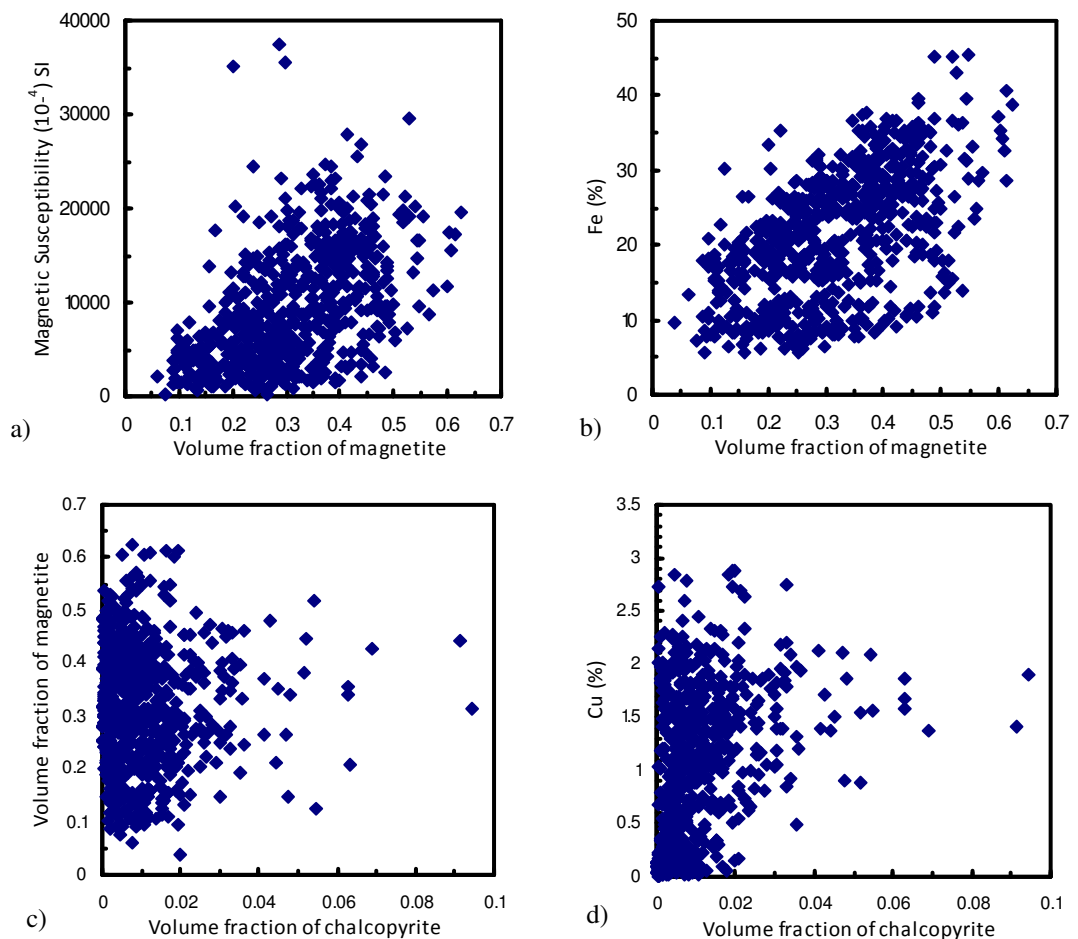


Figure 7.2. Correlation between total volume fraction of magnetite based on original image classification and (a) magnetic susceptibility and (b) Fe grade at Ernest Henry. Correlation between original image-based estimate of volume fraction of chalcopyrite versus and (c) total volume fraction of magnetite and (d) Cu grade. All samples are 2m assay intervals from all six drill holes.

### 7.5.2. Assay-based Volume Correction of Mineral Phases

In order to improve the accuracy of density prediction from Ernest Henry core imagery, the volume fraction of each mineral phase was adjusted in order to ensure that the calculated elemental compositions match the assay data.

Assay data are always available within ore zones. If a sufficient number of elements are assayed, assays alone can provide an estimate of modal mineralogy for simple mixing models (Zhang and Whiten, 2001). At Ernest Henry the assays can be used to check the consistency of the fractional volumes estimated from core images. The major assay elements used here are Cu, S, and Fe.

A linear programming algorithm developed by Fullagar (2009) based on the SIMPLEX algorithm (Morris, 1993) was used to adjust the volume fraction of mineral phases and their proportion in mixed phases. The program determines the extreme point of an objective function (i.e. minimum or maximum) while taking into account a series of constraints. The Cu, S, and Fe assay constraints applied to the Ernest Henry volumes are prescribed below:

$$V_{\text{cpy}} \times \text{Cu}_{\text{cpy}} \times \rho_{\text{cpy}} = \rho_{\text{Sample}} \times \text{Cu}(\%) \quad (7.3)$$

$$V_{\text{cpy}} \times \text{S}_{\text{cpy}} \times \rho_{\text{cpy}} + V_{\text{py}} \times \text{S}_{\text{py}} \times \rho_{\text{py}} = \rho_{\text{Sample}} \times \text{S}(\%) \quad (7.4)$$

$$V_{\text{cpy}} \times \text{Fe}_{\text{cpy}} \times \rho_{\text{cpy}} + V_{\text{py}} \times \text{Fe}_{\text{py}} \times \rho_{\text{py}} + V_{\text{mt}} \times \text{Fe}_{\text{mt}} \times \rho_{\text{mt}} + V_{\text{chl}} \times \text{Fe}_{\text{chl}} \times \rho_{\text{chl}} = \rho_{\text{Sample}} \times \text{Fe}(\%) \quad (7.5)$$

where  $V_{\text{mineral}}$  and  $\rho_{\text{mineral}}$  are the total volume fraction of each mineral phase and the corresponding mineral density respectively.  $\text{Cu}_{\text{mineral}}$ ,  $\text{S}_{\text{mineral}}$ , and  $\text{Fe}_{\text{mineral}}$  are the weight percent of copper, sulphur, and iron in that mineral, as per Table 7.3. Chalcopyrite, pyrite, magnetite and chlorite are abbreviated as “cpy”, “py”, “mt” and “chl” respectively. For example  $\text{Cu}_{\text{cpy}}$  is the weight percent of copper in chalcopyrite, i.e. 34.6%.  $\text{Cu}(\%)$ ,  $\text{S}(\%)$  and  $\text{Fe}(\%)$  are chemical assays, i.e. weight percent of copper, sulphur and iron respectively in total sample. The bulk density,  $\rho_{\text{Sample}}$ , is an unknown parameter and has the following form:

$$\rho_{\text{Sample}} = \sum_{i=1}^n \rho_i V_i \quad (7.6)$$

where  $\rho_i$  is the density of the  $i$ th mineral and where  $V_i$  is the corresponding fractional volume of that mineral.

The physical properties assigned to the minerals in equations (7.3), (7.4) and (7.5) are compiled in Table 7.3. The program maximizes or minimizes the density for each sample subject to assays for Fe, S and Cu and subject to the volume balance condition (i.e. total volume equal to 100%).

The overall magnitude of the changes to the fractional volumes is restricted according to the estimated accuracy of the initial mineral volume estimates. The sum of absolute errors for the ten mineral classes is bounded. These errors are visualized as realizations of ten independent Normal random variables with mean zero. The error condition imposed on the volumes is

$$\sum_{j=1}^{10} \left| \frac{\delta v_j}{\epsilon} \right| \leq 10 \sqrt{\frac{2}{\pi}} \quad (7.7)$$

where  $\delta v_j$  denotes the change in fractional volume for the  $j$ th class (the mixtures being classes, as well as the individual minerals), and where  $\epsilon$  is an estimate of the uncertainty in the fractional volume estimates. The RHS of (7.7) is the expected value for the sum of absolute values (Parker and McNutt, 1980). In other words, if an error with standard deviation 0.01 is attributed to the initial fractional volume estimates, then  $\epsilon=0.01$ , and the total change to the original class volumes is restricted by the condition that

$$\sum_{j=1}^{10} |\delta v_j| \leq 0.08 \quad (7.8)$$

The program has no solution in cases when the assay conditions (Eqns 7.3 to 7.5) and the volume balance condition can not be met for volume changes small enough to satisfy the error condition (Eqn 7.7). The higher the error ( $\epsilon$ ) considered, the less likely the program is to fail as more degrees of freedom are allowed to change in volume fractions. The level of error in original volumes for all six drill holes was considered to be about 3% (i.e.  $\epsilon=0.03$ ). Adopting this value for  $\epsilon$  resulted in failure of the program for only a few samples from each drill hole.

There is uncertainty attached to the mineral properties and, in some case, to the mineral composition, as well as to the estimated mineral grades from core images. However, for simplicity, only errors in volumes are included explicitly here.

Minimum and maximum densities were predicted from core images and assays during adjustment of volumes. Predicted minimum and maximum densities for samples of all six drill holes are in strong correlation ( $R^2=0.99$ ) but predicted maximum densities are higher than minimum densities by about 1%. This small difference between maximum and minimum densities is due to an increase in adjusted volume fraction of magnetite when density for each sample is maximized.

The volume adjustment approach produced volumetric estimates of mineral phases which satisfy the assays and which achieve improved correlations between volume fraction of magnetite and magnetic susceptibility and Fe grade in all drill holes (Figures 7.3a and 7.3b). Also the correlation between the volume fraction of chalcopyrite and volume

fraction of magnetite and Cu assay is significantly improved, as expected (compare Figures 7.3c and 7.3d with Figures 7.2c and 7.2d respectively).

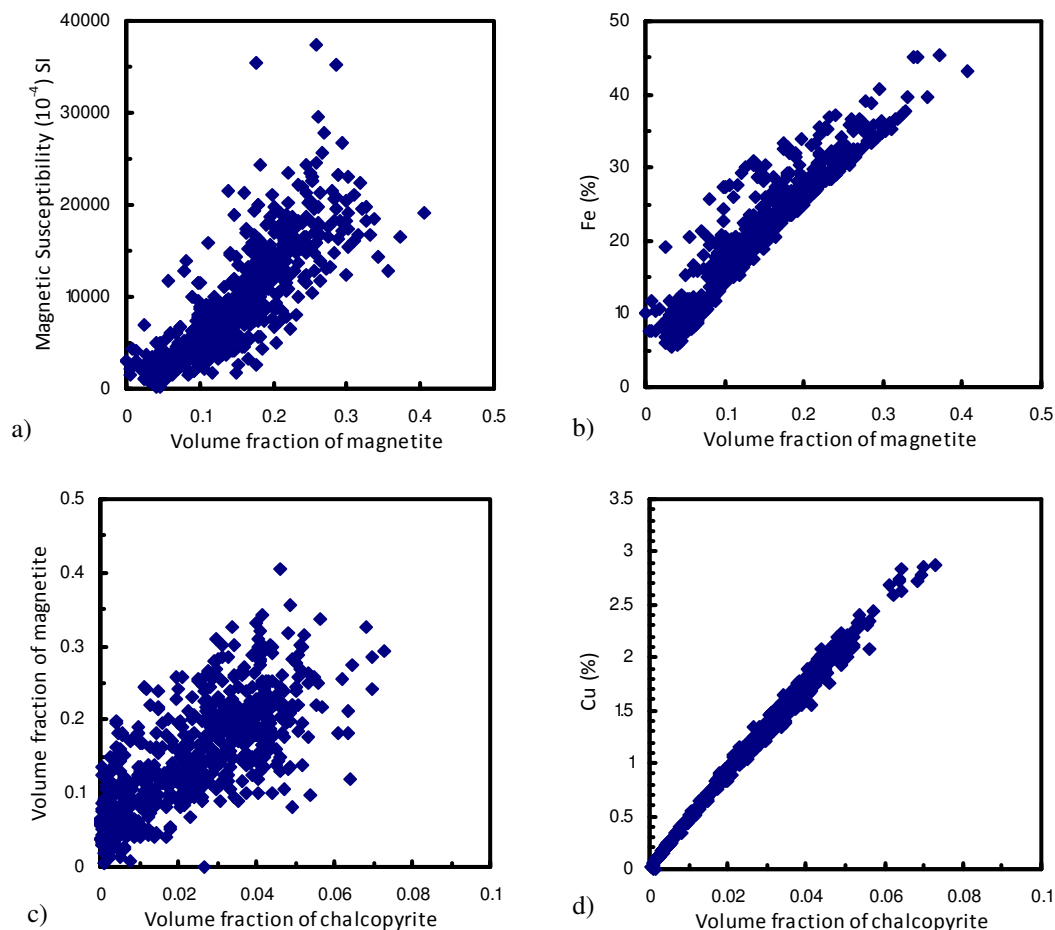


Figure 7.3. Correlation of adjusted volume fraction of magnetite with (a) magnetic susceptibility and (b) Fe grade. Correlation of adjusted volume fraction of chalcopyrite with (c) volume fraction of magnetite and (d) Cu grade. All samples are 2m assay intervals from all six drill holes.

### 7.5.3. Prediction of Density from Core Imagery and Assays

Measured densities for the entire sample set, derived from all six drill holes of Ernest Henry (EH432, EH446, EH556, EH574, EH633, and EH635), are compared with maximum densities predicted from imagery (after volume adjustment) in Figure 7.4. Predicted densities are in good correlation with measured densities (both Geotek and JKMRC immersion densities). Predicted minimum densities showed the same agreement with measured densities. The relative average error of predicted minimum and maximum densities when compared with measured Geotek densities was 3.9% and 3.5%

respectively. Although the difference in relative error of prediction of maximum and minimum density is not particularly significant, due to smaller relative error of prediction for predicted maximum densities they are considered here. Comparison of Figure 7.4 with Figure 7.1 highlights the improvement in density prediction from core images after adjustment of volume fractions of mineral phases to match assay data.

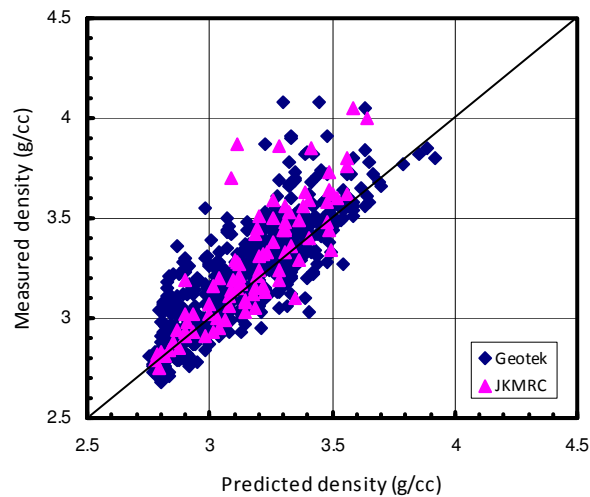


Figure 7.4. Predicted density from classified core imagery (after volume adjustment) versus measured density (Geotek and JKMRC) for 2m assay samples from all drill holes at Ernest Henry.

Comparison of predicted density with the in-house Ernest Henry Mine empirical density model (Chapter 5) shows a strong correlation (Figure 7.5). This engenders confidence in the densities predicted from core imagery. Ernest Henry's empirical model, which is purely based on Fe(%), is much easier for density determination than the approach through core imagery described here. However, the mineral volume fraction model underlying the new density prediction has value in its own right, e.g. for subsequent prediction of other physical and metallurgical properties. Moreover a reliable simple density estimation method based on a single assay parameter is not a situation that exists in all mine sites. Hence the proven ability to predict density simply from core imagery may have the potential to be widely adopted especially in view of resistance to downhole gamma-gamma logging.

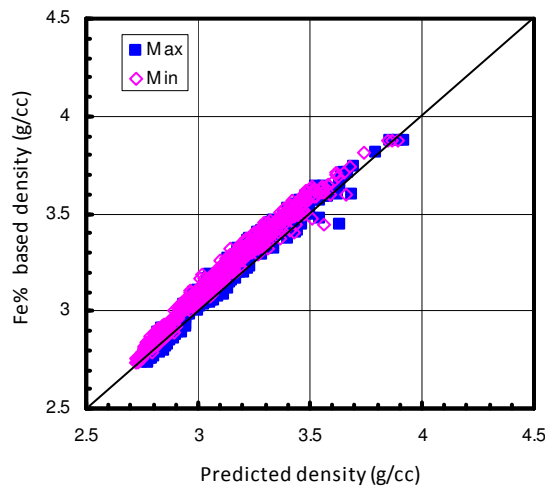


Figure 7.5. Predicted maximum and minimum densities from classified core images (after adjustment of volume fraction of mineral phases) versus measured densities for 2m assay samples from all six drill holes.

#### 7.5.4. Prediction of Magnetic Susceptibility

A wide range of petrophysical properties could be predicted using the mineral volumes, given mineral properties and appropriate numerical models. Here prediction of magnetic susceptibility and P-wave velocity are examined.

The relationship between magnetic susceptibility and magnetite content of rocks has been previously established by many researchers (e.g. Schön, 1996). A positive correlation exists between volume fraction of magnetite and magnetic susceptibility in general. At Ernest Henry there is a positive correlation ( $R^2=0.68$ ) between adjusted total volume fraction of magnetite estimated from classified core images and magnetic susceptibility recorded by the Geotek MSCL system (Figure 7.6). This is a marked improvement over the correlation before volume adjustment (Figure 7.2a). The slope of the regression line suggests a high magnetic susceptibility of approximately 6.5 SI for 100% magnetite. The high susceptibility of 6.5 SI compares closely with a published susceptibility value of 6 SI for magnetite (Schön, 1996). However a wide range of magnetic susceptibility (3 – 10 SI) for magnetite is reported (Dobrin, 1976). The wide range of susceptibility reported for pure magnetite depends on details of the magnetite volume content in the rock and its grain size; the higher the magnetite content and the coarser its grain size, the higher the susceptibility.

The reasonable correlation between magnetite content estimated from core images and magnetic susceptibility suggests that the estimated volume fraction of magnetite can be

used as a mean for prediction of magnetic susceptibility when such measurements are not available. Moreover if the susceptibility of magnetite is known, then the measured magnetic susceptibility data can be imposed as additional constraints during the volume adjustment, hence improving the mineral grade model.

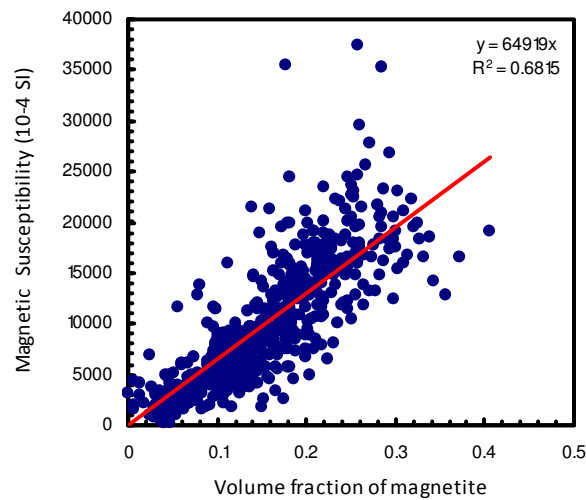


Figure 7.6. Total volume fraction of magnetite determined from classified core images (after adjustment) versus medians of magnetic susceptibility for 2m assay intervals from all drill holes from Ernest Henry. The red line is the linear regression line and as evident from regression equation the slope of regression suggests a high susceptibility of  $\sim 6.5$  SI for magnetite.

### 7.5.5. Prediction of P-wave Velocity

P-wave velocity upper and lower bounds can also be estimated from classified core images of Ernest Henry using the the Voigt and Reuss formulae and the reported P-wave velocities of minerals (Table 7.2). In this study P-wave velocities of mineral phases as shown in Table 7.4 were used. There is a large variation in reported P-wave velocity of some minerals (e.g. magnetite) as indicated by the differences between maximum and minimum reported P-wave velocities in Table 7.2. The range in Table 7.4 indicates this difference. The selection of P-wave velocities in Table 7.4 was on the basis of subjective assessments of the reported values from Table 7.2. Given the low concentration of pyrite at Ernest Henry, use of even highest P-wave velocity (8100m/s) does not have a significant impact on total P-wave velocity estimation.

Table 7.4. Published P-velocity values for mineral phases used for prediction of P-velocity from core images using Reuss and Voigt models

Mineral	Quartz	K-Feldspar	Magnetite	Pyrite	Chalcopyrite	Chlorite	Calcite
Vp (m/s)	6050	5680	6820	7300	4530	4916	6320
Range (m/s)	10	870	3220	743	970	-	380

Predicted P-wave velocities based on equations (7.1) and (7.2) using adjusted mineral volumes from core imagery and the mineral velocities from Table 7.4 are shown in Figure 7.7. Predicted values for each 2m interval are plotted in depth order for each drill hole. The reported P-wave velocity of most mineral constituents is quite high (more than 5500m/s; Table 7.2) resulting in estimation of a high P-wave velocity. Chlorite and chalcopyrite have relatively low P-wave velocity. The relatively low predicted P-wave velocity for EH574 is attributed to high chlorite content in that hole (Figure 7.8).

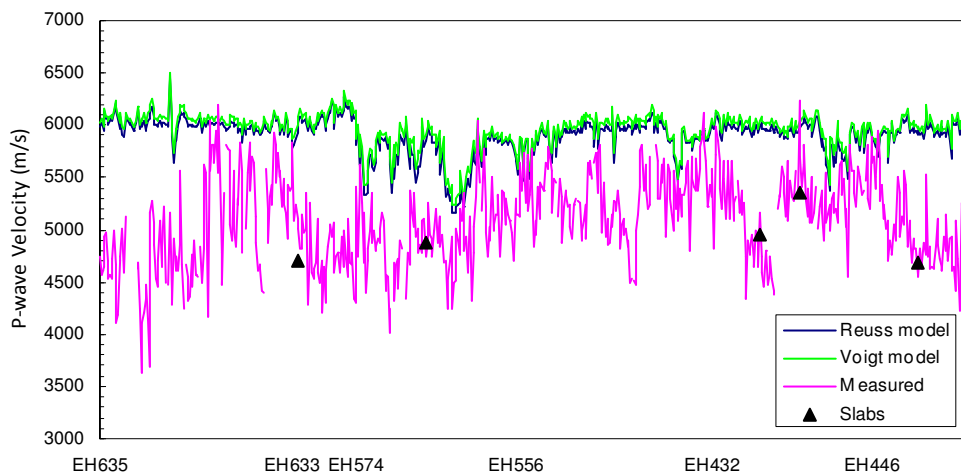


Figure 7.7. Predicted Reuss and Voigt P-wave velocity from classified core images (after adjustment to mineral volumes) compared with measured Geotek P-velocity for 2m assay samples from all drill holes of Ernest Henry. The samples originating from each hole are plotted in depth order. The triangles denote high frequency P-wave velocity measurements on small slabs derived from drill cores

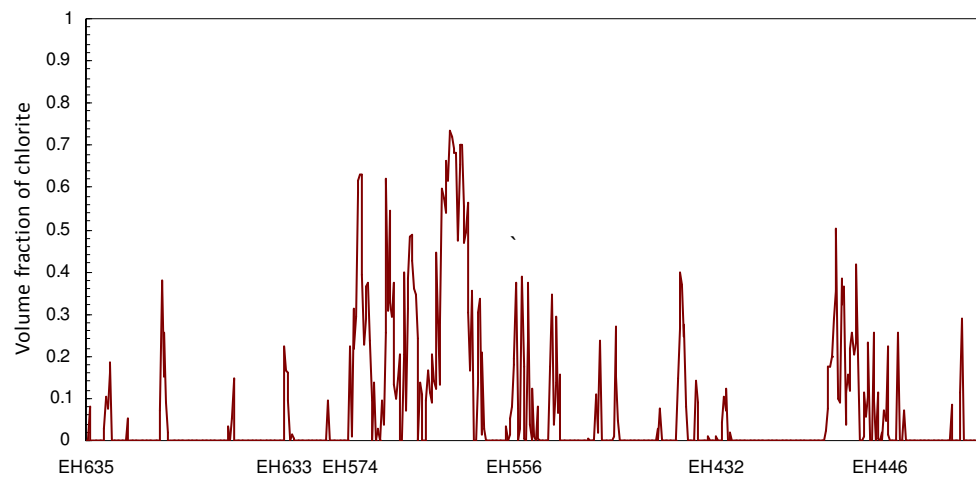


Figure 7.8. Volume fraction of chlorite estimated from classified core images plotted according to drill hole in depth order.

The comparison between predicted P-wave velocities and the P-wave velocity measured on core with the Geotek MSCL is illustrated in Figure 7.7. The image-based predicted P-wave velocities are not comparable with measured Geotek P-wave velocities. The Geotek values (median ~5000 m/s) are significantly lower than the predicted values (median ~6000 m/s). This 20% discrepancy is in part explained by uncertainties both in P-wave velocity measurements (Chapter 3) and predicted P-wave velocity. The best achievable accuracy of P-wave velocity measurements for half NQ size core of Ernest Henry is about  $\pm 3\%$ , i.e. approximately  $\pm 165$  m/s (Chapter 5).

Independent P-wave velocity measurements (as described in Chapter 5) were carried out on small slabs derived from Ernest Henry drill cores. High frequency transducers (i.e. 1MHz) were used for the P-wave velocity measurements. These independent P-wave velocity measurements range from 4600-5300m/s and are comparable to the Geotek P-wave velocities as illustrated in Figure 7.7.

In prediction of P-wave velocity from classified core imagery it was assumed that the only factors controlling bulk velocity are mineral abundances and intrinsic velocities. Other factors such as micro-cracks, P-wave velocity anisotropy, mineral textures and sample porosity could have an influence in P-wave velocity prediction. It should also be noted that the Voigt and Reuss models used for P-wave velocity prediction are simplistic since they presume isotropic samples. As mentioned earlier, there is a large variation in reported P-wave velocity of minerals (Table 7.2). One way to reconcile the predicted and measured P-wave velocities is to adjust the intrinsic P-wave velocities of mineral phases

in order to minimize a misfit measure such as the sum of squared differences between measured P-wave velocity and predicted Voigt P-wave velocity.

Initially intrinsic P-wave velocities for all mineral phases were allowed to vary in an inversion to minimize the misfit. Although this minimization improved the agreement between predicted and measured P-wave velocity however, the optimized P-wave velocity for quartz, carbonate and pyrite were much lower than the reported values. Due to this large discrepancy, intrinsic P-wave velocities for quartz, carbonate and pyrite were then fixed during inversion (Table 7.4) due to the limited range of values reported in the literature. Pyrite has a relatively large velocity range (Table 7.4), however due to small concentration of pyrite at Ernest Henry samples this large variation (743m/s) does not have a significant impact on P-wave velocity prediction.

This minimization improved the agreement between predicted and measured P-wave velocity at Ernest Henry (compare Figures 7.9 and Figure 7.7). The positive bias in predicted P-wave velocities has been removed. The root mean square (RMS) error of prediction is 454m/s. The adjusted intrinsic P-wave velocity of mineral phases is summarized in Table 7.5. The optimized P-wave velocity for magnetite (3604m/s) significantly changed when compared with the initial P-wave velocity estimate (6820m/s). However this optimized P-wave velocity is comparable with the velocity reported by Mavko et al (1998). The P-wave velocity of other mineral phases only marginally changed.

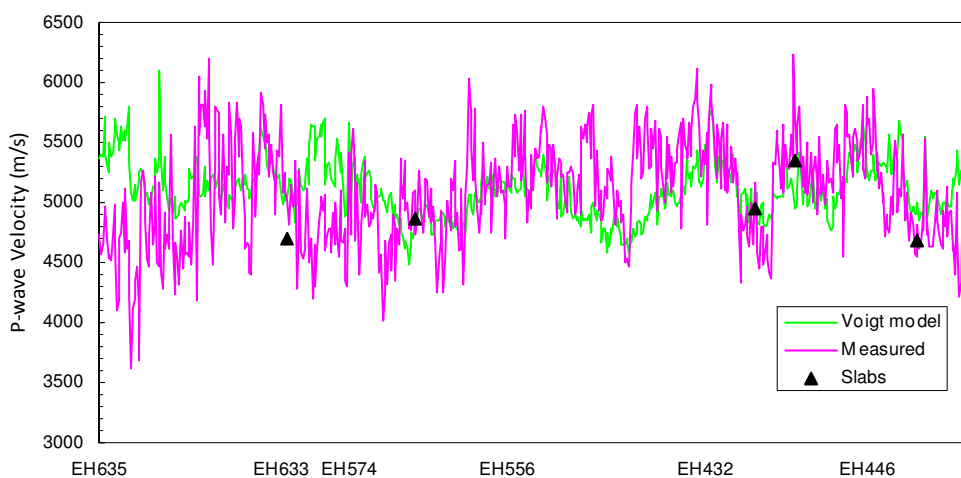


Figure 7.9. Predicted Reuss and Voigt P-wave velocity from classified core images (after adjustment to mineral volumes) using derived P-velocity from Table 7.4 compared with measured Geotek P-velocity for 2m assay samples from all drill holes of Ernest Henry. The samples originating from each hole are plotted in depth order.

Table 7.5. Derived P-wave velocity for mineral phases based on minimizing sum square error of measured P-wave velocity and predicted Voigt P-wave velocity.

Mineral	Quartz	K-Feldspar	Magnetite	Pyrite	Chalcopyrite	Chlorite	Calcite
Initial V <sub>p</sub> (m/s)	6050	5680	6820	7300	4530	4916	6320
Optimized V <sub>p</sub> (m/s)	6050	4911	3604	7300	5021	4808	6320

## 7.6. Relating Mineral Grades to Comminution Attributes

Physical properties can be predicted from core images provided that mineral volumes and their intrinsic properties are known. A similar approach was trialled for prediction of comminution attributes as well. Given that mineral volumes and comminution attributes (A\*b and BMWi) are available for selected intervals a least squares regression approach was adopted to predict “intrinsic comminution properties” for each mineral phase using the Voigt formula. Estimation of “intrinsic comminution properties” enables prediction of A\*b and BMWi in intervals of core where these measurements are not available.

Table 7.6 shows the coefficients (“intrinsic comminution properties”) derived for each mineral phase after least square regression. The correlation coefficient ( $R^2$ ) between measured and predicted A\*b is 0.43. The  $R^2$  value between measured and predicted BMWi is 0.33. The root mean square error of prediction for A\*b and BMWi are 33.3 and 1.68 kWh/t respectively. It should be noted that mineral grade estimates were not available for all comminution test samples and from a total of 142 comminution tests, only 106 tests were used here. Image-based prediction accuracies of A\*b and BMWi are comparable with the universal models based on petrophysical properties (Figure 5.19). However the least square approach for prediction of comminution attributes are based on 7 predictors (i.e. mineral grade).

Stepwise regression (Chapter 4) analysis of A\*b versus volume fraction of mineral phases, indicates that the most important phases that have an impact on A\*b are quartz, magnetite and pyrite. The coefficients of A\*b for these mineral phases were all positive i.e. an increase in volume fraction of any of these three phases will increase A\*b and consequently the rock becomes softer in terms of crushing. This interpretation is based on statistical analysis of regression result. Magnetite and quartz have a positive coefficient in the regression term for A\*b model suggesting an increase in their abundance will increase A\*b and as a results the material become softer for crushing. However given the low proportion of quartz in Ernest Henry drill core sample (average 5%), its effect on A\*b compared to magnetite will be minor.

Similarly stepwise regression analysis of BMWi, indicated that the significant phases are quartz and magnetite. The coefficients of BMWi for these two phases were both negative i.e. an increase in volume fraction of any of phases will decrease the BMWi value, and hence the rock sample will become easier to grind. These conclusions are consistent with observations by Strohmayer et al (1998) that an increase in quartz or magnetite content increases the mill throughput at Ernest Henry.

Table 7.6. Derived coefficients for mineral phases for prediction of A\*b and BMWi.

Mineral	Quartz	K-Feldspar	Magnetite	Pyrite	Chalcopyrite	Chlorite	Calcite
A*b Coefficient	263.5	-12.4	431.4	443.7	-418.2	48.9	58.0
BMWi Coefficient	-6.0	12.7	-0.8	2.7	3.2	11.0	11.9

Predicted and measured A\*b and Bond mill work index for all 2m core samples from Ernest Henry are presented in Figure 7.10 and Figure 7.11 respectively. The predictions are based on the mineral grades estimated from core images and derived coefficients (Table 7.6) substituted into the Voigt formula. Although there are some outliers, the predicted values mostly lie within the range of measured values, and there is a moderate qualitative agreement in terms of the observed trends with depth in each drill hole. However prediction of the high values of BMWi is not accurate. Although these models (Figures 7.10 and 7.11) are not very accurate, they do have potential for general prediction of comminution attributes during the mine planning stage.

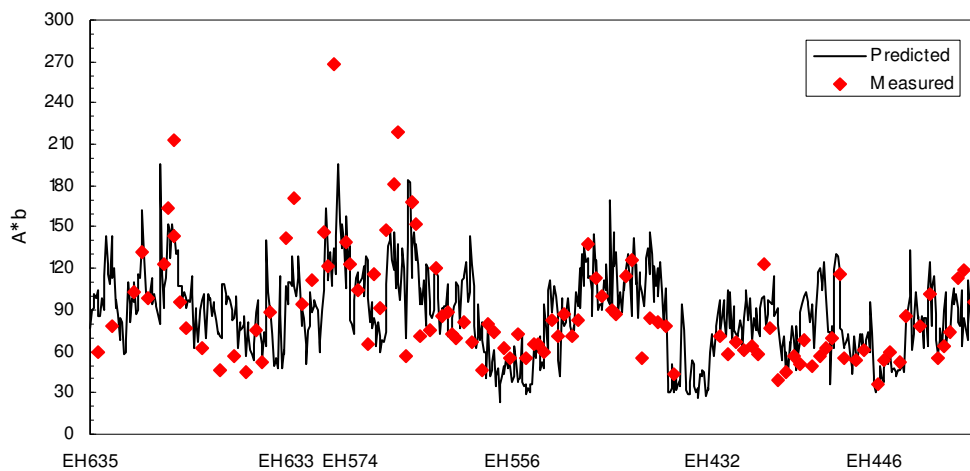


Figure 7.10. A\*b predicted from core imagery for the entire Ernest Henry dataset. The measured A\*b values are plotted for comparison. The samples originating from each drill hole are plotted in depth order.

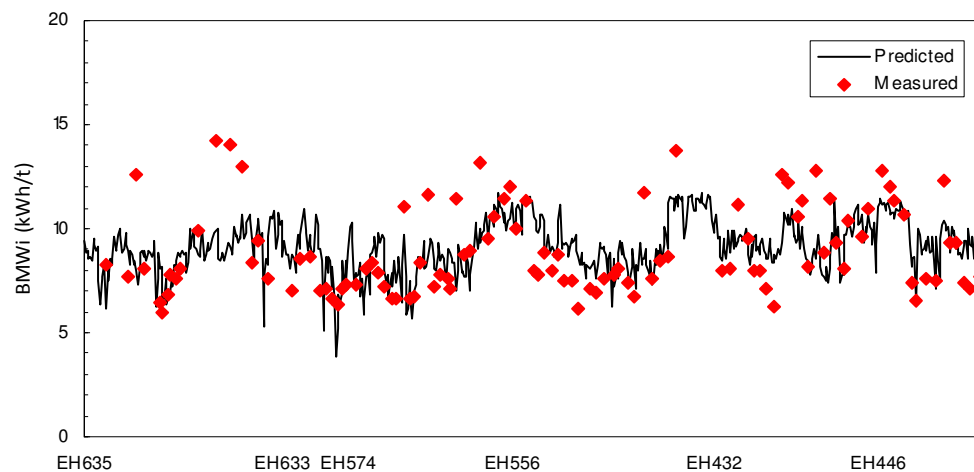


Figure 7.11. BMWi predicted from core imagery for the entire Ernest Henry dataset. The estimated BMWi is also plotted for comparison. The samples originating from each drill hole are plotted in depth order.

Mill throughput can be predicted if  $A^*b$ , BMWi and ore density are available (Chapter 5). Here mill throughput is predicted from image-based predictions of  $A^*b$  (Figure 7.10), BMWi (Figure 7.11) and density (Figure 7.4). In order to visualize throughput variability with depth in the drill holes, predicted throughput for all 2m core samples are plotted in depth order in each drill hole in Figure 7.12.

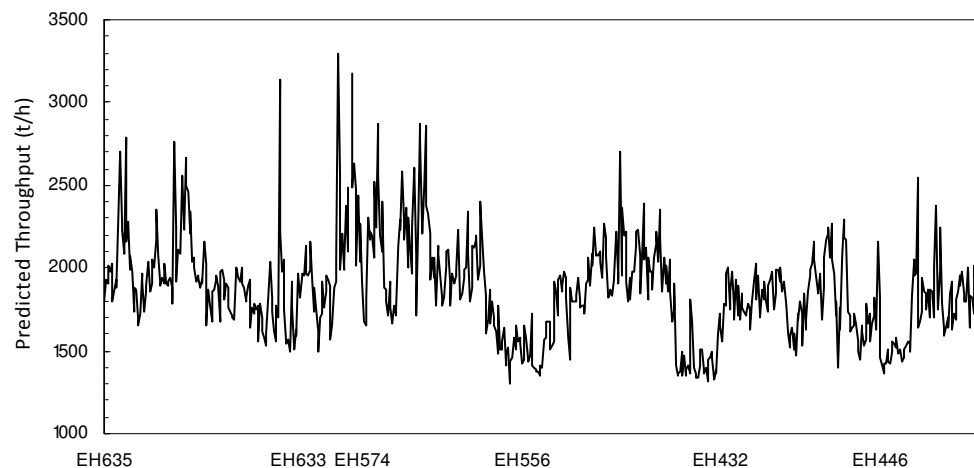


Figure 7.12. Predicted mill throughput. The samples originating from each drill hole are plotted in depth order.

Figure 7.12 shows that low throughput is expected in the upper part of EH556, but throughput increases with depth mainly due to a gradual increase in the proportion of magnetite which renders the samples soft to crush and easy to grind. The trend in EH574 indicates that the throughput is expected to decrease in deeper part of the drill hole.

## 7.7. Concluding Remarks

A novel approach for prediction of physical properties and comminution attributes based on classified core images was presented. High resolution continuous core images were captured using the Geotek MSCL system. Capturing core images is not new, however the MSCL system can provide high spatial resolution imagery with consistent illumination that is suitable for automated classification and analysis. To the best of the author's knowledge, prediction of density, P-wave velocity, magnetic susceptibility and comminution attributes ( $A^*b$  and  $BMWi$ ) from core images has never previously been investigated.

Reliable prediction of bulk density from classified core imagery could represent an important new technique for onsite density determination. Prediction of density from core imagery could provide an alternative approach to conventional sample or downhole measurements.

Prediction of petrophysical properties from core images is affected by factors such as difficulty in identification of mineral phases, limitations of the mixing models, and uncertainty in intrinsic properties of minerals. Discrepancies in the published intrinsic properties are likely due to variations in mineral composition and microstructure together with the diverse range of protocols used for measurement.

The optical estimates of mineral phases at Ernest Henry were not comparable with assay data. Hence predicted density values were not accurate when compared with measured values (average relative error of 8.9%). A linear programming algorithm was used in order to improve the volume estimates of mineral phases. This approach improved the density prediction (average relative error of 3.5%) and provided a degree of confidence in prediction of other physical properties. Measured magnetic susceptibility correlated well with estimated magnetite content. The magnetic susceptibility of pure magnetite used in the mixing models at Ernest Henry was estimated to be 6.5 SI.

Predicted P-wave velocity from classified core images, after volume adjustment, was also compared with the Geotek measured value. Given the uncertainties involved in both measured and predicted P-wave velocity, close agreement between such values was not necessarily expected. However the significant discrepancy (~20%) was well beyond what was expected for statistical and experimental errors and indicated issues with the intrinsic values used in the mixing models. Least squares optimization of P-wave velocity values for mineral phases significantly improved the agreement between measured and predicted

velocity. The optimization process suggested that magnetite at Ernest Henry has a very low P-wave velocity, comparable with the lowest values reported in the literature. Adjustment of the magnetite velocity in the mixing model had the most significant impact on P-wave velocity prediction.

Finally a novel approach for prediction of  $A^*b$  and  $BMWi$  values from mineral volume percentages was presented. The “intrinsic comminution properties” estimated from least square regression provided a means for prediction of  $A^*b$  and  $BMWi$  in intervals of core where these measurements are not available. Although the comminution models are not very accurate, however they have the potential for use during mine planning.

Stepwise regression analysis showed that magnetite, quartz and pyrite are the important mineral phases that have an impact on  $A^*b$  measurements. An increase in the volume fraction of these mineral phases makes the rocks softer for crushing. Quartz and magnetite are the most important mineral phases controlling the grinding behavior with an increase in volume fraction of quartz or magnetite makes the rocks softer for grinding.



# CHAPTER 8

---

## Conclusions

### 8.1. Summary of Main Results

Conventional comminution tests are a vital component in every mine plant design because comminution behaviour governs both the cost of equipment and its operating efficiency. Comminution tests are usually conducted on a limited number of large samples, owing to the high costs and long lead times involved. Therefore a strong incentive exists to find alternative means for efficiently characterizing comminution behavior for a truly representative suite of ore samples. Comminution is affected by factors such as ore physical characteristics (e.g. hardness). Measurement of petrophysical properties is quicker and cheaper than comminution testing. Therefore, petrophysics could represent an important new source of data for development of comminution models. Prediction of comminution attributes could then enable characterisation of mill throughput performance. The relationships between petrophysical parameters and comminution attributes have not been systematically investigated previously.

The potential for inferring comminution behavior from petrophysical properties of drill core has been investigated in this thesis. Magnetic susceptibility, gamma attenuation density, P-wave velocity, P-wave amplitude and digital core imagery were recorded on representative drill core from two case study sites (Ernest Henry IOCG mine and Cadia East Au-Cu Porphyry deposit) using an automated petrophysical core logging system. This thesis was a component of a large AMIRA “geometallurgy” research project (P843). Small-scale comminution tests for crushability ( $A^*b$ ) and grindability (Bond mill work index,  $BMWi$ ) were performed on selected 2m intervals of the same drill core under the auspices of the wider project. The availability of these small-scale physical test data provided a unique opportunity to explore the relationship between the petrophysical properties and comminution behaviour of precisely the same rock samples.

The main issue at Ernest Henry is mill throughput prediction for low grade materials (<0.6% Cu) which are much harder than high grade zones in terms of crushing and grinding. Thus effective characterization of mill performance was a high priority. At Cadia East effective selection of comminution equipment is a challenge. Cadia East ores

are hard (with small dynamic range) in terms of both crushing and grinding. Therefore effective characterisation of comminution behavior was critical.

Universal and class-based modeling approaches were investigated. Modeling of  $A^*b$  generally has better accuracy than BMWi using petrophysical properties. This may be due to the fact that petrophysical properties and crushability are measured on whole rock while BMWi is measured on crushed composite samples. Prediction of high BMWi (>10 kWh/t) is difficult, most probably because particles become more competent at crushed size.

Due to variability of rock types in most mineral deposits, establishment of a reliable universal model is usually problematic. In order to improve the accuracy of prediction, novel class-based geometallurgical modeling approaches were devised and implemented at Cadia East and Ernest Henry. The objective was to divide the deposit into ore classes and to subsequently develop comminution models within each class. Comminution class definition based on petrophysical (or comminution) properties has not previously been investigated in mineral industry. Development of predictive models within classes enables characterization of comminution behaviour on samples where crushability and grindability measurements are not available. Thus, given petrophysical data, mining blocks can be populated with comminution classes and predicted comminution properties. These blocks can then be mined and treated in a selective manner to reduce the mill variability and hence optimize the processing.

At Ernest Henry, petrophysical classification (PC approach) resulted in better modeling of comminution parameters compared to universal models. At Cadia East the problem posed by the hard ore was compounded by the muted petrophysical contrasts typical of porphyry deposits. Nonetheless, a classification based on comminution parameters ( $A^*b$  and BMWi) provided a means for prediction of comminution classes from petrophysical and geochemical data. The results suggest that petrophysical measurements could be useful for prediction of comminution attributes ( $A^*b$  and BMWi) and ultimately, mill throughput, at both sites. "Useful" in this context means that the models could be used in practice during mine feasibility stage for process planning purposes.

Magnetic susceptibility is related to  $A^*b$  at both case study sites. At Ernest Henry, as susceptibility increases  $A^*b$  increases (samples are easier to crush) because magnetite acts as crack initiator. At Cadia East,  $A^*b$  decreases as susceptibility increases. Magnetite mineralization at Cadia East is smaller in concentration than at Ernest Henry. The mineral

association of feldspar with magnetite (i.e. texture) is most probably the reason why low values of  $A^*b$  are generally associated with elevated susceptibility. Susceptibility and density showed a negative nonlinear relationship with  $BMWi$  at Ernest Henry. However no clear relationship was found between  $BMWi$  and magnetic susceptibility at Cadia East.

P-wave velocity and density also showed no clear correlation with  $BMWi$ . As mentioned earlier, this could be due to the fact that particles become more competent at crushed size. At Cadia East P-wave velocity showed a negative correlation with  $A^*b$  but there was no clear relationship between density and  $A^*b$ .

Magnetic susceptibility proved to be effective for characterization of alteration styles at both case study sites. Propylitic and skarn alteration types at Cadia East were characterized by relative high susceptibility. At Ernest Henry, potassic and carbonate alteration classes were characterized by relatively low magnetic susceptibility.

The potential of classified core images for prediction of petrophysical and comminution parameters at Ernest Henry also investigated. Classified core images have the potential for prediction of density. They can also be used to estimate comminution attributes.

This chapter summarizes the results of the present research in the following subsections.

## **8.2. Relationship Between Petrophysics and Comminution**

Published literature suggests that comminution behaviour can be related to both destructive and non-destructive rock strength parameters. Non-destructive measurements (e.g. Young's modulus) are more desirable as they are quicker and easier than destructive tests. Calculation of dynamic Young's modulus requires measurements of density, P-wave and S-wave velocities. However, S-wave velocity measurement is normally not available, in which case P-wave modulus is a good estimator of dynamic Young's modulus.

P-wave velocity has been used in many geotechnical applications for rock strength characterisation. Therefore it was expected that comminution parameters ( $A^*b$  and  $BMWi$ ) would be related to P-wave velocity more effectively than other petrophysical properties. However, at Ernest Henry magnetic susceptibility showed better correlation with comminution parameters than P-wave velocity (Section 8.4).

### 8.3. GEOTEK Multi-Sensor Core Logger (MSCL) System

The geometallurgical mapping and mine modeling project (P843) was focused primarily on drill cores. Boreholes could not be accessed at case study sites for downhole geophysical logging. A Geotek MSCL system for semi-automatic measurement of petrophysical properties and for capturing core images was evaluated. The use of MSCL system within the P843 project provided an opportunity to assess suitability of such system for production petrophysical core logging of archival drill core.

The Geotek system can provide virtually continuous petrophysical data on drill core, both full core and split half core. Within this research the MSCL system has been successfully used to record the petrophysical properties and digital images of drill cores from the Cadia East deposit and the Ernest Henry mine. The system had never been previously used on drill core from metalliferous mines, therefore system evaluation and modification to the sensors was required to adopt the system for diamond drill core logging. Sensors installed on the logger can deliver data with adequate accuracy and precision for geometallurgical purposes if care is taken in system operation and calibration.

The intrinsic sensitivity of the MSCL density, P-wave velocity, and magnetic susceptibility sensors is quite high. The precision and accuracy achievable in production logging are reduced by many factors. However, the main factor contributing to the uncertainty in petrophysical measurement with the MSCL system is the core thickness. As it decreases, small errors in absolute thickness can be responsible for large relative errors in the measured parameter. Thus accurate measurement of petrophysical data on “NQ size” half-core (~2.2cm radius) becomes difficult. In addition, the splitting of the core was poor over many intervals in core from the two case study sites and variability in the “feed” for the logger also translates into greater uncertainty in the petrophysical data.

The accuracy of petrophysical measurements was assessed on a series of NQ size core samples. The average relative error of gamma ray attenuation density compared to standard water immersion density measurement (bulk density) was  $\pm 0.51\%$  for Cadia East cores. For Ernest Henry materials the average relative error between immersion and gamma densities is  $\pm 1.12\%$ . The decrease in accuracy was attributed to an increase in gamma source collimator aperture size. The accuracy of Geotek P-wave velocity compared to Pundit P-wave velocities was  $\pm 2.3\%$ . Comparison of Geotek susceptibilities with a hand held KT-9 kappameter showed an excellent agreement between measurements.

In production logging the accuracy of petrophysical properties is affected by uncertainties due to core thickness. P-wave velocity is affected not only by uncertainties due to core thickness but also by uncertainty in the intrinsic delay time of the transducers and by the travel time through the core boat and sonic gel. The accuracy achieved in production logging was approximately  $\pm 1.35\%$  for density,  $\pm 6.5\%$  for P-wave velocity, and  $\pm 1\%$  for magnetic susceptibility. P-wave amplitude is mainly affected by acoustic coupling.

For future petrophysical measurements using the MSCL, NQ half-core should be avoided if at all possible. If NQ half-core is the only material available, then the core boats should be re-designed, to prevent rotational sliding of the core in the core boat and preferably to permit direct contact between the fluid-filled roller and the underside of the core. The rotation of the core results in incorrect thickness and P-wave velocity and amplitude recording. One modification to existing core boat is making holes in the core boat through which the P-wave velocity measurements are taken. The holes could help coupling issues and would eliminate the need for application of sonic gel. The errors in production measurements across HQ half-core will probably be no larger than NQ half core, since the HQ core boat is wider and the core is heavier so there is less likelihood of significant rotation of one with respect to the other.

Significant effort was devoted to improving the quality of MSCL petrophysical data by modification and replacement of petrophysical sensors, and by refinement of procedures, including calibration. Both half and whole core aluminum calibrators were fabricated for density measurement. To enable magnetic susceptibility measurements on drill cores from Ernest Henry, the system was modified to accommodate susceptibilities up to 1 SI. Also a formula was developed to correct susceptibility measurements on half cores. The P-wave velocity system was reconfigured towards the end of data acquisition to improve coupling by installation of opposing reciprocating transducers. An inductive coil conductivity meter with higher dynamic range compared with original sensor was also incorporated to the MSCL (after core logging of the two case study sites). However, the sensor coil sensor proved very sensitive to temperature.

Overall the “standard” Geotek MSCL system needs significant modification so that it can provide rapid high quality collecting of petrophysical data on archival core material. For future work it would be advantageous to investigate replacement of the existing P-wave velocity system with high frequency ultrasonic devices of “fixed transducers distance” applied to core surface. This change would remove the uncertainty in core thickness measurements and eliminate the transit delays through core boat and sonic gel. Addition

of a natural gamma sensor to the MSCL could potentially provide useful information for ore and alteration characterisation. Recording of a full-wave form sonic log as part of velocity measurement would also likely provide additional detailed information for material characterisation. With additional modifications, the MSCL logging system has the potential to be used for petrophysical data acquisition for mineral exploration programs or environmental studies in addition to geometallurgical applications.

#### 8.4. Geometallurgical Modeling : Universal Approach

Universal models were investigated for both case study sites by regression and neural network methods. At Ernest Henry a positive correlation ( $R^2=0.37$ , RMS error=37.6) was established between susceptibility and  $A^*b$  for 142 samples. This means that the higher the susceptibility (the higher the magnetite content), the softer the rocks are for crushing at Ernest Henry, because magnetite acts as a crack initiator.

Multiple regression of four petrophysical properties (P-velocity, P-amplitude, gamma density and magnetic susceptibility) against all available  $A^*b$  and BMWi data was also investigated at Ernest Henry. The RMS error of prediction for  $A^*b$  and BMWi is 34.3 and 1.61 kWh/t respectively. These models are not very accurate.

Magnetic susceptibility acts as a proxy for prediction of  $A^*b$  at Cadia East, where an increase in susceptibility suggests that the rocks becomes “very hard” in terms of crushing, i.e. a negative correlation between susceptibility and  $A^*b$  ( $R^2=0.23$ ) for 122 samples. Although prediction of  $A^*b$  based purely on susceptibility is not very accurate, the empirical model has merit in terms of its simplicity.

A universal model for prediction of  $A^*b$  from magnetic susceptibility and P-wave modulus using neural network approach was developed for Cadia East. The root mean square error of prediction is 5.31. The neural network approach has a slightly better performance (~1.4% improvement in relative error) than the conventional regression technique. However this difference in prediction accuracy via the two methods is not significant. Therefore it is appropriate to initially assess the simpler conventional statistical techniques as a first step, before applying the more complex neural network approach.

A perfect match between measured and predicted  $A^*b$  is not expected given the uncertainties in determination of  $A^*b$  and petrophysical measurements. The achieved

accuracy of 11.8% for A\*b model could be useful for general characterisation of ore crushability at Cadia East during the mine feasibility stage.

## **8.5. Geometallurgical Modeling : Class-based Approach**

In most cases universal models suffer from ore variability. For this reason, a class-based approach could provide a better prediction of processing behavior. Four different approaches for geometallurgical class definition for development of predictive comminution modeling were devised and implemented at the two case study sites.

Geometallurgical class definition based on geological information (GC approach) is regarded with great caution in the mineral industry. This is mainly because geological observations are subjective, qualitative and often suffer from poor quality control. An advantage of using petrophysical classes (PC approach) in geometallurgical class definition is that petrophysical properties are quantitative and objective. Creation of geometallurgical classes based on comminution parameters (CC approach) is a direct approach for comminution modeling of an orebody. The CC approach requires a sufficient number of comminution tests to represent the processing behavior of the orebody; in such cases potential geometallurgical classes can be determined through integration of petrophysical and comminution attributes (CPC approach).

### **8.5.1. Ernest Henry Comminution Modeling**

Developing comminution models using classes based on combination of lithology and alteration logs was not successful at Ernest Henry because visual logging was inconsistent. Development of predictive comminution models of A\*b and BMWi within petrophysical classes provided an effective characterization of ore comminution behavior and throughput prediction. Four classes were created (PC approach) based on density, magnetic susceptibility, P-wave velocity and P-wave amplitude using a cluster analysis method. Ore crushability (A\*b) and grindability (BMWi) of samples in each class can be predicted from petrophysical properties using multiple regression models.

The models developed for these classes were significantly better than universal models. The overall  $R^2$  and RMS error values between predicted and measured A\*b are 0.63 and 27.3 respectively. The overall  $R^2$  and RMS error between predicted and measured BMWi are 0.51 and 1.39 kWh/t respectively. The predicted values provided a basis for

continuous downhole prediction of mill throughput. Comparison of the pre-existing Ernest Henry throughput model with a class-based throughput model for a wide range of data showed that the class-based models can provide better prediction of mill performance at Ernest Henry. An accuracy of approximately  $\pm 20\%$  in prediction of comminution attributes is adequate in practice for process planning purposes. Therefore petrophysical-based comminution models could be useful for such purposes.

Automated prediction of comminution classes was also assessed using the neural network technique and minimum distance classification approach. The neural network predicted the comminution classes in an independent hole with an accuracy of 72% while the accuracy of the minimum distance algorithm was 60%. The use of neural network methods for prediction of comminution classes is an alternative approach to comminution modeling using petrophysical classes (PC approach). This approach does not require development of separate comminution models for A\*b and BMWi as in the PC approach.

### 8.5.2. Cadia East Comminution Modeling

Classes based on alteration data were tested as potential geometallurgical classes at Cadia East. Classification based on petrophysical properties (PC approach) was also evaluated. However for each classification approach comminution attributes in all classes displayed little variability. For this reason an attempt was made to characterize comminution behavior at Cadia East using comminution classes approach (CC approach).

Four classes were created based on variability of A\*b and BMWi around the respective mean values for the entire population. Therefore each class represents a specific comminution behavior as characterized by A\*b and BMWi values. Created classes were then linked to petrophysical properties and geochemical assays in a “training” set. To assess the performance of different algorithms, comminution classes were predicted in a hole that had not been included in training set. The performance of a minimum distance algorithm and a neural network approach were compared.

In the majority of cases the performance of both approaches in predicting comminution classes was more than 50% accurate. The performance of neural network approach in prediction of comminution behavior in three independent holes was better (by ~10%) than the minimum distance algorithm. The prediction accuracy of neural network approach ranged from 51% to 77%. Accurate prediction of comminution classes using

petrophysical data was difficult at Cadia East. However, comminution classes approach (CC) has the potential to be useful for characterisation of mill performance.

### 8.6. Image Based Prediction of Comminution Behavior

A novel approach for prediction of density and comminution attributes from classified core images from Ernest Henry was illustrated in this thesis. To the best of the author's knowledge, prediction of comminution properties from core images has not been investigated previously.

Classified core images provided volume estimate of mineral phases. Given density values for individual minerals, bulk density can be predicted as a volume weighted sum of those densities.

The classified estimates of mineral abundance were not compatible with assay data at Ernest Henry. Nor were predicted density values accurate when compared with measured values (average relative error of 8.9%). As a result the volume estimates were adjusted using intrinsic densities and chemical formulae of minerals via a linear programming algorithm in order to satisfy the assay data. The adjusted volumes significantly enhanced the density prediction (average relative error of 3.5%). Prediction of density from classified core images can be regarded as an important outcome since it could provide an alternative approach to downhole measurement.

In addition, a novel approach for prediction of  $A^*b$  and  $BMWi$  values from mineral grades was presented. The coefficients estimated for mineral phases from least square regression provided a means for prediction in intervals of core where test measurements are not available. The predicted values provide a basis for prediction of mill throughput as well. The comminution models, however, are not particularly accurate with RMS errors of 33.3 and 1.68 kWh/t for  $A^*b$  and  $BMWi$  respectively.

Use of core images for prediction of petrophysical properties and comminution attributes carries uncertainties. Reliable separation of mineral phases from optical core images is generally difficult. Moreover there is additional uncertainty owing to the variability of chemical composition of mineral species. Also the bound models used in this research are very simple. However, the disadvantages of this approach are compensated by its advantages. Capturing images of drill cores is quick, safe, relatively cheap and logistically simple.

## 8.7. Concluding Remarks

This thesis was motivated by the potential for prediction of comminution attributes from petrophysical data. The AMIRA P843 project provided a golden opportunity to compare petrophysical data directly with small-scale comminution tests conducted on the same core samples. Data from two mine sites (Ernest Henry IOCG and Cadia East porphyry Au-Cu) were acquired and analyzed.

The two case studies from different geological environments, different mineralization styles and different scale of operation showed that petrophysical data can provide useful information for characterization of comminution behavior. Predictive comminution models based on petrophysical properties enabled an alternative prediction of mill throughput performance. The developed comminution models were affected by uncertainties in determination of comminution attributes and measurements of petrophysical properties. Nevertheless the models could be useful for mine planning purposes during mine feasibility assessment. Improved incorporation of spatial variability is the major advantage of the approaches described in this study. The comminution modeling approaches outlined are robust, can be applied to other deposits and can be extended to incorporate other information such as assays or geotechnical data.

A major challenge during this research was recording petrophysical properties using the Geotek system during production core logging while evaluating, modifying and preparing logging protocols. The accuracy achieved in production logging was approximately  $\pm 1.35\%$  for density,  $\pm 6.5\%$  for P-wave velocity, and  $\pm 1\%$  for magnetic susceptibility. Further modification to the current Geotek system is required to make it more suitable for future geometallurgical research. However downhole geophysical logging provides a more efficient option for collecting petrophysical properties when drill holes are accessible.

The performance of petrophysical-based models can be improved by reducing uncertainties in petrophysical and comminution measurements, refining data classification techniques, and probably by increasing the number of petrophysical properties and incorporating other data, including assays, in the analysis.

The new approach for continuous prediction of petrophysical properties and comminution attributes from core imagery is cost-efficient and rapid. The initial work conducted in this field suggests that this approach has significant potential particularly if additional improvements can be made by applying more sophisticated mixing models, better

identification of mineral phases and integration with other data such as Hylogger and assays.

Future work on the link between petrophysical properties and comminution attributes depends primarily on the availability and quality of petrophysical data at mine sites. In addition, characterisation of comminution parameters is most effective when a number of petrophysical properties are recorded on the same samples. Downhole logging is the preferred method for petrophysical data collection due to rapid data acquisition of consistent data. Development of accurate comminution models also requires an adequate number of accurate comminution tests on carefully chosen intervals. It would be best to carry out comminution sampling after analysis of petrophysical, geological and geochemical data in order to ensure that the likely range of ore variability has been effectively sampled. With quality petrophysical data, and well-chosen comminution samples the data classification schemes and modeling techniques presented in this study could be widely applied for definition of geometallurgical domains and for comminution modeling.



# Bibliography

---

Alruiz, O.M., Morrell, S., Suazo, C.J., and Naranjo, A., 2009, A novel approach to the geometallurgical modeling of the Collahuasi grinding circuit, *Minerals Engineering*, Vol 22,12, pp1060-1067.

Annandale, G.J, Lorenzen, L., Van Deventer, J.S.J., and Aldrich, C., 1996, Neural net analysis of the liberation of gold using diagnostic leaching data, *Minerals Engineering*, Vol.9, No.2, pp 195-213.

ARPNSA (Australian Radiation Protection and Nuclear Safety Agency), 2005, Code of practice and safety guide for the safe use of fixed radiation gauge, August, Australian Government.

ASTM, 1978, Standard method for laboratory determination of pulse velocities and ultrasonic elastic constants of rocks, *Annual Book of ASTM Standards*, Part 19, D. 2845-69:356–363.

Aymler, J.A., Eisler, P.L., Methew, P.J., and Wylie, A.W., 1976, The use of natural gamma radiation for estimating the iron content of sedimentary iron formations containing shale bands, in *Nuclear Techniques in Geochemistry and Geophysics*, Vienna.

Baan, M., and Jutten, C., 2000, Neural networks in geophysical applications, *Geophysics*, 65, 4, pp1032-1047.

Balan, B., Mohaghegh, S., and Ameri, S, 1995, State-Of-The-Art in Permeability Determination From Well Log Data: Part 1- A Comparative Study, Model Development, SPE 30978, SPE Eastern Regional Conference & Exhibition, Morgantown, West Virginia, U.S.A., 17-21 September.

Balint, A., 1975, Sorting according to electrical conductivity, *J. S. African Inst. Min. Metall*, 40-44.

Barton, N., 2007, *Rock Quality, Seismic Velocity, Attenuation and Anisotropy*, 729p, Balkema.

Basford, P., Kelso, I., Briggs, T., Clifford, M., Anderson, R., and Fullagar, P., 2001, Development of a short-term model using petrophysical logging at Century Mine, North Queensland: ASEG Preview, No. 92, 19-24.

Basheer, I.A., and Hajmeer, M., 2000, Artificial neural networks: fundamentals, computing, design, and application, *Journal of Microbial Meth*, 43, 3-31.

Bearman, R.A, 1991, *The Application of Rock Mechanics Parameters to the Prediction of Crusher Performance*, Ph.D. Thesis, Camborne School of Mines.

Bearman, R.A., Briggs, C.A, and Kojovic, T., 1997, The Application Of Rock Mechanics Parameters To the Prediction of Comminution Behavior, *Minerals Engineering*, Vol 10,3, pp.255-264.

Berry, R., 2008a, Mineral Mapping, AMIRA P843 Sponsors meeting.

- Berry, R., 2008b, Automated Mineral Identification by Optical Microscopy. In: Section 7, AMIRA P843 Technical Report 1, 2008, p. 7.1-7.11.
- Berry, R., 2009, Mesoscale core imagery and classification, AMIRA P843 Technical Report 3.
- Bieniawski, Z.T., 1975, Point load test in geotechnical practice. *Eng Geol.* 9 (1):1–11.
- Boadu, F.K., 1997, Fractured rock mass characterization parameters and seismic properties: analytical studies. *J Appl Geophys*, 36:1–19.
- Bock, H.H., 1985, On some significance tests in cluster analysis, *Journal of Classification*, 2, 77 -108.
- Bohme, R.C., 1983, The development of a radiometric sorter for South African gold ores, *International Journal of Applied Radiation and Isotope*, 34, 417-428.
- Bojcevski, D., Johnson, N.W., Landmark, V., Mackenzie, J., and Young, M., 1998, Metallurgical Characterisation of George Fischer Ore Textures and Implications for Ore Processing, in *Proceedings: Mine to Mill Conference*, AusIMM: Melbourne, pp. 29-41.
- Bond, F.C., 1952, The Third Theory of Comminution, in *AIME Transactions*, pp. 484-494.
- Bond, F.C., 1960, Confirmation of the Third Theory, in *AIME Transactions*, pp. 139-153.
- Bonnici, N., Hunt, J., Walters, S.G., Berry, R., and Collett, D., 2008, Relating Textural Attributes to Mineral Processing- Developing a More Effective Approach for the Cadia East Cu-Au Porphyry Deposit, 9th International Congress for Applied Mineralogy, Brisbane, QLD, 8 - 10 September 2008.
- Bonnici, N., Hunt, J., Walters, S., Berry, R., Kamenetsky, M., McMahon, C., and Nguyen, K., 2009, Integrating meso- and micro - textural information into mineral processing: an example from the Ernest Henry Iron-Oxide Copper-Gold deposit, Queensland, Australia, 41st Annual Meeting of the Canadian Mineral Processors, Ottawa, Ontario, Canada, pp 259-278.
- Borsaru, M., 1993, Nuclear techniques for in situ analysis of coal and mineral deposits, *Nuclear Geophysics*, 7 (4), 555-574.
- Borsaru, M., M. Biggs, W. Nichols, and F. Bos, 2000, The application of prompt-gamma neutron activation analysis to borehole logging for coal, *Applied radiation & isotopes*, 54, 335-343.
- Borsaru, M., J. Charbucinski, P. Eisler, and C. Ceravolo, 1991, Neutron gamma logging in coal seams of variable iron content, *Nuclear Geophysics*, 5, 117-122.
- Brady, B. H. G. and Brown, E. T., 1985, *Rock Mechanics for underground mining*: London, George Allen & Unwin, 527 p.
- Briggs, N., 1991, Final Year Thesis, WA School of Mines, Curtin University.
- Brownlee, K.A., 1960, *Statistical theory and methodology in science and engineering*, John Wiley & Sons Inc., New York, 236p.

Bulatovic, S.M., Wyslouzil, D.M., and Kant, C., 1997, Operating practices in the beneficiation of major porphyry copper/molybdenum plants from Chile: Innovated technology and opportunities, A review, *Mineral Engineering*, Vol 11, 4, 313-331.

Bulled, D., and McInnes, C., 2005, Flotation Plant Design and Production Planning Through Geometallurgical Modelling, Centenary of Flotation Symposium, Brisbane, QLD, 6 - 9 June 2005, pp. 809-814.

Campbell, G, 1994. Geophysical contributions to mine development planning - a risk reduction approach, XV<sup>th</sup> CMMI Congress, South African Institute of Mining & Metallurgy, Vol. 3, pp283-325.

Cardenas, P., 2009, Personal communication.

Castagna, J.P., Batzle, M.L. and Eastwood, R.L., 1985, Relationship between compressional wave and shear wave velocities in elastic silicate rocks, *Geophysics*, 50, 571-581.

Chang, C., Zobach, M.D., and Khaksar, A., 2006, Empirical relations between rock strength and physical properties in sedimentary rocks, *Journal of Petroleum Science and Engineering*, 51, pp. 223–237.

Chow, J., 2007, Cadia East Open Pit Project Mining Study, Large Open Pit Mining Conference, Perth, WA, 10 - 11 September 2007, pp 37-44.

Clement, B., 2004, Cadia East Metallurgy Concept Study, Newcrest Mining Ltd, Internal Report.

Collier, P.A, and Bryant, J.D., 2003, Successful Mineral Resource Development at the Ernest Henry Copper-Gold Mine, NW Queensland, 5th International Mining Geology Conference, Bendigo, Victoria, 17-19 November, 73-88.

D'Andrea, D.V, Fisher, R.L, and Fogelson, D.E., 1964, Prediction of compression strength from other rock properties. *Colo Sch Mines*, 59 (4B):623–40.

David, D., 2007, The Importance of Geometallurgical Analysis in Plant Study, Design and Operational Phases, Ninth Mill Operators' Conference, Fremantle, WA, pp. 241-247.

Davis, J.C., 1986, *Statistics and data analysis in geology*, New York, John Wiley & Sons, 646p.

Davies, A.L., and McManus, D.A., 1990, Geotechnical application of downhole sonic and neutron logging for surface coal mining, *Exploration Geophysics* (21), 73-81.

Deniz, V. and Ozdag, H., 2003, A new approach to Bond grindability and work index: dynamic elastic parameters, *Minerals Engineering*, 16, pp 211-217.

Djordjevic, N., 2008, Image-based finite element modelling of the influence of rock texture on fragmentation, AMIRA P843 technical report 1, pp 12.1-12.23.

Dobrin, M. B., 1976, *Introduction to Geophysical Prospecting*, 3rd edition., McGraw-Hill, New York.

Doll, A., Barratt, D.J. and Wood, K., 2003, Comparison of UCS to Bond Work Indices, Available online: [http://www.sagmilling.com/articles/UCS\\_Wi\\_paper.pdf](http://www.sagmilling.com/articles/UCS_Wi_paper.pdf).

Donaldson, P.R., and Keller, G.V., 1974, Electromagnetic Surveying and Map Variation in Rock Strength, Colorado School of Mines, Final rept. 1 Nov 72-31 Aug 73.

Edwards, K.W., and Banks, K. M., 1978, A theoretical approach to the evaluation of in-situ Coal, in CIM Bulletin, pp. 124-131.

Ellis, D.V., 1987, Well Logging for Earth Scientists. New York: Elsevier. 532 pp.

Ellwood, B., 1980, Weathering effect on the magnetic properties in the Milledgeville Granite, Georgia., *Erath Planet. Sci. Lett.*, 55, 311-316.

Emerson, D.W, and Yong, M.P., 1994, The electromagnetic and electrical conductivity properties of some sulphide rocks and ores, Final Report, AMIRA Project P369A.

Emilsson, J., 1993, Geophysical multi-parameter logging techniques applied to ore exploration in the Skellefte Field, MSc thesis, Tekniska Högskolan i Luleå, Sweden, (unpubl.).

Entwisle, D C, and McCann, D M, 1990. An assessment of the use of Christensen's equation for the prediction of shear wave velocity and engineering parameters: in *Geological Applications of Wireline Logs* (Eds: A Hurst, M A Lovell, and A. C. Morton), Geological Society Special Publication, No. 48, 347-354.

Evans, H.B., 1965, GRAPE a device for continuous determination of material density and porosity: *Transactions of 6th SPWLA Annual Logging Symposium*, 6 (2): I-25(B).

Everell, M.D., 1972, Empirical relations between grinding selection functions and physical Properties of Rocks, *Trans. SME-AIME*, 252, 300-306.

Fallon, G.N., 2003, Volume Based Petrophysical Interpretation of Mineralogy for Grade Estimation in Metalliferous Deposits, Unpublished PhD Thesis.

Fallon, G.N. and Fullagar, P. K., 1997, Optimising the drilling budget with geophysical logging: *Proceedings of 3rd International Mine Geology Conference*, Launceston, AusIMM Publ. 6/97, 167-174.

Fallon, G.N., Fullagar, P.K., and Zhou, B., 2000, Towards grade estimation via automated interpretation of geophysical borehole logs, *Exploration Geophysics*, 31, 236-242.

Ferrara, G., Preti, U., and Meloy, T.P., 1989, Inclusion shape, mineral texture and liberation, *International Journal of Mineral Processing*, 27, 295-308.

Finn, D.J., 2006, Late Stage Phyllic Alteration in the Cadia East Copper-Gold Porphyry Deposit NSW Implications to Mineralisation, Unpub B.Sc. Hons thesis, University of Tasmania 108 p.

Firth, D, 1999. Log analysis for mining applications, Reeves Wireline Services

Fullagar, P.K., 2000, The Expanding Role of Mine Geophysics: *Proceedings of 4th International Mining Geology Conference*, AusIMM Publication, 3/2000, pp 301-314.

Fullagar, P.K., 2005, A review of meso-scale petrophysics at metalliferous mines: Fullagar Geophysics Pty Ltd Report AM01F-1.

Fullagar, P.K., 2006, Personal communication.

Fullagar, P.K., 2009, Personal Communication.

Fullagar, P.K., and Fallon, G.N., 1997, Geophysics in Metalliferous Mines For Orebody Delineation and Rock Mass Characterisation, in Proceedings of Exploration 97, 4th Decennial International conference on Mineral Exploration, Toronto, edited by A.G. Gubins, pp. 573-584.

Fullagar, P.K., Zhou, B., and Fallon, G.N., 1999, Automated interpretation of geophysical borehole logs for orebody delineation and grade estimation: Mineral Resources Engineering, 8, 269-284.

Fullagar, P.K., Zhou, B, and Turner, R., 2005, Quality Appraisal For Geophysical Borehole Logs, ACARP Project C13016, 53p.

Garrett, J. H., 1994, Where and why artificial neural networks are applicable in civil engineering, J. Geotechnical Eng., 8, 129–130.

GEOTEK, 2000, Documentation for GEOTEK Multi-Sensor Core Logger (MSCL), available online: [www.geotek.co.uk](http://www.geotek.co.uk).

Gerland, S., and Villinger, H., 1995, Nondestructive density determination on marine sediment cores from gamma-ray attenuation measurements, Geo-Marine Letters, 15, 111-118.

Gladwin, M.T., 1982, Ultrasonic stress monitoring in underground mining, Int J Rock Mech Min Sci., 19, 221–8.

Goodman, R. E., 1980, Introduction to rock mechanics, John Wiley & Sons, 478 p.

Grasty, R.L., 1979, Gamma ray spectrometric methods in uranium exploration-theory and operational procedures. In: Hood P.J. (Ed.), Geophysics and Geochemistry in the Search for Metallic Ores. Geological Survey of Canada, Economic Geology Report, 31, 147-161.

Gunn, D., and Best, A., 1998, A new automated nondestructive system for high resolution multi-sensor core logging of open sediment cores: Geo-Marine Letters, 18 (1), 70-77.

Gupta, A. and Yan, D.S., 2006, Mineral Processing Design and Operation An Introduction, Elsevier, 693p.

Hartigan, J.A., 1985, Statistical theory in clustering, Journal of Classification, 2, 63-76.

Hashin, Z., and Shtrikman, S., 1963, A variational approach to the elastic behavior of multiphase materials, J.Mech.Phys.Solids, 11, 127-140.

Hassoun, M. H., 1995, Fundamentals of Artificial Neural Networks, MIT Press, Cambridge.

Hatherly, P.J., Medhurst, T., Sliwa, R and Turner, R., 2005, A rock mass assessment procedure based on quantitative geophysical log analysis of coal measure sequences, *Exploration Geophysics*, 36, 112-117.

Hatherly, P., Sliwa, R., Turner, R., and Medhurst, T., 2003, Quantitative Geophysical Log Interpretation For Rock Mass Characterisation, ACARP Project No C11037, Exploration & Mining Report No 1196F, 128p.

Hattula, A, and Rekola, T, 2000, Exploration geophysics at the Pyhasalmi mine and grade control work of the Outokumpu Group, *Geophysics*, Vol.65,6, pp.1961-1969.

Hearst, J.R., Nelson, P.H., and Paillet, F.L., 2000, Well logging for physical properties: a handbook for geophysicists, geologists, and engineers, 483 pp., John Wiley & Sons.

Hecht, C.A., Bönsch, C. and Bauch, E., 2005, Relations of Rock Structure and Composition to Petrophysical and Geomechanical Rock Properties: Examples from Permocarboneous Red-Beds, *Rock Mech. Rock Engng.*, 38 (3), 197–216.

Hill, R., 1952, The elastic behavior of crystalline aggregate, *Proc.Physical Soc.*, London, A65, 349-354.

Hoek, E., Kaiser, P.K., and Bawden, 1995, Support of underground excavations in hard rock. Balkema, Rotterdam.

Holliday, J.R., Wilson, A.J., Blevin, P.L., Tedder, I.J., Dunham, P.D. and Pfitzner, M., 2002, Porphyry Gold-Copper Mineralisation in the Cadia district, eastern Lachlan Fold Belt, New South Wales, and its relationship to shoshonitic magmatism: *Mineralium Deposita*, v. 37, p. 100-116.

Howarth, D.F., 1984, Apparatus to determine static and dynamic elastic moduli, *Rock Mech Rock Eng.* 17, 255-264.

Huang, Y., and Wanstedt, S., 1998, The introduction of neural network system and its applications in rock engineering, *Engineering Geology Computational methods in engineering geology*, 49 (3-4), 253-260.

Hudson, J.A, and Jones, E.T.W, 1980, New BM. P-wave velocity measurements in a machine bored chalk tunnels. *Quart J Eng Geol.*,13:33–43.

Hung B.N., and Goldstein A., 1983, Acoustic Parameters of Commercial Plastics. *IEEE Transactions on Sonics and Ultrasonics*. Vol. SU-30,-4, 249-254.

Hunt, J., Berry, R., Bonnici, N., Walters, S., Kamenetsky, M., and McMahon, C., 2009, From Drill Core to Processing – A Geometallurgical Approach to Mineralogy and Texture from Meso- to Micro-Scale, Townswill.

Huntington, J., Quigley, M., Yang, K., Roache, T., Young, C., Roberts, I., Whitbourn, I.L., and Mason, P., 2006, A geological overview of Hylogging 18000m of core from the Eastern Goldfields of Western Australia, in *Proceedings Sixth International Mining Geology Conference*, pp 45-50.

ISRM-International Society of Rock Mechanics, 1981, Rock characterisation testing and monitoring. In: Brown ET (ed) Pergamon press, Oxford, 211p.

ISRM-International Society of Rock Mechanics, 1985, Suggested Method for Determining Point Load Strength: *International Journal of Rock Mechanics, Minerals, Science and Geomechanics*, Abstract, v. 22, no. 2, p. 51-60.

Jaeger, J.C., and Cook, N.G.W., 1976, *Fundamentals of rock mechanics*, Chapman and Hall, John Wiley & Sons, New York.

Kahraman, S. and Alber, M., 2006, Predicting the physico-mechanical properties of rocks from electrical impedance spectroscopy measurements, *International Journal of Rock Mechanics & Mining Sciences*, 43, 543–553.

Karakus, M., and Tutmez, B., 2006, Fuzzy and Multiple Regression Modelling for Evaluation of Intact Rock Strength Based on Point Load, Schmidt Hammer and Sonic Velocity, *Rock Mechanics and Rock Engineering*, 39, 45–57.

Karpuz, C., and Pasamehmetoglu, A.G., 1997, Field characterization of weathered Ankara andesites, *Eng Geol*, 46:1–17.

Kate, J.M, Sthapak, A.K., 1995, Engineering behaviour of certain Himalayan rocks. in Daemen JJK, Schultz RA, editors. *Proceedings of the 35th US symposium on rock mechanics*, Rotterdam: Balkema; p. 783–788.

Kilic, A., and Teymen, A., 2008, Determination of mechanical properties of rocks using simple methods, *Bull Eng Geol Environ*, 67, 237–244.

Killeen, P.G., 1997, Borehole geophysics: exploring the third dimension, in *Proceedings of Exploration 97: Fourth Decennial International Conference on Mineral Exploration*, edited by A.G. Gubins, pp. 31-42.

Killeen, P.G., Mwenifumbo, C.J., and Elliott, B.E., 1995, The pseudo-geological log: using geophysical logs as an aid to geological logging in volcanogenic massive sulfides, in *current research of Geological Society of Canada*, pp. 321-330.

Killeen, P.G., Mwenifumbo, C.J., Elliott, B.E., and C.J. Chung, 1997, Improving exploration efficiency by predicting geological drill core logs with geophysical logs, in *Proceedings of Exploration 97: Fourth Decennial International Conference on Mineral Exploration*, edited by A.G. Gubins, pp. 713-716.

Kitto, J.C., 2005, *Lithostratigraphy, Alteration and Geochemistry at the Cadia East Gold-Copper porphyry Deposit, NSW*, Unpub B.Sc. Hons thesis, University of Tasmania 127 p.

Klein, C., and Hurlbut, C.S., 1985, *Manual of Mineralogy*, 20th edition, John Wiley and Sons, 596p.

Knill, T.L., 1970, The application of seismic methods in the interpretation of grout takes in rock. in *Proceedings of the Conference on In Situ Investigation in Soils and Rocks*, British Geotechnical, Society, London, no. 8, p. 93–100.

Kohonen, T., 1982, Self-organized formation of topologically correct feature maps. *Biological Cybernetics*, 43, 59-69.

Kojovic, T., 2008a, Personal communication.

Kojovic, T., 2008b, Overview of Comminution Tests for Ore Characterisation, AMIRA International P843, Technical Report-1, February 2008.

Kojovic, T., 2009, Personal Communication.

Kojovic, T, Shi, F, Larbi-Bram, S and Manlapig, E, 2008. Julius Kruttschnitt rotary breakage tester (JKRBT) – Any ore, any mine, in Proceedings MetPlant 2008 Conference, pp 91-104 (The Australasian Institute of Mining and Metallurgy: Melbourne).

Lama, R.D., Vutukuri, V.S., 1978. Handbook on Mechanical Properties of Rocks, vol. II. Trans Tech Publications, Clausthal, Germany.

Lapointe, P., Chomyn, B.A., and Coles, R.L., 1984, Significance of susceptibility measurements from the Lac du Bonnet batholith, Manitoba, Canada, *Geoexploration*, Vol.22, 217-229.

Lawrence, W., 1999, Interpreting and understanding strata behaviour, 2<sup>nd</sup> Annual Longwall Mining Summit, Yeppoon. AJM Conferences.

Lee, M.W., 2006, A simple method of predicting S-wave velocity, *Geophysics*, 71, 161–164.

Leigh, G. M, 2009, Multi-scale Image Analysis for Process Mineralogy, PhD thesis, Julius Kruttschnitt Mineral Research Centre, University of Queensland, 323 pp.

Lemy, F., Hadjigeorgiou, J., Côté, P., and Maldague, X., 2001, Image analysis of drill core, Technical note published in *Trans. Inst Min Metall. (Sect. A: Min. technol.)*, 110, September–December 2001, The Institution of Mining and Metallurgy.

Lipton, I.T., 1997, A review of density determination methods for iron ore deposit evaluation, in *Ironmaking Resources and Reserves Estimation*, Perth, WA, pp 51-56.

Lu, M., 2006, *In-Situ Rock Stress: Measurement, Interpretation And Application*, Taylor and Francis Publication, 552p.

Magdalinovic, N., 1989, A procedure for rapid determination of the Bond work index hit, *Journal of Mineral Processing*, 27, 125-132.

Mark, G., Oliver, N.H.S., Williams, P.J., Valenta, R.K., and Crookes, R.A., 2000, The evolution of the Ernest Henry Fe-oxide-(Cu-Au) hydrothermal system, in Porter, T.M., ed., *Hydrothermal Iron Oxide Copper-Gold & Related Deposits: A Global Perspective*, volume 1: PGC Publishing, Adelaide, pp. 123-136.

Mark, G., Oliver, N.H.S., and Williams, P.J., 2006, Mineralogical and chemical evolution of the Ernest Henry Fe oxide–Cu–Au ore system, Cloncurry district, northwest Queensland, Australia, *Mineralium Deposita*, 40, 769–801.

Mavko G., Mukerji T. and Dvorkin J., 1998, *The Rock Physics Handbook*, Cambridge University Press.

McCann, D.M., Culshaw, M.G. and Northmore, K., 1990, Rock mass assessments from seismic measurements, in *Field Testing in Engineering Geology*, edited by F.G. Bell, Culshaw, M.G., Cripps, J.C. and Coeffy, J.R., pp. 257-66, Geological Society, London.

McCann, D.M., and Entwisle, D.C., 1992, Determination of Young's modulus of the rock mass from geophysical well logs, Geological Applications of Wireline Logs II: Geological Society Special Publication, 65, pp.317-325.

McNally, G., 1990, The prediction of geotechnical rock properties from sonic and neutron logs. Exploration Geophysics, 21, 65-71.

McNulty, T.P, 1998, Developing innovative technology, Mining Engineering, Vol.50, No.10, Oct., pp.50-55.

McQueen, J., 1967, Some Methods for Classification and Analysis of Multivariate Observations: Proceedings of the 5th Berkeley Symposium on Mathematics, Statistics and Probability, V.1, pp 281-297.

Michaux, S., and Kojovic, T., 2008, Comminution test work and modelling, In section 14, AMIRA P843 Technical report 1.

Mohaghegh, S., and Ameri, S., 1995, Artificial Neural Network as a Valuable Tool for Petroleum Engineers, Society of Petroleum Engineers, SPE 29220, pp1-6.

Morrell, S., 2004, Predicting the Specific Energy of Autogenous and Semi-Autogenous Mills from Small Diameter Drill Core Samples, Minerals Engineering, Vol 17/3, pp 447-451.

Morris, A.H., 1993, NSWC Library of mathematics subroutines, Naval Surface Warfare Centre, Dahlgren, Virginia 22448-5000.

Morris, W.A., and Walker, S.E., 1997, Borehole correlation in mineral deposits using geophysical parameters: Duck Pond, Newfoundland, in Proceedings of Exploration 97: Fourth Decennial International Conference on Mineral Exploration, edited by A.G. Gubins, pp. 705-708.

Moss, B.P., 1997, The partitioning of petrophysical data, in Development in Petrophysics, Geological Society Special Publication No.122, pp. 181-252.

Mueller, E.L., Morris, W.A., Killeen, P.G., and Balch, S., 1997, Combined 3-D interpretation of airborne, surface, and borehole vector magnetics at the McConnell nickel deposit, in Proceedings of Exploration 97: Fourth Decennial International Conference on Mineral Exploration, edited by A.G. Gubins, pp. 657-666.

Mutton, A.J., 1994, Application of Downhole Geophysical Logging to Lithological Correlation and Resource Assessment in Base Metal Deposits, AMIRA Symposium on the application of borehole logging to mineral exploration and mining, Perth, W.A., Australian Mineral Industries Research Association, pp1-36.

Napier-Munn, T. J., S. Morrell, Morrison, R., Kojovic, T., 1996, Mineral Comminution Circuits: Their Operation and Optimisation: Brisbane Australia, JKMR University of Queensland, JKMR Monograph Series in Mining and Mineral Processing 2, 413 pages.

Nelson, P.H., and Johnston, D, 1994, Geophysical and geochemical logs from a copper oxide deposit, Santa Cruz project, Casa Grande, Arizona, Geophysics, 59, 1827-1838.

Newcrest, 2010, Newcrest web site, Available online: <http://www.newcrest.com.au>.

Newcrest Mining Staff, 1998, Cadia gold-copper deposit: in *Geology of Australian and Papua New Guinean Mineral Deposits* (Eds D.A. Berkman and D.H. Mackenzie), pp641-646, AusIMM, Melbourne.

Nicholes, W., 2000, Application of the Sirolog downhole geophysical tool at Callide coalfields, East Central Queensland, in 4th International Mining Geology Conference, pp. 321-329.

Onodera, T.F., 1963, Dynamic investigation of foundation rocks, in situ. In: *Proceedings of the Fifth US Symposium on Rock Mechanics*, Pergamon Press, New York, p. 517-33.

Ortiz, J.D., and Rack, F.R, 1999, Non-invasive sediment monitoring methods. In: Abrantes, F. & Mix, A. (eds) *Reconstructing Ocean History: A Window into the Future*. Kluwer/Plenum, New York, 343-380.

Oyno, L., Tjetland, B.G., Esbensen, K.H., Solberg, R., Scheie, A, and Larsen, T.,1998, Prediction of petrophysical parameters based on digital video core images, *SPE Reservoir Evaluation & Engineering*, Feb 1998, pp 82-87.

Parker, R.L., and McNutt, M.K., 1980, Statistics for the one-norm misfit error, *Journal of Geophysical Research*, 85, pp 4429-4430.

Peaty, M., 2008, Personal communication.

Peng, S and Zhang, J, 2007, *Engineering Geology for Underground Rocks*, Springer, 320p.

Pflug, K.A., Killeen, P.G., and Mwenifumbo, C.J., 1997, Application of borehole geophysics to gold exploration, in *Proceedings of Exploration 97, Fourth Decennial International Conference on Mineral Exploration*, edited by A.G. Gubins, pp. 717-720.

Petrosyan, M.I, 1994, *Rock Breakage by Blasting*, Russian translation series, A.A. Balkema, Rotterdam, 141p.

Petruk, W., 2000, *Applied mineralogy in the mining industry*, Elsevier Science BV, 268p.

Preiss, K., 1968, Non-destructive laboratory measurement of marine sediment density in a core barrel using gamma radiation: *Deep Sea Research and Oceanographic Abstracts*, 15 (3), 401-407.

Preston, D.A., 1976, Correlation of certain physical and chemical properties in sedimentary rocks, *Proc. 17th US Sym. on Rock Mechanics*, pp 2A8-1- 2A8-6.

Price, D.G, Malone A.W, and Knill T.L., 1970, The application of seismic methods in the design of rock bolt system. In *Proceedings of the First International Congress, International Association of Engineering Geology*, Vol. 2, p. 740-52.

Raghu, N.S. and Ghose, K.A., 2006, *Engineered Rock Structures in Mining and Civil Construction*, Taylor & Francis Publication, ISBN 0415400139, 9780415400138, 520 p.

Reuss, A.,1929, Berechnung der fliessgrense von mishkristallen: *Zeitschrift fur Angewandte Mathematik und Mechanik*,9, 49-58.

Roach, M., 2006, Personal communication.

- Ryan, A., 1998, Ernest Henry Copper-Gold Deposit, in Australasian Institute of Mining and Metallurgy, Monograph 22, pp. 759-768.
- Rzhevsky, V. and Novik, G., 1971, The physics of rocks, Mir Publisher, Moscow.
- Salisbury, M.H., Milkereit, B., Ascough, G., Adair, R., Matthews, L., Schmitt, D.R., Mwenifumbo, J., Eaton, D. and Wu, J., 2000, Physical properties and seismic imaging of massive sulfides, *Geophysics*, 65 (6), 1882-1889.
- Schön, J., 1996, Physical properties of rocks: fundamentals and principles of petrophysics, xvi, 583 p. pp., Pergamon, New York.
- Schonharting, G., and Hall, J., 1982, Detailed susceptibility log of Iceland Research Drilling Project, DrillCore, Reydarfjordur, Eastern Iceland., *Journal of Geophysical Research*, 87, 6601-6604.
- Schultheiss, P.J., and McPhail, S. D., 1989, An Automated P-Wave Logger for Recording Fine-Scale Compressional Wave Velocity Structures in Sediments: Proceedings of the Ocean Drilling Program, 407-413.
- Schultheiss, P.J., and Weaver, P., 1992, Multi-sensor Core Logging For Science And Industry: OCEANS'92 'Mastering the Oceans Through Technology'. Proceedings, 2, 608-613.
- Scott, A., (Ed), 1996, Optimisation of open pit blasting, JKMRC, Brisbane.
- Scott, A., David, D., Alvarez, O., and Veloso, L., 1998, Managing fines generation in the blasting and crushing operations at Cerro Colorado mine, Mine to Mill Conference, Brisbane, pp141-148.
- Searle, R.C., 2008, Magnetic Susceptibility as a Tool for Investigating Igneous Rocks—Experience from IODP Expedition 304, *Scientific Drilling*, 6, 52-54.
- Selfe, G., 1997, New application of borehole geophysical logging in mining and mineral exploration, *Exploration Geophysics* (28), 127-129.
- Serra, O., 1986, Fundamentals of Well-log Interpretation, Vol. 2, The interpretation of logging data, Elsevier Science Publication. Co., Inc.
- Sharma, P.K, and Singh, T.N., 2008, A correlation between P-wave velocity, impact strength index, slake durability index and uniaxial compressive strength, *Bull Eng Geol Environ*, 67, 17-22.
- Simkus, A., and Dance, A., 1998, Tracking hardness and size: Measuring and monitoring ROM ore properties at Highland Valley Copper, Mine to Mill Conference, Brisbane, pp113-119.
- Sonmez, H., Gokceoglu, C., Nefeslioglu, H.A., and Kayabasi, A., 2006, Estimation of rock modulus: For intact rocks with an artificial neural network and for rock masses with a new empirical equation, *International Journal of Rock Mechanics and Mining Sciences*, 43 (2), 224-235.
- Starkey, J., 1997, Getting more from drill core: Preliminary SAG design, Randol Gold Forum, Monterey, California, May 18-21, pp 1-11.

Strohmayr, S J, Barns, K E, Brindley, S K and Munro, P D., 1998, Mineralogy Controlling Metallurgy at Ernest Henry Mining, in Proceedings Mine to Mill 1998, pp. 13-18 (The Australasian Institute of Mining and Metallurgy: Melbourne).

Strohmayr, S J, and Valery, W., 2001, SAG Mill Circuit Optimisation at Ernest Henry Mining, SAG 2001 Conference, University of British Columbia, 11-42.

Tan, P., Steinbach, M., and Kumar, V., 2006, Introduction to data mining, Pearson Education Inc., 769p.

Tew, A., Harvey, R., Marun, J., Anderson, R., and Strohmayr, S., 2003, Evolution of SAG Milling Performance – A Comparison of Alumbra and Ernest Henry, 8th Mill Operators' Conference, Townsville, QLD, 27-36.

Turk, N. and Dearman W.R, 1987, Assessment of grouting efficiency in a rock mass in terms of seismic velocities. Bull Int Assoc Eng Geol, 36:101–8.

Turk, N, and Dearman W.R, 1986, A suggested approach to rock characterization in terms of seismic velocities. In: Hartman HL, editor. Proceedings of the 27th US Symposium on Rock Mechanics, Society of Mining Engineers, p. 168–75.

Vatandoost, A and Fullagar, P.K, 2007, Prediction of dynamic Young's modulus from compressional wave velocity and density, in Proceedings 13<sup>th</sup> European Meeting of Environmental and Engineering Geophysics, Istanbul, 3 - 5 September.

Vatandoost, A., and Fullagar, P.K., 2009, Characterisation of Ore Crushability Using Petrophysical Properties, 7<sup>th</sup> International Mining Geology Conference, 17-19 August, Perth, Australia.

Vatandoost, A., Fullagar, P, and Roach, M., 2008a, Automated Multi-Sensor Petrophysical Core Logging, Exploration Geophysics, 39, 181-188.

Vatandoost, A., Fullagar, P, and Roach, M., 2008b, Multi-sensor Petrophysical Core Logging: Data Acquisition, Processing, and Preliminary Interpretation of Cadia East data, AMIRA International P843, Technical Report-1, 4.1-4.31.

Vatandoost, A, Fullagar, P, Walters, S and Kojovic, T., 2009, Towards petrophysical characterisation of comminution behavior, in Proceedings 41<sup>st</sup> Annual Meeting of the Canadian Mineral Processors, Ottawa, pp 619-640.

Voigt, W., 1928, Lehrbuch der Kristallphysik, Teubner, Leipzig.

Walters, S., 2008, Personal Communication.

Walters, S., 2009, Personal Communication.

Walters, S., Kojovic, T., 2006, Geometallurgical mapping and mine modelling (GeM<sup>III</sup>), the way of the future. In: Proceedings of SAG 2006, Vancouver, pp.411–425.

Wanstedt, S., 1993, An overview of recent research on geophysical logging in underground mines in Sweden, in Proceedings of the International Symposium on Borehole Geophysics for Minerals, Geotechnical and Groundwater Applications, Toronto, Oct 24-28.

- Ward, B., 1998, German Creek Mines rock strength from velocity logs. Unpublished report to Capricorn Coal Management Pty Ltd.
- Ward, J.H., 1963, Hierarchical Grouping to Optimize an Objective Function, *Journal of the American Statistical Association*, 58, 236 -244.
- Weber, M.E., Niessen, F., Kuhn, G. & Wiedicke, M., 1997, Calibration and application of marine sedimentary physical properties using a multi-sensor core logger, *Marine Geology*, 136, 151–172.
- Weiss, N.L., 1985, *SME Mineral Processing Handbook*, Society of Mining Engineers.
- White, J E, 1983. *Underground Sound* (Elsevier Publication: Amsterdam; Oxford: New York).
- Whitten, D.G.A. and Brooks, J.R.V., 1972, *The Penguin Dictionary of Geology*, Penguin Books Ltd, ISBN 014051.0494, 520p.
- Williams, S. R. and J. M. Richardson, 2004, Geometallurgical mapping: A new approach that reduces technical risk, 36<sup>th</sup> Annual Meeting of The Canadian Mineral Processors, Ottawa, Ontario.
- Wills, B.A., 1997, *Mineral Processing Technology*, 6<sup>th</sup> Edition, Butterworth-Heineman, Oxford.
- Wilson, A. J., 2003, The geology, genesis and exploration context of the Cadia gold-copper porphyry deposits, NSW, Australia, PhD thesis, University of Tasmania, Hobart, 335 p.
- Witten, I.H and Frank, E., 2005, *Data Mining: Practical machine learning tools and techniques*, Elsevier Inc., 525p.
- Xstrata, 2008, Xstrata Website Available online: <http://archive.xstrata.com>.
- Yang, Y.P., and Emerson, D.W., 1997, Electromagnetic conductivity of rock cores-theory and analogue results, *Geophysics*, 62 (6), 1779-1793.
- Yang, Y., and Zhang, Q., 1997, The Application of Neural Networks to Rock Engineering Systems (RES), *International Journal of Rock Mechanics and Mining Sciences*, 35 (6), 727-745.
- Young, R.P., Hill T.T., Bryan I.R., and Middleton R., 1985, Seismic spectroscopy in fracture characterization. *Quart J Eng Geol*, 18:459–79.
- Zhang, N., and Whiten, W., 2001, Determining mineral composition from assays, *International Heavy Minerals Conference*, Fremantle, WA, pp 81-85.
- Zhou, B., Hatherly, P., Guo, H., and Poulsen, B., 2001, Automated geotechnical characterisation from geophysical logs: Examples from Southern Colliery, Central Queensland, *Exploration Geophysics*, 32, 336-339.